Influence of the variability of the Kuroshio, the Oyashio, and the Pacific decadal oscillation on the northern hemisphere atmospheric circulation during the cold season

Adèle Révelard

THESE DE DOCTORAT DE L'UNIVERSITE PARIS VI

Ecole doctorale des Sciences de l'Environnement d'Ile de France (ED129)

Spécialité : Océanographie Physique et Climat

Présentée par **Adèle Révelard**

Influence de la variabilité du Kuroshio, de l'Oyashio, et de l'Oscillation décennale du Pacifique sur la circulation atmosphérique de l'hémisphère nord pendant la saison froide

Pour obtenir le grade de

DOCTEUR de l'UNIVERSITE PIERRE ET MARIE CURIE

Date de soutenance : 22 Février 2017

devant le jury composé de :

Rym Msadek	Rapporteur	CERFACS
Michel Déqué	Rapporteur	CNRM
Francis Codron	Examinateur	LOCEAN
Serge Planton	Examinateur	CNRM
Claude Frankignoul	Directeur de thèse	LOCEAN
Juliette Mignot	Co-directrice de thèse	LOCEAN

Remerciements

Avant tout, je souhaite remercier le professeur Claude Frankignoul, mon directeur de thèse, pour ces quatre belles années très formatrices que j'ai passées à travailler avec lui. J'ai énormément apprécié sa disponibilité mais aussi la confiance et la liberté qu'il a su m'offrir. Merci pour sa gentillesse et sa bienveillance, et pour nos discussions toujours enrichissantes. Il m'a donné l'opportunité de participer à des conférences internationales et de travailler avec des chercheurs étrangers renommés. Parmi ces chercheurs je remercie particulièrement Yong-Oh Kwon, pour son écoute et ses suggestions toujours très pertinentes.

Je remercie également Juliette Mignot, pour avoir gardé un œil sur moi pendant ces trois ans, avec dynamisme et franc-parler. Merci pour nos réunions toujours animées et stimulantes.

Merci à mes deux rapporteurs Rym Msadek et Michel Déqué, ainsi qu'à tous les membres de mon jury, pour avoir assisté à ma soutenance de thèse et pour la discussion qui s'en est suivie, conviviale et pertinente.

Je tiens à remercier aussi mes « coachs » Nathalie Sénnechael et Christine Provost, pour toutes leurs suggestions dans la préparation de ma soutenance et les nombreux moments passés ensemble dans ce couloir 46-45. Merci également à Julie Deshayes pour son coaching de dernière minute !

Merci à Javier Garcia-Serrano et Guillaume Gastineau, pour leur aide pendant ma première année de thèse pour les calculs de certaines variables synoptiques et la compréhension de la dynamique atmosphérique.

Des pensées pour Dany et Céline, qui m'ont beaucoup aidé lors des démarches administratives. Ce fut un plaisir à chaque fois que d'aller les voir dans leurs bureaux et d'en ressortir comme apaisée par leur positivisme : merci !

Je tiens beaucoup à remercier Lionel Gourdeau, tuteur de mon tout premier stage (en L1) et présent à ma soutenance de thèse. Sans lui, tout cela ne serait peut-être pas arrivé !

Merci à Julien et Paul, grâce à qui je ne me suis jamais sentie seule devant un problème informatique. Merci pour leur amitié et tous ces déjeuners et pauses café passés ensemble... sans oublier les parties de Molkky !

Mes trois années de thèse ont été particulièrement plaisantes grâce à l'atmosphère chaleureuse du bureau 513, ce bureau où il a fait si bon vivre avec mes chers « co-bureau » Anna et Nicolas. Merci pour tous ces moments partagés et toutes nos franches rigolades ! J'ai été tellement heureuse de vivre tout cela avec vous, et vous m'avez tellement manqué quand vous êtes partis ! Merci aussi à Tamara, notre pilote d'avion devenue maman lors de ma deuxième année, pour

m'avoir fait découvrir le tire-lait et pour l'ambiance très insolite du bureau à certains moments. Merci également à Tonia qui nous a rejoint par la suite, pour son amitié et pour avoir contribué au climat chaleureux de ce fameux bureau 513 !

Je remercie aussi Zoé, pour le chemin que nous avons parcouru ensemble depuis le M1, et pour toutes nos discussions captivantes sur les pôles, les voyages, la mer, la vie...

Merci à ma famille pour leur soutien et leur intérêt pour mon travail, et en particulier à mes parents et mes grands-parents, qui ont rendu mon retour à la vie parisienne possible et même confortable !

Enfin, je remercie Adrien, avec qui je vis les instants les plus magiques.

Résumé

L'objectif de cette thèse est d'étudier l'influence sur l'atmosphère de la variabilité des fronts océaniques associés aux extensions du Kuroshio (KE) et de l'Oyashio (OE), et de la différencier de l'influence des modes de variabilité grande échelle de la SST du Pacifique Nord, en particulier l'oscillation décennale du Pacifique (PDO). Nous utilisons pour cela la réanalyse atmosphérique ERA-Interim à partir de 1979, et des index déjà disponibles décrivant la variabilité des courants. Dans une première partie, nous nous focalisons sur l'influence du KE, en utilisant une méthode statistique de régression partielle avec décalage temporel, avec filtrage en amont du signal lié aux téléconnexions ENSO. L'index du KE décrit le caractère dynamique oscillatoire du courant à l'échelle décennale. Lorsque l'index est positif, le KE est plus fort, moins tourbillonnaire et sa trajectoire est plus au nord, et à l'inverse lorsque l'index est négatif. Nous montrons que la phase positive du KE est associée à un réchauffement des eaux de surface dans la région en aval du KE, ce qui induit un dégagement de chaleur et une réponse atmosphérique significative équivalente barotrope pendant la saison d'octobre à janvier (ONDJ), avec une anomalie positive de pression au centre du Pacifique Nord et sur l'ouest des Etats-Unis, et un renforcement du vortex polaire. Nous tentons de discerner les mécanismes pouvant engendrer cette réponse en analysant l'influence du KE sur l'activité synoptique. Dans une deuxième partie, nous utilisons une méthode statistique multivariable permettant d'analyser en parallèle les réponses atmosphériques aux différents forçages océaniques pouvant être corrélés entre eux. Cette méthode permet d'inclure, outre les indices décrivant la variabilité du KE et de l'OE, les principaux modes de variabilité grande échelle de la SST tels que la PDO qui est très corrélée à l'OE, les modes tropicaux tels qu'ENSO, mais également la variabilité de la glace de mer. La réponse atmosphérique étant très dépendante de l'état moyen de l'atmosphère, nous distinguons trois saisons : le début d'hiver (OND), l'hiver (DJF), et la fin d'hiver (FMA). En OND, nous retrouvons les résultats obtenus pour le KE dans la première partie. En hiver et fin d'hiver, en revanche, le KE n'a pas d'influence significative. Nous trouvons une influence significative de l'OE en OND et FMA, avec une réponse ressemblant à l'oscillation du Pacifique Nord indiquant un déplacement vers le nord de la dépression des Aléoutiennes (AL) et du jet stream, en accord avec l'analyse des tourbillons transitoires. En DJF, une trop forte multicollinéarité nous a contraint à ne pas considéré l'OE pour cette saison. La réponse à la PDO n'est pas très différente en OND et FMA, indiquant un déplacement vers le nord de l'AL et un renforcement du jet stream. En DJF, la structure de la réponse atmosphérique est différente et indique un déplacement vers le sud. La disparité entre nos résultats et ceux d'autres études précédentes s'expliquent par la différence

des périodes étudiées. La non stationnarité de la réponse atmosphérique est donc une question clé pour les recherches futures.

Abstract

The aim of this work is to study the influence on the atmosphere of the variability of the oceanic fronts associated with the Kuroshio and Oyashio Extensions (KE and OE), and to differentiate it from the influence of the main SST mode of the North Pacific, in particular the Pacific Decadal Oscillation (PDO). We use the atmospheric reanalysis ERA-Interim starting from 1979, and indices that describe the variability of the KE and OE that are already available. In the first part of this work, we focus on the KE influence, using lag partial regression analysis with the ENSO signal removed. The KE index describes the dynamical state oscillation of the current at decadal timescale. When the index is positive, the KE is strengthened, less turbulent, and its path is shifted north. The reverse holds when the index is negative. We show that the positive phase of the KE is associated with an anomalous warming of the oceanic surface in the region downstream of the KE, which generates enhanced heat flux to the atmosphere, and in October to January (ONDJ) leads to a downstream barotropic high response in the central North Pacific and over western United States, and an enhanced polar vortex. We try to understand the mechanisms behind this atmospheric response analyzing the KE influence on the synoptic activity. In the second part, we use a multivariate statistical method that allows us to analyze in parallel the atmospheric response to different oceanic forcings that may be correlated to each other. In addition to the KE and OE indices, we include in the analysis the main modes of SST variability of the tropical and northern hemisphere oceans, such as the PDO in the North Pacific and ENSO in the tropical Pacific. We also include sea ice variability in the Arctic. The atmospheric response being very dependent on the mean background flow, we distinguish between three seasons : early winter (OND), winter (DJF) and late winter (FMA). In OND, the multivariate analysis confirms the earlier results of the KE found by partial regression in ONDJ. In winter and late winter, however, the KE does not have any significant influence. We found a significant influence of the OE in OND and FMA, which resembles the North Pacific Oscillation (NPO), indicating a poleward shift of the Aleutian Low (AL) and the Jet Stream, in agreement with the analysis of the transient eddies. In DJF, too much multicollinearity constrained us to not consider the OE in this season. The response to the PDO is similar in OND and FMA, indicating a strengthening of the Jet Stream and a poleward shift of the AL. In DJF, however, the response is different and rather indicates a southward shift of the jet stream. The disparity between our results and past studies are explained by the difference in the periods considered. The non stationarity of the atmospheric response is therefore a key question for future researches.

Table des matières

Chapitre 1

Introduction

1.1 Le système océan-atmosphère : un système couplé

Le système climatique est un système d'interactions complexes entre l'atmosphère, l'océan, la cryosphère, la lithosphère et la biosphère. Parmi ces sous-systèmes, l'océan et l'atmosphère sont les principales composantes du système climatique, et leurs interactions sont fondamentales pour comprendre les processus dynamiques qui gouvernent le climat et sa variabilité. Tous deux communiquent leur énergie via des flux de chaleur radiatifs et turbulents (sensible et latent). Ces derniers dépendent d'une seule variable océanique, la température de surface de l'océan (SST pour *Sea Surface Temperature* en anglais), et de différentes variables atmosphériques, principalement la température de l'air, la vitesse des vents de surface, l'humidité relative et la couverture nuageuse. La SST joue donc un rôle clé dans le système climatique. Une anomalie de SST (définie comme l'écart par rapport à la moyenne saisonnière à long terme) génère un échauffement ou un refroidissement de l'atmosphère sus-jacente, ce qui modifie la température de l'air, le vent, et éventuellement la circulation atmosphérique de grande échelle. Ces changements vont, en retour, altérer le contenu thermique de l'océan et renforcer (rétroaction positive) ou atténuer (rétroaction négative) l'anomalie de SST. C'est ainsi que la variabilité de l'océan et l'atmosphère forment un système couplé. L'océan ayant une mémoire thermique beaucoup plus importante que l'atmosphère, les chercheurs ont suspecté, et ce dès les années 50, que les anomalies de SST pouvaient être utilisées pour la prévision du climat (Namias 1959, 1963, 1965 ; Bjerknes 1959, 1964, 1972).

Le couplage océan-atmosphère est beaucoup plus fort dans les tropiques que dans les moyennes latitudes, car la dynamique atmosphérique est différente dans les tropiques. Les eaux de surfaces sont plus chaudes et la chaleur latente dégagée par l'évaporation des eaux de surface peut rapidement affecter la convection profonde atmosphérique et la convergence ou la divergence des vents de surface, altérant ainsi les circulations de Walker et de Hadley. La circulation atmosphérique est donc fortement influencée par la SST. Une anomalie de SST engendre une réponse thermique directe de l'atmosphère, conduisant le plus souvent à des anomalies tropicales de grande échelle qui peuvent exciter des ondes de Rossby planétaires se propageant vers les hautes latitudes, affectant ainsi le climat global dans de nombreuses régions du globe via des effets atmosphé-

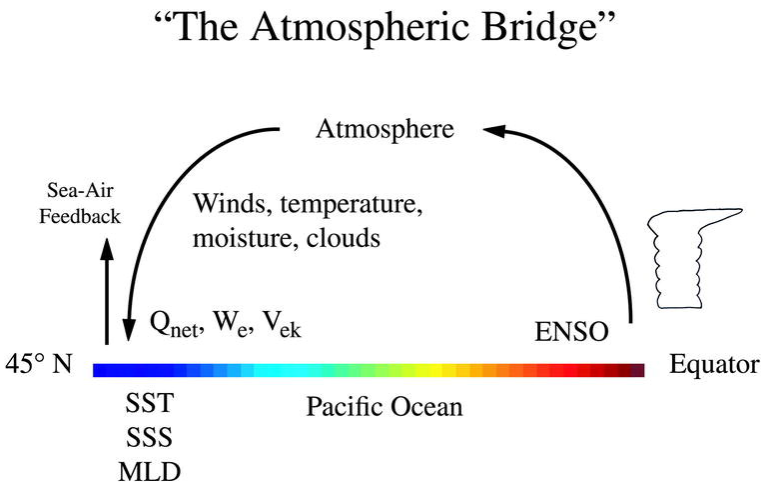

FIGURE 1.1 – Schéma du « pont atmosphérique » entre le Pacifique équatorial et le Pacifique Nord. Ce mécanisme est également valide dans le Pacifique Sud, l'Atlantique, et l'océan Indien. Q_{net} est le flux de chaleur net en surface, W_e le taux d'entrainement de la couche de mélange, V_{ek} les courants d'Ekman, SSS la salinité de surface, et MLD la profondeur de la couche de mélange. D'après Alexander et al. (2002) (Fig. 1)

riques à distance que l'on nomme « téléconnexions ». Le phénomène El Niño (El Niño Southern Oscillation, ENSO) est l'exemple le plus spectaculaire du couplage océan-atmosphère dans les tropiques, et les téléconnexions qui lui sont associées engendrent les fluctuations climatiques les plus importantes observées à l'échelle saisonnière et interannuelle dans les deux hémisphères. Durant un épisode El Niño, qui se produit tous les 3 à 7 ans, la SST est anormalement chaude au centre et/ou à l'est du Pacifique tropical, et le dégagement de chaleur latente déplace les zones de convection profonde vers le centre du Pacifique équatorial. Ces changements sont accompagnés par une convergence des vents de surface et une divergence des vents d'altitude, ce qui crée des anomalies de vorticité et excite des ondes de Rossby planétaires (e.g. Hoskins and Karoly, 1981). Ces ondes transportent de l'énergie vers les plus hautes latitudes et impactent le climat dans des régions lointaines à travers le mécanisme du « pont atmosphérique » illustré sur la figure 1.1 : en se propageant vers les plus hautes latitudes, ces ondes influencent les interactions entre l'écoulement moyen et le rail des dépressions (Trenberth et al. 1998), ce qui génère des anomalies de vent, de température, d'humidité et de couverture nuageuse dans ces régions, conduisant à des anomalies de courant d'Ekman, de flux de chaleur et de quantité de mouvement. L'océan répond à ces anomalies, modifiant la profondeur de la couche de mélange, la salinité et la SST. Ainsi, le phénomène ENSO a un fort impact global et peut générer des anomalies de SST dans les océans des moyennes et hautes latitudes via des téléconnexions atmosphériques. L'Amérique du Nord, où la variabilité naturelle du climat est en partie conditionnée par le mode Pacifique Nord-Américain (PNA), est fortement influencée par les téléconnexions ENSO.

Dans les moyennes latitudes, les anomalies de SST peuvent aussi être de grande échelle (échelle du bassin océanique) et compte tenu de la forte inertie thermique et dynamique de l'océan, ces anomalies peuvent persister plusieurs mois voire plusieurs années, ce qui peut constituer un forçage thermique considérable. Cependant, l'impact climatique est moindre car la dy-

namique atmosphérique y est différente et le dégagement de chaleur latente qui leur est associé n'induit pas une réponse aussi directe et intense que dans les tropiques (Hoskins et Karoly 1981). Dans les années 60, il a été supposé que la persistance des anomalies grande échelle de SST était due à une rétroaction positive de l'atmosphère sur l'océan (e.g. Namias 1963). Mais les travaux de recherche menés sur le sujet ont montré par les observations que l'atmosphère forçait l'océan, et non l'inverse (Davis, 1976 ; Trenberth, 1975 ; Haworth 1978). Ce constat a été confirmé par les simulations numériques de Salmon et Hendershott (1976) et le modèle stochastique de climat de Hasselmann (1976) et Frankignoul et Hasselmann (1977). Ce modèle a permis de montrer qu'au premier ordre, les interactions océan-atmosphère dans les moyennes latitudes sont dominées par le forçage de l'atmosphère sur l'océan, et que les anomalies persistantes de SST résultent du forçage stochastique de l'atmosphère. En effet, l'atmosphère ayant une faible persistance dans les moyennes latitudes (de l'ordre de quelques jours), le forçage de l'atmosphère sur l'océan peut être considéré en première approximation à basse fréquence comme un bruit blanc. Le modèle stochastique montre alors que le spectre de la réponse de l'océan à ce forçage est rouge, en accord avec les observations, la variance se concentrant sur les longues échelles de temps, fonction de la dissipation et des rétroactions air-mer. Ainsi, l'océan des moyennes latitudes se comporte comme un intégrateur de la variabilité intrinsèque de l'atmosphère, et les anomalies extratropicales de SST sont principalement la conséquence des anomalies de vent, de température et d'humidité associées à la variabilité naturelle stochastique de l'atmosphère. Aux plus longues échelles de temps, toutefois, l'advection océanique joue un rôle important dans l'évolution de la SST. Dans l'Atlantique Nord par exemple, la SST à basse fréquence est dominée par l'Oscillation Atlantique Multidecennale (AMO) (Kerr 2000), qui est un mode lié à la variabilité de la circulation thermohaline (Delworth et Mann 2000). Notons aussi la forte variabilité de la SST à méso-échelle, liée à l'activité tourbillonnaire de l'océan.

Bien que le modèle stochastique considère au premier ordre l'atmosphère sans longue « mémoire », Hasselmann (1976) a montré que des rétroactions étaient nécessaires afin que la variance n'augmente pas indéfiniment, ce qui n'exclue pas une variabilité plus basse fréquence de l'atmopshère. Les observations montrent en effet que l'atmosphère des moyennes latitudes varie également sur des plus longues échelles de temps. La variabilité atmosphérique se caractérise alors par des fluctuations de grande échelle correspondant à des modulations des différences de pression aux différents points du globe. Ces fluctuations peuvent être décrites par des structures spatiales fixes que l'on appelle « modes de variabilité » (Blackmon, 1976). Des techniques statistiques telles que la décomposition orthogonale aux valeurs propres (EOF pour *Empirical Orthogonal Function* en anglais) permettent de définir ces structures, en décomposant les données en fonctions orthogonales de manière à maximiser la variance expliquée par ces modes. Ainsi, la première EOF (EOF1) correspond à la structure de variabilité spatio-temporelle qui explique la variance la plus importante. Chaque EOF est associée à une composante principale, qui représente l'évolution temporelle de cette structure EOF. Dans le Pacifique Nord, l'analyse en composantes principales de la pression au niveau de la mer (SLP pour *Sea Level Pressure*) suggère qu'il existe deux modes de variabilité atmosphérique principaux : le premier est associé aux changements de la dépression des Aléoutiennes (AL pour *Aleutian Low*), tandis que le se-

cond consiste en un dipôle nord-sud et se nomme l'Oscillation Nord Pacifique (NPO pour *North Pacific Oscillation*) (Ceballos et al., 2009) (Figure 1.2).

Ces modes se projettent à plus haute altitude sur des structures de téléconnexion qui leur sont associées : l'AL est lié à la téléconnexion Pacifique Nord Américaine (PNA), et la NPO est liée à la téléconnexion du Pacifique Ouest (WP pour *West Pacific* en anglais). Ces modes de variabilité et leurs téléconnexions sont plus forts en hiver qu'en été, et modulent le climat eurasien et nord-américain en affectant le rail des dépressions, la température et les précipitations (e.g. Seager et al. 2004 ; Linkin et Nigam 2008). Ils résultent essentiellement de la variabilité intrinsèque de l'atmosphère, c'est à dire qu'ils n'ont besoin d'aucun forçage pour exister. Cependant, cela n'exclut pas qu'ils soient aussi influencés par un forçage externe. Alors que le mode NPO/WP varie essentiellement sur des courtes échelles de temps (< 1 mois ; Linkin et Nigam, 2008), le mode AL/PNA présente également des variations à l'échelle décennale (e.g. Overland et al. 1999) (Figure 1.3). Bien que le phénomène ENSO engendre des téléconnexions ressemblant à la PNA et explique une partie de cette variabilité basse fréquence, une part de celle-ci est indépendante des tropiques. L'océan des moyennes latitudes ayant une forte mémoire thermique, il a depuis longtemps été supposé que sa variabilité avait une influence sur l'atmosphère à grande échelle et pouvait ainsi générer de la variabilité décennale (Latif et Barnet 1994, 1996 ; Saravanan et al. 2000 ; Marshall et al. 2001).

A travers les changements de flux de chaleur et de tension de vents qui leur sont associés, ces

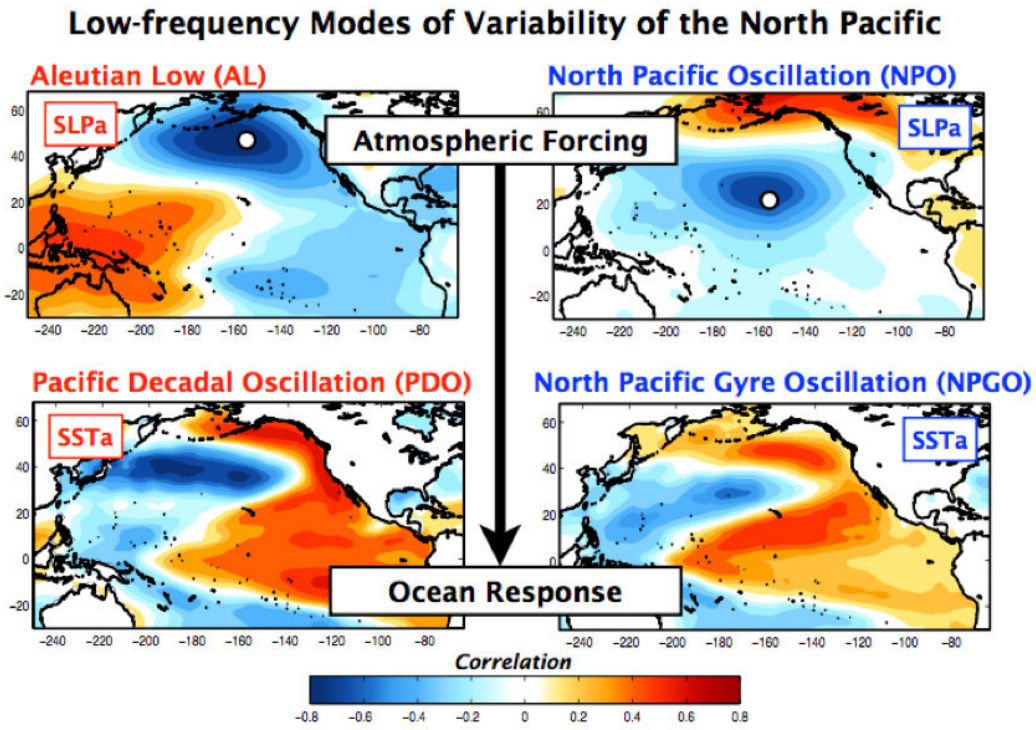

FIGURE 1.2 – (Haut) Cartes des corrélations des deux premiers modes de variabilité des anomalies de SLP (SLPa) dans le Pacifique Nord. (Bas) Cartes des corrélations des deux premiers modes de variabilité des anomalies de SST (SSTa) dans la même région. D'après Di Lorenzo et al. (2013) (Fig. 3)

modes de variabilité atmosphérique forcent des modes de variabilité océanique. Les deux premiers modes de variabilité de la SST dans le Pacifique Nord sont l'Oscillation Pacifique Décennale (PDO pour *Pacific Decadal Oscillation* en anglais) et l'Oscillation de la Gyre Nord Pacifique (NPGO pour *North Pacific Gyre Oscillation*) (Figure 1.2). Ces modes ont une partie équatoriale, et une partie extratropicale (e.g. Chen et Wallace 2016). Au nord de 20°N, la PDO se caractérise par une anomalie négative de SST au centre du bassin et près du Japon, et une anomalie positive au nord et le long de la côte ouest des Etats-Unis, ayant ainsi la forme d'un fer à cheval. La NPGO extratropicale se caractérise par une anomalie négative dans la gyre subtropicale, et une anomalie positive dans la gyre subpolaire. Dans les tropiques, la PDO est liée au phénomène ENSO et en particulier au mode El Niño canonique, c'est à dire au mode d'ENSO caractérisé par un échauffement maximal de l'océan dans la partie est du Pacifique équatorial. La PDO est ainsi associée à une anomalie positive de SST au centre et à l'est du Pacifique équatorial, et une anomalie négative dans le Pacifique Ouest. A contrario, la NPGO est liée au mode non-canonique d'ENSO (ou El Niño Modoki, Ashok et al., 2007), c'est à dire au mode d'ENSO qui se caractérise par un échauffement maximal de l'océan dans la partie centrale du Pacifique équatorial. Ceci reflète qu'une part importante de la variabilité interannuelle (périodes de 2 à 7 ans) et décennale (>7 ans) du Pacifique Nord est liée à celle du phénomène ENSO (Deser et al. 2004 ; Alexander et al. 2002 ; 2008 ; Vimont, 2005 ; Newman et al. 2003 ; Di Lorenzo et al. 2010 ; 2013). Cependant, au premier ordre, la partie extratropicale de la PDO et la NPGO sont forcés respectivement par l'AL et la NPO (Newman et al. 2003 ; Di Lorenzo et al. 2008 ; 2010 ; Chhak et al. 2009). Ce forçage se fait directement à travers les flux de chaleur et les courants d'Ekman, mais également de manière indirecte à travers des processus dynamiques océaniques qui résultent de ces modes de variabilité atmosphériques. En effet, l'AL et la NPO génèrent des anomalies dans le rotationnel du vent, provoquant des variations du pompage d'Ekman dans la région centre-est du Pacifique et ainsi des anomalies de hauteur de mer (SSH pour *Sea Surface Height* en anglais). La PDO et la NPGO sont d'ailleurs très bien corrélées aux deux premiers modes de

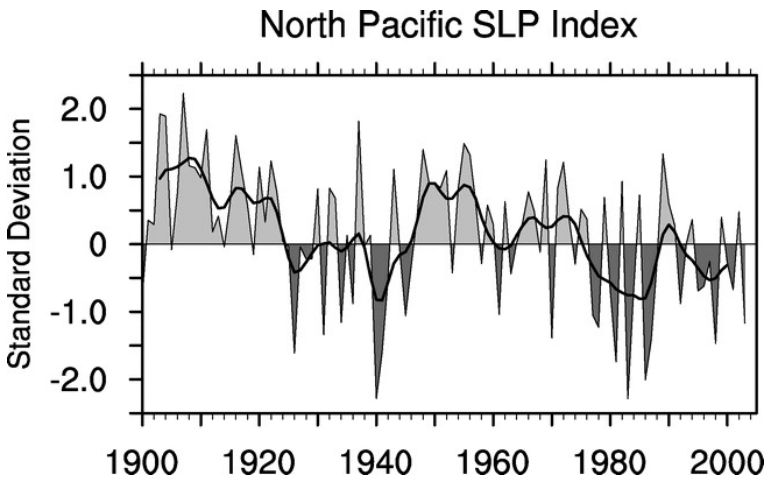

Figure 1.3 – Série temporelle normalisée de la pression au niveau de la mer moyennée sur la période décembre-mars et sur la région 30°-65°N, 160°-140°W. La courbe noire représente la moyenne glissante pondérée à 7 ans. D'après Deser et al. (2004) (Fig. 1)

variabilité de la SSH (Chhak et al. 2009 ; Di Lorenzo et al. 2008). Ces anomalies de SSH vont être propagées vers l'ouest par ajustement de l'océan à travers des ondes de Rossby barotropes et baroclines, ce qui génère des anomalies de SST dans les régions ouest et centrale du Pacifique par modulation de la profondeur de la thermocline (Seager et al. 2001 ; Schneider et al. 2002) ou par des changements dans l'advection zonale océanique (Qiu, 2003). Ainsi, les anomalies de SST représentées par la PDO et la NPGO résultent de la superposition de différentes anomalies de SST ayant différentes origines, y compris la dynamique océanique. Schneider et Cornuelle (2005) ont montré que la contribution des différents forçages de la PDO était fonction de la fréquence. Alors qu'aux échelles de temps interannuelles, la PDO est principalement forcée par l'AL et ENSO, la contribution de la dynamique océanique devient aussi importante que les autres forçages aux échelles de temps décennales.

L'une des questions qui subsiste est donc de savoir si ces anomalies de SST et la dynamique océanique impactent l'atmosphère à grande échelle et influencent la basse fréquence des modes de variabilité atmosphérique. Les avancées dans la compréhension des interactions océan-atmosphère dans les tropiques ont généré une grande amélioration dans la prévision du climat. Les interactions extratropicales sont donc devenues le nouveau défi pour améliorer la prévision du système climatique.

1.2 Rétroaction de l'océan extratropical sur l'atmosphère

Les premiers indices d'une influence possible de la SST des moyennes latitudes sur la circulation atmosphérique de grande échelle ont été obtenus dans les années 80, à travers des études sur la prévision statistique du climat (e.g. Namias et Cayan 1981 ; Barnett et Somerville 1983). Ces études ont montré que la SST dans certaines régions et pendant certaines saisons était significativement corrélée à l'atmosphère lorsque la SST précédait, et donc que les anomalies de SST pouvaient être des prédicteurs adéquats pour la prévision du climat à court terme, en particulier pendant la saison froide, même si le rapport signal/bruit est limité. Cependant, étant donné la corrélation possible entre les anomalies de SST de différentes régions, les zones où la SST présente le plus de potentiel de prévision n'ont pas été clairement mises en évidence. En outre, les contributions relatives de la SST tropicale et de la SST des moyennes latitudes sont difficile à établir, étant donnée la forte influence des tropiques sur les moyennes latitudes.

Le deuxième indice d'une influence possible de la SST des moyennes latitudes nous a été apporté par des expériences numériques dès les années 90. L'utilisation de simulations de modèles de circulation générale atmosphérique (AGCM pour *Atmospheric Global Circulation Model*) a montré que les anomalies de SST pouvaient avoir une influence significative sur l'atmosphère, bien au delà de la couche limite atmosphérique, mais l'amplitude de cette réponse était faible comparée à la variabilité interne de l'atmosphère (de l'ordre de 10-20 m par degré Kelvin à 500 hPa ; Kushnir et al. 2002), sans doute en partie parce que la résolution des modèles était trop basse. Ces expériences ont aussi montré que la réponse atmosphérique était très sensible à la localisation de l'anomalie de SST, et qu'une même anomalie de SST pouvait générer des réponses atmosphériques drastiquement différentes d'un mois à l'autre, en fonction de l'état moyen de

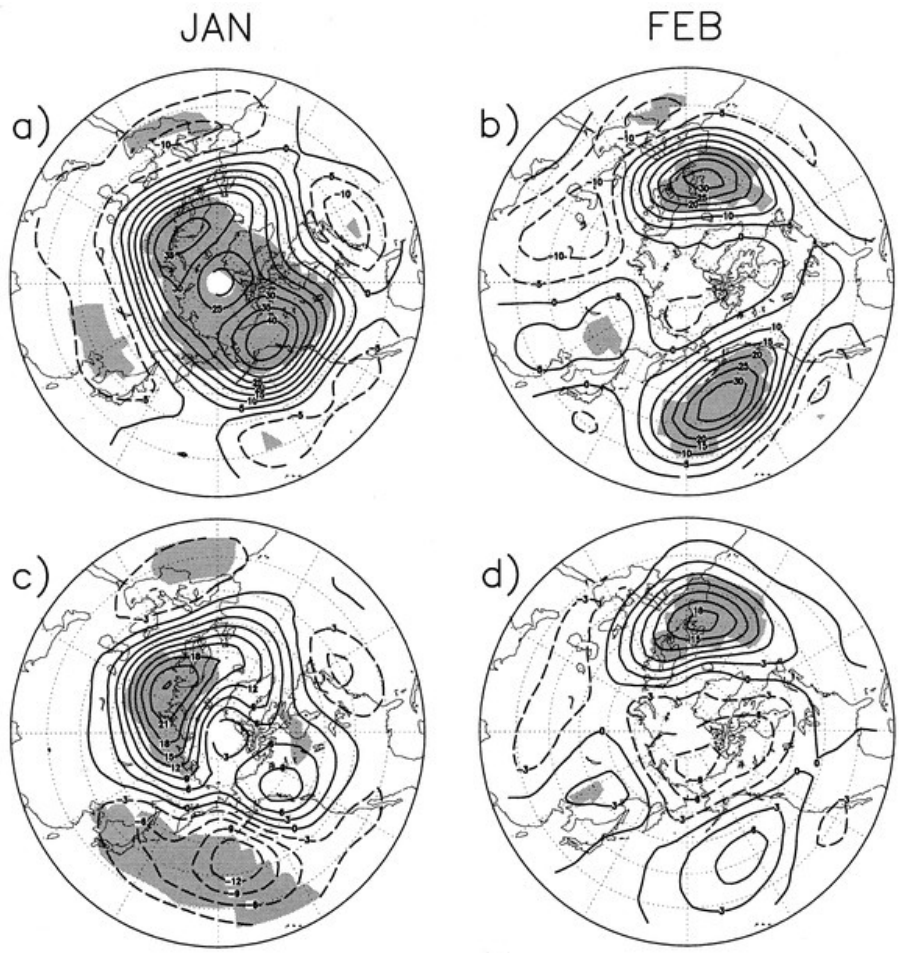

Figure 1.4 – Réponse atmosphérique à (a),(b) 250 et (c), (d) 850 mb en (a),(c) janvier et (b),(d) février dans un modèle atmosphérique soumis à une même anomalie de SST dans le Pacifique Nord. D'après Peng et Whitaker (1999) (Fig. 2)

l'atmosphère (Peng et al. 1997 ; Peng et Whitaker, 1999) (Figure 1.4). Cette forte sensibilité s'explique par le rôle crucial que jouent les tourbillons transitoires dans le développement de la réponse atmosphérique. En effet, la réponse dépend fortement de l'interaction entre l'influence directe barocline induite par la SST et les tourbillons transitoires. Or ces tourbillons transitoires dépendent fortement de la climatologie. Sur le Pacifique Nord, on observe un minimum de l'activité synoptique en décembre-janvier, au moment où le jet subtropical est maximum (Fig. 1.5, Nakamura 1992). L'état moyen de l'atmosphère est donc très différent en janvier et en février. Il apparaît également dans ces expériences que la réponse atmosphérique se projette fortement sur les modes de variabilité interne de l'atmosphère, qui sont eux aussi gouvernés par des interactions entre les tourbillons transitoires et l'écoulement moyen. Ainsi, la réponse atmosphérique induit des changements dans la distribution de probabilité des modes de variabilité internes. Autrement dit, les anomalies de SST ont tendance à modifier la fréquence d'occurrence de certains modes de variabilité internes, plutôt que de créer de nouveaux modes de variabilité (Peng et Robinson 2001 ; Cassou et al. 2004).

La réponse atmosphérique étant faible par rapport à la variabilité intrinsèque de l'atmo-

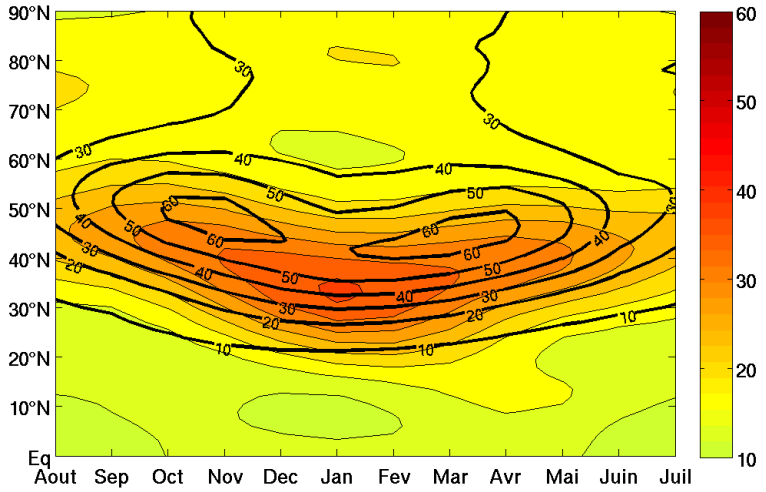

FIGURE 1.5 – Section temps-latitude du cycle saisonnier moyenné sur le Pacifique Nord (160°E-160°W) du vent zonal à 500 hPa (couleur, en ms^{-1}) et du rail des dépressions (contours, en m) défini par la variance du géopotentiel à 500 hPa après application du filtre passe-bande de Blackmon (Blackmon et Lau, 1980 ; Hurrel et Deser, 2009) pour ne retenir que la variabilité sur des périodes de 2 à 6 jours. On peut y voir le minimum de l'activité synoptique en décembre-janvier.

sphère, les études basées sur les observations ont eu beaucoup de mal à mettre en évidence cette réponse en raison du faible ratio signal/bruit. D'autre part, les interactions étant, au premier ordre, dominées par le forçage de l'atmosphère sur l'océan, il fallait séparer le forçage de la réponse. Enfin, les tropiques ayant une forte influence sur tout le globe, il fallait séparer l'influence des tropiques de celle des moyennes latitudes. Il a fallu attendre la fin des années 90 pour que l'influence des anomalies grande échelle de SST dans les moyennes latitudes soit mise en évidence dans les observations. A l'aide d'une analyse de maximum de covariance (MCA), Czaja et Frankignoul (1999 ; 2002) ont montré que la SST dans l'Atlantique Nord pendant la saison chaude était significativement corrélée au géopotentiel à 500hPa l'hiver suivant, et que la réponse atmosphérique avait une structure similaire à celle de la l'Oscillation Nord Atlantique (NAO). En utilisant à la fois des observations et des expériences numériques, Rodwell et Folland (2002) trouvent le même résultat. Depuis, des études similaires ont été conduites pour le Pacifique Nord, confirmant l'impact, certes relativement limité, des anomalies extratropicales de SST sur le climat. En utilisant également une MCA, Liu et al. (2006) et Frankignoul et Sennéchael (2007) ont montré qu'il existait une relation significative entre la circulation atmosphérique pendant la fin de l'été et des anomalies de SST ressemblant à la PDO quelques mois avant, indépendamment des téléconnexions ENSO qui ont préalablement été retirées du signal. Frankignoul et Sennéchael (2007) ont aussi trouvé une relation significative en début d'hiver entre le mode PNA et une structure d'anomalies de SST quadripolaire. De la même manière, Gan et Wu (2013) ont étudié la relation entre les anomalies de SST dans le Pacifique Nord et le rail des dépressions et ont montré que sur des échelles de temps interannuelles à décennales, des

anomalies grande échelle de SST pendant l'hiver ressemblant à la PDO sont significativement corrélées avec une intensification du rail des dépressions les hivers d'après. A l'échelle saisonnière, en revanche, le rail des dépressions en décembre est significativement corrélé avec des anomalies de SST en septembre-octobre ressemblant en partie à la NPGO.

Une approche différente a été utilisée par Wen et al. 2010 et Liu et al. 2012 qui ont appliqué une récente technique d'analyse statistique multivariable : GEFA (*Generalized Equilibrium Feedback Analysis*). Cette technique développée par Liu et al. (2008) est une généralisation de la méthode univariable de Frankignoul et al. (1998) et permet d'estimer la réponse atmosphérique à différentes anomalies de SST préalablement prescrites, à l'inverse de la MCA qui n'impose pas l'anomalie de SST. En outre, contrairement aux autres méthodes qui doivent s'affranchir des téléconnections tropicales en supprimant ce signal en amont, cette méthode permet d'inclure les modes de variabilité tropicaux de manière explicite et ainsi différencier l'impact des moyennes latitudes à celui des tropiques sans filtrer un signal à priori. En prescrivant les principaux modes de variabilité de la SST des océans Pacifique, Atlantique et Indien, Wen et al. (2010) et Liu et al. (2012) ont montré que, bien que les principaux modes de variabilité impactant l'atmosphère soient les modes tropicaux des océans Pacifique et Indien, la PDO semble également avoir une influence. Leurs résultats montrent que la réponse atmosphérique à la PDO consiste en un renforcement de l'AL, légèrement décalé et étendu vers le sud-ouest, et un signal dans l'Atlantique Nord ressemblant à la NAO.

En parallèle de ces études sur l'impact des anomalies de SST grande échelle, des études basées sur des observations satellites à haute résolution ont montré qu'à méso-échelle et près des fronts de SST, l'influence de l'océan sur l'atmosphère apparaît comme très forte. En effet, dans ces zones, il y a une corrélation positive entre la SST et les vents de surface (i.e. des vents plus forts là où la SST est plus élevée), suggérant une influence de l'océan sur l'atmosphère. Cette influence se fait principalement à travers deux mécanismes (revues par Xie 2004 et Small et al. 2008). Le premier est lié au mélange turbulent et au transfert de quantité de mouvement sur la verticale : une SST plus élevée génère une déstabilisation de la colonne d'air et un renforcement du mélange turbulent vertical, induisant un approfondissement de la couche limite et un transfert de quantité de mouvement depuis la partie supérieure de la couche limite vers la surface. Le deuxième est lié à l'ajustement hydrostatique de la pression : le réchauffement de la couche limite atmosphérique par une SST plus élevée engendre une diminution de la pression, ce qui produit un gradient de pression à l'origine d'une circulation secondaire avec convergence des vents au-dessus de la SST plus élevée, proportionnelle au laplacien de la pression. Ainsi, les fronts de SST influencent la circulation atmosphérique. Or les principaux fronts de SST dans les moyennes latitudes sont ceux associés aux courants de bord ouest et leurs extensions.

1.3 Les courants de bord ouest : le siège d'intenses interactions air-mer

Les courants de bord ouest sont le siège d'intenses interactions air-mer, car c'est dans ces régions que les masses d'eau libèrent le plus leur chaleur à l'atmosphère. Les courants de bord

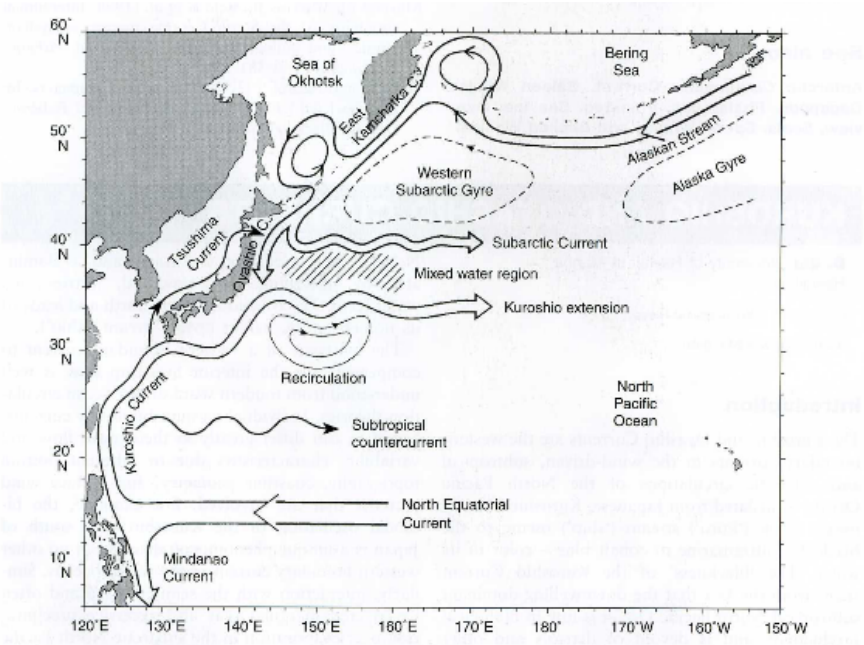

FIGURE 1.6 – Circulation schématique associée aux gyres subtropicale et subarctique dans le nord-ouest de l'océan Pacifique. D'après Qiu (2001) (Fig. 1)

ouest sont les courants de retour des gyres subtropicales ou subpolaires. Les courants de bord ouest des gyres subtropicales transportent des eaux chaudes subtropicales vers le nord, dans des régions où la température de l'air est plus froide, en particulier en hiver, ce qui génère un fort dégagement de chaleur de l'océan à l'atmosphère (Kelly et al. 2010). 70% du transfert de chaleur de l'océan à l'atmosphère se fait entre 25°N et 45°N, et à 35°N, le transfert de chaleur vers les pôles est à 78% effectué par l'atmosphère, et 22% par l'océan (Trenberth et Caron 2001). Les courants de bord ouest jouent donc un rôle clé dans le système climatique.

Dans le Pacifique Nord, les courants de bord ouest des gyres subtropicales et subpolaires sont respectivement le Kuroshio et l'Oyashio. Lorsque ces courants se séparent des côtes japonaises et se déversent dans le bassin océanique du Pacifique, on parle de leurs extensions. Ainsi, l'Extension du Kuroshio (Kuroshio Extension, KE) et l'Extension de l'Oyashio (Oyashio Extension, OE) sont le prolongement des courants du Kuroshio et de l'Oyashio lorsque ceux-ci bifurquent vers l'est (Figure 1.6). Le KE et l'OE sont donc des courants zonaux s'écoulant vers l'est et libres de toute contrainte continentale. Plus à l'est, ces masses d'eau rejoignent le courant subarctique et forment le courant Nord Pacifique.

Le Kuroshio et l'Oyashio advectant respectivement des eaux chaudes vers le nord et des eaux froides vers le sud, la région des extensions du Kuroshio et de l'Oyashio est une zone de fort gradient méridien de température, constituée de deux fronts quasi-zonaux : le front de l'Oyashio (ou front subarctique), un peu au nord de 40°N, et le front du Kuroshio, vers 35°N. Ensemble, ils forment le système de l'Extension du Kuroshio et de l'Oyashio (*Kuroshio Oyashio Extension*, KOE). Ces deux fronts ont une structure verticale différente (Nonaka et al., 2006). Le KE est associée à un front de température jusqu'en profondeur, avec un gradient méridien maximal de température entre 300 et 500 m, alors que le front de l'OE est moins profond, avec un gradient

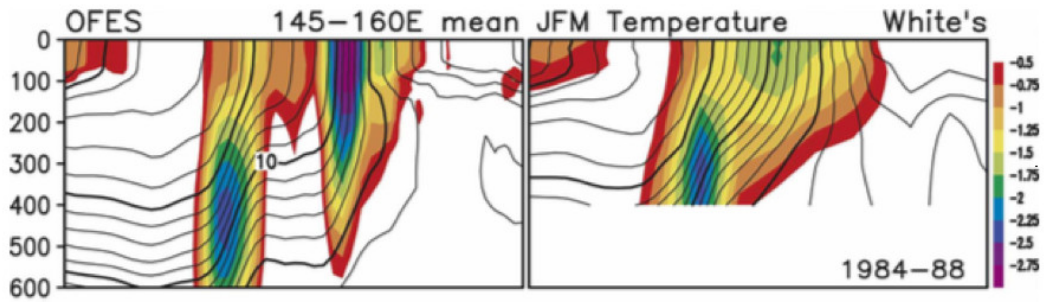

Figure 1.7 – Température (contours) et gradient méridien de température (couleur) pendant la période hivernale calculés par le modèle OFES (gauche) et par des observations hydrographiques (à moins bonne résolution spatiale) compilées par White (1995) (droite). D'après Nonaka et al. (2006) (Fig. 9)

de température maximal en surface (Figure 1.7). Sauf en hiver, le gradient de SST est beaucoup plus marqué sur le front de l'OE que sur le front du KE. En outre, l'Oyashio advectant des eaux relativement peu salées venant du nord, le gradient de SST de l'OE est largement compensé par un gradient de salinité, ce qui fait que le gradient de densité est faible, contrairement à la région du KE. Les courants associés au front de l'OE sont donc beaucoup plus faibles que ceux du KE, qui est marqué par un fort gradient de hauteur de mer (SSH), comme illustré dans la section 2.2.

Ces zones de fronts de SST coïncident avec les régions où se développent et se renforcent les dépressions extratropicales. Sanders et Gyakum (1980) ont été les premiers à établir un lien entre les tempêtes extratropicales et les fronts de SST. Par la suite, de nombreuses études ont montré l'importance du dégagement de chaleur et d'humidité par l'océan dans les régions du Kuroshio et du Gulf Stream pour le développement des tempêtes (Hoskins et Valdes, 1990 ; Nuss et Kamikawa, 1990 ; Kuo et al. 1991 ; Neiman et Shapiro, 1993 ; Bengston et al. 2006). La baroclinicité de l'atmosphère étant proportionnelle au gradient horizontal de la température de l'air, il est supposé que les zones de fort gradient de SST favorisent le développement d'instabilités baroclines et la cyclogénèse, ancrant le rail des tempêtes juste au dessus des fronts (Nakamura et Shimpo 2004 ; Nakamura et al. 2004). Cette hypothèse est en accord avec différentes expériences numériques explorant l'influence du lissage des fronts sur la circulation atmosphérique (e.g. Nakamura et al. 2008 ; Sampe et al. 2010 ; Nonaka et al. 2009 ; Taguchi et al 2009).

Ainsi, les fronts océaniques conditionnent la variabilité synoptique de l'atmosphère. Les observations satellites ont révélé que les fronts de SST impactent l'atmosphère sur plusieurs kilomètres d'altitude, affectant en particulier la distribution des nuages et des orages (Liu et al. 2007 ; Tokinaga et al. 2009 ; Kobashi et al. 2008 ; Minobe et al. 2008). Tokinaga et al. (2009) ont regroupé des observations in-situ et satellites et ont montré que pendant l'hiver des nuages de haute altitude se développent préférentiellement au dessus du flanc chaud (sud) du Kuroshio, là où le dégagement de chaleur est le plus fort, et que ces nuages s'accompagnent d'une forte activité orageuse. Minobe et al. (2008) ont montré que les eaux chaudes du Gulf Stream génèrent un mouvement ascendant de l'air jusqu'à 300 hPa ainsi qu'une divergence horizontale du vent, impactant les nuages et les orages. Si de la convection profonde est observée le long du Gulf

Stream, il a été supposé que des ondes planétaires pouvaient être excitées par cette énergie et impacter le climat à grande-échelle.

1.4 La variabilité basse fréquence du Kuroshio et de l'Oyashio

Les observations montrent que le KE et l'OE sont caractérisés par des méandres de large amplitude et une forte activité tourbillonnaire, comme tous les courants de bord ouest. En outre, l'OE et le KE présentent une variabilité sur des échelles de temps plus longues. Cette variabilité se caractérise en particulier par un déplacement méridien de la trajectoire des courants, et une modulation de leur intensité. En utilisant des données altimétriques, Qiu and Chen (2010) ont montré que le KE oscillait entre un état dynamiquement stable, caractérisé par une trajectoire plus au nord et un courant plus intense, et un état dynamiquement instable, pendant lequel la trajectoire est plus au sud et le courant plus faible (voir section 2.2 pour plus de détails). De même, des observations montrent que l'OE pénètre certaines années plus au sud qu'à la normale (Sekine, 1988) (voir section 2.3). Cette variabilité interannuelle a été également observée dans des simulations de modèles océaniques à haute résolution (Nonaka et al., 2006), qui ont montré que les variations des deux fronts n'étaient pas nécessairement cohérentes, ce qui suggérait qu'elles étaient gouvernées par des mécanismes différents.

Bien que le caractère bimodal du KE soit également dû à des modes de variabilité intrinsèques non-linéaires (Taguchi et al. 2007 ; Pierini 2006, Pierini et al. 2009), il est bien établi que la dynamique des courants de bord ouest est contrôlée par le rotationnel du vent à l'échelle de la gyre. Ainsi, la variabilité du KOE est liée à celle des modes de variabilité AL et NPO, qui, en générant des anomalies dans le rotationel du vent, provoquent des variations de SSH dans la région centre-est du Pacifique qui vont ensuite être propagées vers l'ouest à travers la propagation d'ondes de Rossby barotropes et baroclines. Avec un certain retard en fonction de la vitesse de propagation des ondes, ces anomalies de SSH atteignent la région du KOE et modulent les courants à travers des variations de la profondeur de la thermocline ou de l'advection zonale. Des études basées sur des modèles linéaires ont montré que le KE répondait aux anomalies de vent liées à l'AL ou la NPO avec un délai de 2 à 4 ans (Qiu, 2003 ; Taguchi et al. 2007 ; Ceballos et al., 2009), alors que l'OE répondait principalement à celles liées à l'AL avec un délai de 3 ans (Nonaka et al., 2008). Il semblerait que l'Oyashio soit également gouverné par une réponse rapide à ces changements de vent, liée à la propagation des ondes de Rossby barotropes (Isoguchi and Kawarnura, 1997).

Cette variabilité basse fréquence du KE et de l'OE n'est pas sans conséquence sur la SST. La région du KOE est en effet marquée par une forte variabilité interannuelle et décennale du contenu thermique de la couche supérieure de l'océan, et cette variabilité est principalement générée par des processus océaniques, comme le déplacement des fronts (Xie et al. 2000 ; Seager et al. 2001 ; Nakamura et Kazmin 2003 ; Nonaka et al. 2006, 2008), le déferlement d'ondes de Rossby (Schneider et Miller 2001 ; Qiu 2003 ; Taguchi et al. 2007), et l'advection thermique par le KE (Qiu 2000 ; Vivier et al. 2002 ; Scott et Qiu 2003). Ainsi, les flux de chaleur qui résultent de ces anomalies de SST reflètent l'impact de la variabilité océanique basse fréquence

sur l'atmosphère. Sur des échelles de temps interannuelles et plus longues, les flux de chaleur montrent en effet une très forte variabilité dans les régions des courants de bord ouest (Wallace et Hobbs, 2006). Ainsi, la région du KOE est une région clé dans la variabilité décennale du système océan-atmosphère des moyennes latitudes.

1.5 Influence de la variabilité océanique du Pacifique Nord sur l'atmosphère

Si les courants de bord ouest modulent l'atmosphère sus-jacente, leur variabilité peut alors impacter la circulation atmosphérique et modeler la variabilité du climat. Dans plusieurs modèles couplés, les interactions océan-atmosphère au dessus des courants de bord ouest jouent un rôle clé dans la variabilité décennale des moyennes latitudes (Pierce et al. 2001 ; Wu et Liu 2005 ; Kwon et Deser 2007). Cependant, ce n'est que récemment qu'on a pu montrer à partir d'observations que la variabilité des fronts océaniques avait un impact significatif (Joyce et al. 2009 ; Frankignoul et al. 2011, Taguchi et al 2012 ; O'Reilly and Czaja 2014, Révelard et al. 2016).

Les expérimentations numériques de Peng et al. (1997), Peng et Whitaker (1999), Liu et Wu (2004), Liu et al. (2007), et Gan et Wu (2012) suggèrent qu'une anomalie grande échelle de SST dans la région du KOE est capable d'induire une réponse atmosphérique grande échelle, bien que celle-ci soit très sensible à l'état moyen de l'atmosphère, et dépende donc drastiquement de la saison (Fig. 1.4). Dans les observations, les premières études qui ont pu mettre en évidence une influence des anomalies de SST du Pacifique Nord sur l'atmosphère se sont basées sur la MCA (section 1.2), recherchant la covariabilité entre la SST et la dynamique atmosphérique. Cependant, cette méthode ne permet pas d'imposer une anomalie particulière de SST ni de différencier les différents processus océaniques responsables de ces anomalies. Afin d'étudier la réponse atmosphérique aux fluctuations du KE ou de l'OE, des indices décrivant leur variabilité sont nécessaires. A partir de données de température, Frankignoul et al. (2011) (par la suite FSKA) ont crée des indices pour représenter la variabilité du KE et de l'OE et ont détecté une réponse atmosphérique aux déplacements méridiens des courants. La réponse observée était robuste, en particulier pour l'Oyashio, et était différente pour les deux courants.

L'Oyashio ayant un fort gradient de SST, l'indice de l'Oyashio utilisé par FSKA est défini par la première composante principale de la latitude du gradient maximum de SST. Cependant, la signature en SST associée à cet indice montre des anomalies grande échelle ressemblant à la PDO (figure 1.8, panel du haut), même une fois que le signal ENSO a été retiré du signal (figure 1.8, panel du bas). Le Kuroshio étant marqué par un gradient de température plus en profondeur, l'indice du Kuroshio utilisé lors de cette étude est basé sur l'isotherme de 14°C à 200 m de profondeur. Cependant, les observations hydrographiques étaient très limitées, ce qui a nécessité un lissage temporel important ne permettant pas de tenir compte de la saisonnalité des interactions océan-atmosphère. En outre, la variabilité du KE n'est pas bien déterminée par la température à 200 m de profondeur (figure 1.7), et il aurait fallu disposer de mesures plus profondes. Par ailleurs, Qiu et Chen (2010) ont montré que la hauteur de mer était un meilleur indicateur des fluctuations du KE, et Qiu et al. (2014) ont crée un nouvel indice basé

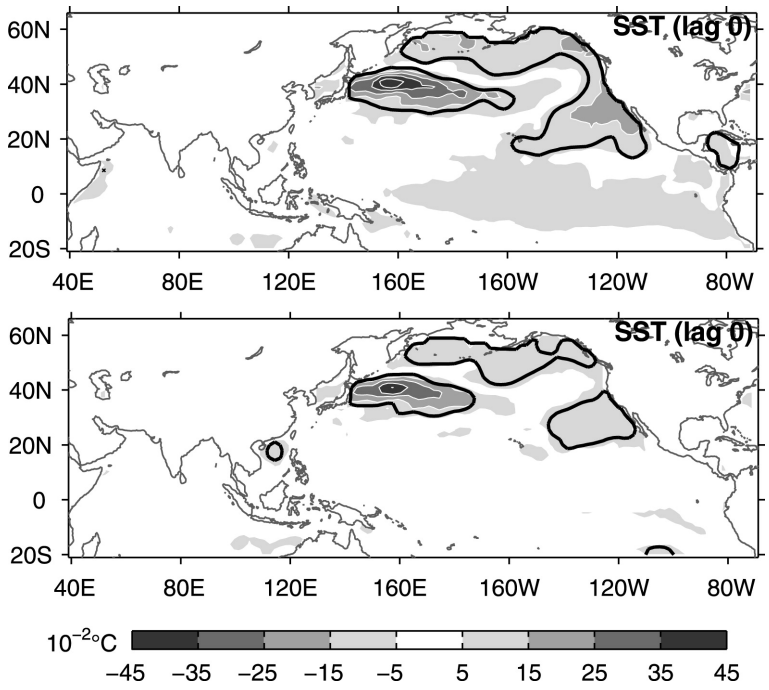

FIGURE 1.8 – Régression des anomalies de SST sur l'indice de l'OE avant filtrage d'ENSO (haut) et après filtrage d'ENSO (bas). Les contours blancs (gris) indiquent des valeurs négatives (positives). Les contours noirs indiquent la significativité statistique au niveau de 10%. D'après Frankignoul et al. (2011) (Fig. 5)

sur les observations satellites et un modèle à haute résolution (section 2.2). Ce nouvel indice n'est que très peu corrélé ($r = 0.52$) avec la série basée sur l'isotherme de 14°C. Ainsi, une meilleure estimation de la réponse atmosphérique aux fluctuations du KE devait être possible en utilisant ce nouvel indice (chapitre 3). De même, O'Reilly et Czaja (2014) ont créé un indice du KE basé sur une analyse en maximum de covariance entre la SST et le gradient de SSH et ont montré que les fluctuations du KE impactaient le transport méridien de chaleur par les tourbillons transitoires. Mais les données de SST à haute résolution ne sont disponibles qu'à partir de 2002, ce qui fait que leur indice du KE a été étendu à 1993 par projection et ne montre que très peu de variabilité basse fréquence entre 1993 et 2002 comparé à l'index de Qiu et al. (2014).

Taguchi et al. (2012) ont étudié l'impact de la variabilité de l'OE et ont montré qu'une anomalie de SST dans la région du KOE avait un fort impact sur la circulation atmosphérique grande échelle en janvier, et un plus faible impact de signe presque opposé en février. Leur indice de l'OE a été défini par la série temporelle des anomalies de SST moyennées sur une région centrée sur l'OE, correspondant à la région dans laquelle à la fois le gradient méridien de SST et la variabilité de la SST sont particulièrement forts. Cependant, cette région est aussi la région dans laquelle la PDO a une forte amplitude, ce qui fait que l'influence attribuée à l'OE pourrait en partie être causée par la PDO. Du reste, Smirnov et al. (2014) ont montré que les anomalies de SST principalement générées par la dynamique océanique se limitaient à la région du KOE, à l'ouest de 180°W. Afin de prescrire l'anomalie de SST associée à un déplacement vers

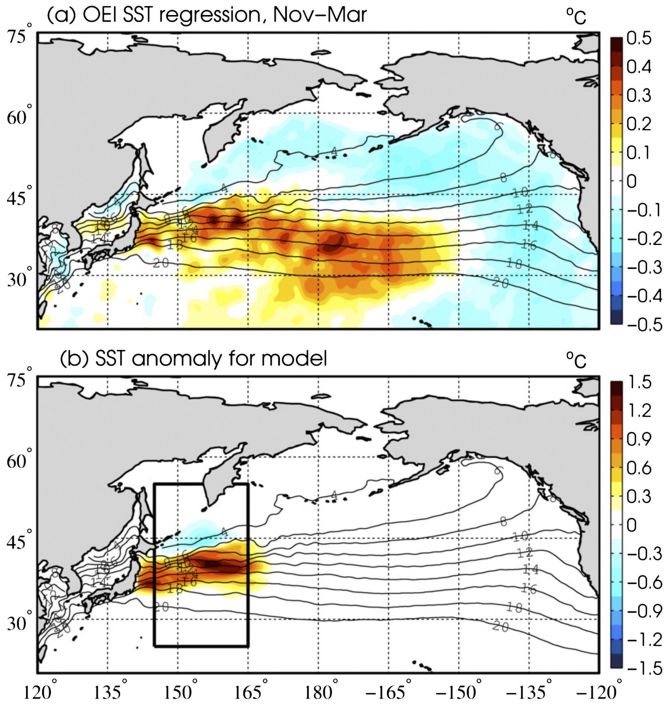

Figure 1.9 – (a) Régression des anomalies de SST sur l'indice de l'OE de FSKA de novembre à mars sur la période 1982-2008. (b) Anomalie de SST prescrite au modèle. D'après Smirnov et al. (2015) (Fig. 1)

le nord de l'OE dans une simulation numérique, Smirnov et al. (2015) ont limité l'anomalie de SST à la région de l'OE de manière empirique, en appliquant un filtre et en excluant la région dans laquelle les anomalies de SST sont principalement générées par l'atmosphère (Figure 1.9). Il est donc important de pouvoir mieux distinguer les anomalies de SST liées aux courants de bord ouest de celles liées aux modes de variabilité grande échelle.

1.6 Objectifs de cette thèse

L'objectif de cette thèse est d'établir l'impact à grande échelle de la variabilité des courants de bord ouest du Pacifique Nord sur la circulation atmosphérique de l'hémisphère nord, et de bien distinguer l'impact du KE et de l'OE de celui des principaux modes de variabilité de la SST dans le Pacifique Nord, à savoir la PDO et la NPGO. Le but est aussi de faire le lien avec la variabilité synoptique de l'atmosphère, pour une meilleure compréhension des mécanismes conditionnant la réponse atmosphérique. Cette réponse étant très sensible à la saison, mon travail s'est focalisé sur la saison froide, car c'est pendant cette saison que le dégagement de chaleur de l'océan vers l'atmosphère est le plus important.

Dans le chapitre 3, j'ai mis en évidence l'impact de la variabilité décennale du KE, en utilisant le nouvel indice défini par Qiu et al. (2014) et une régression partielle avec décalage temporel. Afin de comprendre par quels mécanismes les fluctuations du KE peuvent influencer la circulation atmosphérique grande échelle, j'ai analysé en détails l'impact du KE sur différentes

variables atmosphériques liées à l'activité synoptique et au rail des dépressions. Cette analyse montre que les fluctuations du KE génèrent une réponse atmosphérique grande échelle impactant le climat sur tout l'hémisphère. Cependant, les anomalies de SST associées aux fluctuations du KE décrites par l'indice de Qiu et al. (2014) ont une grande étendue spatiale qui va bien au delà de la région du front de SST associé au KE, de même que les anomalies de SST associées aux fluctuations de l'OE décrites par l'indice de FSKA. Ceci pourrait venir du fait que ces anomalies grande échelle sont forcées par le même forçage atmosphérique qui a engendré les fluctuations des courants. De même, la réponse aux fluctuations du KE et de l'OE pourrait engendrer une réponse non locale en SST, comme dans les simulations numériques de Kwon et Deser (2007) et donc étendre la région directement affectée par les deux courants. En outre, ces anomalies non locales de SST peuvent être dues à une corrélation entre la variabilité temporelle du KE et de l'OE et d'autres modes de variabilité grande échelle de SST, tels que la PDO. Autrement dit, est-ce vraiment le KE ou l'OE qui forcent, et non la PDO ? Il est impératif de tenter de mieux établir l'influence spécifique du KE et de l'OE en la distinguant des forçages simultanés liés aux autres modes de variabilité de la SST.

Au chapitre 4, j'ai donc utilisé la méthode GEFA permettant d'analyser la réponse atmosphérique à différents forçages pouvant être corrélés entre eux. Pour tenter d'être complet, j'ai inclus dans cette analyse multivariable, outre les indices représentatifs de la variabilité du KE et de l'OE, les principaux modes de variabilité de la SST des différents bassins océaniques de l'hémisphère nord et des tropiques. J'ai aussi considéré la variabilité de la couverture de glace, celle-ci ayant montré dans les observations un impact significatif sur l'atmosphère (Frankignoul et al. 2014 ; Garcia-Serrano et al. 2015). Le but de cette analyse est de distinguer la réponse atmosphérique au KE et à l'OE de l'influence des autres forçages. En outre, l'attention sera portée à l'influence des deux modes principaux de variabilité de la SST dans le Pacifique Nord, la PDO et la NPGO.

Chapitre 2

Données utilisées

2.1 Données atmosphériques

Les données atmosphériques utilisées dans cette étude proviennent principalement de la réanalyse ERA-Interim fournie par l'ECMWF (European Center for Medium-Range Weather Forecasts) (Dee et al. 2011). Les réanalyses sont obtenues par assimilation d'observations au sein d'un modèle numérique. Cette technique permet d'obtenir un bon compromis entre les données observées, pas toujours uniformes dans le temps et dans l'espace, et les résultats du modèle, vérifiant les lois physiques et dynamiques. Les variables atmosphériques d'ERA-Interim sont archivées toutes les 6h et définies sur une grille spectrale T255 à 23 niveaux verticaux. Ces données sont ensuite interpolées sur une grille gaussienne de résolution horizontale de 0.75° (∼80km). La réanalyse procure des données journalières depuis janvier 1979. La résolution horizontale utilisée ici est de 1.5° pour la SLP, le géopotentiel et les vents horizontaux, et de 0.75° pour la SST, les flux de chaleur et la vitesse verticale. Étant donné que les flux de chaleur de surface sont généralement mal représentés dans les réanalyses atmosphériques où la température océanique superficielle est prescrite, nous avons aussi utilisé pour ces variables les données OAFlux (Objectively Analysed air-sea Fluxes) (Yu et Weller 2007). Celles-ci sont issues de l'analyse de données météorologiques de surface observées par satellites et par application d'un algorithme poussé utilisant les formules aérodynamiques fiables, et sont mises à disposition par la Woods Hole Oceanographic Institution.

Afin de travailler sur des périodes plus longues, j'ai également utilisé les données de la réanalyse NCEP-NCAR (National Centers for Environmental Prediction–National Center for Atmospheric Research) (Kalnay et al. 1996). Cette réanalyse offrent des données depuis 1948, mais avec une moins bonne résolution horizontale que ERA-Interim. Elle est définie sur une grille spectrale T62 avec 28 niveaux verticaux, permettant d'obtenir des données sur une grille gaussienne de résolution horizontale de 2° (∼200km). Nous avons considéré la période 1958-2014, car avant 1958, les observations sont peu nombreuses et n'offrent pas de couverture spatiale suffisante pour donner de la fiabilité aux réanalyses.

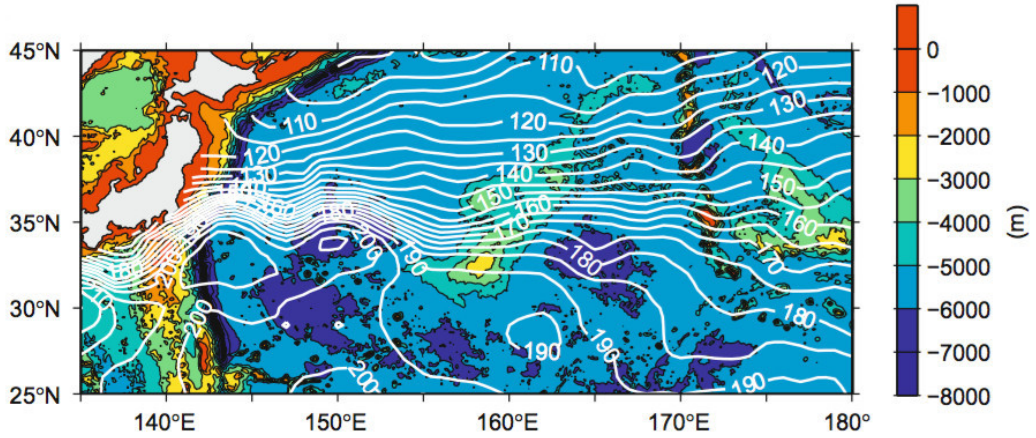

FIGURE 2.1 – Carte de bathymétrie (en couleur) et de l'anomalie moyenne de hauteur de mer en cm (contours blancs). D'après Qiu et Chen (2010) (Fig. 1)

2.2 Série temporelle des fluctuations de l'Extension du Kuroshio

Depuis 1992, les données de hauteur de mer (SSH) mesurées par satellites altimétriques ont permis de montrer que la trajectoire du KE était bien représentée par l'isocontour de 170 cm, situé au niveau du gradient méridien maximum de SSH (Figure 2.1). Une manière visuelle de décrire la variabilité décennale du KE est de superposer des « snapshots » de sa trajectoire défini par cet isocontour (Figure 2.2, Qiu et Chen 2005, 2010). Ces dernières montrent que le KE a une trajectoire relativement plus stable certaines années (i.e. en 1993-95, 2002-05, et 2010-12), et une trajectoire plus disparate d'autres années (i.e. en 1996-99 et 2006-09). Afin de caractériser la variabilité du KE, Qiu et Chen (2010) ont défini quatre indices :

- la latitude de l'isoligne de 170 cm moyennée entre 141° et 158°E, indiquant les déplacements méridiens du KE
- la longueur de cet isoligne intégrée entre 141° et 158°E, qui est un indicateur des méandres et tourbillons du KE
- l'énergie cinétique turbulente calculée dans la région 32°-38°N et 141°-153°E
- l'intensité du transport calculée par intégration de l'anomalie de SSH (SSHa) dans la région 141°-158°E

Sur la période altimétrique (1993-2013), il s'avère que ces quatre caractéristiques dynamiques sont bien corrélées entre eux. Qiu et Chen (2010) ont ainsi montré que le KE oscillait à l'échelle décennale entre un état dynamique stable et un état dynamique instable. Lorsque le KE est dans l'état dynamique stable, sa trajectoire est plus laminaire et plus au nord, le courant est plus intense, et l'énergie cinétique turbulente est réduite. A l'inverse, lorsque le KE est dans l'état dynamique instable, sa trajectoire est plus disparate et plus au sud, le courant est plus faible et l'énergie cinétique turbulente est plus importante.

Etant donnée la bonne corrélation entre les quatre caractéristiques dynamiques cités plus haut, et leur représentativité plus complète de la dynamique, Qiu et al. (2014) ont estimé plus juste de définir un nouvel indice « synthétisé » se basant sur la moyenne de ces quatre séries

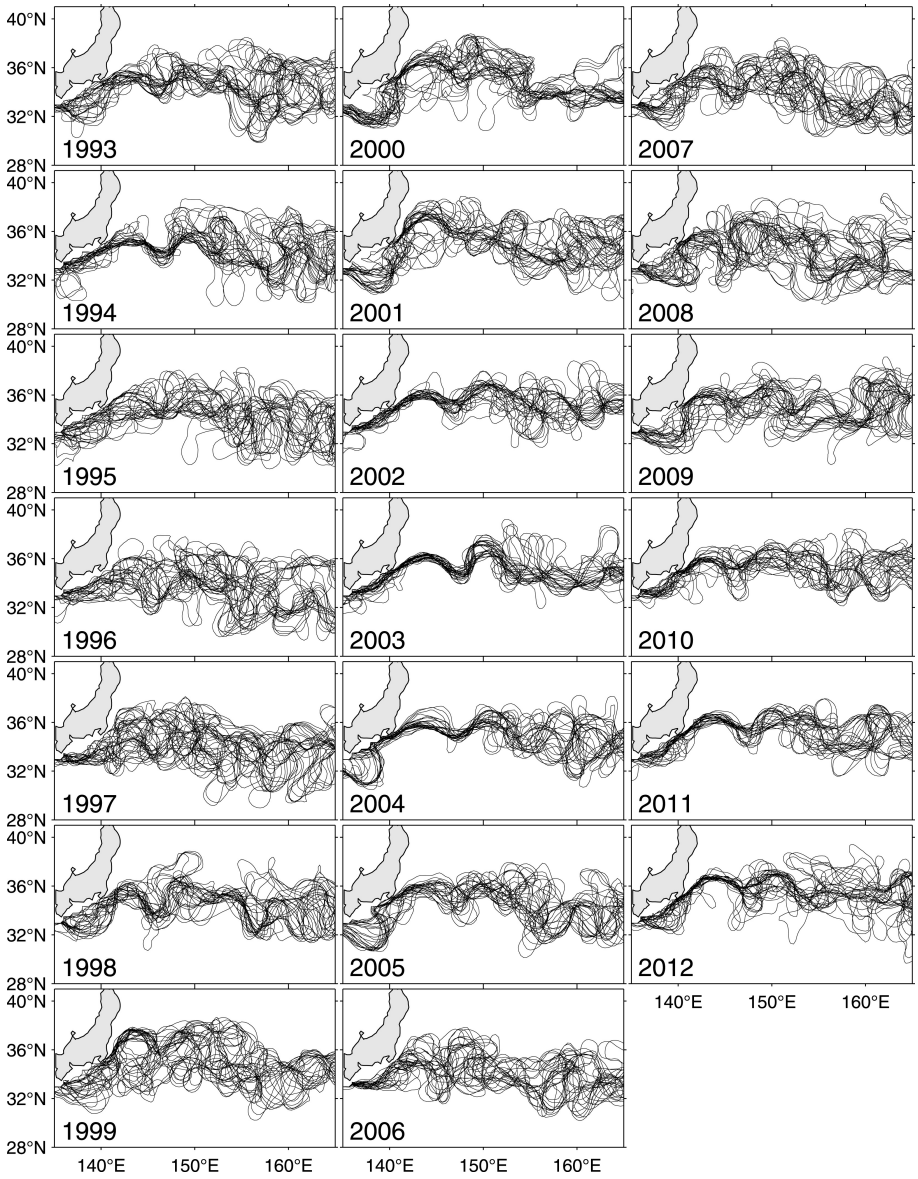

Figure 2.2 – Superposition de « snapshots » de l'isocontour de 170 cm de SSH donnant la trajectoire du KE mesuré tous les 14 jours par satellite. D'après Qiu et al. (2014) (Fig. 2)

temporelles, normalisées par leur variance respective (Figure 2.3 a). Or, une régression linéaire entre ce nouvel indice et la SSHa du Pacifique Nord montre un fort lien entre cette série et les SSHa dans la région 31˚-36˚N et 140˚-165˚E (Figure 2.3 c), et la série temporelle de SSHa moyennée dans cette région est en effet bien corrélée à la série se basant sur les quatre indices dynamiques ($r = 0.84$) (Figure 2.3 b). Ainsi, la SSHa moyennée dans la région 31˚-36˚N et 140˚-165˚E est un bon indicateur des fluctuations du KE, et l'indice du KE depuis novembre 1992 est défini par cette variable.

Afin de disposer d'une série temporelle s'étalant sur une période plus longue, Qiu et al. (2014) ont utilisé les données provenant du modèle OFES (Ocean General Circulation Model For the Earth Simulator) simulé par le Earth Simulator Center à Yokohama (Japon). Il résout

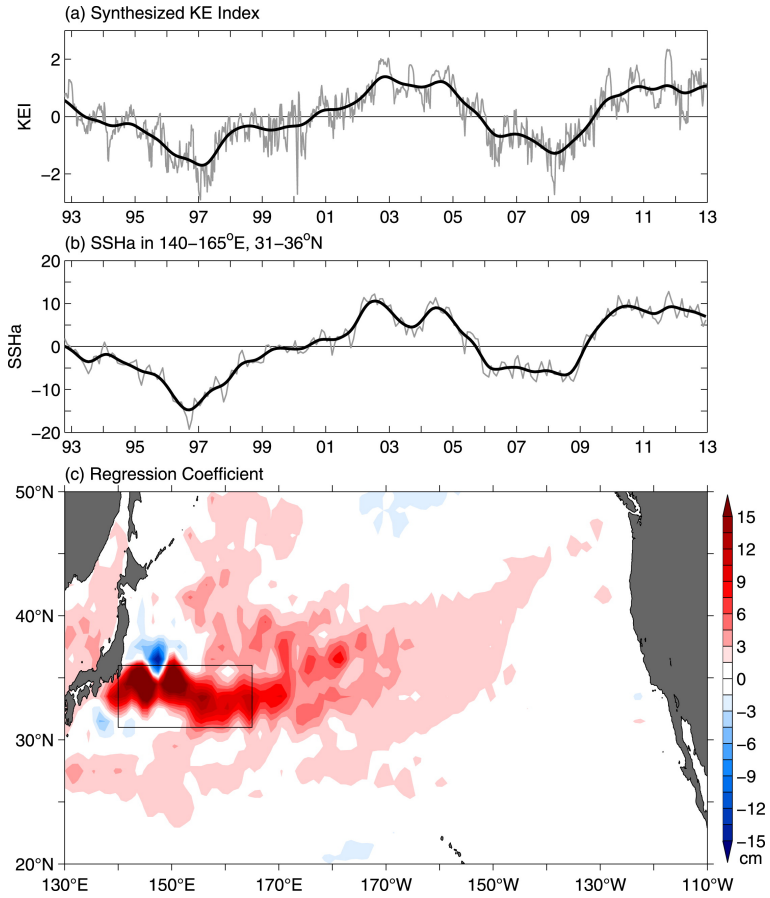

FIGURE 2.3 – (a) Indice du KE basé sur la moyenne entre les quatre séries temporelles décrites dans le texte. (b) Série temporelle de la SSHa moyennée sur la région 31˚-36˚N et 140˚-165˚E représentée par le rectangle sur la figure (c). Les lignes grises et noires désignent respectivement les valeurs hebdomadaires et les données filtrées. (c) Carte de régression entre l'indice du KE de la figure (a) et les SSHa du Pacifique Nord. D'après Qiu et al. (2014) (Fig. 4)

les équations primitives sous les approximations hydrostatiques et de Boussinesq, et est forcé par le vent et les flux de chaleur et d'eau douce provenant de la réanalyse NCEP-NCAR. D'une résolution horizontale de 1/10˚, il résout de manière correcte les tourbillons de méso-échelle et les fronts océaniques (Nonaka et al, 2006). Taguchi et al. (2007) ont montré que les sorties de ce modèle étaient remarquablement en accord avec les observations in-situ et altimétriques (Figure 2.4), ce qui en fait un outil puissant pour étudier la période précédant l'ère altimétrique. Les sorties du modèle sont disponibles depuis 1950.

Qiu et al. (2014) ont ainsi calculé l'anomalie de hauteur de mer moyennée dans la région 31˚-36˚N et 140˚-165˚E à partir des sorties de ce modèle. La bonne corrélation ($r = 0.81$) entre cette série et celle calculée à partir des données altimétriques observées confirme qu'OFES capture bien les fluctuations décennales du KE. L'indice du KE pour la période précédent 1992 a donc été défini par cette série. Cependant, la variabilité du KOE a fortement changé depuis le changement climatique observé de 1976/1977 (Seager et al., 2001), et les fluctuations du KE sont moins bien corrélées avec la variabilité de la SSHa avant cette date. De plus, une étude préliminaire en cours

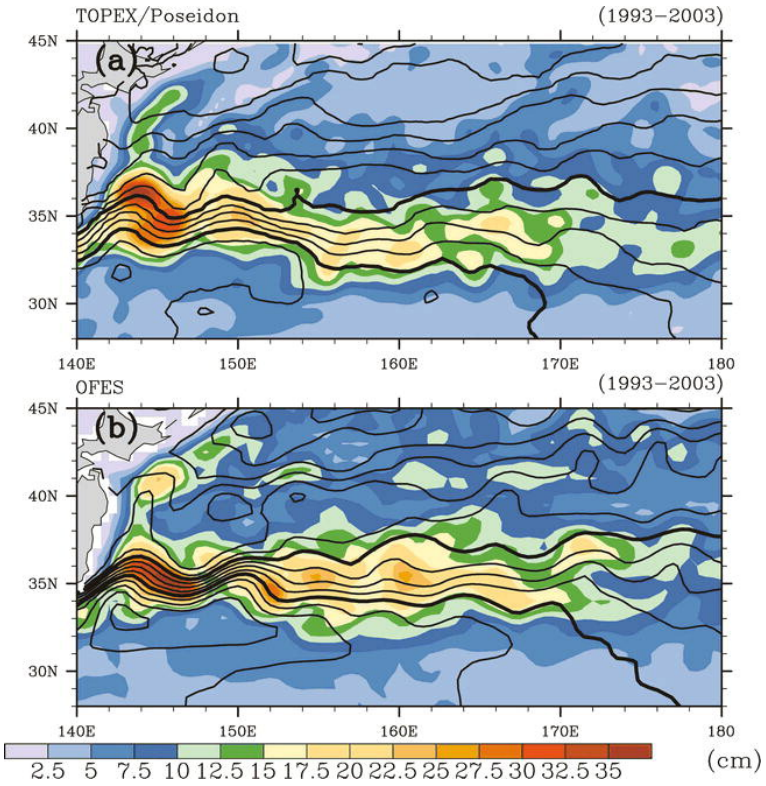

FIGURE 2.4 – Ecart-type de la SST (après filtre passe-bas de 12 mois) (couleur) et moyenne de la SSH absolue (contours à 10 cm d'intervalle, les contours de 60 cm et 100 cm en gras délimitent la zone frontale du KOE) observée par altimétrie (a) et simulée par le modèle OFES (b). D'après Taguchi et al. (2007) (Fig. 1)

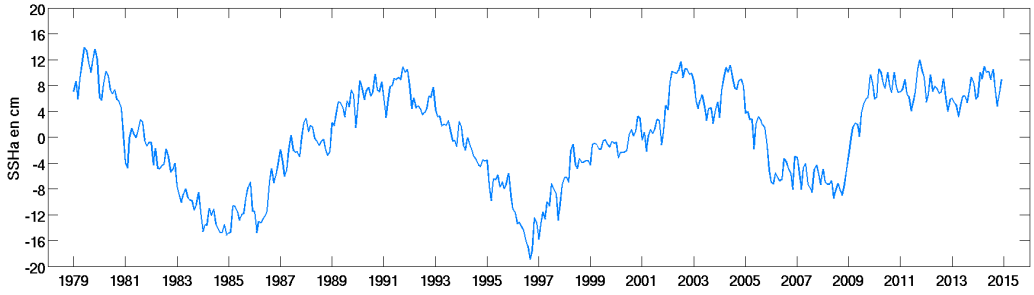

FIGURE 2.5 – Série temporelle depuis 1979 de l'indice du KE défini par Qiu et al. (2014), en cm.

montre que l'intensité et la latitude du KE sont moins bien corrélées avant 1977. Ainsi, dans la majeure partie de ma thèse, je n'ai considéré l'indice du KE qu'à partir de 1979, car c'est à partir de cette date que les données atmosphériques ERA-Interim sont disponibles. Avant 1977, il n'est pas clair si cet indice est aussi approprié pour décrire la variabilité du KE.

La série temporelle décrivant les fluctuations du KE depuis 1979 est montrée sur la figure 2.5. On peut voir que ces fluctuations sont clairement dominées par une variabilité décennale. Lorsque l'indice du KE est positif, le KE est dans l'état dynamique stable, sa trajectoire est plus au nord, le courant est plus fort, et l'activité tourbillonaire est réduite (i.e. les années 1989-92,

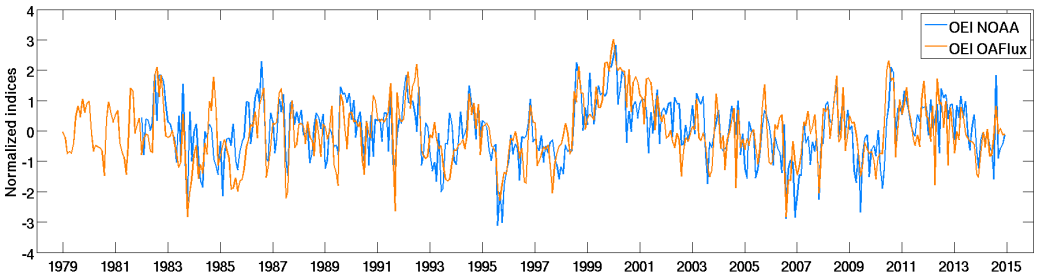

FIGURE 2.6 – Séries temporelles des indices de l'OE basés sur les données NOAA (bleu) et OAFlux (orange).

2002-05 et 2010-13), et inversement pour les valeurs négatives (i.e. les années 1983-87, 1995-99 et 2006-09).

2.3 Série temporelle des fluctuations de l'Extension de l'Oyashio

La série temporelle représentant la variation de la position en latitude de l'Extension de l'Oyashio que j'ai utilisée a été calculée par Young-Oh Kwon (Woods Hole Oceanographic Institution). Cet indice est basé sur la même méthode que celle de FSKA, mais appliquée à un autre jeu de données pour une plus grande étendue temporelle. Le front de l'Oyashio étant marqué par un fort gradient de SST, FSKA ont défini l'indice de l'OE par la série temporelle de la première composante principale de l'anomalie de la latitude du gradient méridien maximum de SST entre 35° et 47°N et 145° et 170°E. La région à l'ouest de 145°E a été exclue car le KE et l'OE ne sont pas clairement distincts dans cette région, et la région à l'est de 170°E n'a pas non plus été prise en compte car le front de l'OE y devient trop diffus. Pour construire cette série temporelle, trois étapes de calcul ont été effectuées. Tout d'abord, le gradient de SST est calculé. Ensuite, la latitude de l'OE à chaque longitude et chaque pas de temps est définie par la latitude du gradient méridien maximal de SST entre 35° et 47°N. La tendance cubique ainsi que le cycle saisonnier ont ensuite été retirés du signal, et enfin, le calcul d'EOF est appliqué à la latitude de l'OE. La première EOF représente un déplacement nord-sud du front de l'OE. Lorsque cette méthode est appliquée aux données mensuelles NOAA OISST (NOAA Optimum Interpolation SST Analysis, données estimées par satellites) qui ont une résolution de 0.25° et sont disponibles depuis 1982, cet EOF explique 13% de la variance en données mensuelles, et 32% si un filtre triangulaire sur 13 mois est appliqué avant le calcul des EOFs (FSKA). Mais pour disposer d'une série temporelle avant 1982, les données de SST de OAFlux ont été utilisées. Elles sont disponibles depuis 1958 et ont une résolution de 1°. L'indice basé sur les données NOAA et l'indice basé sur les données OAFlux ont une corrélation de 0.66 sur leur période commune 1982-2014.

Les séries temporelles de l'indice de l'OE calculées à partir des données OAFlux et NOAA sont données sur la figure 2.6. Contrairement aux variations du KE qui sont dominées par une variabilité décennale, les déplacements en latitude de l'OE montrent une variabilité à plus haute fréquence. La persistence du signal associé au Kuroshio est donc nettement plus grande que celle du signal associé à l'Oyashio, ce qui se reflètera dans notre analyse. Les séries de l'OE et du KE

sont peu corrélées entre elles ($r = 0.18$ en phase avec les données OAFlux et une corrélation maximale de 0.27 lorsque l'OE précède de 10 mois, et $r = 0.19$ en phase avec les données NOAA et une corrélation maximale de 0.29 lorsque l'OE précède de 14 mois), ce qui justifie que dans une première partie (chapitre 3), l'OE n'est pas considéré dans l'analyse de l'influence du KE. Néanmoins, cette corrélation peut augmenter en fonction de la saison considérée (chapitre 4).

Notons enfin que des indices basés sur le gradient méridien de SST sont mieux adaptés à l'estimation de la position d'un front quasi-zonal comme l'OE que la température moyenne autour du front, comme Taguchi et al. (2012). L'indice de Taguchi et al. (2012) est corrélé à 0.41 avec l'indice basé sur les données NOAA, et à 0.57 avec l'indice basé sur les données OAFlux sur leurs périodes communes. On peut donc s'attendre à trouver une réponse atmosphérique un peu différente.

Chapitre 3

Réponse atmosphérique à la variabilité décennale du Kuroshio

Dans cette première partie, j'ai étudié la réponse atmosphérique à la variabilité de l'Extension du Kuroshio (KE), en utilisant l'index défini par Qiu et al. (2014) présenté dans la section 2.2. J'ai utilisé la méthode de régression partielle de Frankignoul et al. (1998), en filtrant le signal lié au téléconnections ENSO par régression sur les deux premières R-EOFs des anomalies de SST dans l'océan Indo-Pacifique. En analysant la réponse atmosphérique sur des saisons glissantes de 2 mois (de septembre-octobre à février-mars), nous avons trouvé qu'une réponse atmosphérique cohérente était observée entre octobre et janvier, mais que celle-ci devenait différente à partir de février. Dans le reste de l'étude, nous nous sommes donc focalisé sur la réponse pendant la saison d'octobre à janvier (ONDJ). Lorsque l'index du KE est positif, le KE est dans un état dynamiquement stable, et les anomalies de SST associées montrent un réchauffement des eaux de surfaces dans la région du KOE. Ce réchauffement génère un flux de chaleur de l'océan vers l'atmosphère et un mouvement ascendant de l'air, ainsi qu'une extension vers le Nord-Est de la baroclinicité, des flux méridiens de chaleur et d'humidité par les tourbillons, et du rail des dépressions. La réponse atmosphérique est grande échelle et consiste en un signal équivalent barotrope de structure tripolaire, avec une anomalie positive de pression sur le Pacifique Nord et l'ouest des Etats-Unis, et une anomalie négative sur l'Arctique, générant un renforcement du vortex polaire. L'échauffement de l'atmosphère par l'océan et les anomalies dans les tourbillons transitoires excitent des ondes de Rossby stationnaires qui propagent le signal vers les pôles et vers l'est. L'état dynamique stable du KE est lié à un échauffement de l'atmosphère de 0.6°K à 900 hPa sur l'est de l'Asie et l'ouest des Etats-Unis, ce qui réduit la couverture de neige de 4 à 6%. Un mois plus tard, pendant la saison de novembre à février (NDJF), une anomalie positive de pression apparait sur le nord-ouest de l'Europe, et la téléconnexion hémisphérique ressemble à l'Oscillation Arctique. Une analyse en composite montre que cette réponse atmosphérique apparait lors de la phase positive du KE, mais qu'aucune réponse significative apparait lors de la phase négative. Cette forte asymétrie peut s'expliquer par la différence entre l'impact d'une anomalie positive de SST et celui d'une anomalie négative, l'anomalie positive de SST générant un réchauffement de la colonne d'air plus en profondeur, avec une anomalie maximale à 400 hPa.

Influence of the Decadal Variability of the Kuroshio Extension on the Atmospheric Circulation in the Cold Season

ADÈLE RÉVELARD, CLAUDE FRANKIGNOUL, AND NATHALIE SENNÉCHAEL

Sorbonne Universités (UPMC, Univ. Paris 06) CNRS/IRD/MNHN, LOCEAN/IPSL, Paris, France

YOUNG-OH KWON

Woods Hole Oceanographic Institution, Woods Hole, Massachusetts

BO QIU

Department of Oceanography, University of Hawai'i at Mānoa, Honolulu, Hawaii

(Manuscript received and in final form 23 July 2015)

ABSTRACT

The atmospheric response to the Kuroshio Extension (KE) variability during 1979–2012 is investigated using a KE index derived from sea surface height measurements and an eddy-resolving ocean general circulation model hindcast. When the index is positive, the KE is in the stable state, strengthened and shifted northward, with lower eddy kinetic energy, and the Kuroshio–Oyashio Extension (KOE) region is anomalously warm. The reverse holds when the index is negative. Regression analysis shows that there is a coherent atmospheric response to the decadal KE fluctuations between October and January. The KOE warming generates an upward surface heat flux that leads to local ascending motions and a northeastward shift of the zones of maximum baroclinicity, eddy heat and moisture fluxes, and the storm track. The atmospheric response consists of an equivalent barotropic large-scale signal, with a downstream high and a low over the Arctic. The heating and transient eddy anomalies excite stationary Rossby waves that propagate the signal poleward and eastward. There is a warming typically exceeding 0.6 K at 900 hPa over eastern Asia and western United States, which reduces the snow cover by 4%–6%. One month later, in November–February, a high appears over northwestern Europe, and the hemispheric teleconnection bears some similarity with the Arctic Oscillation. Composite analysis shows that the atmospheric response primarily occurs during the stable state of the KE, while no evidence of a significant large-scale atmospheric response is found in the unstable state. Arguments are given to explain this strong asymmetry.

1. Introduction

The Kuroshio Extension (KE) is an eastward flowing inertial jet extending the western boundary current of the North Pacific subtropical gyre after it separates from the Japan coast. It is accompanied by large-amplitude meanders and energetic pinch-off eddies (e.g., Qiu and Chen 2005; Kelly et al. 2010). Its path is well defined by the maximum meridional gradient of the sea surface height (SSH), which is located near 35°N. This is south of the North Pacific subarctic frontal zone (SAFZ) associated with the Oyashio Extension (OE), an extension of the western subarctic gyre, which is defined by the maximum meridional sea surface temperature (SST) gradient and found somewhat north of 40°N. The two currents have a different vertical temperature structure as the KE front is strongest between 200 and 600 m but has a modest SST gradient, while the OE is shallow and has a strong SST gradient (Nonaka et al. 2006).

The KE system exhibits large decadal fluctuations between relatively stable and unstable states (Qiu and Chen 2005, 2010; Taguchi et al. 2007; Qiu et al. 2014). When it is in the stable state, the KE jet is strengthened, its path is shifted northward, the regional eddy kinetic energy is lower, and the southern recirculation gyre

Corresponding author address: Adèle Révelard, LOCEAN/IPSL, Université Pierre et Marie Curie, 4 Place Jussieu, 75252 Paris CEDEX 05, France.
E-mail: arlod@locean-ipsl.upmc.fr

DOI: 10.1175/JCLI-D-15-0511.1

intensified. The reverse holds in the unstable state. Previous studies have shown that the KE responds to basin-scale wind forcing over the central North Pacific with a delay of 3–4 years linked to baroclinic Rossby wave propagation (e.g., Seager et al. 2001; Schneider et al. 2002) and that frontal-scale inertial fluctuations initiated by the arrival of the Rossby waves narrow the KE jet (Taguchi et al. 2007; Sasaki et al. 2013). Qiu (2003) suggested that the SSH in the KE region is mainly driven by fluctuations in the strength and location of the Aleutian low, whereas Ceballos et al. (2009) argued that the main driver of the KE strength change was the North Pacific Oscillation, although the two modes are not well separated either in the satellite altimetry era (Qiu and Chen 2010) or in the period considered in the present paper. On the other hand, the transport and meridional position of the OE respond rapidly to the wind stress changes associated with the Aleutian low via barotropic Rossby wave propagation and Ekman currents, while being also remotely forced near 160°–170°E about three years before (e.g., Qiu 2002; Nonaka et al. 2008). Hence, the decadal variability of the KE and the OE is not necessarily coherent (Nonaka et al. 2006). Frankignoul et al. (2011b, hereafter FSKA) indeed found negligible correlation between their KE and OE indices.

The Kuroshio–Oyashio Extension (KOE) region is an area of maximum heat release from the ocean to the atmosphere and strong interannual SST variability, especially on its northern side along the OE (Kelly et al. 2010; Kwon et al. 2010). Vivier et al. (2002) showed that interannual changes in the upper ocean heat content of the KE are dominated by geostrophic advection, with a clear signature in SST. Sugimoto and Hanawa (2011) showed that SST changes are primarily responsible for turbulent heat flux variations. Because of the strong ocean-to-atmosphere fluxes of heat and moisture, the KOE is a region of large cyclogenesis, as major storm tracks are organized along or just downstream of the main oceanic frontal zones (Hoskins and Hodges 2002; Bengtsson et al. 2006). Nakamura et al. (2004) and Taguchi et al. (2009) have argued that differential heat supply across the North Pacific SAFZ acts to maintain surface baroclinicity, sustaining storm development and the anchoring effect of the SST frontal zones, and they suggested that their variations may affect storm-track activity and the westerly jets.

Observational evidence that North Pacific SST anomalies influence the large-scale atmospheric circulation has been found in several studies, based on its relation with preceding SST fluctuations (Liu et al. 2006; Frankignoul and Sennéchael 2007; Wen et al. 2010; Taguchi et al. 2012; Gan and Wu 2013). Modeling studies have also documented the ocean-to-atmosphere feedback in the KOE region (Peng and Whitaker 1999; Kushnir et al. 2002; Liu and Wu 2004; Gan and Wu 2012; Smirnov et al. 2015). These experiments suggest that the atmospheric response is primarily governed by nonlinear transient eddy feedbacks, which act both to amplify the downstream response and make it equivalent barotropic. It is sensitive to the mean background flow, and consequently to the season considered. Smirnov et al. (2015) focused on the local atmospheric response to an Oyashio frontal shift by prescribing in a high-resolution AGCM the corresponding SST anomaly. The others used a basinwide SST pattern centered in the KOE region, and the possible links with the variability of the western boundary current extensions were not investigated. However, Joyce et al. (2009) found that the year-to-year shifts in the KE path were followed by significant changes in the near-surface synoptic activity, and FSKA suggested that the meridional shifts of the KE during 1980–2006 had a significant impact on the large-scale atmospheric circulation, as a northward shift of the KE was primarily followed by high pressure anomalies centered in the northwestern North Pacific and hemispheric teleconnections. Kwon and Joyce (2013) showed that in this case the northward heat transport by the synoptic atmospheric eddies was decreased. In these studies, the meridional shifts of the KE were derived from temperature data at 200-m depth, with very limited spatial and temporal resolution. They were only moderately correlated ($r = 0.52$) with the meridional shifts more accurately derived from satellite altimetry, probably because of the strong spatial smoothing and the relatively shallow level used to define the KE path. In addition, the temporal resolution was too coarse to investigate seasonal dependency in the air–sea coupling. More recently, O'Reilly and Czaja (2015) produced a more accurate KE index derived from a maximum covariance analysis between SST and SSH gradient observations, but SST observations with high spatial resolution were only available since June 2002, so that a longer KE index (1992–2011) was obtained by projecting the 2002–11 SSH spatial pattern onto the full SSH record.

It is thus of interest to use data with higher temporal resolution that describe the KE variability over a longer duration, so that its influence on the atmosphere and its seasonal dependency can be better assessed. In the present paper, we use the SSH-based KE index that was derived by Qiu et al. (2014) by combining satellite SSH measurements and an eddy-resolving ocean general circulation model (OGCM) hindcast, providing an accurate description of the KE state at monthly resolution during the 1955–2012 period. Qiu et al. (2014) showed

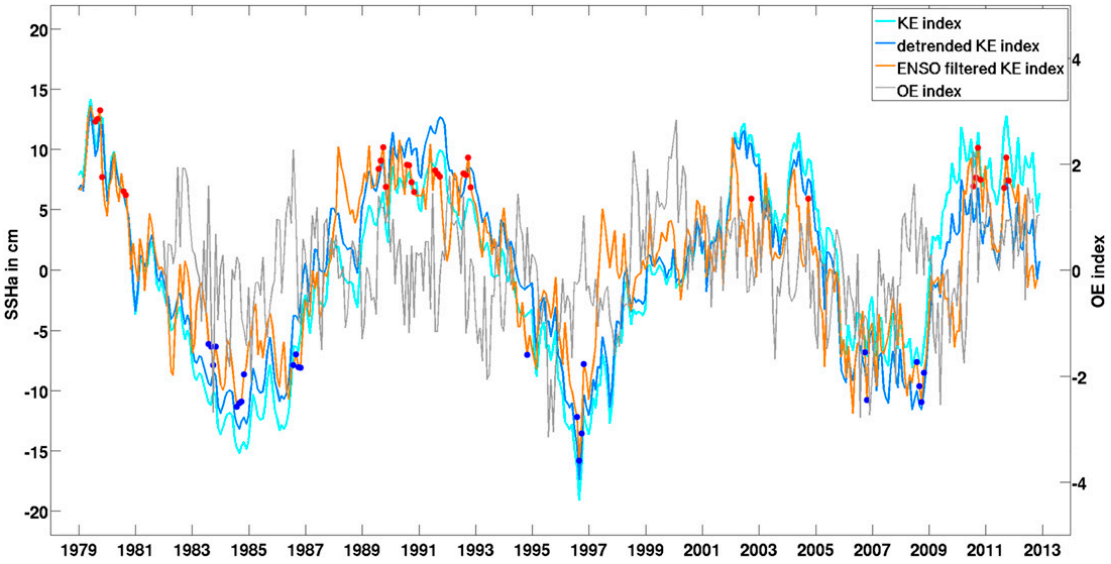

FIG. 1. Monthly KE index time series before (cyan) and after (blue) cubic trend removal, and after ENSO filtering (orange) (see text) and OE index (thin gray) defined by the leading principal component of the latitude of the maximum meridional SST gradient between 145° and 170°E (left-hand *y* axis; Frankignoul et al. 2011b). Dots denote positive (red) and negative (blue) extreme events during the ASON season, as used in the composite analysis.

that the KE fluctuations changed character around the 1976–77 regime shift in the North Pacific climate system (Trenberth and Hurrell 1994). Here we focus on the 1979–2012 period, which is characterized by large decadal fluctuations of the KE and is covered by ERA-Interim (Dee et al. 2011). The data and method are described in sections 2 and 3. In section 4, we show that the KE precedes a large-scale atmospheric signal in the cold season, and we discuss the possible mechanisms by which the KE changes affect the large-scale atmospheric circulation. In section 5, the response asymmetry is analyzed. The results are summarized and discussed in section 6.

2. Data

To represent the variability of the KE, we use the index of Qiu et al. (2014), which is defined by the SSH anomaly averaged in the region 31°–36°N, 140°–165°E (Fig. 1, cyan curve). A positive KE index denotes a stable state in which the KE jet has a steady and northerly path, an increased surface transport, an enhanced southern recirculation gyre, and a decreased regional eddy kinetic energy. A negative KE index reflects the reversed properties. From October 1992 to December 2012, the KE index is based on satellite altimeter observations. To extend the time series prior to the satellite altimeter period, Qiu et al. (2014) used a hindcast simulation of the eddy-resolving Ocean General Circulation Model for the Earth Simulator (OFES) as it captures the KE decadal variability realistically (Nonaka et al. 2006; Taguchi et al. 2007; Qiu et al. 2014). The model output extends from 1950 to 2012, but the KE index inferred from OFES exhibits shorter and less regular fluctuations prior to the 1976–77 North Pacific climate shift (Qiu et al. 2014). Here, we focus on the 1979–2012 period, which corresponds to the availability of the latest reanalysis from the European Centre for Medium-Range Weather Forecasts (ECMWF) (ERA-Interim; Dee et al. 2011). The mean seasonal cycle of the KE index was subtracted by regression onto the first two annual harmonics, which accounted for 2.4% of the total variance.

Monthly anomalies of sea level pressure (SLP), geopotential height, horizontal wind velocity, wind stress, temperature, and humidity were taken from ERA-Interim at 1.5° resolution, while a ¾° resolution was used for SST, turbulent and radiative heat fluxes, and vertical wind. Masunaga et al. (2015) have shown that the improvement of the resolution of the prescribed SST in ERA-Interim (from 1° to ¼°) starting in January 2002 exerts substantial impacts on the representation of the marine atmospheric boundary layer, cloudiness, and precipitation. Hence, our analysis of the local influence of the KE variability should be viewed with caution. Nonetheless, our results were verified using the NCEP–NCAR reanalysis (Kalnay et al. 1996) that has a lower resolution (T63 spectral truncation). This suggests that data assimilation is sufficient to strongly constrain the large-scale atmospheric flow, and that the improvement of the SST resolution in 2002 does not significantly influence our estimation of the large-scale response to the

KE fluctuations. Transient eddy activity and fluxes were estimated from high-pass daily values, using the Blackmon filter to retain fluctuations with periods between 2 and 8 days (Blackmon and Lau 1980; Hurrell and Deser 2009). In addition, the latent and sensible heat fluxes were taken from the 1° objectively analyzed air–sea fluxes (OAFlux) product provided by the Woods Hole Oceanographic Institution (Yu and Weller 2007). Sea ice cover (SIC) and snow cover extent (SCE) datasets provided by NOAA/National Climatic Data Center (NCDC) were also considered. The SIC dataset comes from the passive microwave monthly sea ice concentration provided by the National Snow and Ice Data Center. The SCE dataset is a record of weekly Northern Hemisphere snow cover extent provided by the Rutgers University Global Snow Laboratory. As for the KE index, the mean seasonal cycle was removed from each variable.

3. Method for estimating the atmospheric response

To estimate the atmospheric response to the KE variability, we follow the lag regression approach of Frankignoul et al. (1998). Its principle is that, given the limited persistence of the atmosphere intrinsic variability compared to the oceanic one, ocean-to-atmosphere impact can be estimated by the covariance between the ocean and the atmosphere, with the ocean leading by more than the intrinsic atmospheric persistence but less than the oceanic one, which is about 2–3 years for the KE index. However, this requires that there be no other persistent signal in the atmosphere, which does not hold in the presence of trends and atmospheric teleconnections with the tropics. Hence, before calculating the regressions, a cubic polynomial estimated by least squares fit was removed from each variable (linear detrending yields very similar results). The ENSO signal was also removed, as described in the appendix. The impact of this correction on the KE index is small, except during the strong ENSO events in 1982/83, 1997/98, 2003, and 2010 (Fig. 1).

To distinguish the atmospheric response to the KE variability from that to the OE front, we first used bivariate regression on the KE index and FSKA's index of the meridional shifts of the OE derived from the maximum meridional SST gradient, using the 1982–2012 period when both indices are available. As the results were very similar to those given by univariate regression, consistent with the poor correlation between the two indices ($r \sim 0.2$) (Fig. 1), only univariate regressions onto the KE index are shown below.

a. The statistical model

Earlier numerical modeling studies suggest that the atmospheric response to anomalous SST or other boundary forcing in the extratropics takes 1–2 months to reach its maximum amplitude (Ferreira and Frankignoul 2005; Deser et al. 2007). This delay reflects the time for eddy–mean flow interactions to transform the initial baroclinic local response into a large-scale equivalent barotropic one. However, recent high-resolution experiments suggest that the maximum amplitude may be reached slightly faster (Smirnov et al. 2015), so that we assume that the response time to the SST fingerprint of the KE is 1 month. As discussed in Frankignoul et al. (2011a), the monthly atmospheric fields have some persistence and a lag of 1 month may mix atmospheric forcing and response. Considering the ocean leading by at least 2 months is therefore the safest way to single out the response (see also section 4a). Moreover, the SST fingerprint of the KE becomes slightly stronger and more extended after a delay of 1 month (not shown), consistent with the prevalent role of SST advection in the KE region (Vivier et al. 2002). Hence, we assume that the atmospheric response time to the KE is 2 months, so that an atmospheric variable X is decomposed into

$$X(t) = \alpha K(t-2) + be(t-1) + n(t), \qquad (1)$$

where $K(t)$ is the KE index, e is the ENSO signal, and $n(t)$ is the atmospheric noise, considered as white at low frequency. To take into account the time for ENSO teleconnections to reach the North Pacific, we have assumed a one-month delay, which corresponds to the maximum ENSO teleconnections, as estimated by the root-mean-square of the regression coefficients of North Pacific SLP (north of 20°N) onto the ENSO signal. To estimate α, we remove the ENSO signal, using the method of FSKA, which yields (see the appendix)

$$\tilde{X}(t) = \alpha \tilde{K}(t-2) + n(t), \qquad (2)$$

where $\tilde{X}$ and $\tilde{K}$ denote the ENSO filtered atmospheric variable and KE index. As the KE index is standardized, the regression of $\tilde{X}(t)$ onto $\tilde{K}(t-2)$ provides an estimate of the typical amplitude of the response, corresponding to one standard deviation change in the KE index. In the following, such regressions are referred to as the estimated response to the KE variability (unless evidence is found that other concomitant boundary forcing may have contributed to the atmospheric response). Note that there is some arbitrariness in our choice, since the regressions when $\tilde{K}$ leads by 3 or 4 months show similar patterns (see Fig. 3 below).

Estimating the response at lag 3 instead of lag 2 months would slightly increase its amplitudes, as the covariance between $\tilde{X}$ and $\tilde{K}$ would be divided by the lag-1 autocorrelation of $\tilde{K}(t)$.

b. *Statistical significance*

Statistical significance was estimated in two ways, with comparable results. First we used a standard Student's t test in which the effective number of degrees of freedom N_{eff} is estimated as $N_{\text{eff}} = N(1 - r_1 r_2)(1 + r_1 r_2)^{-1}$ in order to take into account the time series persistence, where N is the sample size (132 in most cases, when we use 4 months for 33 years), and r_1 and r_2 are the lag-1 autocorrelation of the KE index and the time series being regressed (Bretherton et al. 1999). Note that the KE index is highly persistent [$r_1 = 0.86$ for the August–November (ASON) season], but atmospheric time series have only little autocorrelation. The second method is a block bootstrap approach, randomly permuting the atmospheric time series 1000 times in blocks of 3 years (e.g., von Storch and Zwiers 1999). The Student's t test gives a slightly larger statistical significance. However, both approaches may well underestimate significance (Decremer et al. 2014). Hence, the Student's t test is used in all figures except for vectors, whose significance was estimated by bootstrap scrambling.

4. Cold season atmospheric response to KE fluctuations

Consistent with the seasonal changes in the atmospheric dynamics, the ocean–atmosphere interactions exhibit strong seasonal variations (e.g., Czaja and Frankignoul 2002; Taguchi et al. 2012). Indeed, regressions on the KE index based on all months of the year largely differ from those only based on summer or winter months (not shown). Here, we focus on the cold season, when air–sea interactions are strongest in western boundary current regions because of large heat release to the atmosphere. A close examination of the cold season suggests that there also exist substantial month-to-month variations in the atmospheric response pattern. Figure 2 shows the regression of the geopotential height anomaly at 250 hPa (Z250) on the KE index 2 months earlier in sliding sets of 2 months, from September–October (SO) to February–March (FM). A broadly coherent tripolar atmospheric response pattern is found from October to January, while it is not yet established in September–October, and becomes quite different in February–March. This is consistent with observational and modeling studies (Peng and Whitaker 1999; Liu and Wu 2004; Liu et al. 2007; Gan and Wu 2012; Taguchi et al. 2012) showing that the North Pacific Ocean feedback to the atmosphere is dominated by the early-winter response, and that the late winter one differs significantly. Note that October–November (ON) and December–January (DJ) show slightly different patterns, especially over the United States. The ON response is very similar to the one found by Okajima et al. (2014) for October 2011, while it is slightly different in DJ. Nonetheless, the analyses presented in this paper show broadly the same results if applied separately to the two seasons (not shown). Hence, in order to maximize the number of degrees of freedom without substantially distorting the signal by seasonal changes, we focus on the atmospheric response estimated from monthly anomalies in October–January (ONDJ). Note that we use monthly anomalies (four values per year at each grid point). However, using seasonal means gives very similar results.

a. *Lead–lag analysis*

One of the difficulties in estimating the midlatitude atmospheric response to oceanic fluctuations is to distinguish it from the atmospheric forcing that generated the oceanic variability. As discussed in section 1, the low-frequency variability of the KE is largely controlled by large-scale wind stress curl variations that lead to oceanic adjustment via baroclinic Rossby wave propagation, which also initiates frontal-scale inertial fluctuations. The observations and linear Rossby wave models suggest that the KE is primarily forced by wind stress curl anomalies with a delay of 3–4 years (Ceballos et al. 2009; Qiu 2003). Hence, the covariance between the KE and the atmosphere leading by approximately 3–4 years shows the atmospheric forcing pattern. On the other hand, the covariance at lag ≥ 2 months (positive lag indicates that the KE leads) should reflect the atmospheric response to the KE if the ENSO signal is removed, and α can be estimated from (2). If there was no direct local forcing and the KE was only remotely forced, the covariance at lag ≤ 1 month would also reflect the atmospheric response at short lag, as $\tilde{K}(t)$ would be uncorrelated with prior values of $n(t)$. Hence, the lead–lag regression would be symmetric about lag 2 months, within sampling uncertainties. However, this is not the case as the KE also responds rapidly to the atmosphere, either because of local forcing or because of a fast barotropic adjustment, so that the covariance at lag ≤ 1 month mixes the atmospheric forcing and response.

The lead and lag relation between the KE index and the SLP, Z250, and the Ekman pumping in ONDJ is illustrated by the regressions in Fig. 3. The atmospheric forcing of the KE is shown at lag -42 months, but a very similar pattern is found at lags from -14

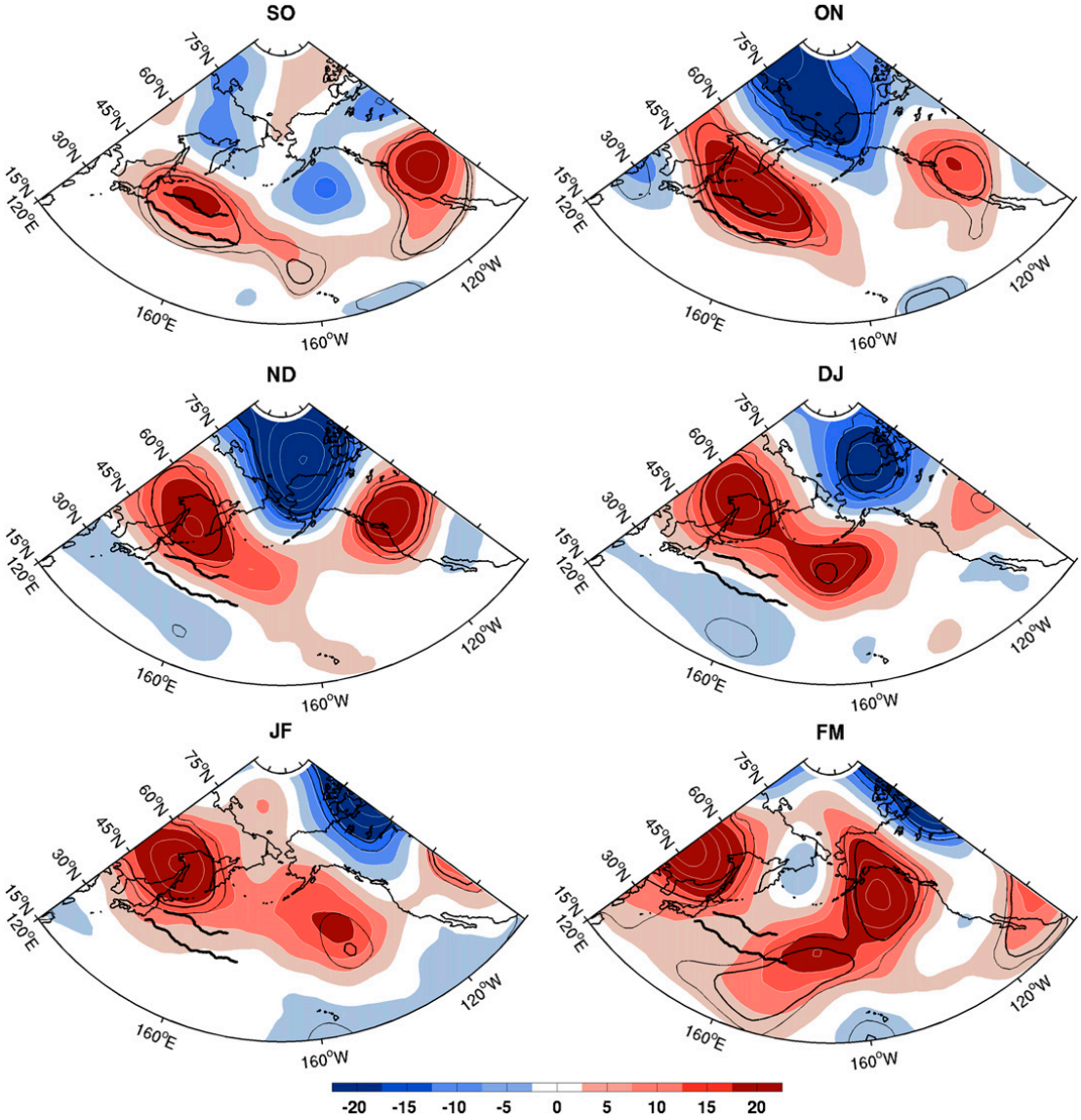

FIG. 2. Lagged regression of the Z250 anomaly onto the KE index 2 months earlier (m) for seasons of 2 months during the cold season, from SO to FM. Thick black lines denote the mean KE and OE paths defined by the mean latitude of the maximum meridional SSH and SST gradient respectively [KE mean path from Kelly et al. (2010)], and thick (thin) black contours indicate 10% (5%) significance. Contour interval is 5 m.

to −48 months (i.e., when the atmosphere leads the KE by 1.5–4 years). The atmospheric pattern broadly resembles the North Pacific Oscillation in its positive phase, with a negative Ekman pumping anomaly in the subtropical gyre and a positive one in the subpolar gyre. The regressions at lag ≥ 2 months with the ENSO signal removed reflect the atmospheric response to the KE. Because of the high autocorrelation of the KE index (33-month zero crossing), the regression patterns are very similar for lags between 2 and 6 months. On the other hand, the regression patterns at lag ≤ 1 month are somewhat different, with a stronger SLP high in the eastern Pacific. At lag ≤ 0, the ENSO signal was not removed because it does not make sense to remove ENSO when looking at the atmospheric forcing of the KE variability, since the KE responds as an integrator of the forcing, which includes the ENSO teleconnections. However, the differences between lead and lag are even larger when ENSO is removed (not shown), confirming that lag ≤ 1 month mixes the atmospheric forcing and response.

The ONDJ atmospheric response is thus best detected when the KE leads by at least 2 months. The following analysis is mostly based on lag 2 months, shown again for clarity in Fig. 4. The atmospheric response in ONDJ consists of a high over the central and

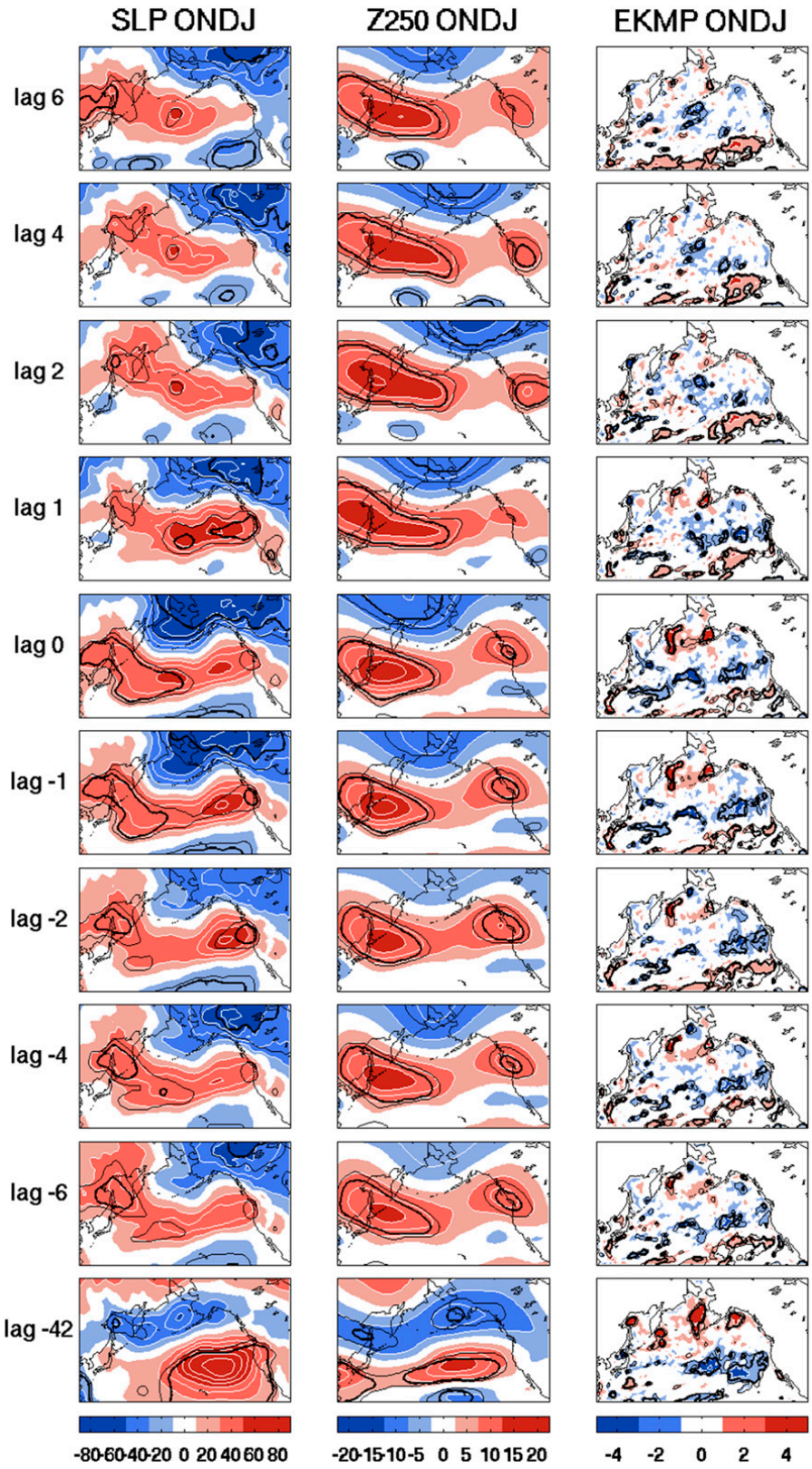

FIG. 3. Lagged regressions of (left) sea level pressure (SLP), (middle) Z250, and (right) Ekman pumping (EKMP) anomaly fixed in ONDJ onto the KE index for lags given on the left (month). Positive (negative) lags mean the KE leads (lags) the atmosphere. Contour intervals are from left to right 20 Pa, 5 m, and 2×10^{-7} m s^{-1} and red (blue) color shading is for positive (negative) anomaly. Thin (thick) black contours indicate 10% (5%) significance.

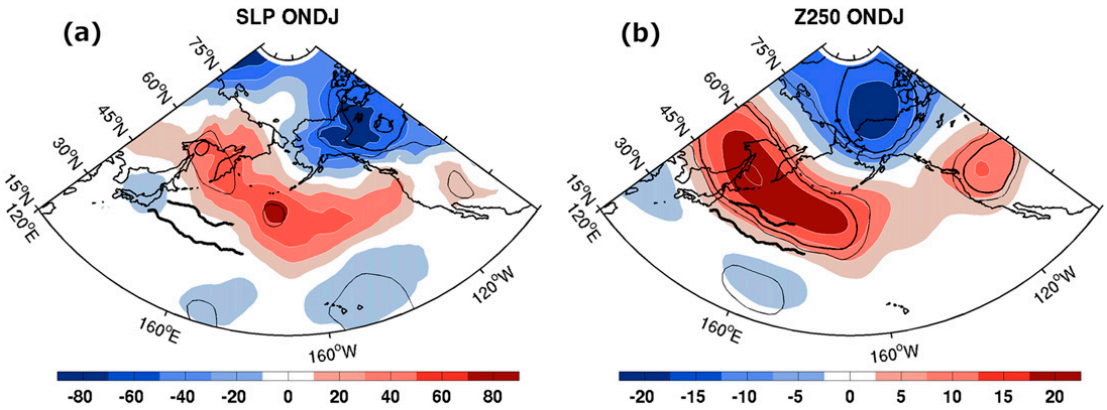

FIG. 4. Estimated response of (a) the SLP (Pa) and (b) the Z250 (m) in ONDJ to the KE index 2 months earlier. Contour intervals are 20 Pa in (a) and 5 m in (b). Thick black lines denote the mean KE and OE paths, and thin (thick) black contours indicate 10% (5%) significance.

northwestern Pacific, typically reaching 0.6 hPa at sea level and 20 m at 250 hPa, and a low of similar amplitude over Alaska and Canada. There is also a smaller high over the western United States at 250 hPa. The structure appears to be broadly barotropic with a westward tilt with height, characteristic of baroclinicity. The associated zonal-mean zonal wind anomaly (not shown) has a deep vertical structure up to 50 hPa that is statistically significant, with positive anomaly of 1–2 m s^{-1} at about 55°N and negative anomaly of 2–3 m s^{-1} at about 35°N, indicating a poleward shift of the eddy driven jet. This suggests that the atmospheric response to the KE decadal fluctuations is closely associated with changes in the transient eddy activity. The Ekman pumping anomaly is positive south of 35°N and negative to the north of it, opposite to the atmospheric forcing pattern (at lag = −42 months), albeit slightly shifted to the south. This suggests a negative feedback on the KE changes, in agreement with Qiu et al. (2014, their Fig. 6), who found a broadly similar but less noisy pattern by considering all the months of the year. The following analysis attempts to explain the mechanisms by which the KE variability leads to such atmospheric response.

It should be noted that the atmospheric response seems to be primarily driven by the decadal variability of the KE. Indeed, repeating the analysis, but regressing onto a high-pass- and low-pass-filtered KE index with a cutoff at 6 years gave very similar results when using the low-pass filtered KE index, but different and more noisy ones when using the high-pass filtered one (not shown).

b. SST anomalies and heat flux feedback

The KE variability influences the atmosphere through SST changes that generate air–sea heat flux anomalies (Fig. 5). For an atmospheric response time of 1 month, the SST in September–December (SOND) should be considered. It shows a broad warming of typically about 0.3–0.5 K in the KOE region, which is in part driven by the intensified advection of warm water coming from the subtropics, as discussed by Vivier et al. (2002), Kelly et al. (2010), and Qiu et al. (2014), among others. The warming is much broader than that associated with the meridional shifts of the KE front east of 155°E during winter (Seo et al. 2014), presumably because the index of Qiu et al. (2014) represents more general KE changes, including the eddy activity that strongly affects the SST and might spread the warming. The surface easterlies response to the KE may also provide a positive feedback as anomalous Ekman transport brings warm water into the KOE region. Although the SST pattern may be artificially broad due to the low resolution of ERA-Interim, recent studies have shown that the KE generates a northeastward quasi-stationary driven jet that separates from the KE around 155°E and transports subtropical water to the subarctic region (Isoguchi et al. 2006; Sugimoto 2014; Wagawa et al. 2014). The KE can therefore have an influence on the SST much farther north than its mean path, and in particular along the OE front, as seen in Fig. 5a, where the SST anomaly is maximum north of the KE mean path, in the confluence region, just south of the OE front. This suggests that, even if the KE and OE indices are not strongly correlated (Fig. 1), there might be some influence of the KE on the OE front that does not significantly impact its latitude.

There is no warming in the western end of the confluence zone where the SST is strongly affected by warm eddies (Sugimoto and Hanawa 2011). These eddies are fewer when the KE index is positive, especially west of 150°E, thus possibly opposing the intensified advection. There are also small remote SST anomalies that covary

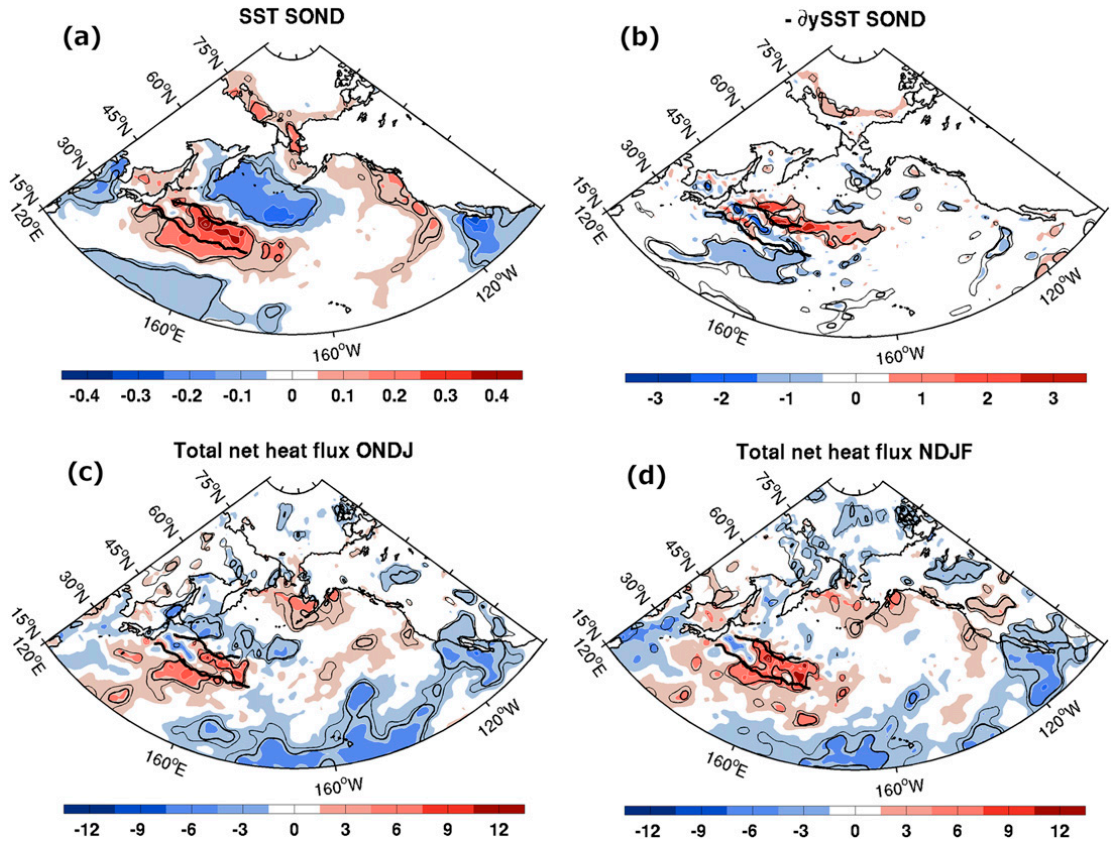

FIG. 5. (a) Estimated response of the SST anomaly in SOND onto the KE index 1 month earlier (K). (b) As in (a), but for the meridional SST gradient (10^{-3} K km^{-1}). (c) As in (a), but for the net heat flux anomaly onto the KE index 2 months earlier (positive upward; W m^{-2}). (d) As in (c), but for NDJF (estimated response after 3 months). Contour intervals are 0.1 K in (a), 1×10^{-3} K km^{-1} in (b), and 3 W m^{-2} in (c) and (d). Thick black lines denote the mean KE and OE paths, and thin (thick) black contours indicate 10% (5%) significance.

with the KE. They may reflect the SST response to atmospheric changes forced by the KE or SST variations forced by the atmospheric fluctuations that affect the KE on short time scale, since they disappear for lags larger than a few months (not shown). In particular, the cooling in the subpolar gyre could be attributed to the intensification of the westerly winds coming from northeastern Siberia due to the high pressure anomaly that precede the KE (Fig. 3), generating anomalous southward Ekman transport. The meridional SST gradient anomaly is positive on the northern flank of the OE east of 150°E, and negative to the south of it (Fig. 5b). Since the climatological SST gradient is maximum along the OE, the OE front is more extended eastward and slightly shifted north when the KE is in positive phase, as remarked above. Note that the concomitant SST anomalies in the other ocean basins are small.

Frankignoul et al. (1998) have shown that the thermal forcing generated by SST anomalies can only be determined when the heat flux lags SST by at least 1 month. It is indeed after a lag of 2–3 months that the heat flux feedback is observed. The anomalous net surface heat flux (latent + sensible + longwave + shortwave) at lag 2 is dominated by the turbulent heat flux, and tends to be positive (heat loss from the ocean) in the KOE region, suggesting a damping of SST anomalies (i.e., a negative feedback; Fig. 5c). This does not hold immediately off Japan where the SST anomalies are negligible, presumably because the turbulent heat flux in the Kuroshio–Oyashio confluence region strongly responds to anticyclonic (warm) eddies, which are less active when the KE index is positive (Sugimoto and Hanawa 2011). However, the heat flux pattern is noisy, and OAFlux may not fully resolve the influence of the KE variability because its estimation relies on atmospheric reanalysis data with relatively low horizontal resolution. Interestingly, the heat flux feedback is clearer one month later, in November–February (NDJF), as shown in Fig. 5d where the heat flux lags the KE index by 3 months. This does not reflect the larger time lag, but atmospheric seasonal differences as the heat flux feedback is stronger during winter (Frankignoul and Kestenare 2005; Park et al. 2005). This

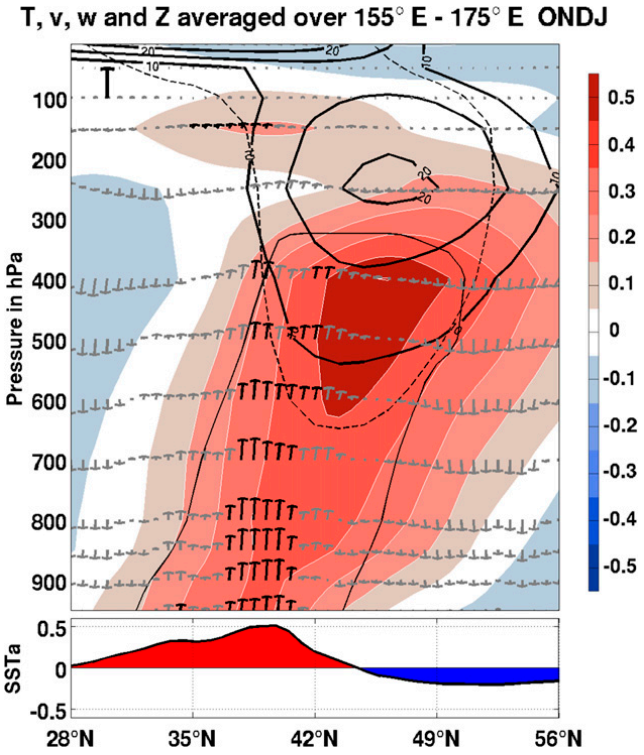

FIG. 6. (top) Estimated response averaged over 155°–175°E of the meridional and vertical wind velocity anomaly (vectors; scaling arrow in the top-left corner of 50 m s^{-1}, for the meridional component and 5×10^{-3} Pa s^{-1} for the vertical component), of the air temperature (K; shading, with contour interval of 0.1 K) and of the geopotential height (m; thick black contours) in ONDJ onto the KE index 2 months earlier. Thin (dashed) black contour indicates 5% temperature (geopotential) significance, and black vectors indicate 10% significance. (bottom) SST anomaly (K) profile shown in Fig. 5a averaged over the same longitude band.

could also be due to the interannual-to-decadal variability of the East Asian monsoon and the associated air–sea heat exchange over the KOE region in early winter (Nakamura and Yamagata 1999; Nakamura et al. 2002; Yoshiike and Kawamura 2009; Kwon et al. 2010). Very similar results are found with the turbulent heat flux from ERA-Interim instead of OAFlux, but it also suffers from limited resolution (section 2).

c. *Changes in convection and synoptic activity*

To explore the dynamical mechanisms involved in the ocean-to-atmosphere interaction, we show the estimated response in ONDJ of several key atmospheric variables, which are thus in phase with the atmospheric response in Fig. 4. The warming of the KOE region generates a positive air temperature anomaly that extends throughout the troposphere and tilts northward with height, with maximum amplitude of 0.6 K at the 400-hPa level (Fig. 6, top). There is a significant anomalous upward motion in the longitude band of 155°–175°E, on the northern side of the KE, where the SST anomaly is maximum. Although it is not statistically significant, there is downward motion north and south of it, as in the simulated response to an OE shift in Smirnov et al. (2015). The upward motion is strongest at 850 hPa, near the top of the marine atmospheric boundary layer, and it reaches 400 hPa, with a northward tilt with height, as above the Gulf Stream (Minobe et al. 2010). The positive SST anomaly thus contributes to the destabilization of the air column above it, and the convective available potential energy is indeed increased (not shown). Although very noisy, there is a positive anomaly in convective precipitation over the KOE region, which leads to a small but significant correlation of about 0.17 when lagging the KE index by 1–12 months if it is averaged over the KOE warming (not shown). Although no net precipitation anomaly could be found, possibly because ERA-Interim precipitation is questionable due to very few observations and pronounced spinup effects over oceans and midlatitude storm tracks (Dee et al. 2011), we conclude that convection is enhanced. This suggests wind convergence at low level, but no corresponding response in the surface wind stress was found.

The KE variability has a strong impact on the synoptic-scale activity, as shown by the Eady growth rate anomaly at 850 hPa (Fig. 7a). The Eady growth rate is given by $\sigma = 0.31N^{-1}|f||\partial V(z)/\partial z|$, where f is the Coriolis parameter, $V(z)$ the vertical profile of the horizontal wind, and N the Brunt Väisälä frequency. It measures the theoretical growth rate of the most unstable synoptic mode, and it was verified that it is largely determined by the air temperature gradient because of the thermal wind balance. A strong negative anomaly appears on the southern flank of the KE due to the weaker SST gradient (Fig. 5b), while the opposite occurs over western Canada. Given the location of the climatological Eady growth rate maximum (green curve), the anomaly pattern indicates a weakening along the KE and a slight downstream northeastward extension of the zone of maximum baroclinicity. Downstream of the Eady growth rate anomaly, the storm track is increased over the eastern North Pacific and Alaska, as shown in Fig. 7b by the anomaly in the root-mean-square of 500-hPa geopotential height. Chang (1993) has shown that the downstream development of unstable baroclinic waves is the main mechanism by which the storm track is extended from highly unstable regions (western North Pacific) into relatively stable regions downstream (eastern North Pacific). Such downstream impact on storm track is also in agreement with Rivière (2009), who showed that latitudinal variations of the Eady growth rate generate a positive eddy feedback that

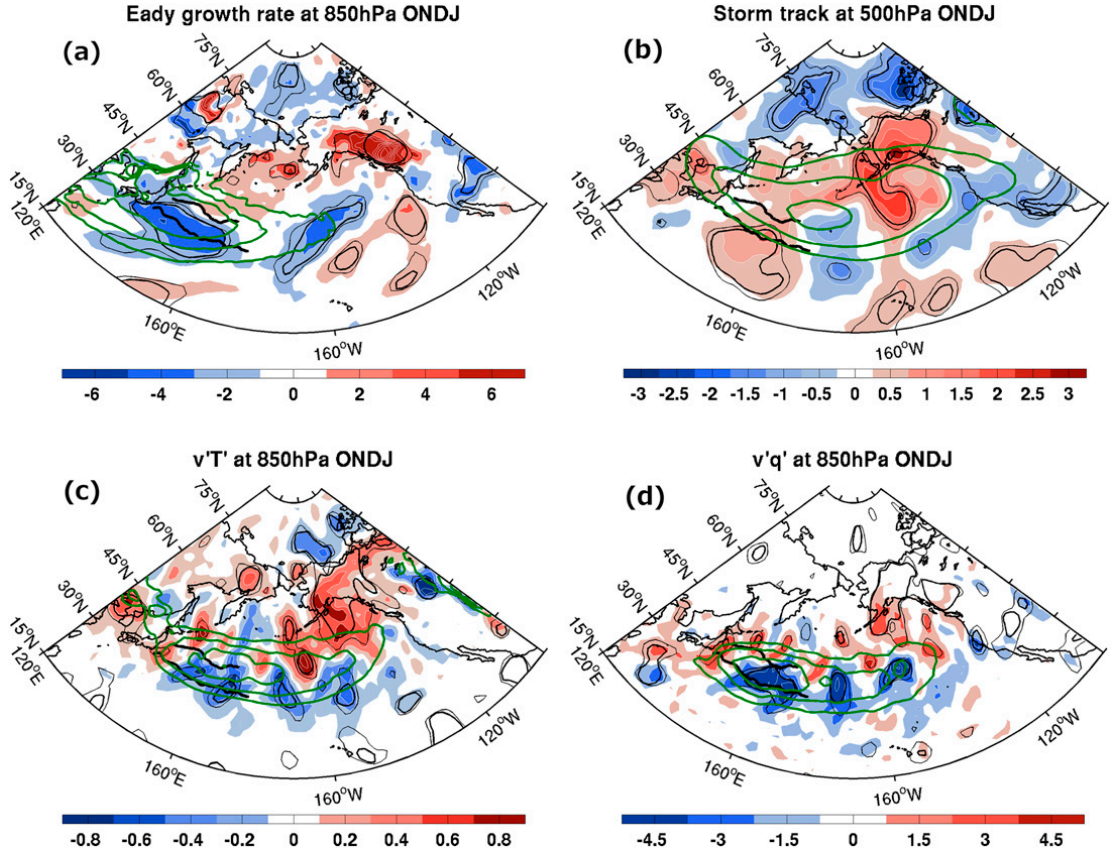

FIG. 7. Estimated response of (a) the Eady growth rate anomaly at 850 hPa (10^{-2} day^{-1}), (b) the storm-track anomaly at 500 hPa (m), (c) the meridional transient eddy heat flux anomaly at 850 hPa (K m s^{-1}), and (d) the meridional transient eddy moisture flux anomaly at 850 hPa (10^{-4} m s^{-1}), in ONDJ onto the KE index 2 months earlier. Contour intervals are 2×10^{-2} day^{-1} in (a), 0.5 m in (b), 0.2 K m s^{-1} in (c), and 1.5×10^{-4} m s^{-1} in (d). Green contours denote the ONDJ climatology, with contours at 50, 70, and 85×10^{-2} day^{-1} in (a); 40, 50, and 60 m in (b); 6, 8, 10, and 12 K m s^{-1} in (c); and 30, 40, and 50×10^{-4} m s^{-1} in (d). Thick black lines denote the mean KE and OE paths, and thin (thick) black contours indicate 10% (5%) significance.

amplifies the variations downstream of the source region. They also showed that a more poleward baroclinicity favors anticyclonic wave breaking (AWB) events. This pushes the eddy driven jet poleward, favoring AWB in the region of maximum eddy activity and leading to a more southwest–northeast orientation of the jet. This should lead to an anticyclonic anomaly in the central basin and is in agreement with the northward shift of zonal wind discussed above and with the SLP response in Fig. 4. Hence, by means of baroclinic waves and eddy activity, the impact on the storm track of the KE warming is primarily downstream.

To document the KE influence on the meridional heat and moisture transfer by the transient eddies, the transient eddy heat and moisture fluxes, $\langle v'T' \rangle$ and $\langle v'q' \rangle$, respectively, were considered, where the prime denotes high-pass daily values and the angle brackets denote monthly averages. The anomalies driven by the KE fluctuations are given at the 850-hPa level in Figs. 7c and 7d, but very similar results are found for the integrated transports between 950 and 700 hPa. For both fluxes, there is a positive anomaly in the eastern North Pacific, on the northeastern flank of the climatological maximum, and a negative anomaly on the southern flank. This indicates a weakening and a northeastward extension of the zone of maximum transient eddy fluxes, consistent with the changes in Eady growth rate and storm track. This is slightly different from the northward shift found by Qiu et al. (2014) using all the months of the year. In zonal averages, the meridional eddy humidity transport is weakened during a positive KE phase, in agreement with Kwon and Joyce (2013), although they found a very different spatial pattern using the KE index based on the temperature at 200-m depth in January–March (JFM). On the other hand, the zonally averaged eddy heat transport is weakened at about 35°N but enhanced at around 60°N because of the large positive anomaly over Alaska.

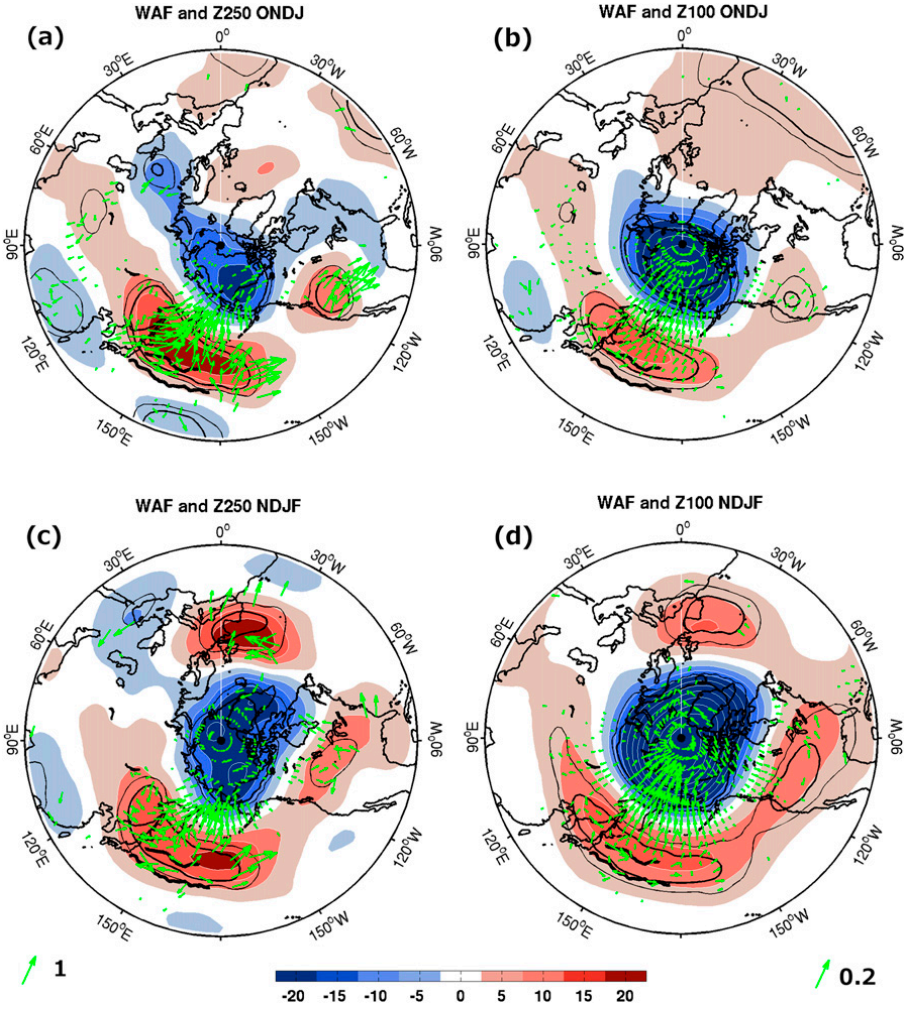

FIG. 8. Estimated response of the geopotential height anomaly at (a),(c) 250 hPa and (b),(d) 100 hPa (m; shading, with contour interval of 5 m) in (a),(b) ONDJ onto the KE index 2 months earlier and (c),(d) NDJF onto the KE index 3 months earlier, and corresponding WAF ($m^2\ s^{-2}$; green vectors, scaling given on the bottom-left for the 250 hPa level and on the bottom-right for the 100-hPa level). Thick black lines denote the mean KE and OE paths, and thin (thick) black contours indicate 10% (5%) significance. For clarity, only 10% significant WAF vectors are plotted, and only every third vector is plotted equatorward of 60°N and every fifth one poleward of 60°N.

d. An influence up to the stratosphere

The SST-driven changes in atmospheric stability and transient eddy activity are likely the main mechanisms by which the KE has an influence in the upper atmosphere. The vertical profile of the geopotential height anomaly shows a maximum at the 250-hPa level, above the maximum temperature anomaly (the maximum geopotential height and temperature anomalies occur where the corresponding mean vertical gradient is maximum), and a strong anomaly in the stratosphere (Fig. 6). The hemispheric Z250 teleconnection pattern (Fig. 8a) reveals a low over the Chukchi Sea and a high over United States.

To understand how the signal propagates into the whole hemisphere, we show the anomalous wave activity flux (WAF) at 250 hPa (the same is found at 500 hPa) derived from the monthly geopotential height and temperature anomalies, following the formulation of Takaya and Nakamura (2001), which is a generalization of Plumb's (1985) flux applicable to a zonally varying basic flow. The WAF is a diagnostic tool for illustrating the propagation of quasigeostrophic stationary Rossby waves. Its divergence (convergence) gives the source (sink) of wave activity, and it is, in principle, independent of wave phase and parallel to their local three-dimensional group velocity. It is therefore suited for a snapshot diagnostic of wave packets of stationary

eddies, but it is not a momentum flux, unlike the Eliassen–Palm flux. Figure 8a shows that the KOE region is a source of wave activity propagating primarily poleward toward the low over the Chukchi Sea. There is also some hint of a wavy propagation toward the high anomaly over western United States. This wavy propagation from the KOE region to United States going through the Arctic is even clearer in the lower stratosphere, at 100-hPa level (Fig. 8b). Hence, this analysis suggests that stationary Rossby waves play an important role in extending the atmospheric response poleward and eastward.

Interestingly, one month later, in NDJF, the low pressure lobe is elongated over Greenland and the North Atlantic (reflecting a strengthened polar vortex), the high pressure lobe over western United States has spread eastward, and a significant anomalous high is found over northwestern Europe (Figs. 8c,d). The pattern has some similarity with the Arctic Oscillation, albeit slightly shifted poleward, displacing the eddy-driven jet northward. The wave activity flux may explain the spreading over the Arctic and the United States, but it shows no significant link to western Europe. As there is little change in the SST anomalies in NDJF and no significant SST anomalies are observed in the North Atlantic (not shown), the spreading toward Europe cannot be attributed to downstream or remote changes in SST. Therefore, the anomalous high over Europe might come from a downward propagation of the stratospheric vortex changes into the troposphere, thus influencing the North Atlantic Oscillation (Baldwin and Dunkerton 1999; Polvani and Waugh 2004). Alternatively, the high over northwestern Europe could be due to the KE-driven changes in the storm track. Indeed, the North Atlantic storm-track activity depends in large part on the Pacific storm-track behavior via the link between synoptic wave breaking events in the eastern Pacific and the Atlantic (Chang 2004; Drouard et al. 2013). Disturbances in the Pacific could therefore induce changes in the Atlantic. In fact, the storm track in NDJF is strengthened over northwestern Canada and Iceland (not shown), which could trigger the anomalous high over Europe through eddy–mean flow interactions. However, the **E**-vector divergence anomaly (Hoskins et al. 1983) was too noisy to confirm this hypothesis. Another possible explanation could be that the Pacific-induced anomaly is trapped and redistributed by the time-mean tropospheric jets, which act as waveguides (Branstator 2002).

Although stationary Rossby waves play an important role in spreading the signal horizontally, the strengthening of the polar vortex implies that the upward injection of planetary-wave activity from the troposphere to the stratosphere is reduced (Baldwin and Dunkerton 1999; Polvani and Waugh 2004). To confirm this hypothesis, we consider the zonally averaged meridional eddy heat flux $[v^*T^*]$ at 100 hPa, where the asterisks denote departures from the zonal mean, which is a diagnostic of the troposphere-to-stratosphere wave activity propagation (Polvani and Waugh 2004) and is directly proportional to the vertical component of the conventional Eliassen–Palm flux (Andrews et al. 1987; Nishii et al. 2010). As shown in Fig. 9b, the positive phase of the KE is followed by a reduced wave activity entering the stratosphere, and the spatial distribution of v^*T^* (Fig. 9a) indicates that the reduced wave activity primarily takes place north of the KOE. The same result is obtained when using the vertical WAF from Takaya and Nakamura (2001), but with less statistical significance (not shown). In summary, anomalous wave activity flux propagates horizontally from the KOE region and contributes to spreading the signal poleward and eastward (Figs. 8a,b), but less wave activity flux penetrates into the stratosphere, strengthening the polar vortex one month later (Fig. 8d).

e. *Impact on near-surface climate*

The atmospheric response to KE fluctuations has significant impacts on near-surface climate. As expected from the SST signature of the KE variability, the air temperature in the KOE region is warmer (Fig. 10a). There is also a significant warming over western and central North America, northeastern Asia, and northern Africa. This warming is likely the cause of the concomitant reduced snow cover extent seen in Fig. 10b, since it only appears when the KE index leads by at least 2 months. Consistent with the anomalous low, the temperature over the Arctic Ocean is colder. However, although significant, the temperature perturbations are small, and the potential predictability over these regions based on the KE index is overall limited. This was investigated conducting a one-year-out cross validation. For each year and grid point, we perform the lag regression of the air temperature on the KE index while removing this year, and we use the regression to predict the removed year. The predicted air temperature time series is then correlated to the observed one. This analysis suggests statistically significant, albeit limited, potential predictability over the KOE region and the northern central and western United States, where the cross-validated correlation only reaches 0.2 (0.3 for seasonal means). Later in winter, the weak warming over Iceland is reinforced and has propagated toward northern Europe (not shown). Cross validation suggests that at 3 and 4 months

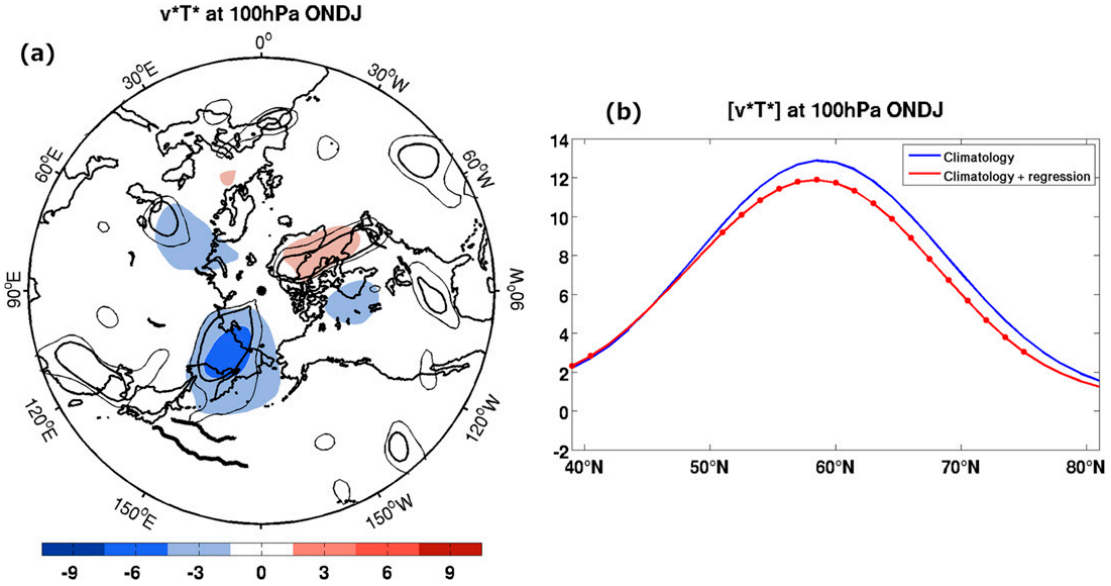

FIG. 9. (a) Estimated response of the meridional eddy heat flux v^*T^* at 100 hPa (K m s^{-1}) in ONDJ onto the KE index 2 months earlier, with contour intervals of 3 K m s^{-1}. Thick black lines denote the mean KE and OE paths, and thin (thick) black contours indicate 10% (5%) significance. (b) Climatology and climatology plus regression of the zonal-mean eddy heat flux $[v^*T^*]$ at 100 hPa (K m s^{-1}) in ONDJ onto the KE index 2 months earlier. The dots denote 5% significance.

lead there is a weak potential predictability over the United States and northwestern Europe.

5. Asymmetry

To investigate whether the stable and the unstable states of the KE influence the atmosphere in a symmetric way, composites were constructed for the response to large positive and negative KE events, namely when the absolute value of the KE index for individual months of the ASON season is higher than one standard deviation. As indicated by the red and blue dots in Fig. 1, the sample is limited, as 27 months qualify as positive events and 24 months as negative events. Therefore, the results should be considered with caution, although asymmetric regression analysis gives basically the same results (not shown). Also, the same analysis was conducted for seasonal means, and the results are identical.

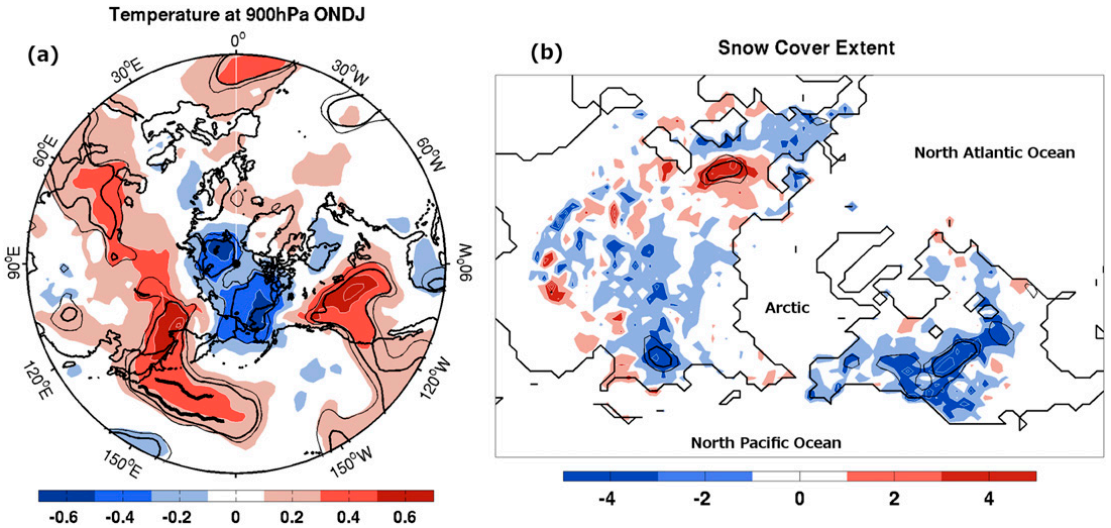

FIG. 10. Estimated response of (a) the temperature anomaly at 900 hPa (K) and (b) the snow cover extent (%) in ONDJ onto the KE index 2 months earlier. Contour intervals are 0.1 K and 2% in (a) and (b), respectively. Thick black lines in (a) denote the mean KE and OE paths. Thin (thick) black contours indicate 10% (5%) significance.

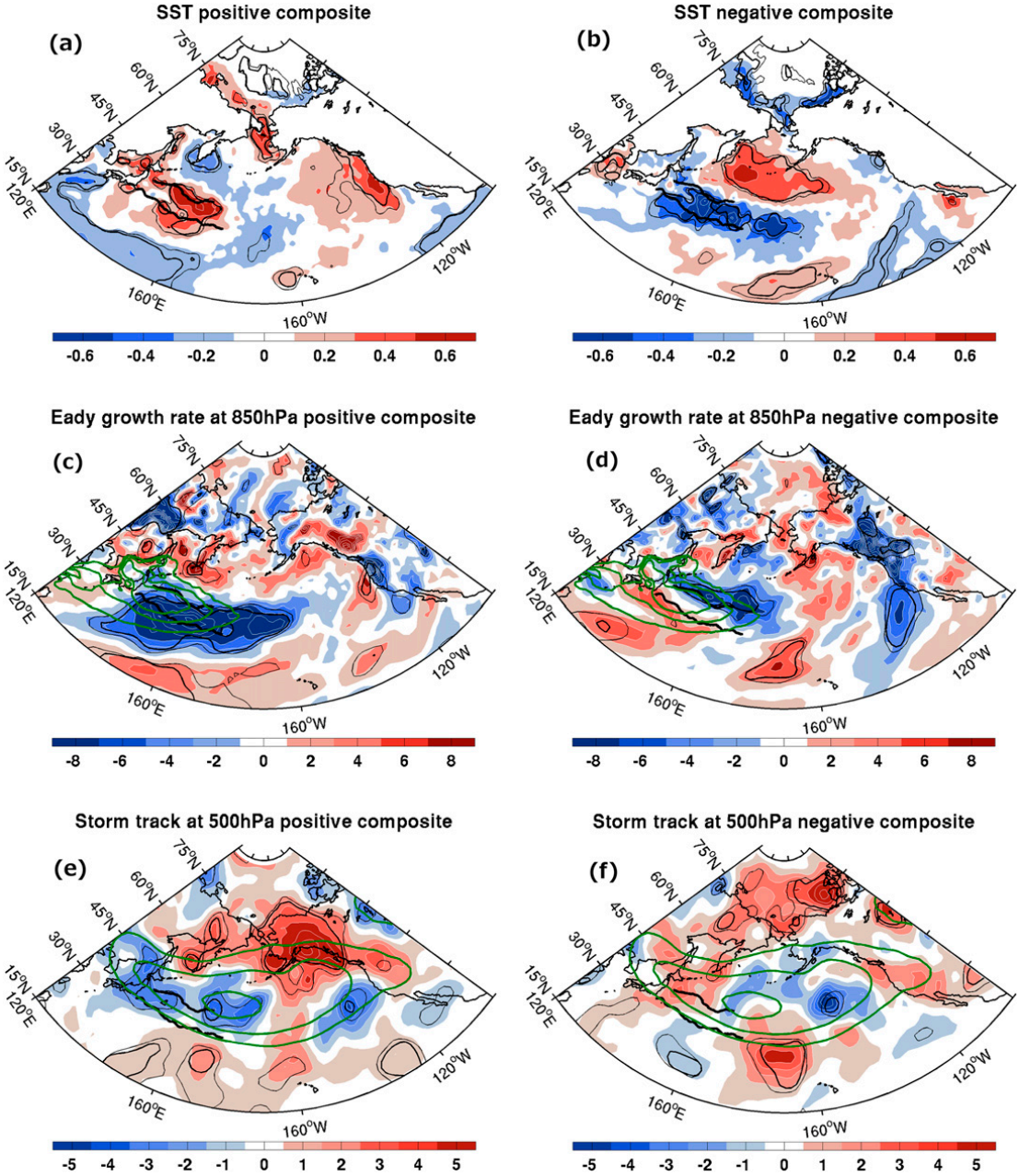

FIG. 11. (a) Positive and (b) negative composite of the SST anomaly (K) in SOND for extreme KE events in ASON. (c),(d) As in (a),(b), but for the Eady growth rate at 850 hPa in ONDJ (10^{-2} day^{-1}). (e),(f) As in (a),(b), but for the storm-track anomaly at 500 hPa in ONDJ (m). Contour intervals are 0.2 K in (a),(b); 2×10^{-2} day^{-1} in (c),(d); and 1 m in (e),(f). Green contours denote the ONDJ climatology, with contours at 50, 70, and 85 $\times$ 10^{-2} day^{-1} in (c) and (d), and at 40, 50, and 60 m in (e) and (f). Thick black lines denote the mean KE and OE paths, and thin (thick) black contours indicate 10% (5%) significance.

A significant asymmetry is found in the large-scale atmospheric response, but much less in the local features. The SST anomaly in the KOE region is roughly symmetric in pattern and amplitude, although the negative anomaly is more longitudinally extended (Figs. 11a,b). There are also clear effects of the oceanic eddy activity. During the positive state, eddy activity is much weaker, in particular west of 150°E. The warming is therefore only observed east of 150°E, whereas the cooling during the negative phase is found much closer to the Japanese coast. Also, the anomalies on either sides of the KOE region are asymmetric. A negative SST anomaly is found in the subtropical gyre when the KE is in a stable state, while a positive SST anomaly in the subpolar gyre is found in the unstable state. Hence, as shown by the meridional SST gradient in Fig. 12, a

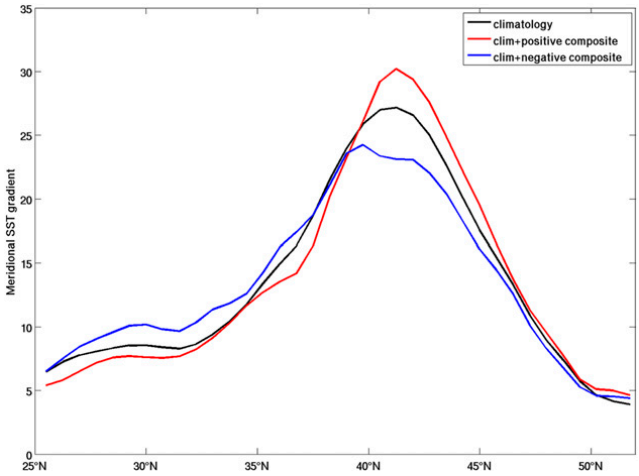

FIG. 12. Climatology of the meridional SST gradient (10^{-3} °C km^{-1}) in SOND zonally averaged over 155°–175°E (black curve), climatology plus positive composite (red curve), and climatology plus negative composite (blue curve).

positive event is associated with a stronger and northward-shifted SST front near the OE, while negative events are linked to a weaker and southward-shifted SST front. The heat flux anomaly is broadly symmetric, more clearly so in NDJF, primarily reflecting the heat flux feedback (not shown). Stronger differences are seen in the Eady growth rate anomaly, as there is a strong weakening of the baroclinicity along the KE during the positive phase, so that the region of maximum baroclinicity is weakened, while it is only slightly shifted south during the negative phase (Figs. 11c,d). Since the baroclinicity is largely determined by the temperature gradient, this is consistent with the strong asymmetry in the air temperature anomaly discussed below. The storm track is enhanced in the northeastern Pacific during a positive phase, while there is no clear signal during a negative phase, but only small patches of positive anomaly all around the climatological maximum (Figs. 11e,f). This suggests that the storm track is less anchored in this case, which might result from the weaker SST front along the OE (Fig. 12), consistent with the anchoring mechanism of Nakamura et al. (2004).

The large-scale atmospheric response reveals an even stronger asymmetry. During the stable KE state, the SLP and Z250 anomalies reflect the regression analysis above, except that the North Pacific high is broader and more extended eastward than in Fig. 4 (Figs. 13a,b). The WAF indicates propagation in both the north and the south direction, which may explain the weak low pressure anomaly in the subtropics. However, the propagation does not reach the tropics as far as in Miyasaka et al. (2014), since it does not spread farther south than 16°N. During the unstable KE state, on the other hand, the atmospheric response is small and noisy. It is reduced to a more localized high over the KOE region and a downstream low that are 3 times weaker than the anomalous high during the stable state, and also tilt westward with height (Figs. 13c,d). The WAF indicates that this region is a source of eastward stationary Rossby wave propagation, but not of poleward propagation, so it is not clear that the positive anomaly over Canada and western United States is linked to the KE.

The asymmetry can be attributed to the fact that, although the SST anomalies are similar in amplitude, a positive SST anomaly has a stronger impact on the air column above it than a negative SST anomaly. As discussed in Deser et al. (2004), such asymmetry is due, in small part, to the nonlinear dependence of evaporation upon SST according to the Clausius–Clapeyron relation, and in larger part by the differences in the deep convective component of the anomalous heating. Indeed, cooling from below is an inherently stabilizing process while heating from below is a destabilizing one, conducive to convective overturning and deeper vertical penetration. Similarly, Sheldon and Czaja (2014) have shown that during winter, convective instabilities are very frequent over the KOE region, and a lower SST would lead to fewer occurrences, while a warmer SST would increase it. As shown in Fig. 14, although the temperature anomaly within the boundary layer has similar amplitude for positive and negative phases of the KE, the positive anomaly amplifies with height, while the negative one does not, so the temperature anomaly in the midtroposphere is considerably stronger in the positive case, consistent with the geopotential anomaly. As a stronger temperature anomaly has a stronger impact on baroclinicity, the changes in baroclinicity and storm track are small in the negative case compared to the positive one (Figs. 11c–f). Since baroclinicity and storm-track anomalies are likely the mechanisms by which a local response leads to a large-scale atmospheric signal, the atmospheric response in the unstable state remains localized, and teleconnections are almost nonexistent.

6. Summary and conclusions

Using the KE index of Qiu et al. (2014), we have shown by regression and composite analyses that the decadal variability of the KE has a significant influence on the large-scale atmospheric circulation in the Northern Hemisphere during the cold season. A close examination of the month-to-month variability in the atmospheric response pattern led to the focus on the months between October and January (ONDJ), when the atmospheric response is broadly coherent. This is

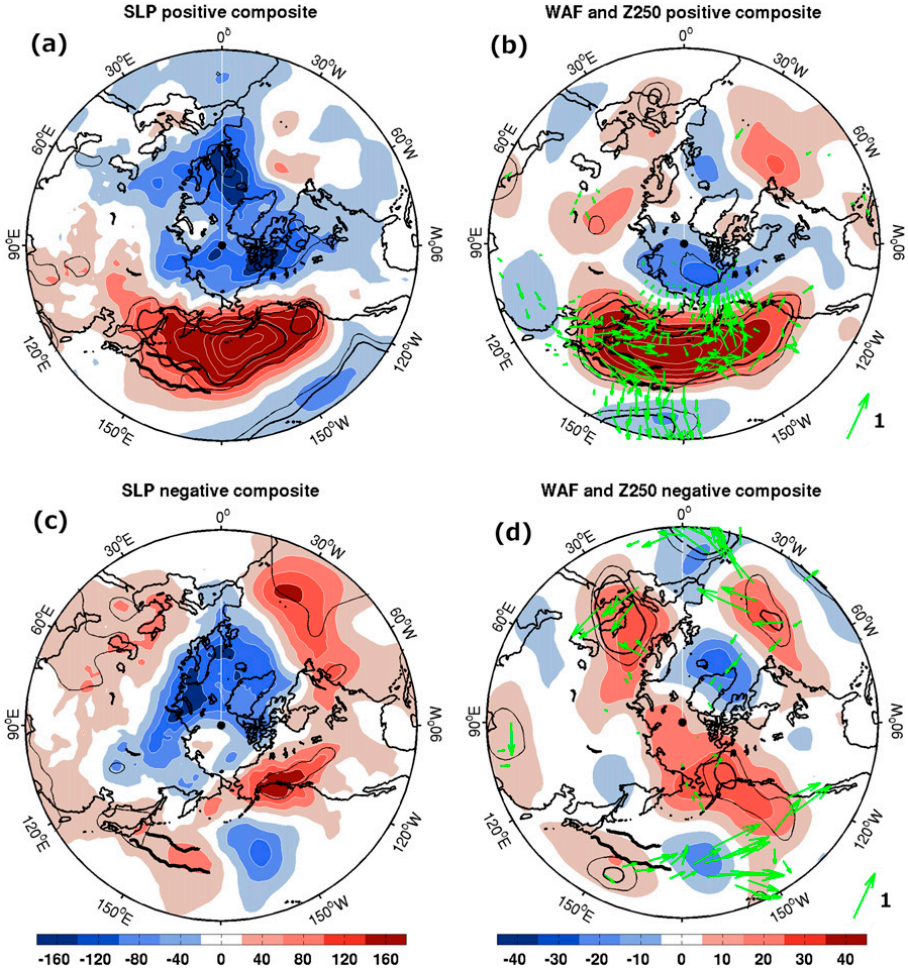

FIG. 13. (a) Composite of the SLP anomaly in ONDJ for positive extreme KE events in ASON (Pa). (b) As in (a), but for Z250 (m; shading) and the WAF ($m^2 s^{-2}$; green vectors, scaling arrow is given on the bottom-right corner). (c),(d) As in (a),(b), but for negative KE events. Contour intervals are 40 Pa in (a),(c) and 10 m in (b),(d). Thick black lines denote the mean KE and OE paths, and thin (thick) black contours indicate 10% (5%) significance. For clarity, only 10% significant WAF vectors are plotted, and only every third vector is plotted equatorward of 60°N and every fifth one poleward of 60°N.

consistent with the observational and modeling studies (Peng and Whitaker 1999; Liu et al. 2007; Gan and Wu 2012; Taguchi et al. 2012) that showed that the North Pacific SST feedback to the atmosphere is dominated by the early-winter atmospheric response, and that the response differs in late winter.

When the KE is in a stable state (positive KE index), during which the KE jet is strengthened, shifted northward, and the regional eddy kinetic energy is lower, enhanced advection by the mean flow generates a broad positive SST anomaly of typically about 0.4–0.6 K in the KOE region, leading to a stronger and more eastward extended OE front, possibly via the eddy-driven jet described in Wagawa et al. (2014), although it does not substantially impact the OE latitude. This warming enhances the heat release to the atmosphere (negative heat flux feedback), in agreement with Qiu et al. (2014) and Joyce et al. (2009). The heat flux anomaly leads to a significant upward motion above the SST anomaly maximum and an increase in the convective available potential energy and convective precipitation above the warm SST. However, no corresponding anomaly in the surface wind convergence or the net precipitation was found. Baroclinicity is weakened along the KE, and there is a northeastward downstream extension of the eddy heat and humidity fluxes and the storm track. This is consistent with Rivière (2009), who showed that latitudinal variations in the Eady growth rate generate positive eddy feedback that amplifies the variation downstream of the source region. The impact on eddy activity and storm track is probably the mechanism that generates stationary Rossby waves that propagate from

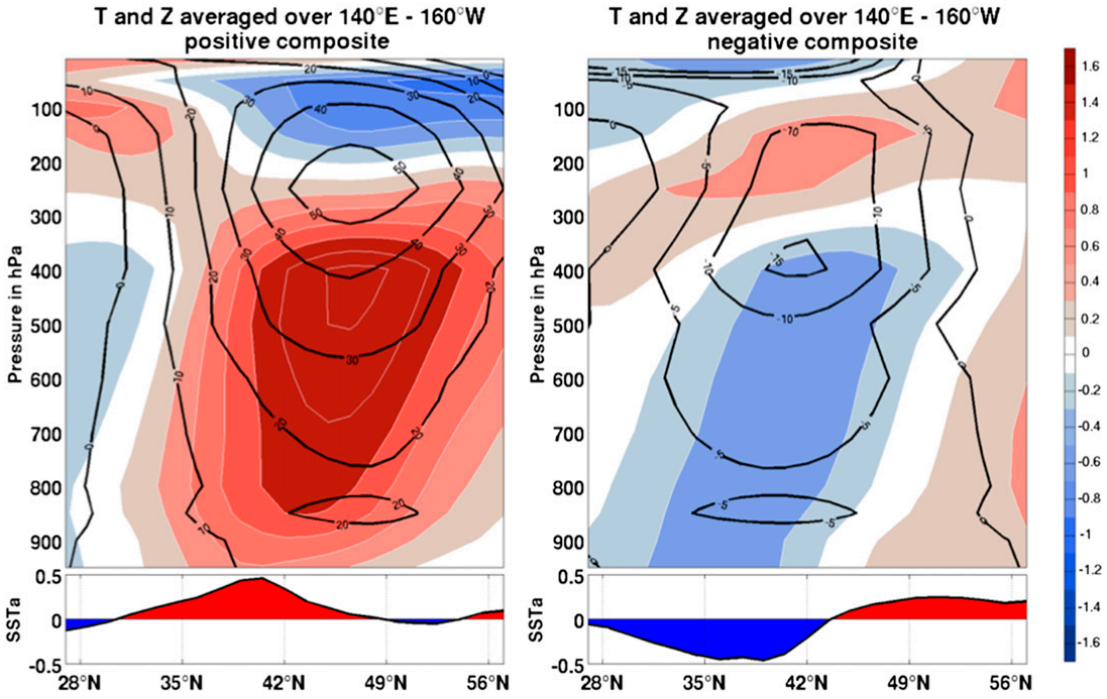

FIG. 14. (left) Positive and (right) negative composite averaged over 140°E–160°W of the air temperature anomaly (K; shading, contour interval 0.2 K) and the geopotential height (m; contours) in ONDJ for extreme KE events in ASON. (bottom) The SST anomaly profile of the corresponding composite averaged over the same longitude band is shown.

the KOE region toward the Arctic and western United States. The hemispheric response thus consists of a high in the central and western North Pacific, and a low over Alaska and the Chukchi Sea, and a weaker high over western United States. There is a westward tilt with height, characteristic of baroclinicity. The amplitude of the signal is limited, however, typically reaching 0.6 hPa at sea level and 20 m at 250 hPa. This is broadly comparable to the amplitude of the response to a shift of the Oyashio Extension found by FSKA and in the modeling study of Smirnov et al. (2015), where the response difference between the warm and cold high-resolution experiments is about 3 hPa at sea level and 50 m at 300 hPa for a SST difference along the Oyashio Extension of 2–3 K.

The disturbance in the upper troposphere leads to reduced injection of wave activity in the stratosphere, strengthening the polar vortex one month later, in NDJF, when the atmospheric response is extended toward Europe and has some similarity with a positive phase of the Arctic Oscillation. The wave activity explains the signal over the Arctic and United States, but the signal over Europe is more likely due to downward propagation of the stratospheric polar vortex changes into the troposphere (Baldwin and Dunkerton 1999; Polvani and Waugh 2004) or to changes in the storm track and eddy–mean flow interactions (Chang 2004; Drouard et al. 2013). These teleconnections have a small but significant climatic impact, albeit with very limited potential predictability, with cooling in the Arctic and heating over Asia and United States, where the snow cover extent is reduced.

Composite analysis suggests a significant asymmetry in the large-scale atmospheric response. While a strong impact on the large-scale atmospheric circulation is found during the KOE warming (positive phase), there is little large-scale response during the negative phase. This asymmetry may result from the difference between positive and negative SST impact on the overlying atmosphere, as a positive temperature anomaly leads to more convective instabilities and deeper vertical penetration in the atmosphere (Deser et al. 2004; Sheldon and Czaja 2014). Indeed, the air temperature anomaly has a deep vertical structure and amplifies with height in the positive case, but not in the negative case. The positive KE phase has therefore a strong impact on baroclinicity and transient eddies, which produce a large-scale atmospheric response, while the negative phase only has a local impact.

While our results are in agreement with the study of Qiu et al. (2014), who used the same KE index but did not distinguish between seasons nor explore the tropospheric response, they differ from other studies based on estimated meridional shifts of the KE. This is perhaps

because Qiu et al.'s (2014) index does not simply reflect a latitudinal shift of the KE front, but a much broader dynamical state oscillation, which leads to a different SST signature and thus a different impact on the atmosphere. It might also be because different periods were considered. FSKA found an equivalent barotropic high centered in the northwestern North Pacific and a much weaker low over the KOE region in response to a northward shift of the KE during 1980–2006, using a KE index with very limited spatial and temporal resolution, so that no distinction was made between seasons. In addition, it was based on temperature profiles that may be too shallow to accurately define the KE path. O'Reilly and Czaja (2015) found that, during the 1992–2010 period, the transient eddy heat transport in winter and spring has a dipolar structure with an increase in the western North Pacific and a decrease in the east when the KE is shifted north and the SST front is stronger, unlike in the present analysis. They used (unlagged) composites based on an index derived from a maximum covariance analysis between SST and SSH gradients during 2002–10. In this period, their index is very similar to Qiu et al.'s (2014) index, and we verified that the two indices lead to similar regression patterns in SLP, geopotential, Eady growth rate, and eddy heat transport, albeit different from those discussed here, presumably because the sample is too short to emphasize the decadal KE changes that dominate the response in the present paper. However, the KE indices differ considerably during 1992–2001 when O'Reilly and Czaja's (2015) index was extended by SSH projection, with much larger decadal changes in Qiu et al.'s (2014) index. Whether the differences in the two analyses are primarily due to the differences in the KE indices or their dominant time scale, or nonstationarity in the atmosphere, remains to be established.

On the other hand, our results are broadly comparable with the observational and modeling studies of Liu et al. (2007) and Gan and Wu (2012), who considered the averaged SST anomaly over the KOE region. In early winter (November–January), they found a warm SST-equivalent barotropic high response over the central North Pacific and a low over Alaska and western United States. Similarly, our results do not substantially differ from those obtained with the method used by Taguchi et al. (2012)—a regression onto the SST in a box of 5° latitude centered on the OE—when it is applied to the 1979–2012 period considered here (not shown). However, Taguchi et al. found that in the 1956–2006 period the atmospheric response to their OE SST index in early winter consisted of a weakening of the Aleutian low, which differs from the central and northwestern Pacific high found in this paper. This again suggests that there may be changes in the atmospheric response over time, presumably linked to changes in the large-scale atmospheric circulation and the transient eddy feedback, which play a critical role in the atmospheric response (Peng and Whitaker 1999). Also, the relation between the KE and OE influence on the atmosphere needs to be investigated further.

Acknowledgments. This research has received funding from the European Union 7th Framework Program (FP7 2007–2013) under Grant Agreement 308299 (NACLIM), from NSF Grant AGS CLD 1035423, and from Agence Nationale de la Recherche under the reference ANR 2011 Blanc SIMI 5-6 014 01. We thank Takafumi Miyasaka and Hisashi Nakamura for providing the wave-activity flux code, Chris O'Reilly for providing his KE index, and Bunmei Taguchi and Francis Codron for stimulating discussion. We also thank the reviewers for their constructive and helpful comments on a previous version of this paper.

APPENDIX

Removing ENSO Teleconnections

Some care is required to estimate the atmospheric response to extratropical boundary forcing in the presence of ENSO teleconnections. To remove the ENSO signal from atmospheric variable $X(t)$, we define

$$\tilde{X}(t) = X(t) - Ae(t-1), \tag{A1}$$

where $A = C_{Xe}(1)/C_{ee}(0)$ is the regression of $X(t)$ onto $e(t-1)$ and $C_{xy}(\tau)$ denotes the covariance between x and y at lag τ. Replacing in (1) yields

$$\tilde{X}(t) = \alpha K(t-2) + \left[b - \frac{C_{Xe}(1)}{C_{ee}(0)}\right] e(t-1) + n(t). \tag{A2}$$

Estimating α by regression of $\tilde{X}(t)$ on $K(t-2)$, as often done, does not entirely remove the ENSO effects. To get an unbiased estimate, we define a modified KE index

$$\tilde{K}(t) = K(t) - Be(t+1), \tag{A3}$$

where $B = C_{Ke}(-1)/C_{ee}(0)$ is the regression of $K(t)$ onto $e(t+1)$. Replacing in (A2) yields

$$\tilde{X}(t) = \alpha\tilde{K}(t-2) + \left[b + \alpha\frac{C_{Ke}(-1)}{C_{ee}(0)} - \frac{C_{Xe}(1)}{C_{ee}(0)}\right] e(t-1) + n(t). \tag{A4}$$

Since n and e are uncorrelated, one has from (1)

$$C_{Xe}(1) = \alpha C_{Ke}(-1) + bC_{ee}(0) \tag{A5}$$

so that (A4) reduces to (2).

The reasoning is easily generalized to several ENSO indices. Here the ENSO signal is defined by the first two principal components [rotated principal components (R-PCs)], after rotation of the EOFs, of monthly SST anomalies in the tropical Pacific between 12.5°N and 12.5°S. To take into account the asymmetry and the seasonality of the ENSO teleconnections, the regression is done separately for positive and negative values of the R-PCs, and the regression coefficients are seasonally varying, with the multivariate regression for a particular calendar month also using the preceding and the following month. The ENSO removal for a particular month, say February, is thus based on regressions from January through March on the two ENSO R-PCs one month earlier [in December–February (DJF)] estimated separately for positive and negative values of the R-PCs:

$$\tilde{X}(\text{Feb}) = X'(\text{Feb}) - \sum_{i=1}^{2} \alpha_i^{+}(\text{JFM}) \times \text{PC}_i^{+}(\text{Jan}) - \sum_{i=1}^{2} \alpha_i^{-}(\text{JFM}) \times \text{PC}_i^{-}(\text{Jan}), \tag{A6}$$

with

$$\alpha_i^{\pm}(\text{JFM}) = \frac{\sum X^{\pm\prime}(\text{JFM}) \times \text{PC}_i^{\pm\prime}(\text{DJF})}{\sum \text{PC}_i^{\pm\prime}(\text{DJF}) \times \text{PC}_i^{\pm\prime}(\text{DJF})},$$

where the plus (minus) superscript index indicates positive (negative) values of the R-PCs, and the prime indicates departure from the mean. Only very small SST anomalies were associated with the KE fluctuations in the other tropical oceans, and the results are similar when calculating the EOFs in the Indo-Pacific tropical region.

REFERENCES

Andrews, D. G., J. R. Holton, and C. B. Leovy, 1987: *Middle Atmosphere Dynamics.* Academic Press, 489 pp.

Baldwin, M. P., and T. J. Dunkerton, 1999: Propagation of the Arctic Oscillation from the stratosphere to the troposphere. *J. Geophys. Res.*, **104**, 30 937–30 946, doi:10.1029/1999JD900445.

Bengtsson, L., K. I. Hodges, and E. Roeckner, 2006: Storm tracks and climate change. *J. Climate*, **19**, 3518–3543, doi:10.1175/JCLI3815.1.

Blackmon, M. L., and N.-C. Lau, 1980: Regional characteristics of the Northern Hemisphere wintertime circulation: A comparison of the simulation of a GFDL general circulation model with observations. *J. Atmos. Sci.*, **37**, 497–514, doi:10.1175/1520-0469(1980)037<0497:RCOTNH>2.0.CO;2.

Branstator, G., 2002: Circumglobal teleconnections, the jet stream waveguide, and the North Atlantic Oscillation. *J. Climate*, **15**, 1893–1910, doi:10.1175/1520-0442(2002)015<1893:CTTJSW>2.0.CO;2.

Bretherton, C. S., M. Widmann, V. P. Dymnikov, J. M. Wallace, and I. Bladé, 1999: The effective number of spatial degrees of freedom of a time-varying field. *J. Climate*, **12**, 1990–2009, doi:10.1175/1520-0442(1999)012<1990:TENOSD>2.0.CO;2.

Ceballos, L. I., E. Di Lorenzo, C. D. Hoyos, N. Schneider, and B. Taguchi, 2009: North Pacific gyre oscillation synchronizes climate fluctuations in the eastern and western boundary systems. *J. Climate*, **22**, 5163–5174, doi:10.1175/2009JCLI2848.1.

Chang, E. K. M., 1993: Downstream development of baroclinic waves as inferred from regression analysis. *J. Atmos. Sci.*, **50**, 2038–2053, doi:10.1175/1520-0469(1993)050<2038:DDOBWA>2.0.CO;2.

——, 2004: Are the Northern Hemisphere winter storm tracks significantly correlated? *J. Climate*, **17**, 4230–4244, doi:10.1175/JCLI3195.1.

Czaja, A., and C. Frankignoul, 2002: Observed impact of Atlantic SST anomalies on the North Atlantic Oscillation. *J. Climate*, **15**, 606–623, doi:10.1175/1520-0442(2002)015<0606:OIOASA>2.0.CO;2.

Decremer, D., C. E. Chung, A. M. L. Ekman, and J. Brandefelt, 2014: Which significance test performs the best in climate simulations? *Tellus*, **66A**, 23139, doi:10.3402/tellusa.v66.23139.

Dee, D. P., and Coauthors, 2011: The ERA-Interim reanalysis: Configuration and performance of the data assimilation system. *Quart. J. Roy. Meteor. Soc.*, **137**, 553–597, doi:10.1002/qj.828.

Deser, C., G. Magnusdottir, R. Saravanan, and A. Phillips, 2004: The effects of North Atlantic SST and sea ice anomalies on the winter circulation in CCM3. Part II: Direct and indirect components of the response. *J. Climate*, **17**, 877–889, doi:10.1175/1520-0442(2004)017<0877:TEONAS>2.0.CO;2.

——, R. A. Tomas, and S. Peng, 2007: The transient atmospheric circulation response to North Atlantic SST and sea ice anomalies. *J. Climate*, **20**, 4751–4767, doi:10.1175/JCLI4278.1.

Drouard, M., G. Rivière, and P. Arbogast, 2013: The North Atlantic Oscillation response to large-scale atmospheric anomalies in the northeastern Pacific. *J. Atmos. Sci.*, **70**, 2854–2874, doi:10.1175/JAS-D-12-0351.1.

Ferreira, D., and C. Frankignoul, 2005: The transient atmospheric response to midlatitude SST anomalies. *J. Climate*, **18**, 1049–1067, doi:10.1175/JCLI-3313.1.

Frankignoul, C., and E. Kestenare, 2005: Air–sea interactions in the tropical Atlantic: A view based on lagged rotated maximum covariance analysis. *J. Climate*, **18**, 3874–3890, doi:10.1175/JCLI3498.1.

——, and N. Sennéchael, 2007: Observed influence of North Pacific SST anomalies on the atmospheric circulation. *J. Climate*, **20**, 592–606, doi:10.1175/JCLI4021.1.

——, A. Czaja, and B. L'Heveder, 1998: Air–sea feedback in the North Atlantic and surface boundary conditions for ocean models. *J. Climate*, **11**, 2310–2324, doi:10.1175/1520-0442(1998)011<2310:ASFITN>2.0.CO;2.

——, N. Chouaib, and Z. Liu, 2011a: Estimating the observed atmospheric response to SST anomalies: Maximum covariance analysis, generalized equilibrium feedback assessment, and maximum response estimation. *J. Climate*, **24**, 2523–2539, doi:10.1175/2010JCLI3696.1.

——, N. Sennéchael, Y.-O. Kwon, and M. A. Alexander, 2011b: Influence of the meridional shifts of the Kuroshio and the Oyashio Extensions on the atmospheric circulation. *J. Climate*, **24**, 762–777, doi:10.1175/2010JCLI3731.1.

Gan, B., and L. Wu, 2012: Modulation of atmospheric response to North Pacific SST anomalies under global warming: A statistical assessment. *J. Climate*, **25**, 6554–6566, doi:10.1175/JCLI-D-11-00493.1.

——, and ——, 2013: Seasonal and long-term coupling between wintertime storm tracks and sea surface temperature in the North Pacific. *J. Climate*, **26**, 6123–6136, doi:10.1175/JCLI-D-12-00724.1.

Hoskins, B. J., and K. I. Hodges, 2002: New perspectives on the Northern Hemisphere winter storm tracks. *J. Atmos. Sci.*, **59**, 1041–1061, doi:10.1175/1520-0469(2002)059<1041:NPOTNH>2.0.CO;2.

——, I. N. James, and G. H. White, 1983: The shape, propagation and mean-flow interaction of large-scale weather systems. *J. Atmos. Sci.*, **40**, 1595–1612, doi:10.1175/1520-0469(1983)040<1595:TSPAMF>2.0.CO;2.

Hurrell, J. W., and C. Deser, 2009: North Atlantic climate variability: The role of the North Atlantic Oscillation. *J. Mar. Syst.*, **78**, 28–41, doi:10.1016/j.jmarsys.2008.11.026.

Isoguchi, O., H. Kawamura, and E. Oka, 2006: Quasi-stationary jets transporting surface warm waters across the transition zone between the subtropical and the subarctic gyres in the North Pacific. *J. Geophys. Res.*, **111**, C10003, doi:10.1029/2005JC003402.

Joyce, T. M., Y.-O. Kwon, and L. Yu, 2009: On the relationship between synoptic wintertime atmospheric variability and path shifts in the Gulf Stream and the Kuroshio Extension. *J. Climate*, **22**, 3177–3192, doi:10.1175/2008JCLI2690.1.

Kalnay, E., and Coauthors, 1996: The NCEP/NCAR 40-Year Reanalysis Project. *Bull. Amer. Meteor. Soc.*, **77**, 437–471, doi:10.1175/1520-0477(1996)077<0437:TNYRP>2.0.CO;2.

Kelly, K. A., R. J. Small, R. M. Samelson, B. Qiu, T. M. Joyce, Y.-O. Kwon, and M. F. Cronin, 2010: Western boundary currents and frontal air–sea interaction: Gulf Stream and Kuroshio Extension. *J. Climate*, **23**, 5644–5667, doi:10.1175/2010JCLI3346.1.

Kushnir, Y., W. A. Robinson, I. Bladé, N. M. J. Hall, S. Peng, and R. Sutton, 2002: Atmospheric GCM response to extratropical SST anomalies: Synthesis and evaluation. *J. Climate*, **15**, 2233–2256, doi:10.1175/1520-0442(2002)015<2233:AGRTES>2.0.CO;2.

Kwon, Y.-O., and T. M. Joyce, 2013: Northern Hemisphere winter atmospheric transient eddy heat fluxes and the Gulf Stream and Kuroshio–Oyashio Extension variability. *J. Climate*, **26**, 9839–9859, doi:10.1175/JCLI-D-12-00647.1.

——, M. A. Alexander, N. A. Bond, C. Frankignoul, H. Nakamura, B. Qiu, and L. A. Thompson, 2010: Role of the Gulf Stream and Kuroshio–Oyashio systems in large-scale atmosphere–ocean interaction: A review. *J. Climate*, **23**, 3249–3281, doi:10.1175/2010JCLI3343.1.

Liu, Q., N. Wen, and Z. Liu, 2006: An observational study of the impact of the North Pacific SST on the atmosphere. *Geophys. Res. Lett.*, **33**, L18611, doi:10.1029/2006GL026082.

Liu, Z., and L. Wu, 2004: Atmospheric response to North Pacific SST: The role of ocean–atmosphere coupling. *J. Climate*, **17**, 1859–1882, doi:10.1175/1520-0442(2004)017<1859:ARTNPS>2.0.CO;2.

——, Y. Liu, L. Wu, and R. Jacob, 2007: Seasonal and long-term atmospheric responses to reemerging North Pacific Ocean variability: A combined dynamical and statistical assessment. *J. Climate*, **20**, 955–980, doi:10.1175/JCLI4041.1.

Masunaga, R., H. Nakamura, T. Miyasaka, K. Nishii, and Y. Tanimoto, 2015: Separation of climatological imprints of the Kuroshio Extension and Oyashio fronts on the wintertime atmospheric boundary layer: Their sensitivity to SST resolution prescribed for atmospheric reanalysis. *J. Climate*, **28**, 1764–1787, doi:10.1175/JCLI-D-14-00314.1.

Minobe, S., M. Miyashita, A. Kuwano-Yoshida, H. Tokinaga, and S.-P. Xie, 2010: Atmospheric response to the Gulf Stream: Seasonal variations. *J. Climate*, **23**, 3699–3719, doi:10.1175/2010JCLI3359.1.

Miyasaka, T., H. Nakamura, B. Taguchi, and M. Nonaka, 2014: Multidecadal modulations of the low-frequency climate variability in the wintertime North Pacific since 1950. *Geophys. Res. Lett.*, **41**, 2948–2955, doi:10.1002/2014GL059696.

Nakamura, H., and T. Yamagata, 1999: Recent decadal SST variability in the northwestern Pacific and associated atmospheric anomalies. *Beyond El Niño: Decadal and Interdecadal Climate Variability*, A. Navarra, Ed., Springer, 49–72.

——, T. Izumi, and T. Sampe, 2002: Interannual and decadal modulations recently observed in the Pacific storm track activity and East Asian winter monsoon. *J. Climate*, **15**, 1855–1874, doi:10.1175/1520-0442(2002)015<1855:IADMRO>2.0.CO;2.

——, T. Sampe, Y. Tanimoto, and A. Shimpo, 2004: Observed associations among storm tracks, jet streams and midlatitude oceanic fronts. *Earth Climate: The Ocean–Atmosphere Interaction*, *Geophys. Monogr.*, Vol. 147, Amer. Geophys. Union, 329–346.

Nishii, K., H. Nakamura, and Y. J. Orsolini, 2010: Cooling of the wintertime Arctic stratosphere induced by the western Pacific teleconnection pattern. *Geophys. Res. Lett.*, **37**, L13805, doi:10.1029/2010GL043551.

Nonaka, M., H. Nakamura, Y. Tanimoto, T. Kagimoto, and H. Sasaki, 2006: Decadal variability in the Kuroshio–Oyashio Extension simulated in an eddy-resolving OGCM. *J. Climate*, **19**, 1970–1989, doi:10.1175/JCLI3793.1.

——, ——, ——, ——, and ——, 2008: Interannual-to-decadal variability in the Oyashio and its influence on temperature in the subarctic frontal zone: An eddy-resolving OGCM simulation. *J. Climate*, **21**, 6283–6303, doi:10.1175/2008JCLI2294.1.

Okajima, S., H. Nakamura, K. Nishii, T. Miyasaka, and A. Kuwano-Yoshida, 2014: Assessing the importance of prominent warm SST anomalies over the midlatitude North Pacific in forcing large-scale atmospheric anomalies during 2011 summer and autumn. *J. Climate*, **27**, 3889–3903, doi:10.1175/JCLI-D-13-00140.1.

O'Reilly, C. H., and A. Czaja, 2015: The response of the Pacific storm track and atmospheric circulation to Kuroshio Extension variability: Response of storm tracks to Kuroshio Extension variability. *Quart. J. Roy. Meteor. Soc.*, **141**, 52–66, doi:10.1002/qj.2334.

Park, S., C. Deser, and M. A. Alexander, 2005: Estimation of the surface heat flux response to sea surface temperature anomalies over the global oceans. *J. Climate*, **18**, 4582–4599, doi:10.1175/JCLI3521.1.

Peng, S., and J. S. Whitaker, 1999: Mechanisms determining the atmospheric response to midlatitude SST anomalies. *J. Climate*, **12**, 1393–1408, doi:10.1175/1520-0442(1999)012<1393:MDTART>2.0.CO;2.

Plumb, R., 1985: On the three-dimensional propagation of stationary waves. *J. Atmos. Sci.*, **42**, 217–229, doi:10.1175/1520-0469(1985)042<0217:OTTDPO>2.0.CO;2.

Polvani, L. M., and D. W. Waugh, 2004: Upward wave activity flux as a precursor to extreme stratospheric events and subsequent

anomalous surface weather regimes. *J. Climate*, **17**, 3548–3554, doi:10.1175/1520-0442(2004)017<3548:UWAFAA>2.0.CO;2.

Qiu, B., 2002: Large-scale variability in the midlatitude subtropical and subpolar North Pacific Ocean: Observations and causes. *J. Phys. Oceanogr.*, **32**, 353–375, doi:10.1175/1520-0485(2002)032<0353:LSVITM>2.0.CO;2.

——, 2003: Kuroshio Extension variability and forcing of the Pacific decadal oscillations: Responses and potential feedback. *J. Phys. Oceanogr.*, **33**, 2465–2482, doi:10.1175/2459.1.

——, and S. Chen, 2005: Variability of the Kuroshio Extension jet, recirculation gyre, and mesoscale eddies on decadal time scales. *J. Phys. Oceanogr.*, **35**, 2090–2103, doi:10.1175/JPO2807.1.

——, and ——, 2010: Eddy–mean flow interaction in the decadally modulating Kuroshio Extension system. *Deep-Sea Res. II*, **57**, 1097–1110, doi:10.1016/j.dsr2.2008.11.036.

——, ——, N. Schneider, and B. Taguchi, 2014: A coupled decadal prediction of the dynamic state of the Kuroshio Extension system. *J. Climate*, **27**, 1751–1764, doi:10.1175/JCLI-D-13-00318.1.

Rivière, G., 2009: Effect of latitudinal variations in low-level baroclinicity on eddy life cycles and upper-tropospheric wave-breaking processes. *J. Atmos. Sci.*, **66**, 1569–1592, doi:10.1175/2008JAS2919.1.

Sasaki, Y. N., S. Minobe, and N. Schneider, 2013: Decadal response of the Kuroshio Extension jet to Rossby waves: Observation and thin-jet theory. *J. Phys. Oceanogr.*, **43**, 442–456, doi:10.1175/JPO-D-12-096.1.

Schneider, N., A. J. Miller, and D. W. Pierce, 2002: Anatomy of North Pacific decadal variability. *J. Climate*, **15**, 586–605, doi:10.1175/1520-0442(2002)015<0586:AONPDV>2.0.CO;2.

Seager, R., Y. Kushnir, N. H. Naik, M. A. Cane, and J. Miller, 2001: Wind-driven shifts in the latitude of the Kuroshio–Oyashio Extension and generation of SST anomalies on decadal timescales. *J. Climate*, **14**, 4249–4265, doi:10.1175/1520-0442(2001)014<4249:WDSITL>2.0.CO;2.

Seo, Y., S. Sugimoto, and K. Hanawa, 2014: Long-term variations of the Kuroshio Extension path in winter: Meridional movement and path state change. *J. Climate*, **27**, 5929–5940, doi:10.1175/JCLI-D-13-00641.1.

Sheldon, L., and A. Czaja, 2014: Seasonal and interannual variability of an index of deep atmospheric convection over western boundary currents. *Quart. J. Roy. Meteor. Soc.*, **140**, 22–30, doi:10.1002/qj.2103.

Smirnov, D., M. Newman, M. A. Alexander, Y.-O. Kwon, and C. Frankignoul, 2015: Investigating the local atmospheric response to a realistic shift in the Oyashio sea surface temperature front. *J. Climate*, **28**, 1126–1147, doi:10.1175/JCLI-D-14-00285.1.

Sugimoto, S., 2014: Influence of SST anomalies on winter turbulent heat fluxes in the eastern Kuroshio–Oyashio confluence region. *J. Climate*, **27**, 9349–9358, doi:10.1175/JCLI-D-14-00195.1.

——, and K. Hanawa, 2011: Roles of SST anomalies on the wintertime turbulent heat fluxes in the Kuroshio–Oyashio confluence region: Influences of warm eddies detached from the Kuroshio Extension. *J. Climate*, **24**, 6551–6561, doi:10.1175/2011JCLI4023.1.

Taguchi, B., S.-P. Xie, N. Schneider, M. Nonaka, H. Sasaki, and Y. Sasai, 2007: Decadal variability of the Kuroshio Extension: Observations and an eddy-resolving model hindcast. *J. Climate*, **20**, 2357–2377, doi:10.1175/JCLI4142.1.

——, H. Nakamura, M. Nonaka, and S.-P. Xie, 2009: Influences of the Kuroshio/Oyashio Extensions on air–sea heat exchanges and storm-track activity as revealed in regional atmospheric model simulations for the 2003/04 cold season. *J. Climate*, **22**, 6536–6560, doi:10.1175/2009JCLI2910.1.

——, ——, ——, N. Komori, A. Kuwano-Yoshida, K. Takaya, and A. Goto, 2012: Seasonal evolutions of atmospheric response to decadal SST anomalies in the North Pacific subarctic frontal zone: Observations and a coupled model simulation. *J. Climate*, **25**, 111–139, doi:10.1175/JCLI-D-11-00046.1.

Takaya, K., and H. Nakamura, 2001: A formulation of a phase-independent wave-activity flux for stationary and migratory quasigeostrophic eddies on a zonally varying basic flow. *J. Atmos. Sci.*, **58**, 608–627, doi:10.1175/1520-0469(2001)058<0608:AFOAPI>2.0.CO;2.

Trenberth, K. E., and J. W. Hurrell, 1994: Decadal atmosphere–ocean variations in the Pacific. *Climate Dyn.*, **9**, 303–319, doi:10.1007/BF00204745.

Vivier, F., K. A. Kelly, and L. A. Thompson, 2002: Heat budget in the Kuroshio Extension region: 1993–99. *J. Phys. Oceanogr.*, **32**, 3436–3454, doi:10.1175/1520-0485(2002)032<3436:HBITKE>2.0.CO;2.

von Storch, H., and F. W. Zwiers, 1999: *Statistical Analysis in Climate Research*. Cambridge University Press, 484 pp.

Wagawa, T., S.-I. Ito, Y. Shimizu, S. Kakehi, and D. Ambe, 2014: Currents associated with the quasi-stationary jet separated from the Kuroshio Extension. *J. Phys. Oceanogr.*, **44**, 1636–1653, doi:10.1175/JPO-D-12-0192.1.

Wen, N., Z. Liu, Q. Liu, and C. Frankignoul, 2010: Observed atmospheric responses to global SST variability modes: A unified assessment using GEFA. *J. Climate*, **23**, 1739–1759, doi:10.1175/2009JCLI3027.1.

Yoshiike, S., and R. Kawamura, 2009: Influence of wintertime large-scale circulation on the explosively developing cyclones over the western North Pacific and their downstream effects. *J. Geophys. Res.*, **114**, D13110, doi:10.1029/2009JD011820.

Yu, L., and R. A. Weller, 2007: Objectively analyzed air–sea heat fluxes for the global ice-free oceans (1981–2005). *Bull. Amer. Meteor. Soc.*, **88**, 527–539, doi:10.1175/BAMS-88-4-527.

Cross validation

Comme indiqué dans la partie 4.e. de l'article, nous avons testé le potentiel de prédictabilité du KE sur différentes variables atmosphériques. Pour ce faire, nous avons utilisé la méthode de "cross validation" consistant à prédire la variable atmosphérique à partir de la régression. Pour chaque point de grille et chaque année de 1979 à 2012, la régression linaire est calculée en supprimant les quatre mois de l'année correspondante, puis ces quatre mois sont prédits par projection. Cela nous permet d'obtenir une série temporelle de prédiction de 1979 à 2012. Nous comparons alors cette série avec la série réelle (de ERA-Interim), en analysant leur corrélation.

La figure 3.1 montre les cartes de corrélation entre les séries temporelles de base et les séries prédites pour le géopotentiel à 250 hPa et la température de l'air à 900 hPa. La corrélation ne dépasse pas 0.3 pour la température et 0.2 pour le géopotentiel, et dans les deux cas, des corrélations significatives sont observées uniquement dans des régions peu étendues. Des corrélations encore plus faibles sont obtenues avec la SLP (non montré). Le potentiel de prédictabilité est donc très limité.

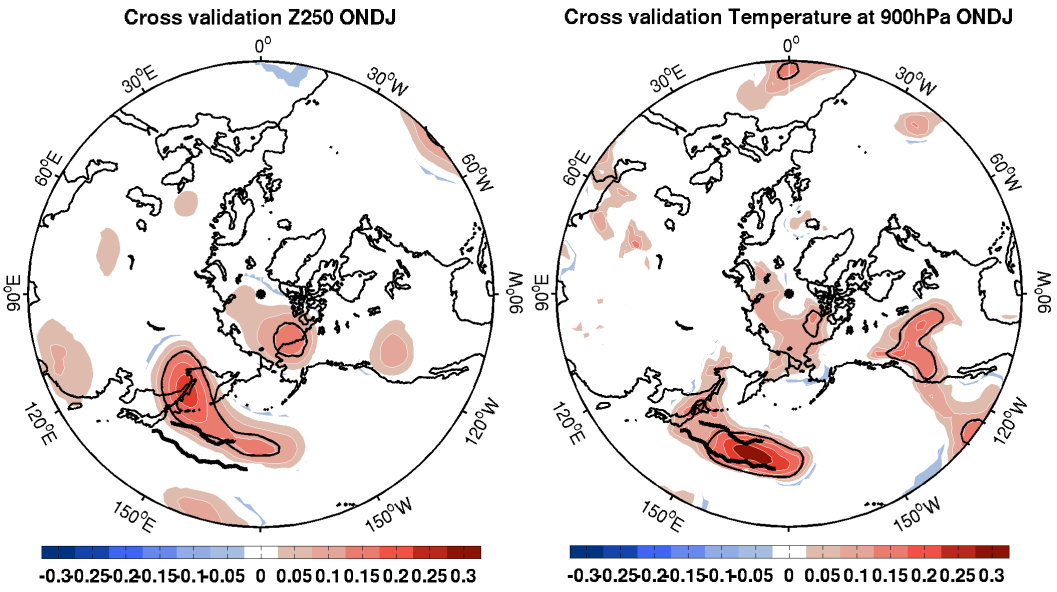

FIGURE 3.1 – Carte de corrélation entre la série prédite par cross-validation et la série de base de ERA-Interim pour (à gauche) le géopotentiel à 250 hPa et (à droite) la température de l'air à 900 hPa. Les contours noirs montrent la significativité statistique au niveau de 10%, et les deux traits épais noirs montrent les trajectoires moyennes du Kuroshio et de l'Oyashio.

Chapitre 4

Réponse atmosphérique au Kuroshio, Oyashio et PDO en analyse multivariable

4.1 Introduction

As detailed in chapter 1, the first observational studies that have convincingly shown that the North Pacific (NP) SST variability has a significant impact on the atmospheric circulation were based on lag maximum covariance analysis (MCA), searching for the maximum covariability between SST and the large-scale atmospheric circulation when SST leads by more than the atmospheric persistence (Liu et al. 2006 ; Frankignoul and Sennéchael 2007 ; Gan and Wu 2013). This was done after removing the strong El Niño Southern Oscillation (ENSO) teleconnections (e.g., Liu and Alexander 2007) by regression analysis. A different approach was used by Wen et al. (2010) and Liu et al. (2012), who, unlike in the MCA, prescribed the SST forcing patterns (using the dominant SST anomaly modes) and used a multivariate method, the Generalized Equilibrium Feedback Analysis (GEFA), to distinguish the atmospheric response to multiple tropical and extratropical SST modes. Using monthly anomaly data during 1958-2007 and a lag of 1 month, they found as response to the Pacific Decadal Oscillation (PDO) a significant strengthening of the Aleutian Low (slightly shifted and extended southwestward) and a downstream response in the North Atlantic sector resembling the negative phase of the North Atlantic Oscillation (NAO), so that the whole pattern resembles the Aleutian-Icelandic seesaw (Honda et al. 2005).

These studies emphasize the atmospheric impact of main SST anomaly modes that were largely driven by direct atmospheric forcing associated with the intrinsic atmospheric variability and by ENSO teleconnections. As discussed by Schneider and Cornuelle (2005), Newmann et al. (2016) and others, different processes can drive PDO-like SST patterns, including changes in zonal advection in the Western Boundary Current Extensions region, so that the PDO arises from the superposition of SST fluctuations from different dynamical origins. On the other hand, the variability of the frontal zones associated with the Kuroshio and Oyashio Extension (KOE) also has an imprint of SST that may not appear as a dominant, basin-wide SST anomaly mode, yet may play an important role in driving an atmospheric response since the oceanic fronts maintain surface baroclinicity and sustain storm development, anchoring the storm tracks along

or just downstream of the main oceanic frontal zones (Nakamura et al. 2004).

Hence, indices of the WBC variability were used in lag regression analysis to single out the response to frontal variability (FSKA ; Taguchi et al. 2012 ; Révelard et al. 2016). Although care was taken to remove the influence of ENSO teleconnections, the SST imprint of these WBC changes was accompanied by weaker SST anomalies of much larger scale than expected frontal changes. For example, the KE SST footprint of the index from Qiu et al. (2014) shows a large-scale SST anomaly over the KOE region and downstream, with a maximum anomaly along the OE (Révelard et al. 2016). Similarly, the OE SST footprint extends in the northeastern Pacific basin and strongly resembles the PDO (Fig. 1.8 from FSKA and Fig. 1.9 from Smirnov et al. 2015). This may have been due in part because larger-scale SST anomalies were forced by the same atmospheric pattern that drove a rapid response of the Western Boundary Current Extensions, as suggested for the OE by FSKA, or because the response to the meridional displacement of the fronts generated larger scale SST patterns as in the simulations of Kwon and Deser (2007). However, they could also be due to the concomitant influence of SST anomaly modes in the North Pacific and other ocean basins, which are partly forced by the same atmospheric forcing and covary with the Western Bounday Current variability. For example, both the OE and the PDO are partly forced by the Aleutian Low, and the PDO shows a large-scale SST pattern with a strong anomaly over the KOE region. Therefore, the atmospheric response to a specific oceanic forcing is difficult to isolate if various correlated forcings can drive the same KOE SST anomaly. Smirnov et al. (2014) used the Linear Inverse Model approach to show that ocean-driven SST anomalies were limited to the KOE region, west of the dateline, so that

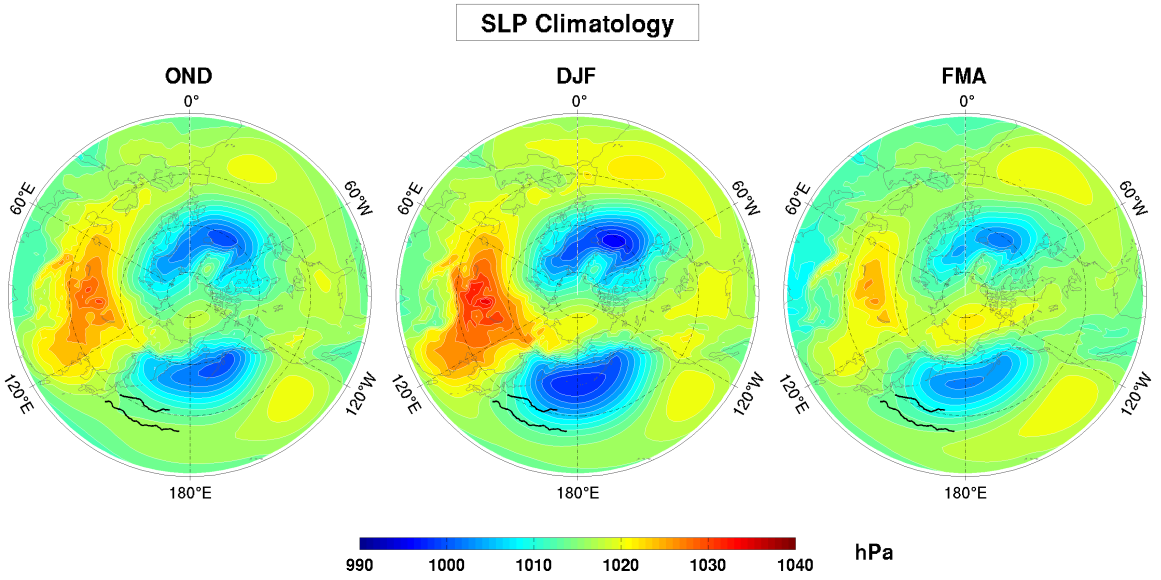

FIGURE 4.1 – Moyenne saisonnière de la climatologie de la pression au niveau de la mer pour les trois saisons considérées dans cette étude : automne (OND), hiver (DJF) et fin d'hiver (FMA). Les traits noirs désignent les chemins moyens du Kuroshio et de l'Oyashio, définis respectivement par la latitude moyenne du gradient méridien maximal de SSH et SST (chemin moyen du KE d'après Kelly et al. 2010).

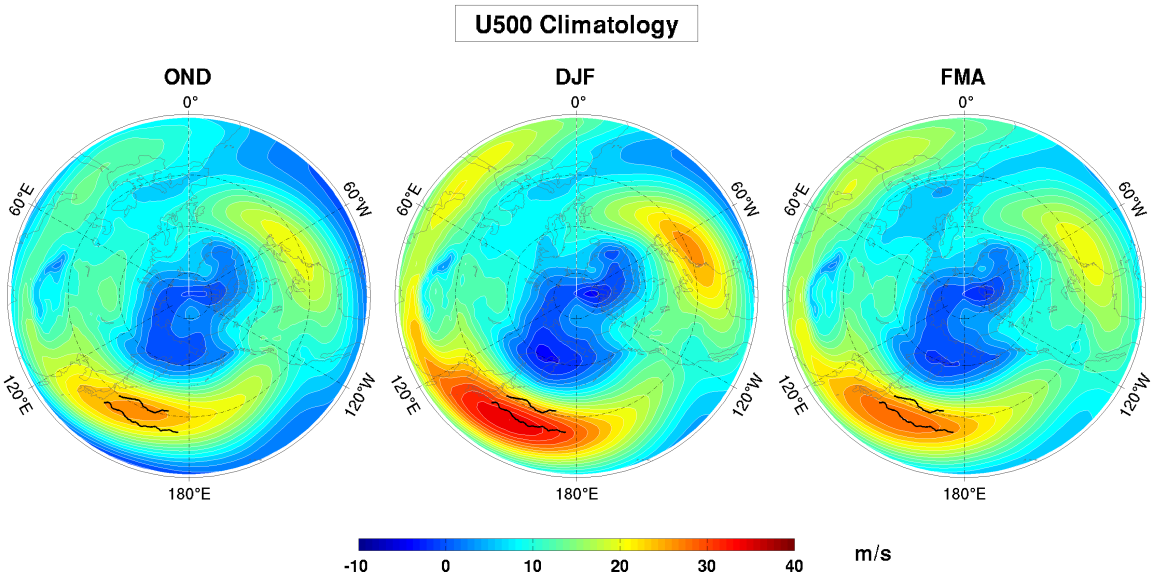

FIGURE 4.2 – Comme la figure 4.1, mais pour le vent zonal à 500 hPa.

Smirnov et al. (2015) limited the SST imprint to a narrow region along the OE in the sensitivity studies.

Hence, the impact of the SST associated to the OE needs to be differentiated from that of the KE and from that of the large-scale SST associated to the PDO in order to understand the mechanisms of the influence of the PDO, OE and KE on the atmosphere. Furthermore, although the dominant atmospheric teleconnection is the one associated with ENSO and the Pacific tropical SST (Trenberth et al. 1998), there has been more and more observational evidences that the SST in other basins can also have a remote significant impact on the atmosphere, such as the North Atlantic (e.g. Czaja and Frankignoul 2002), the tropical Atlantic (e.g. Frankignoul and Kestenare 2005 ; Haarsma et Hazeleger 2007), the tropical Indian Ocean (e.g. Saji et al. 1999 ; Lau et al. 2005 ; Yang et al. 2007), as well as the sea-ice cover (SIC) in the Arctic Ocean (e.g. Frankignoul et al. 2014 ; Garcia-Serrano et al. 2015). Therefore, the estimation of the atmospheric response to North Pacific SST variability can be biased if other concomitant forcings are not taken into account.

In order to distinguish between the atmospheric responses to the different SST modes and the Western Bounday Curren Extensions, we use the GEFA method that was shown to be of particular interest for this purpose. We stratify the analysis by seasons since the atmospheric circulation varies seasonnaly, with stronger asymetries and a stronger westerly jet in mid-winter (Fig. 4.1, 4.2). Many observational studies have stressed that the response varies with the season (e.g. Liu et al. 2007 ; FSKA ; Taguchi et al. 2012, Révelard et al. 2016). The strong sensitivity to the season was also shown by modeling results (Peng et al. 1997 ; Peng and Whitaker 1999 ; Liu and Wu 2004 ; Gan and Wu 2012). Hence here, we focus on the cold season and we distinguish between three different seasons : autumn/early winter (OND), winter (DJF), and late winter/early spring (FMA). We choose to analyze seasonal responses (using monthly anomalies

or seasonal means) rather than search for the response in each calendar month in order to increase the sample size (or decrease the noise) since the focus is on a limited time period (1979 – 2014), covered by the latest reanalysis from the European Center for Medium-Range Weather Forecasts (ECMWF) (ERA-Interim ; Dee et al. 2011). Section 4.2 describes the data and how the set of forcings is constructed. Section 4.3 gives the GEFA method applied in the context of our application. The results for the OND season are given in section 4.4, while the results in DJF and FMA and described in section 4.5. The main results are summarized and discussed in section 4.6.

4.2 Data

4.2.1 Atmospheric variables

The atmospheric variables are given by the ERA-Interim reanalysis (Dee et al. 2011). They cover the 1979-2014 period. Monthly fields of sea level pressure (SLP) and geopotential height are taken at 1.5° resolution, while a 0.75° resolution is used for the SST, air temperature, wind velocity and latent and sensible heat fluxes. To investigate the impact on the synoptic activity, we consider several variables linked to the transient eddies : the Eady growth rate, the meridional transient eddy heat flux <v'T'> at 850 hPa (the prime denotes high-pass daily values and < > monthly averages) and the storm track at 500 hPa. The Eady growth rate is calculated at 850 hPa and is given by

$$\sigma = 0.31|f|\frac{|\frac{\partial V(z)}{\partial z}|}{N}$$

where f is the Coriolis parameter, $V(z)$ the vertical profile of the horizontal wind, and N the Brunt-Väisälä frequency. It measures the theoretical growth rate of the most unstable synoptic mode, and it is partly determined by the potential temperature gradient, because of the thermal wind balance, and the atmospheric stability. Transient eddy heat flux is estimated at 850 hPa from high-pass daily values, using the Blackmon filter to retain fluctuations with periods between 2 and 8 days (Blackmon and Lau 1980 ; Hurrell and Deser 2009). The storm track is represented by the root-mean-square of high-pass 500 hPa geopotential height filtered with the Blackmon filter. Monthly anomalies during 1979-2014 are obtained by subtracting the first two annual harmonics of the mean seasonal cycle and removing a cubic trend (a linear trend yields very similar results). The oceanic variables are treated similarly.

4.2.2 The western boundary current extensions of the North Pacific

As in Chapter 3, the variability of the KE is given by the index of Qiu et al. (2014), presented in section 2.2. This index is defined by the SSH anomaly averaged in the domain (31°–36°N, 140°–165°E) (Fig. 4.3, black curve). A positive KE index denotes a stable state in which the KE jet has a steady and northerly path, an increased surface transport and a decreased eddy

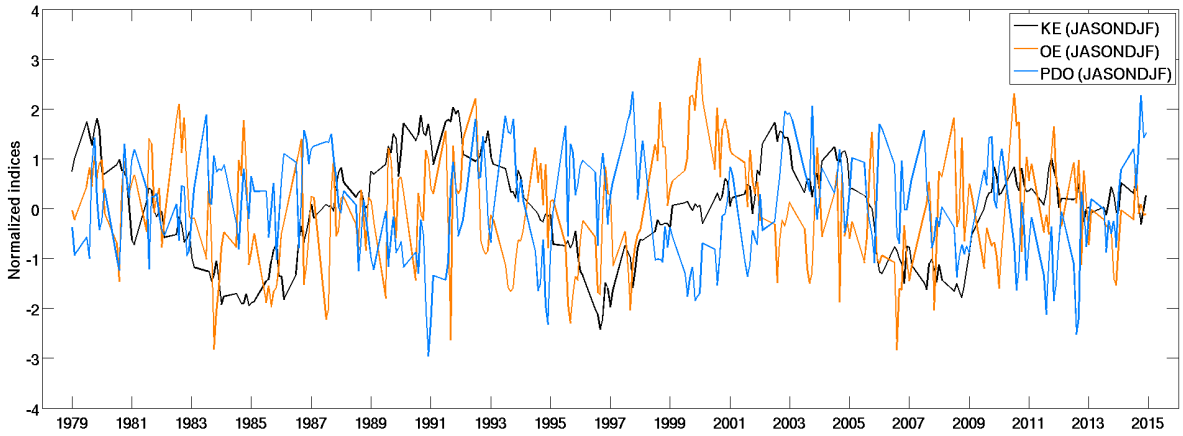

FIGURE 4.3 – Normalized and detrended monthly KE index (black), OE index (orange), and PDO index (blue) in the JASONDJF season.

kinetic energy in the KOE region. A negative KE index reflects the reversed properties. The KE index is based on satellite altimetry between October 1992 and December 2014, and otherwise on a hindcast with the eddy-resolving OFES model, which captures the KE decadal variability realistically (Nonaka et al. 2006 ; Taguchi et al. 2007 ; Qiu et al. 2014).

To represent the variability of the OE, we use an index of its north-south shift defined by the leading principal component (PC) of the latitude of the maximum monthly-mean meridional SST gradient between 145° and 170°E (Fig. 4.3, orange curve), as in FSKA. In order to have an OE index starting from 1979, the OAFlux SST product with 1° resolution for 1979-2014 is used instead of the NOAA OISST with 0.25° resolution as in FSKA. In the overlapping period 1982-2014, the two indices have a correlation r of 0.66, and our results are quite similar in the 1982-2014 period, when the index based on NOAA product is used.

4.2.3 The SST forcings

The SST is taken from ERA-Interim, excluding grid points where the March sea ice concentration (SIC) climatology from ERA-Interim exceeds 5%. The SST anomaly modes are represented by the main Empirical Orthogonal Functions (EOFs) or Rotated EOFs (R-EOFs) (Fig. 2) and their associated PCs in different subbasins (Fig. 4.4). To focus on the cold season while limiting the sampling uncertainty, the (R-)EOFs are calculated for JASONDJF (months are referred to by their first letter), since the atmospheric response is estimated between October and April using oceanic indices preceding by 2 or 3 months (see section 4.3.1). (R-)EOFs calculated from the whole year would not represent as well the main oceanic forcing patterns in the cold season, and would increase the multicollinearity (see section 4.3.2), since the PCs in a subbasin would be more correlated in each season than when estimated from JASONDJF. On the other hand, using different (R-)EOFs for each season would often lead to patterns with limited robustness, as the sample is limited.

The ocean is divided into : the Tropical-Indo Pacific (TIP ; 20°S–20°N, 20°E–70°W), the Tropical Indian (TI ; 20°S–20°N, 20°–100°E), the North Pacific (NP ; 20°–60°N, 120°E–120°W),

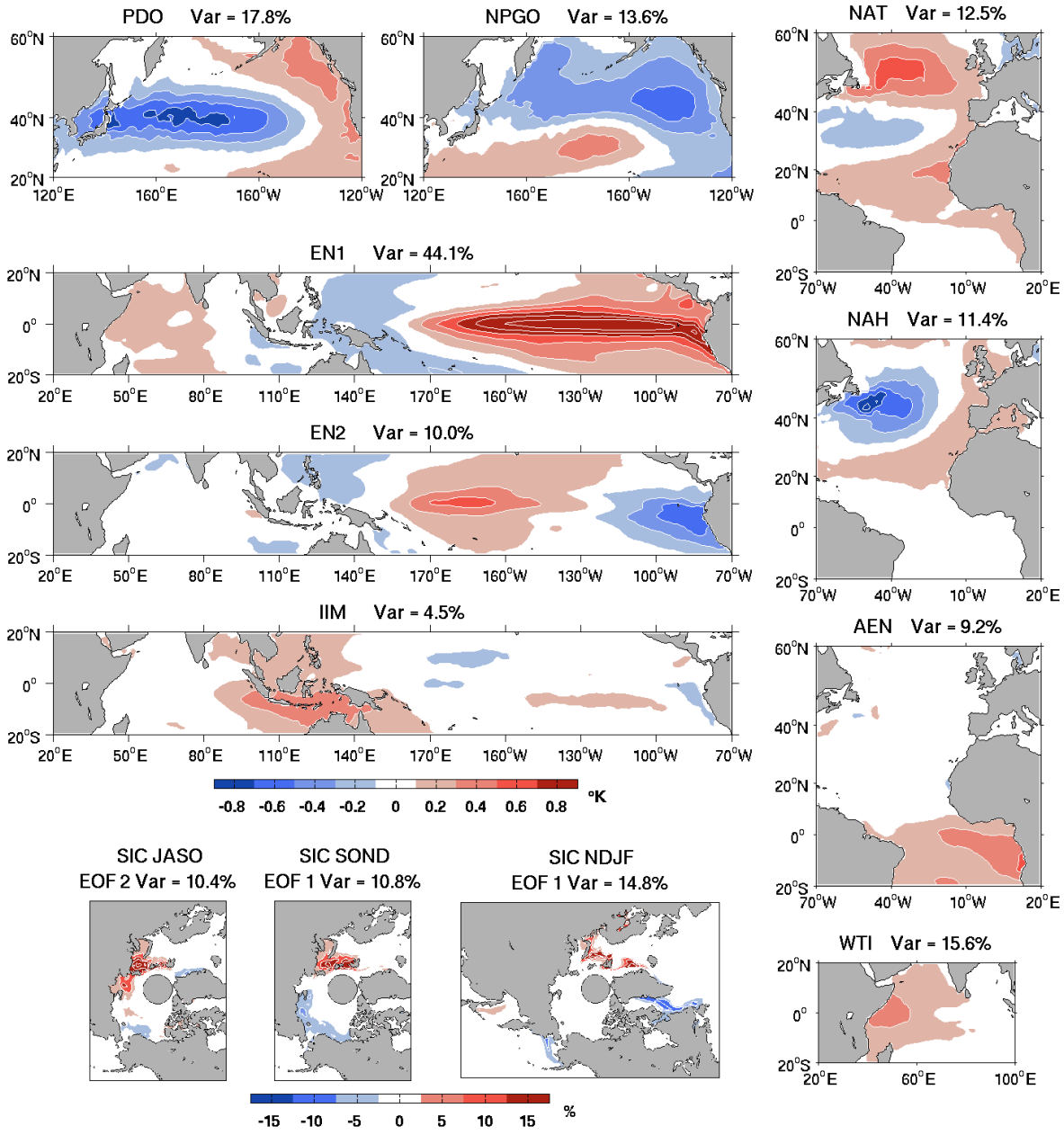

FIGURE 4.4 – SST R-EOF or EOF patterns in JASONDJF chosen as regressors for the four domains (contour interval 0.2˚K) and SIC EOF pattern for JASO, SOND and NDJF (contour interval 5%). Red (blue) shading is for positive (negative) anomaly. The percentage of represented variance is indicated.

and the North-Tropical Atlantic (NTA ; 20˚S–60˚N, 70˚W–20˚E). These subbasins do not overlap, except for TI and TIP. In the TIP, the first three R-EOFs are used (Fig. 4.4). TIP1 and TIP2 (hereafter EN1 and EN2) correspond to the El Niño modes and represent 44.1% and 10% of the variance, respectively. EN1 is highly correlated with the Niño 3.4 index ($r = 0.94$) and EN2 is highly correlated with the Trans-Niño index ($r = -0.94$) (Trenberth and Stepaniak 2001). EN2 thus mostly represents the decay of the El Niño events during the months following the winter peak. The third R-EOF of TIP (4.5% of the variance) corresponds to a monopole in the

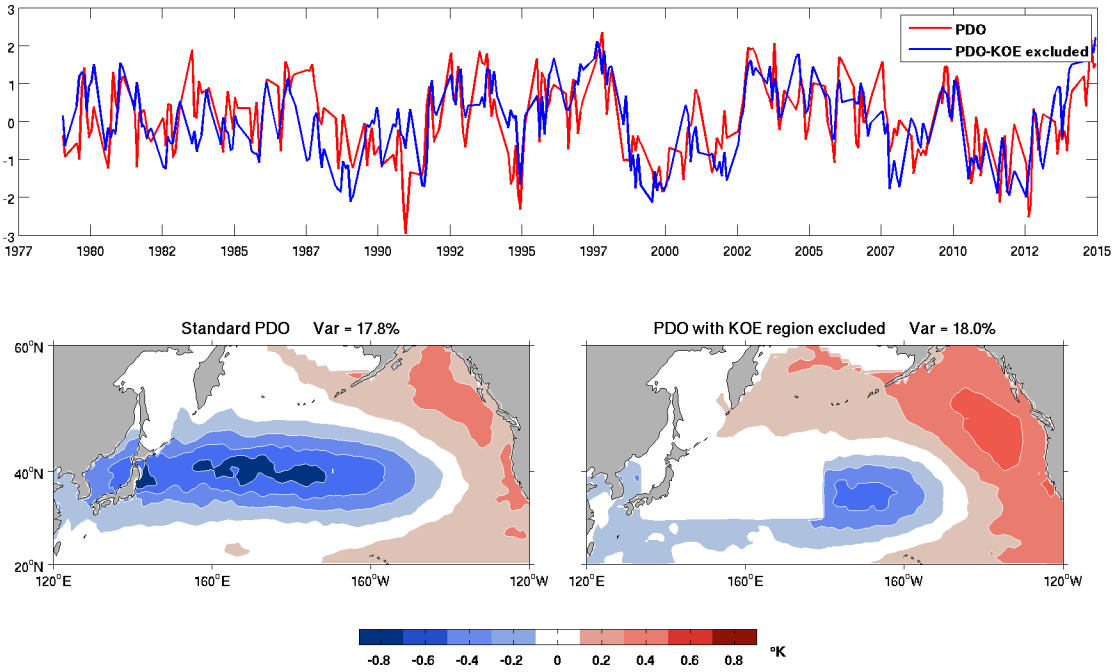

FIGURE 4.5 – (Bottom panels) SST EOF 1 pattern in JASONDJF in the North Pacific, when all the SST data points are included (left panel), and when the KOE region is excluded (right panel) (contour interval 0.2˚K). Red (blue) shading is for positive (negative) anomaly. (Upper panels) corresponding PCs time series. The percentage of represented variance is indicated.

Indonesian Seas and the eastern Indian Ocean (hereafter IIM, for Indonesian Indian Monopole), which is moderately correlated with the Indian Ocean Dipole (Saji et al. 1999) ($r = -0.55$). To represent the SST variability in the western and central parts of the Indian Ocean, which is not represented by the first three TIP R-EOFs (nor by the fourth one), we add the first R-EOF of the Indian Ocean SST anomaly residuals obtained after subtracting by regression the signal related to the first three R-PCs of TIP. This regional R-EOF (hereafter WTI for Western Tropical Indian) corresponds to a warming in the western part of the Indian Ocean, and its corresponding PC is also somewhat correlated with the Indian Ocean Dipole ($r = 0.37$). For the Atlantic, we use the first three R-EOFs : the first one (NAT) resembles the North Atlantic Tripole, and the second (NAH) broadly resembles the North Atlantic Horseshoe pattern (e.g. Czaja and Frankignoul 2002), while the third R-EOF is the tropical Atlantic El Niño mode (AEN, e.g. Zebiak 1993 ; Wang 2002). On the other hand, we use the first two standard EOFs for the North Pacific since they are the traditional way to represent the PDO, defined by the leading SST EOF in the North Pacific region (Mantua et al. 1997). Its time behavior (the PC) is represented in Fig. 4.3 (blue curve). The second EOF corresponds to the North Pacific Gyre Oscillation (NPGO) (e.g., Di Lorenzo et al. 2008).

Because the PDO has different dynamical origins, including zonal advection in the KOE region (Schneider and Cornuelle 2005), it has a strong SST signature in the KOE region and its

time evolution is significantly correlated to that of the OE ($r = -0.4$ in JASONDJF). Hence, it may be difficult to distinguish between the influence of the SST anomalies linked to the PDO and the influence of the SST anomalies linked to the KOE dynamics. In order to separate better the PDO and the KE and OE, we have also considered the case where the PDO is defined as the leading EOF of the North Pacific SST north of 20°N, but with the KOE region excluded, as indicated by the white box in Fig. 4.5. An EOF analysis reveals that the PDO still appears as the leading mode, explaining 18% of the variance, but the maximum cooling is weaker and displaced eastward, while the warming along the US west coast is stronger and more extended. In the following, this mode will be referred to as "PDO-KOE", as opposed to the standard PDO. Its time evolution is less correlated to that of the OE ($r = -0.25$ in JASONDJF), and it is rather well correlated with the standard PDO ($r = 0.63$ in JASONDJF). The low frequency variability (interranual to interdecadal) of the standard PDO is well-captured by this mode (Fig. 4.5). The PDO-KOE will be considered when determining which SST anomalies mostly control the ocean-to-atmosphere impact.

4.2.4 The sea ice forcing

Sea Ice Concentration (SIC) comes from the passive microwave monthly SIC provided by the National Snow and Ice Data Center. Its variability is represented differently because of the strong seasonal and long-term variations of the sea ice edge. At each grid point, SIC anomalies are estimated separately for each calendar month after subtracting a cubic trend. To capture the variability of the sea-ice edge, EOFs are calculated separately for each season (JASO, SOND and NDJF, see section 4.3.1 for the choice of the seasons), keeping only the grid points where the seasonal climatological mean concentration is <90% and >2% (seasonal R-EOFs gives very similar results).

We found that the addition of the SIC modes has little impact on our estimation of the atmospheric response to the other oceanic modes, while unnecessarily increasing the number of regressor variables. For each season, it turns out that only one EOF has a significant impact on the atmosphere. For completeness, we include this SIC PC in our analysis. In JASO, only the second EOF has an atmospheric impact, so only PC2 is retained, while in SOND and NDJF, only the first PC is retained. The corresponding EOFs are shown in Figure 4.4. SIC2 in JASO mostly corresponds to an increasing SIC in the Barents and Kara Seas. SIC1 in SOND corresponds to an increasing SIC in the Barents Sea and a decreasing SIC in the Chukchi Sea. SIC1 in NDJF has increasing SIC in the Barents and Greenland Seas and the Sea of Okhotsk, and decreasing SIC in the Labrador Sea and the Bering Strait. In total, we thus consider 12 oceanic explanatory variables.

4.3 Multivariate estimation of the atmospheric response

In order to distinguish between the atmospheric response to the different oceanic forcing, we use the Generalized Equilibrium Feedback Analysis (GEFA) method (Liu et al. 2008 ; Liu and Wen 2008 ; Wen et al. 2010). GEFA is a multivariate generalization of the univariate approach

of Frankignoul et al. (1998). A full discussion of GEFA is given in Liu et al. (2008) and Liu and Wen (2008). The method is described below in the present context.

4.3.1 The statistical model

Let $Y_j(t)$ be the j oceanic timeseries (standardized KE and OE indices, and PCs). This set of timeseries provides a representation of the anomalous oceanic forcing. We assume that, at each grid point and month t, the variability of an atmospheric anomaly $Z(t)$ can be described as the sum of a stochastic internal variability $n(t)$ and a linear function of the oceanic forcing. We also assume that the atmospheric response is not instantaneous at monthly timescale but takes a time d to reach its maximum amplitude. This can be written

$$Z(t) = \mathbf{B}\mathbf{Y}(t-d) + n(t) = \sum_{j=1}^{J} b_j Y_j(t-d) + n(t) \tag{4.3.1}$$

where $\mathbf{B}$ is the response (feedback) matrix, with b_j representing the impact of the j^{th}forcing (regressor variable) on Z. Several studies suggest that d = 1-2 months is appropriate for the extratropical atmosphere (Hoerling et al. 1997 ; Ferreira and Frankignoul, 2005, 2007 ; Deser et al. 2007 ; Semmler et al. 2016), but recent high-resolution experiments indicate that the maximum response to fronts may be reached slightly faster (Smirnov et al., 2015). If the maximum atmospheric response to oceanic forcing occurs after a delay d, one should search for the atmospheric response at lag $\geq d$. The response matrix at lag $d+\tau$ can be derived after multiplying (4.3.1) by the transpose of $Y(t-(d+\tau))$. Since $C_{nY}(d+\tau) = 0$ for $d+\tau$ longer that the persistence time of n, this yields :

$$\mathbf{B} = \frac{C_{ZY}(d+\tau)}{C_{YY}(\tau)} \tag{4.3.2}$$

where $C_{ZY}(d+\tau) = \sum_{j=1}^{J}\sum_{t=1}^{T} Z(t)Y_j(t-(d+\tau))$ is the covariance between $\mathbf{Z}$ and $\mathbf{Y}$ at lag $d+\tau$, and $C_{YY}(\tau) = \sum_{j=1}^{J}\sum_{t=1}^{T} Y_j(t-d)Y_j(t-(d+\tau))$ is the autocovariance matrix of $\mathbf{Y}$ at lag τ. The $Y_j(t)$ being standardized, the covariance matrix is in fact a correlation matrix, and our estimated response matrix $\mathbf{B}$ gives the typical response magnitude.

The appropriate value of the delay d can be derived from the lag regression of monthly atmospheric anomalies onto the oceanic indices, as illustrated in Fig. 4.6 for the PDO. Since the North Pacific ocean influence on the atmosphere may be different between early and late winter (section 4.1), three seasons are considered : autumn/early winter (OND), winter (DJF), and late winter/early spring (FMA). The regression maps of Fig. 4.6 are based on multivariate regression, except for lag -1 (SLP leads by 1 mo) that clearly represents the forcing of the PDO by the variability of the Aleutian Low. Consistent with the stochastic climate model (Frankignoul and Hasselmann 1977), lag 0 mostly represents the atmospheric forcing, as the patterns at lag 0 are very similar to the patterns at lag -1. This stresses that the response to extratropical SST anomalies cannot be estimated from unlagged relations (even at low frequencies, Frankignoul 1999). At a lag of 1 month, the SLP pattern changes drastically, but it is not very significant, probably because the atmospheric response hasn't fully developed. At a lag of 2 months, the

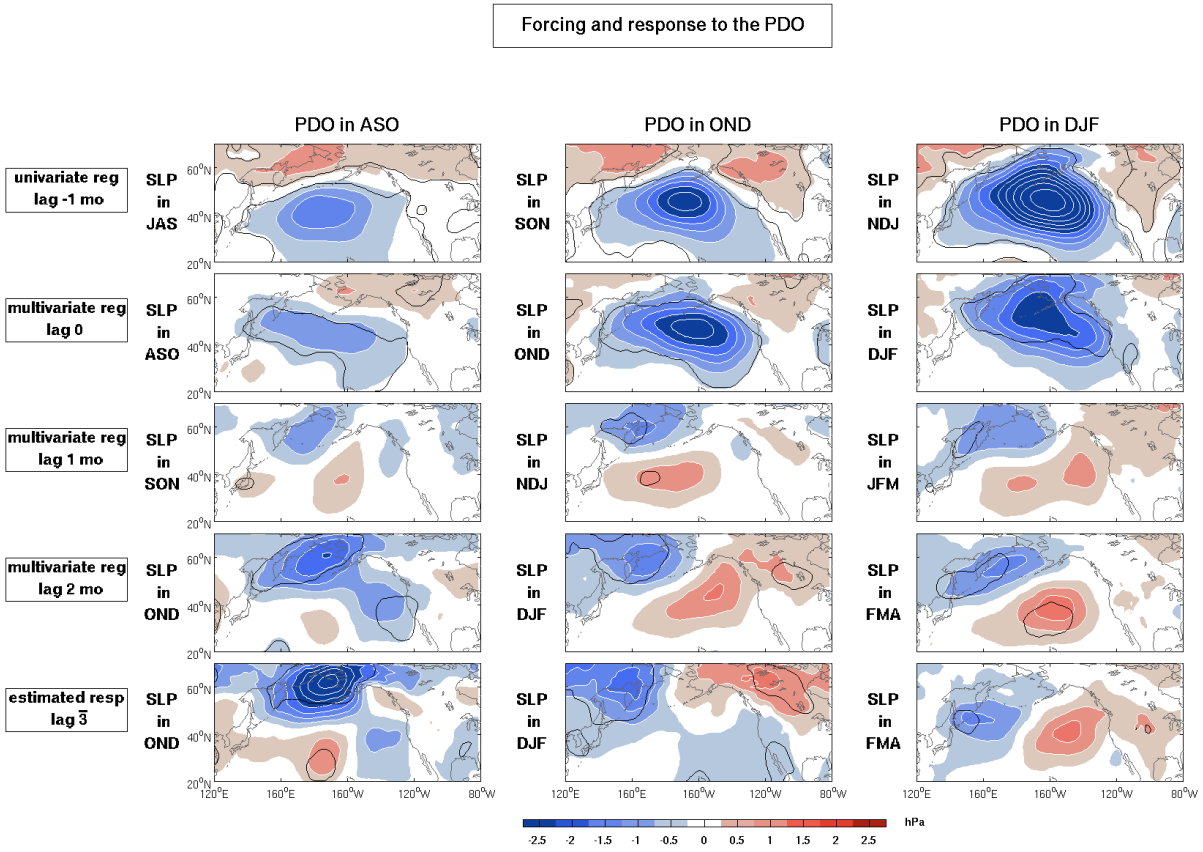

FIGURE 4.6 – (Upper panels) univariate regression of the SLP on the PDO index with the PDO lagging by one month, (second, third and fourth row panel) multivariate regression of monthly SLP on the PDO index leading by 0, 1 and 2 months, (bottom row panels) GEFA estimation of SLP on the PDO using 3-month means and a lag of one season (lag $\overline{3}$). The PDO index is taken in (left column) ASO, (middle column) OND and (right column) DJF, and the SLP is taken in the season indicated on the left of each panel. Red (blue) shading is for positive (negative) anomaly, and black contours indicate 10% significance.

pattern broadly resembles the one at lag 1 but becomes stronger and more significant. This suggests that $d = 2$ months is an appropriate choice.

In order to reduce the influence of the day-to-day changes in the atmospheric variables, and thus increase the signal-to-noise ratio, we choose to estimate the response with seasonal means (3-month means). The bottom panels of Fig. 4.6 show that the regression pattern at a lag of 2 months is very similar to the estimated atmospheric response based on a lag of 1 season (3 months). We thus choose $d + \tau = 3$ months, which corresponds to $\tau = 1$ month since $d = 2$ months. This small value of τ is pertinent since τ has to be minimized to achieve a better condition on $C_{YY}(\tau)$, and a reduced sampling error in Eq. (4.3.2) (Liu et al. 2006).

However, we verified that the atmospheric response patterns are not too sensitive to the assumed delay d. Figure 4.7 shows the OND GEFA estimations of the SLP and Z250 responses to the KE, the OE and the PDO derived in two cases : at a lag of 2 months using monthly values and assuming $d = 1$ month, and at lag $\overline{3}$ using seasonal means and assuming $d = 2$ months. In

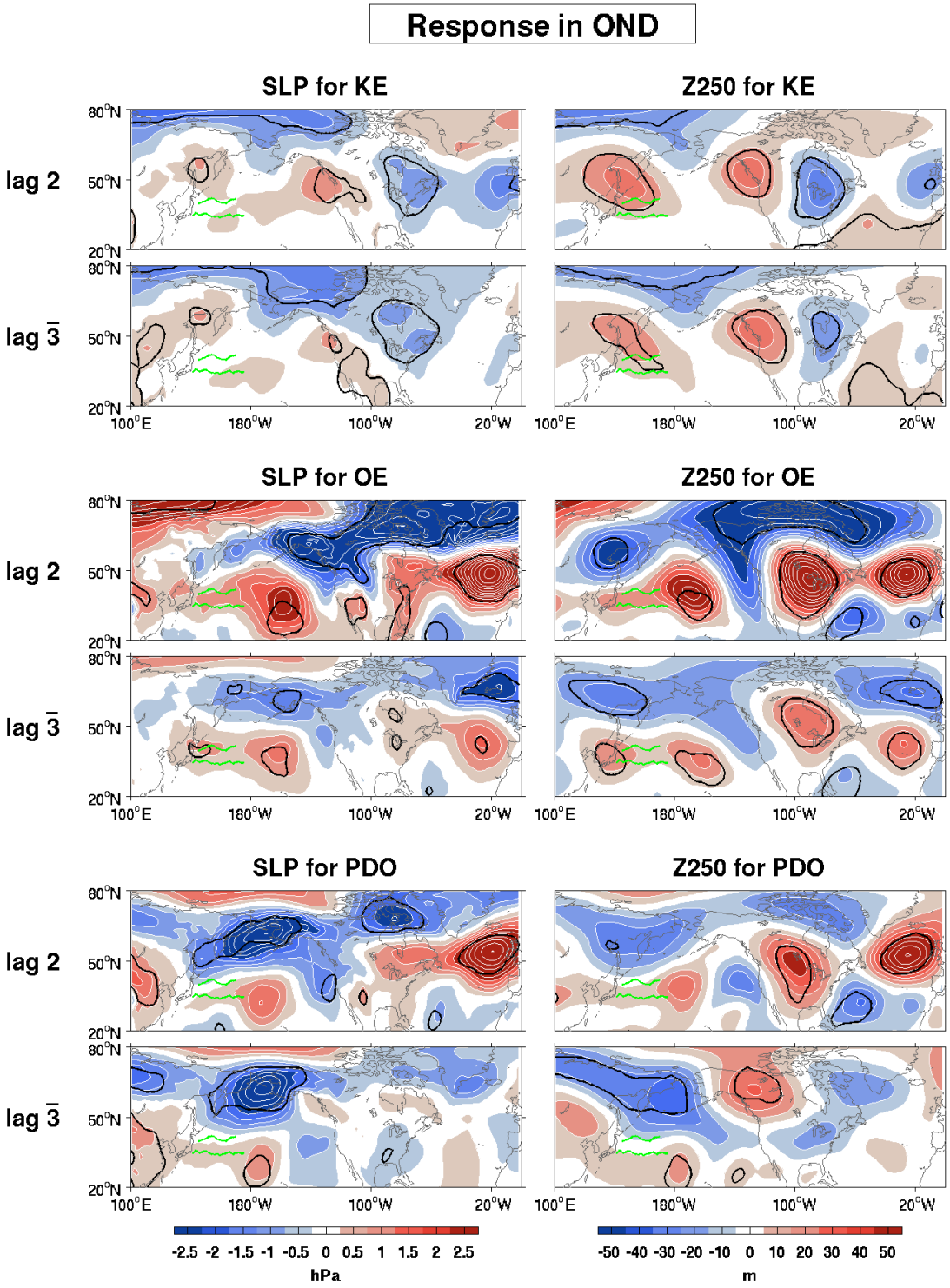

FIGURE 4.7 – Response in OND of (left panels) SLP and (right panels) Z250 to (upper panels) the KE, (middle panels) the OE and (lower panels) the PDO, estimated at lag 2 with $d = 1$ month and monthly values (first, third and fifth row), and at lag 3 with $d = 2$ months with seasonal means (second, fourth and sixth row). Red (blue) shading is for positive (negative) anomaly, and black contours indicate 10% significance.

both estimations we thus have $\tau = 1$ month. The response patterns based on monthly data are largely similar to those estimated from seasonal averages. However, using monthly data increases the intrinsic atmospheric noise and reduces the persistence of some oceanic time series, like the OE index. This reduces the lag autocorrelation of the corresponding regressors, which may lead to much higher amplitudes, as shown by Eq. (4.3.2). Hence, the estimated response can be much larger, as for the OE (Fig. 4.7). This is because the OE autocorrelation at lag 1 is small in this season (0.58), while it is always ≥ 0.89 in seasonal averages. On the other hand, the response to the KE and the PDO are broadly comparable with $d = 1$ or 2 months, as their persistence is much higher. Therefore, the magnitude of the response is much less sensitive to the persistence of the regressor if estimated with seasonal averages than with monthly values. Note that a 2-month atmospheric response time was also used in FSKA and Révelard et al. (2016). On the other hand, the atmospheric response was assumed to be instantaneous ($d = 0$) on the monthly time scale in previous GEFA applications, where the atmospheric response was estimated at a 1-month lag ($\tau = 1$) (Wen et al. 2010 ; Liu et al. 2012).

Throughout this study, statistical significance is tested with a Monte Carlo method, randomly permuting the atmospheric time series 500 times in blocks of 3 years (e.g. von Storch and Zwiers 1999).

4.3.2 Multicollinearity

The advantage of GEFA is that it should in principle separate the atmospheric response to different oceanic forcings, even if they are correlated to each other. The GEFA estimation (4.3.2) requires inverting the lag correlation matrix $C_{YY}(\tau)$. If τ=0, $C_{YY}(0)$ is symmetric, with diagonal elements equal to 1, and it is generally well conditioned. However, symmetry is lost for nonzero τ, and as τ increases, $C_{YY}(\tau)$ tends to become singular and hard to invert, and the sampling errors in $\mathbf{B}$ become too large. Even for small τ, a strong correlation between the regressor variables may yield too much multicollinearity and make it difficult to separate the effects of the different oceanic forcings.

One way to detect multicollinearity is by calculating the condition number, which is the ratio between the largest and smallest singular values of $C_{YY}(\tau)$. It characterizes the sensitivity of the response matrix $\mathbf{B}$ to small changes of $\mathbf{Y}$. If it is low (typically < 10), the matrix is well conditioned and its inverse can be computed with good accuracy. If it is very large (> 10) $C_{YY}(\tau)$ tends to be singular and $\mathbf{B}$ is prone to large errors. In this study, the condition number never exceeds 3. However, Stewart (1987) has shown that the condition number is a too crude indicator of collinearity.

A better way to quantify the multicollinearity is to provide the variance inflation factor (VIF) (Kendall's 1946). The VIF is the factor by which the variance of the estimator b_j is increased by considering the other regressor variables. Let us consider the univariate case (called EFA for distinction), in which Y_j is the only regressor variable. We have

$$a_j = \frac{C_{ZY_j}(d+\tau)}{C_{Y_jY_j}(\tau)}$$

where a_j is the EFA response to the j^{th} and only forcing. It can be shown that the variance of a_j is given by

$$Var(a_j) = \frac{\sigma_j^2}{\sum_{i=1}^{N}(y_{ij} - \overline{y_j})^2}$$

where σ_j^2 is the variance of Y_j. In the case of multivariate regression, in which various correlated regressors are included in the model, it can be shown that the variance of the estimator b_j is (Kendall's 1946)

$$Var(b_j) = \frac{\sigma_j^2}{\sum_{i=1}^{N}(y_{ij} - \overline{y_j})^2} \times \frac{1}{1 - R_j^2}$$

where R_j^2 is the R-squared value (coefficient of determination) obtained by regressing the j^{th} regressor on the remaining regressors. R_j^2 represents the proportion of the variance of Y_j that is explained by the other regressors. The VIF of the j^{th} regressor is therefore given by :

$$VIF_j = \frac{1}{1 - R_j^2}$$

If the correlation of the regressor Y_j with the other regressors is large, so is R_j^2, resulting in a higher variance of b_j. The VIF is also the diagonal element of the inverse correlation matrix $C_{YY}(\tau)^{-1}$. A general rule is that VIFs exceeding 5 are signs of a severe multicollinearity (Judge et al. 1988). Hence, we only consider results when the VIFs are smaller than 4.

Note that EFA and GEFA can be linked through the so-called forcing matrix **M** (Liu et al. 2008 ; Liu and Wen 2008 ; Wen et al. 2010). It can be shown that

$$a_j = \sum_{i=1}^{J} b_i m_{ij} \qquad with \qquad m_{ij} = \frac{C_{Y_i Y_j}(\delta)}{C_{Y_j Y_j}(\delta)}$$

where m_{ij} is the weight of the contribution of the i^{th} forcing onto the atmospheric response to the j^{th} forcing. In other words, the EFA atmospheric response to the j^{th}forcing a_j is the sum of the contribution from each forcing (the GEFA response), weighted by m_{ij}. If there is no correlation between the regressors, $m_{ij} = 0$ for $i \neq j$ and the EFA response if the same than the GEFA response, $a_j = b_j$.

The correlation matrix $C_{YY}(\tau)$ is a good indicator of the interactions between the different regressor variables. Since $\tau = 1$ month in our study, $C_{YY}(\tau)$ is not symmetric : each row i gives the correlation between the i^{th} forcing and the other forcings lagging by 1 month, and each column j gives the correlation between the j^{th} forcing and the other forcings preceding by 1 month. Hence, in each row i, high correlations indicate the oceanic regressors for which the i^{th} forcing strongly contributes to their univariate atmospheric response. In each column j, high correlations indicate the oceanic regressors that most contribute to the univariate atmospheric response to the j^{th} forcing. The correlation matrix for the OND season is shown in Fig. 4.8, together with the VIF of each regressor variable and the condition number. As the maximum

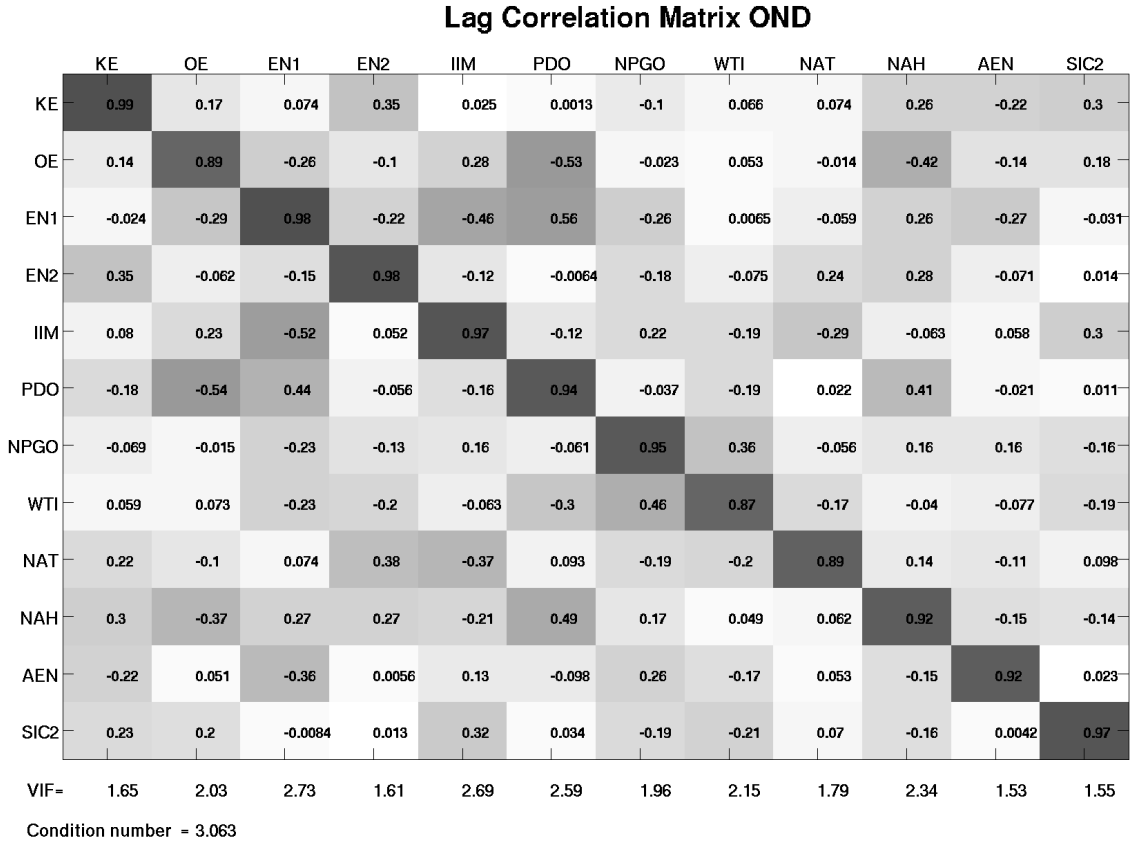

FIGURE 4.8 – Lag-1 correlation matrix used for the calculation of the response in OND. Correlation matrix among the KE and OE indices, the twelve SST (R)EOF of TIP, NP, TI and NTA, and the second EOF of SIC in JASO. Each row and column uses the season ASO and JAS respectively. The bottom row is the variance inflation factor (VIF) of each predictor, and the condition number is given at the bottom left. Grey shading goes from -1 to 1, with darker grey indicating higher absolute values, and lighter grey lower absolute values.

VIF is 2.73 (for EN1), there is no strong problem of multicollinearity in this season.

In DJF, however, the condition number is similar but there is more collinearity as the VIF reaches 4.11 for the OE and 3.58 for the NPGO, leading to large sampling errors (Fig. 4.9). The increased collinearity reflects the stronger lag correlations between many regressors, in particular between OE and NPGO ($C_{2,7}$ = 0.42 (-0.02) in DJF (OND)), between OE and IIM ($C_{2,5}$ = 0.41 (0.28)), and between OE and NAT ($C_{2,9}$ = 0.29 (-0.01)). There is also a much higher correlation in DJF between NPGO and EN2 ($C_{4,7}$ = -0.32 (-0.18)), NPGO and IIM ($C_{5,7}$ = 0.44 (0.22)), and NPGO and PDO ($C_{6,7}$ = -0.33 (-0.04)).

To get more robust response estimates in DJF, it is thus advisable to reduce the number of regressors. In order to keep the North Pacific forcings, which are of most interest in this study, we first considered the suppression of the North Atlantic forcings (NAH and NAT), since it substantially lowers the VIFs. However, strong remote SST signals related to the OE and resembling the NAH were then found in the North Atlantic. Moreover, GEFA was not able to isolate the OE SST footprint in the North Pacific, as discussed below (section 4.5). As other

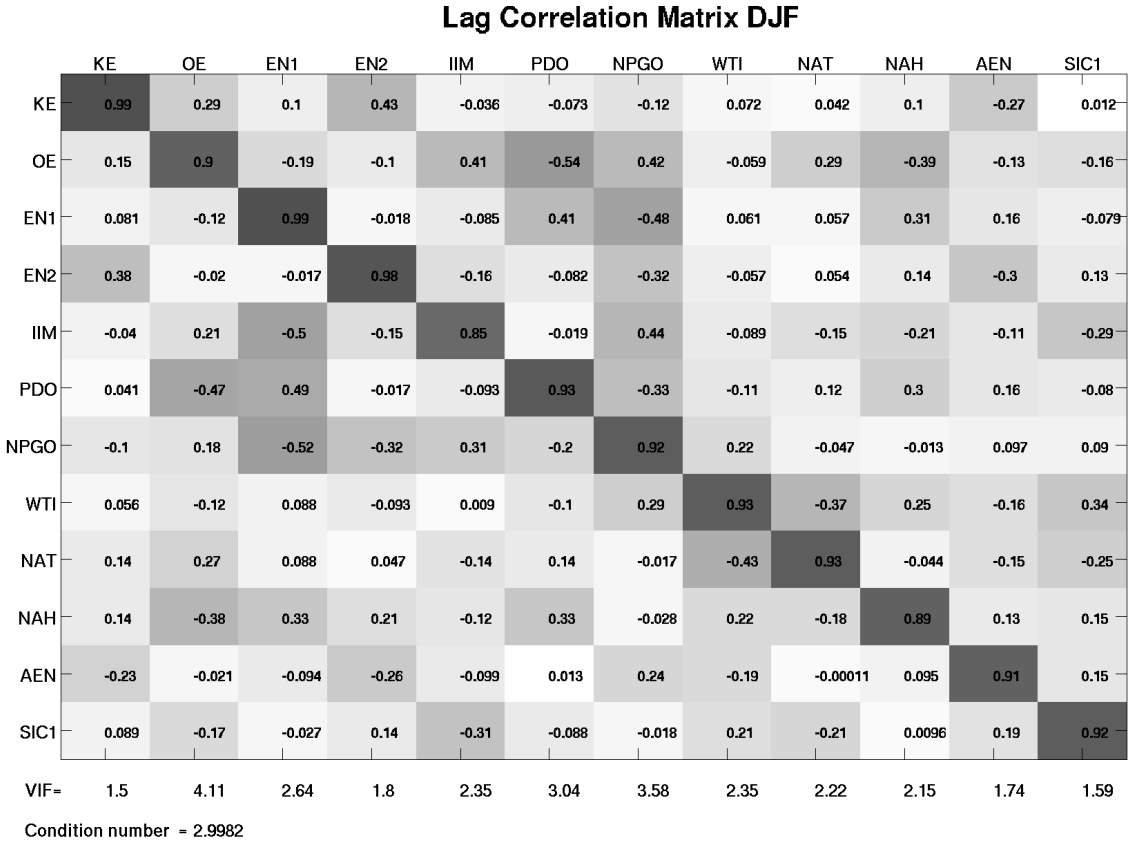

Figure 4.9 – Same as figure 4.8, but for the response in DJF, with the first EOF of SIC in SOND. Each row and column uses the season OND and SON respectively.

attempts at keeping the OE regressor were not satisfactory, we preferred to renounce estimating the DJF response to the OE. Omitting the OE regressor in GEFA substantially lowers the VIFs, which all become lower than 2.5, except 3.29 for NPGO (not shown). This value is relatively high, but it was verified that omitting the NPGO regressor leads to similar amplitudes but a less accurate isolation of the SST footprints. Hence, we keep the NPGO as regressor.
In FMA, multicollinearity is limited, with VIF < 3, except for EN1 and IIM, whose VIF reach 3.68 and 3.61, respectively (Fig. 4.10), because of the high correlation between the two ($C_{3,5} = 0.73$, when EN1 leads IIM by one month). This leads to an artificially large response to EN1 and IIM, but it was verified that it does not affect the estimated response to the other oceanic variables.

4.4 Atmospheric response in autumn/early winter (OND)

4.4.1 The full GEFA results

As our statistical model of the atmospheric response is based on a delay $d = 2$ months, the SST anomalies that generate an atmospheric response in OND should be shown two months earlier, in ASO. We thus show in Fig. 4.11 and 4.12 the SST signature in ASO of the twelve

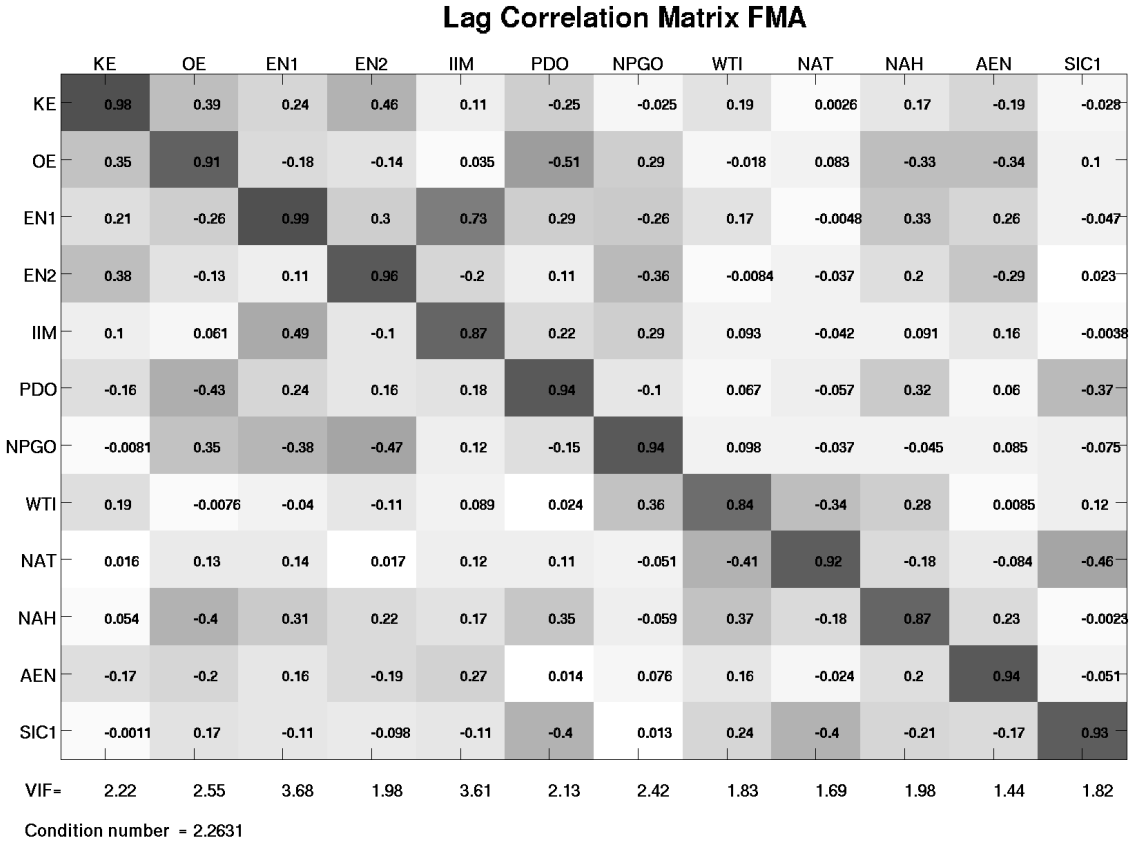

FIGURE 4.10 – Same as figure 4.8, but for the response in FMA, with the first EOF of SIC in NDJF. Each row and column uses the season DJF and NDJ respectively.

oceanic regressors considered in this study, estimated by univariate (EFA, left) and multivariate (GEFA, right) regression. As illustrated by the univariate regression, the regressors variables are not independent and the associated SST anomalies extend much beyond their domain of definition. For instance, EN1 has a clear North Pacific PDO-like extension, and the PDO is associated with an equatorial Pacific warming, reflecting the well-known influence of ENSO on the PDO (e.g. Lau and Nath 1996 ; Schneider and Cornuelle 2005 ; Newman et al. 2016). In fact, most regressors are associated with an SST anomaly in the equatorial Pacific and/or with substantial cross-basin correspondences, which reflect atmospheric bridges, ocean dynamics, coordinated atmospheric forcing, and sample limitation. Correspondingly, univariate estimates of the atmospheric response would reflect the complexity of the oceanic forcing.

On the other hand, when all the oceanic time series are considered simultaneously, the SST anomaly patterns become largely regional (Fig. 4.11 and 4.12, right panels). In all cases, the ENSO-like anomalies are properly removed. The KE and OE remote SST anomalies mostly disappear, and the PDO and NPGO are restricted to their extratropical signatures. The Pacific SST anomalies associated with NAT, NAH and AEN mostly disappear, as well as the SST anomalies in the Atlantic and Pacific that are associated with WTI and IIM. Similarly, the extratropical signatures of EN1 and EN2 are largely removed. SIC2 becomes primarily associated with a warming in the Norwegian Sea. Although some small remote SST anomalies are still

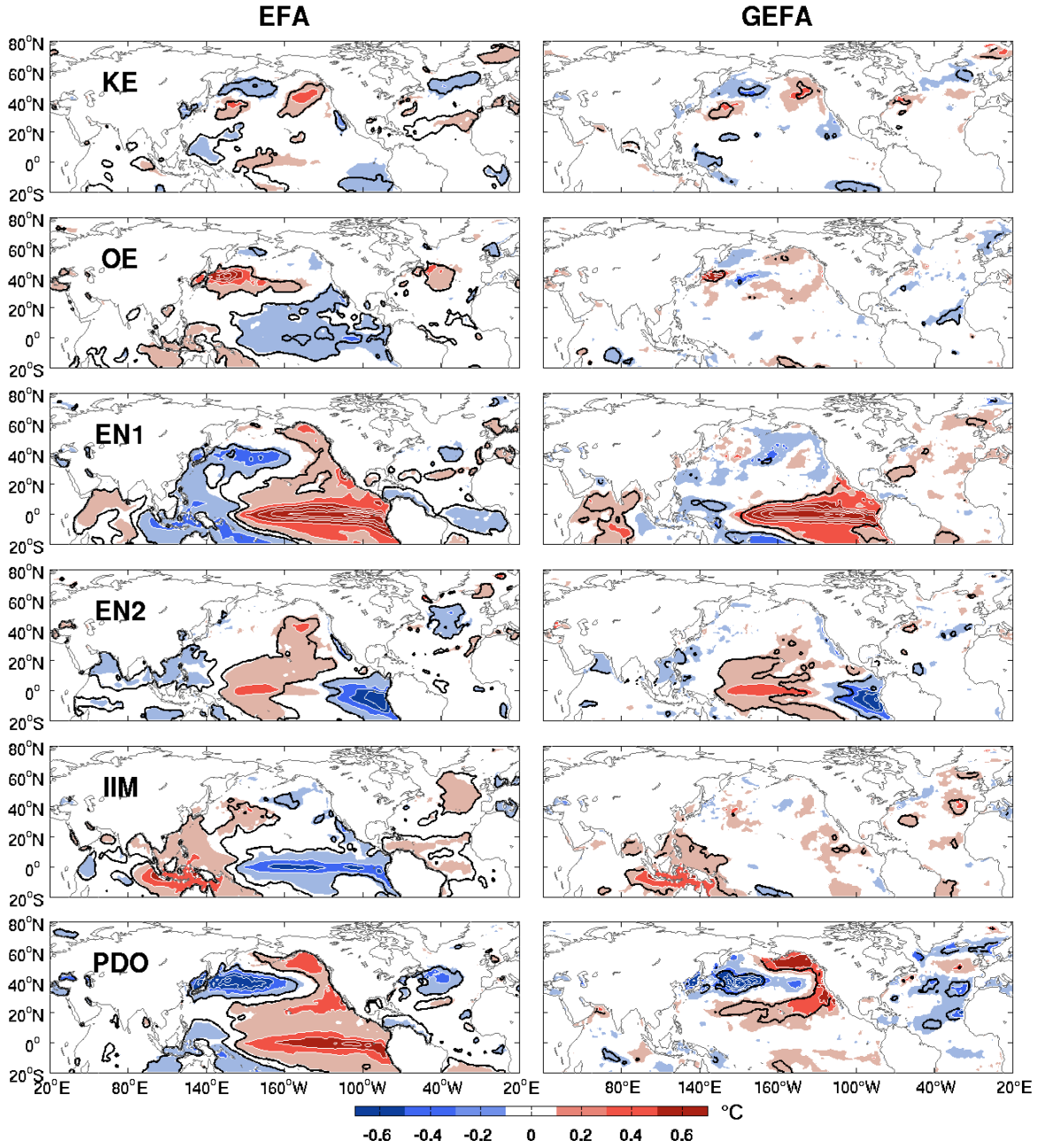

Figure 4.11 – SST signature in ASO of each forcing as indicated on the left, in the case of univariate regression (left colmun) and multivariate regression (right column). Red (blue) shading is for positive (negative) anomaly, and contour intervals are 0.2 ˚K.

present, the multivariate GEFA approach has strongly modified the SST imprint of each regressor variable, leading a more localized SST anomaly patterns and a better separation between tropical and extratropical forcing. This is an interesting aspect of the multivariate approach that was not noted in earlier GEFA applications, and is particularly useful for investigating atmospheric responses, in view of the differences between tropical and extratropical dynamics. Note that the separation between EN1 and PDO achieved here is opposite to that in Chen and Wallace (2016), where the ENSO signal was even more limited to the equatorial band and the PDO had the

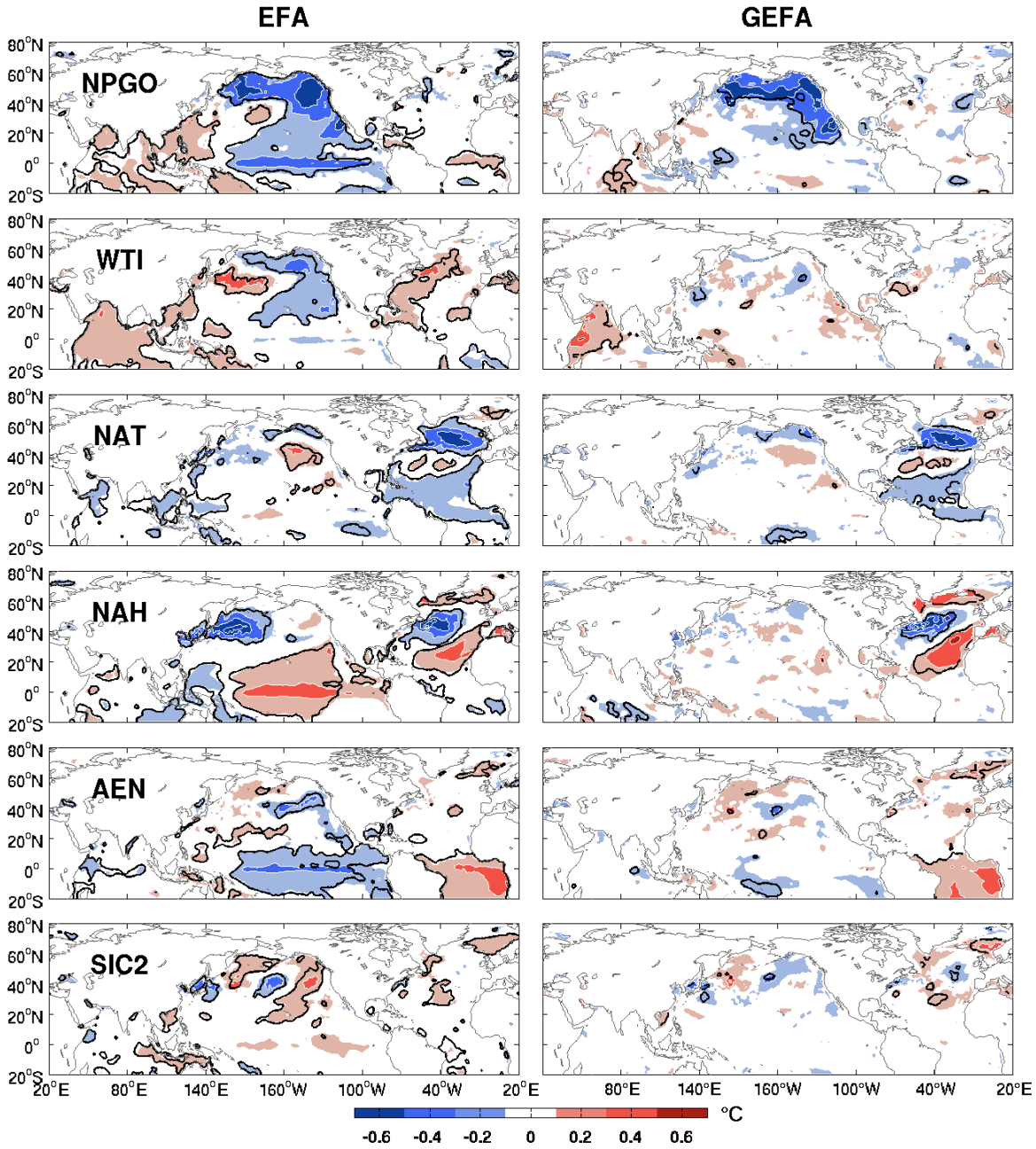

FIGURE 4.12 – Same as Fig. 4.11, but for the other forcings.

equatorial component that characterize its decadal variations. In the rest of this chapter, the atmospheric response to the PDO should thus be understood as the response to the extratropical part of the PDO.

The estimated atmospheric response in OND to all the oceanic forcings is shown in Fig. 4.13 for Z250 and in Fig. 4.14 for the SLP, using GEFA with the twelve oceanic regressors. Although our emphasis is on the atmospheric response to the North Pacific western boundary current variability and the PDO, the estimated response to the other boundary forcing is first briefly commented upon. Given that GEFA leads to SST anomalies that are largely confined to their

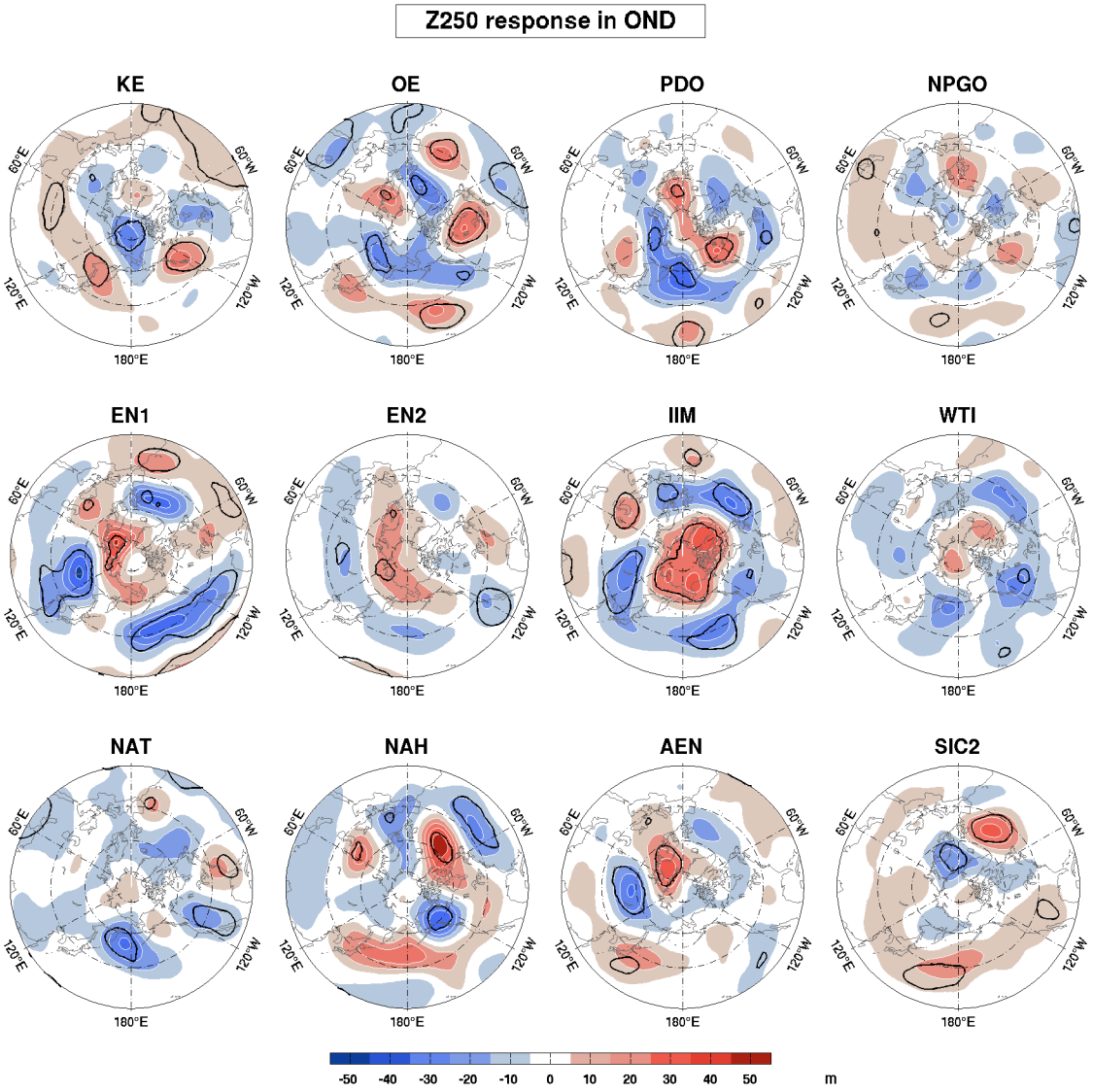

Figure 4.13 – Z250 response to the twelve predictors in OND, north of 20°N. The response is assessed by GEFA with the twelve regressors, with lag-covariance matrix of figure 4.8. Red (blue) shading is for positive (negative) anomaly, and contour intervals are 0.5 hPa. Thick black contours indicate 10% significance. Latitude circles are shown every 20°.

region of definition, and that multicollinearity is limited in this season, we are fairly confident that the estimated response to each oceanic forcing shown in Fig. 4.13 and 4.14 largely reflects its impact.

The Z250 response to EN1 shows some differences with the typical response pattern to El Niño, which is usually shown in winter (DJF) when it is stronger (Guilyardi et al. 2003 ; Borlace et al. 2013). The EN1 teleconnection in OND is characterized by a circumglobal high in the tropics (barely seen in Fig. 4.13, which is limited to 20°N), a strong elongated low over the northeastern Pacific and a weakening of the Siberian high, which typically reach 20 to 40 m, consistent with the atmospheric bridge discussed by Alexander et al. (2002). However, the upper-level high anomaly that is usually seen over western Canada as a response to ENSO is attributed here

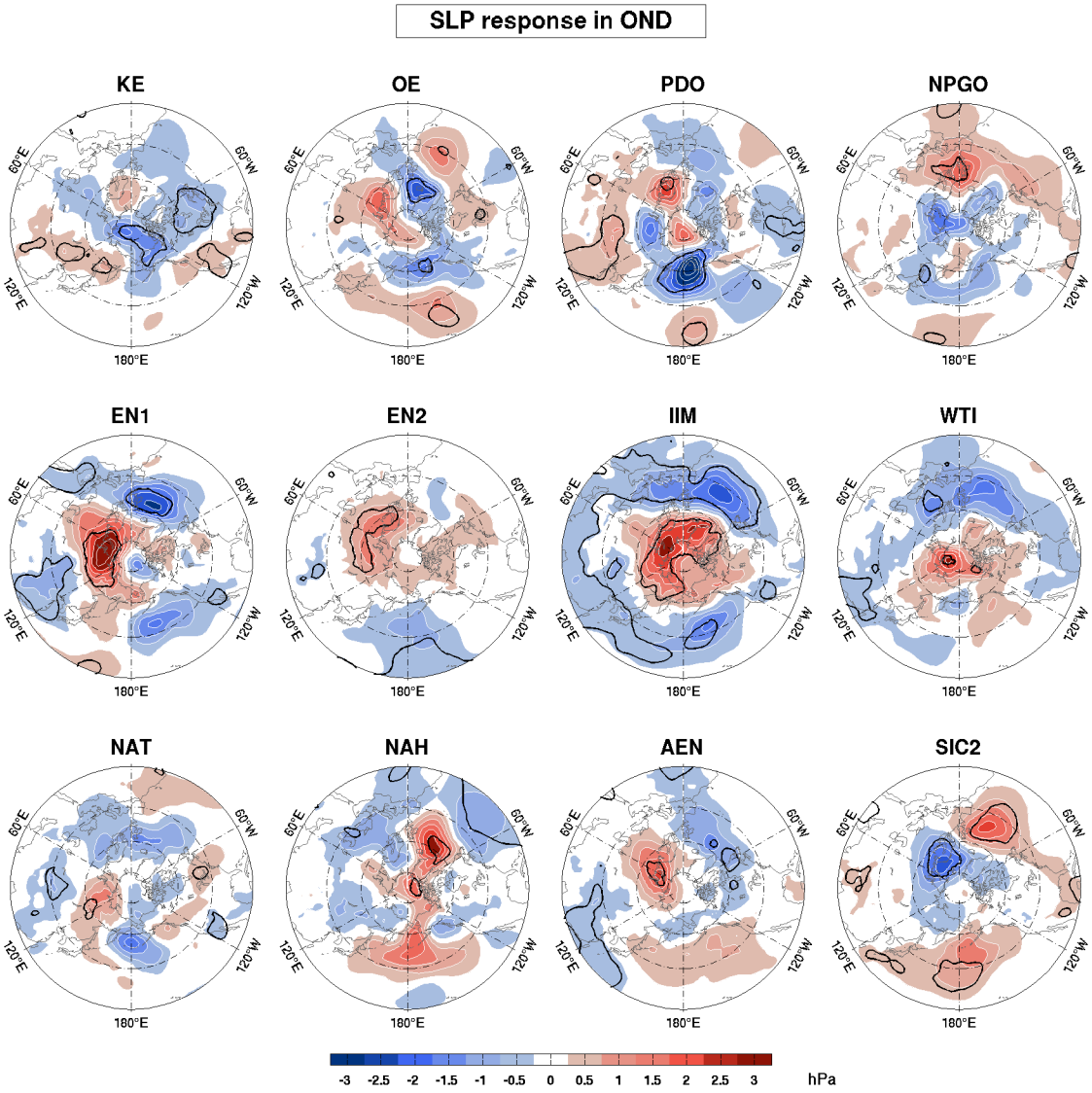

FIGURE 4.14 – As in figure 4.13, but for SLP.

to the (extratropical) PDO. This pattern is understood as barotropic Rossby wave propagation towards the extratropics in response to a deep equatorial heating and a baroclinic equatorial Rossby wave response. In the tropics, the SLP signal resembles the Southern Oscillation but differs elsewhere (Fig. 4.14) from the SLP pattern shown by Alexander et al. (2002) for the SON season (their Fig. 6), as there is no significant signal in the North Pacific sector. This is because the multivariate regression separates the influence of the tropical SST (El Niño) from the influence of the extratropical SST (the PDO). Indeed, if the PDO is omitted in GEFA, the SLP response to EN1 becomes very similar to that in Alexander et al. (2002), more clearly showing the Southern Oscillation in the North Pacific (Fig. **??**). Since the Z250 response to EN1 in the extratropics is, contrary to the SLP, little affected by the addition of the PDO into GEFA, our analysis is coherent with the mechanism of the atmospheric bridge of Alexander et al. (2002), in which the tropical SST has an impact in the extratropics through the upper troposphere.

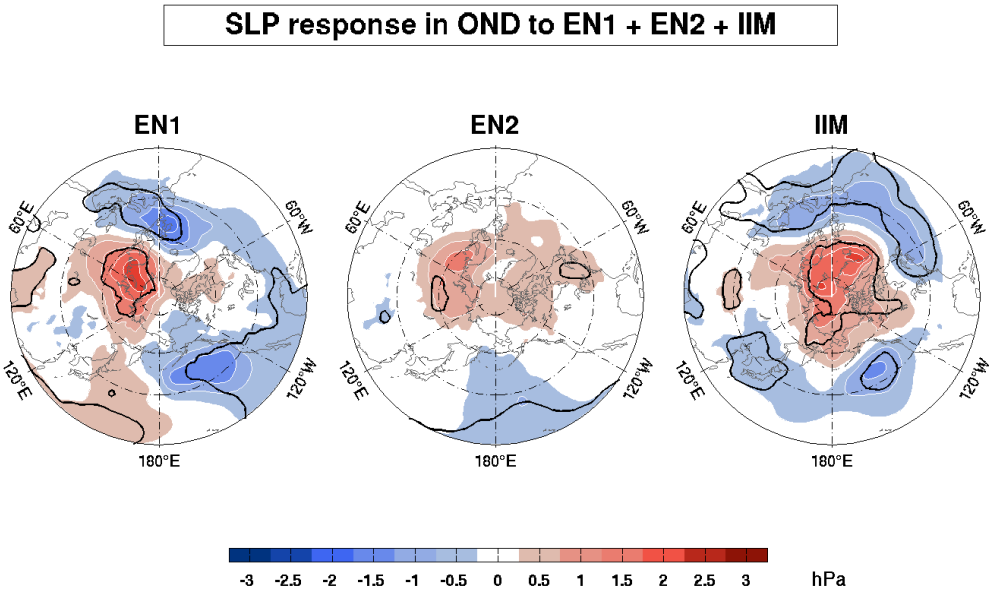

Figure 4.15 – SLP response to the three R-EOFs of TIP in OND, north of 20˚N. The response is assessed by GEFA with the three R-EOFs of TIP only. Red (blue) shading is for positive (negative) anomaly, and contour intervals are 0.5 hPa. Thick black contours indicate 10% significance. Latitude circles are shown every 20˚.

Except for an elongated high over northern Eurasia that is only significant in SLP, EN2 drives little extratropical atmospheric response, even with fewer regressors or in univariate regression (not shown). However, the SLP response to EN2 shows a significant low over the central Pacific (Fig. 4.14), presumably in response to the equatorial heating. On the contrary, the IIM has a strong barotropic impact, with a strong positive anomaly over the polar vortex, and primarily negative anomalies in the latitude band of 35˚-60˚N. This indicates that a warming in the Indonesian Seas leads to a weakening of the polar vortex and a poleward shift of the eddy driven jet.

The NPGO does not lead to a significant atmospheric response, and the WTI impact seems limited to a North Atlantic low. The NAT primarily drive a baroclinic signal in the tropical North Atlantic, although there are hints of a weak wave-like extratropical signal with a low over Western United States. The strongest influence of the North Atlantic SST comes from the NAH, which leads a negative NAO-like barotropic pattern over the North Atlantic, albeit shifted west, in agreement with Czaja and Frankignoul (2002). There is also a teleconnection over the North Pacific in the upper troposphere, with a low over Alaska and a high over the Aleutian Islands, albeit not significant. Note that this pattern has a much smaller amplitude if the PDO is not used as regressor, as NAH and PDO are well correlated ($C_{10,6} = 0.49$, Fig. 4.8). The AEN drives a stationary wave train in the upper troposphere with a high in the tropical North Atlantic, a weak low over the North Atlantic, albeit not significant, a high over the Barents Sea, and a strong low over Siberia. There is also a significant barotropic high over Japan. This pattern already appears in univariate regression and has some limited similarity with the East Atlantic pattern-

like response detected by Frankignoul and Kestenare (2005) in the observations. Haarsma and Hazeleger (2007) identified the same response pattern in a coupled model, and have found that a warming in the equatorial cold tongue region was able to generate a sufficiently large upper level divergence during late summer, when the ITCZ is located above the same region, to induce a significant extratropical Rossby wave in early winter.
Finally, SIC2, which mostly corresponds to an increasing SIC in the Barents and Kara Seas (Fig. 4.4) and is associated with a positive SST anomaly in the Norwegian Sea (Fig. 4.12), leads to a barotropic pattern over the North Atlantic that reflects a northward shift of the eddy driven jet. This response is broadly consistent with a positive phase of the NAO, as in Garcia-Serrano et al. (2015), albeit slightly shifted north. There is also a significant high over the central North Pacific.

4.4.2 Response to the OE variability

We now discuss in more details the OND atmospheric response to the OE. To first illustrate the effect of adding an increasing number of oceanic regressors in GEFA, we show in Fig. 4.16 the estimated response in SLP (middle column) and Z250 (right column) to the OE, using increasing sets of oceanic forcings. In parallel, we show the corresponding SST signature of the OE forcing in the North Pacific, estimated two months earlier in ASO (left column).

The upper panels in Fig. 4.16 represent the univariate (EFA) case in which the OE is the only forcing. The SST signature shows a broad warming over the KOE region, with a maximum along the OE reaching 1˚K, a small elongated warming in the central basin, and a smaller cooling in the central and eastern tropical Pacific Ocean. The EFA estimate of the SLP and Z250 response reveals a weak broadly barotropic, wave-like extratropical structure that originates in the upper tropical troposphere, with a high over the central basin, a low over the Gulf of Alaska, and a upper level high over the eastern US. However, as discussed in section 4.3.1, the univariate regression mixes the different forcings that covary with the OE (Eq. 4.3.2). During the ASO season, the KE and OE are poorly correlated ($r = 0.17$), so adding the KE has no impact (not shown). On the other hand, the OE is moderately correlated with EN1 ($r = 0.25$) and IIM ($r = 0.32$). Hence, these regressors significantly contribute to the univariate regression. Adding the 3 TIP R-EOFs (second row) leads to a somewhat more localized SST footprint in the North Pacific and largely suppresses the tropical Pacific SST anomalies. Adding the PDO is what most impacts the estimated response to the OE, as they are highly correlated ($r = -0.55$). It confines the SST warming to the mean OE path, west of 160˚E,, and slightly reduces its amplitude to 0.6˚K. The cooling in the eastern tropical Pacific is also totally suppressed, but a PDO-like pattern has appeared in the eastern part of the basin, albeit with a small amplitude and low significance. Adding the PDO thus suitably narrows the warming over the KOE region, but it probably removes too much signal, so that a weak PDO-like SST signal is emerging. However, it is weakened when the other oceanic regressors are taken into account (fourth row). When the PDO is included in GEFA, the anomalous high in the central basin is unaltered, but a strong low has appeared over Alaska and northeastern Asia, so that the main SLP response is now a dipole structure resembling the North Pacific Oscillation (NPO) in positive phase. Z250 has a

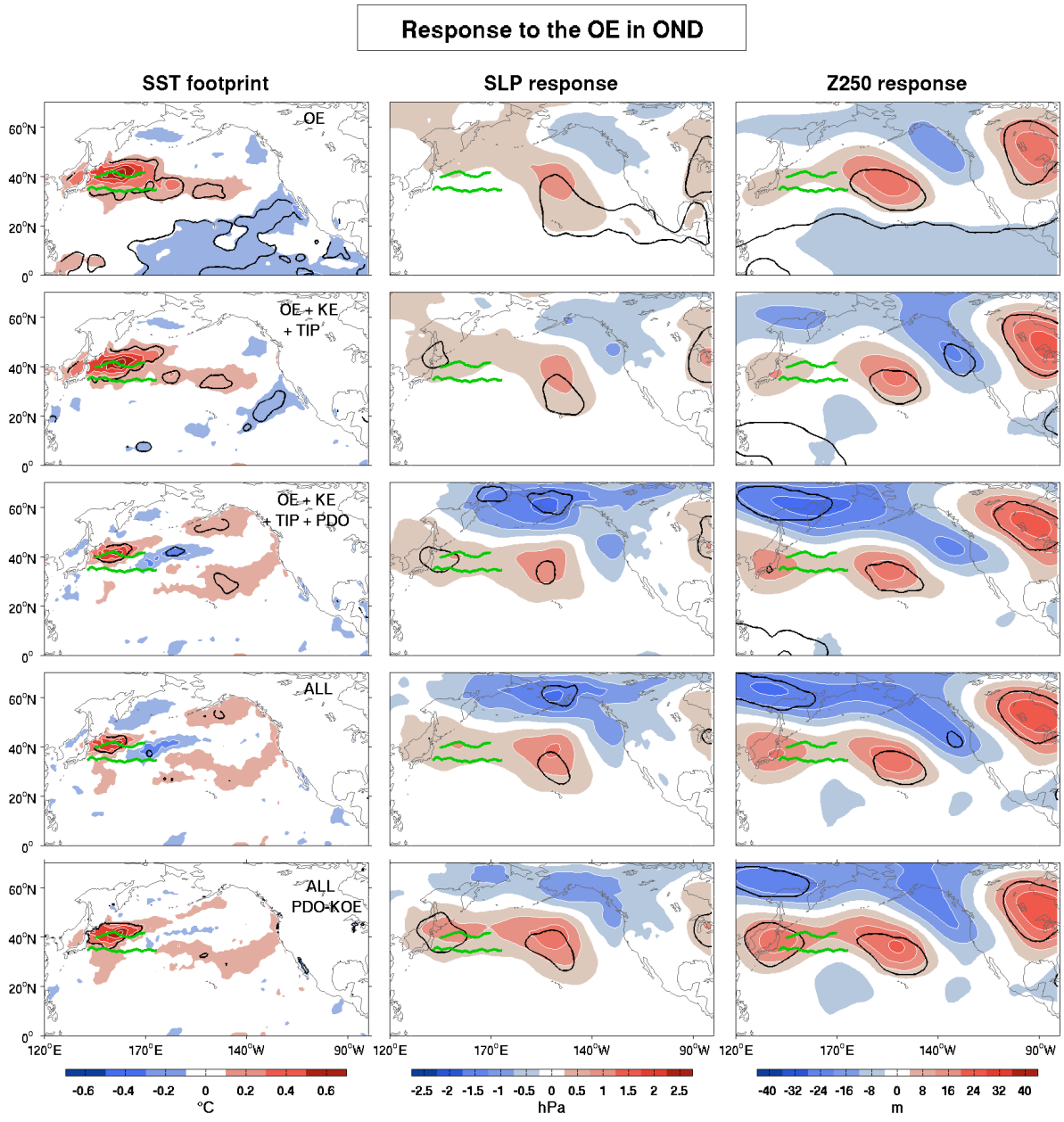

Figure 4.16 – (left column) SST signature of the OE in ASO (CI = 0.2°K) and the OND response of (middle column) SLP (CI = 0.5 hPa) and (right column) Z250 (CI = 8 m) to the OE. The signature and response are assessed with (upper row) the OE index alone, (second row) the OE, KE and the first three R-EOFs of TIP, (third row) the OE, KE, the first three R-EOFs of TIP and the PDO, (fourth row) all the regressors, and (bottom row) all the regressors but with the PDO-KOE. Red (blue) shading is for positive (negative) anomaly, and black contours indicate 10% significance. Green lines denote the mean KE and OE paths.

similar structure, but the low over Alaska is extended westward and southeastward over the US west coast, and there is a high over eastern US, so that the pattern broadly resembles the West Pacific (WP) teleconnection pattern (Linkin and Nigam, 2008). Hints of the NPO/WP signal

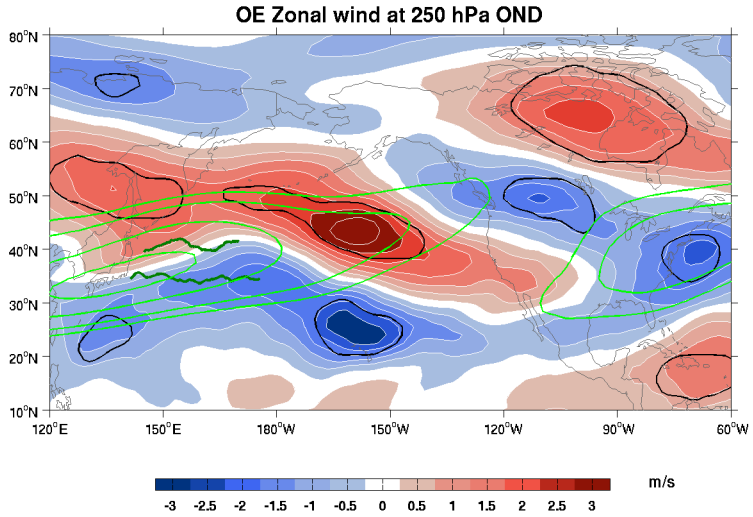

FIGURE 4.17 – Zonal wind response at 250 hPa to the OE in OND, estimated by GEFA. Red (blue) shading is for positive (negative) anomaly, and contour intervals are 0.5 ms^{-1}. Green thick lines denote the mean KE and OE paths, and black contours indicate 10% significance. Green contours denote the OND zonal wind climatology, with contours at 25, 30, 40, 50 and 60 ms^{-1}

were already seen before adding the PDO, but without any statistical significance. Interestingly, the inclusion of the Atlantic forcing has little influence, even though the OE is moderately correlated with the NAH ($r = -0.42$). This likely occurs because NAH is also well correlated to the PDO ($r = 0.49$), so that the impact of NAH is somehow already "included" with the PDO.

To assess the robustness of the estimated response and further differentiate OE and PDO forcing, GEFA was also performed using PDO-KOE instead of the standard PDO (Fig. 4.16, bottom row panels). The OE SST footprint is stronger (0.8°K) and a little broader. In addition, the weak PDO-like signal northeastern Pacific disappears, so that the SST footprint has become largely local. We thus feel that this case best singles out the influence of the OE meridional shift, consistent with the expected impact of the OE meridional shifts and the dominant role of ocean dynamics in generating SST anomalies in the KOE region (Smirnov et al. 2014). Nonetheless, the atmospheric response pattern remains similar, although the high near Japan is strengthened and has become statistically significant. However, we verified that our results are very similar using PDO-KOE instead of the standard PDO, so we keep the standard PDO in the rest of this chapter.

In summary, the response to the OE variability is NPO/WP-like in OND, reaching about 2 hPa at sea level and 30 m at 250 hPa, together with a northeastward propagating wave train. The hemispheric views given in Fig. 4.13 and 4.14 show a NAO-like teleconnection over the North Atlantic, confirming the resemblance with the WP teleconnection pattern. This pattern is quite similar to the atmospheric response found by FSKA using the OE index based on NOAA product from 1982 to 2008 and based on all the months of the year (their Fig. 8) or the NDJ season (their Fig. 10). However, the low over the Bering Sea is more elongated here, and the high

over the subtropical Pacific is narrower. The teleconnections patterns were basically unchanged with PDO-KOE instead of the standard PDO. This pattern indicates a poleward shift of the jet stream, as indicated by the zonal wind response at 250 hPa (Fig. 4.17). Understanding the mechanisms by which the OE can lead to such an atmospheric response is the purpose of the two next sections.

Heat flux feedback

Since SST anomalies influence the atmosphere via surface heat exchanges, we use GEFA to determine how the OE meridional shift affects the surface turbulent heat flux. The thermal forcing generated by SST anomalies is best detected at lag ≥ 1 month (Frankignoul et al., 1998), as it separates cause and effect. Here, the heat flux feedback is assessed with GEFA at lag = 1 month (thus leading the SLP and Z250 response by 1 month) using monthly anomalies instead of seasonal means (which would require lag ≥ 3 months). As the turbulent heat flux feedback is noisy and broadly similar in the three seasons, we show it for the whole cold period SONDJFM, which encompasses the three seasons considered in this study. Because of the strong seasonal variations of the sea ice edge, the SIC forcing is not included in this estimation of the heat flux feedback. However, when it is estimated in each season separately, it has a negligible influence on the heat flux driven by the other oceanic forcings (not shown).

If the atmospheric response at lag 1 is already substantial, the heat flux anomaly associated at lag 1 to a large-scale SST pattern may mix the heat flux feedback driven by the SST and the heat flux associated with the large-scale atmospheric response (its heat flux imprint), as discussed in Gastineau and Frankignoul (2012). However, this contribution should be weak, since the atmospheric response may not have reached full amplitude at lag 1, as illustrated in Fig. 4.6. To estimate the heat flux imprint, we compute the time evolution of the SLP response pattern obtained by GEFA at lag 1 (similarly based on the whole cold period) by projecting it onto the concomitant SLP anomalies (in phase). This provides the time evolution of the SLP response pattern, independently from the oceanic forcing, thus including the natural SLP variability. Regressing the turbulent heat flux anomalies onto this time series provides the heat flux imprint of the atmospheric response, which can be subtracted from the GEFA estimate, yielding our best estimate of the heat flux feedback onto the OE SST footprint, which we call "residual".

The GEFA estimate, the contribution from the atmospheric response and the residual are given for the OE in the top row panels of Fig. 4.18. Interestingly, although the local SST footprint of the OE is affected by the addition of other forcings into GEFA, the heat flux is much less sensitive to the number of regressor variables, including ENSO and the PDO, so that locally over the OE, the heat flux feedback is broadly similar in univariate and multivariate regression (not shown). The GEFA heat flux estimate (left column) shows a broad positive anomaly (positive heat flux is upward) over the OE and northward. The maximum amplitude is at about the same location than the maximum OE SST footprint shown in Fig. 4.16, but the pattern is much broader. However, the heat flux imprint of the atmospheric response (middle column) shows

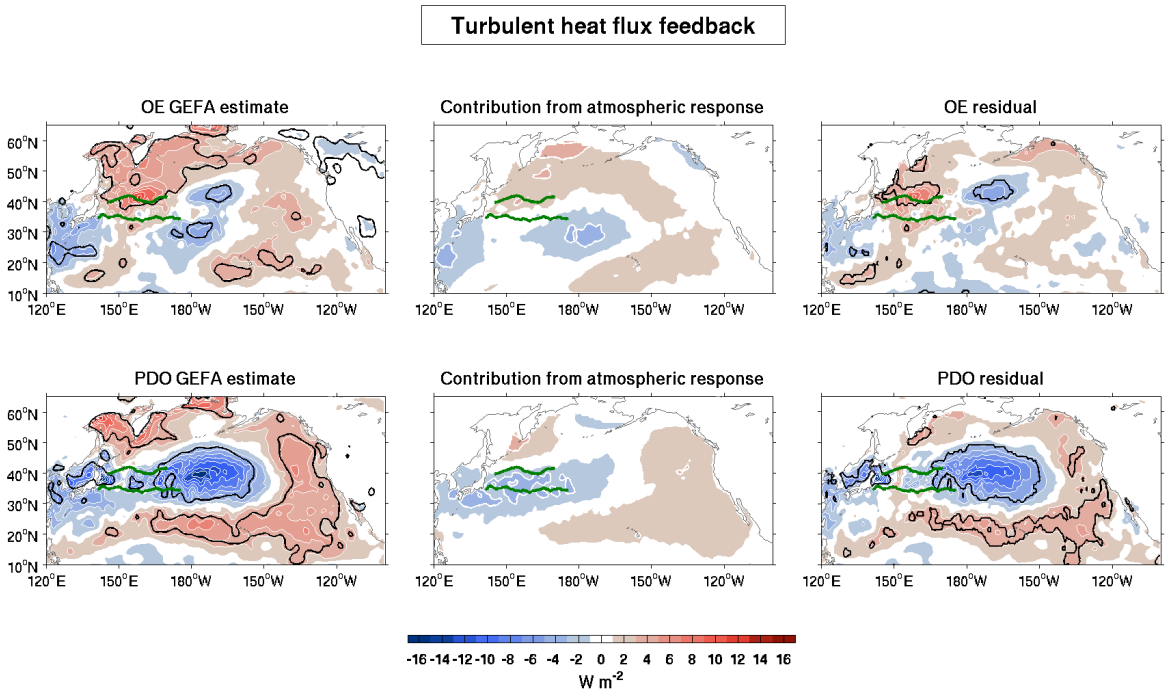

FIGURE 4.18 – Turbulent heat flux feedback in SONDJFM to the OE (upper row) and the PDO (bottom row), with the GEFA estimate (left column), the contribution from the atmospheric response (middle column, see text), and the residual (right column). Red (blue) shading is for positive (negative) anomaly (positive means upward), and contour intervals are 2 Wm^{-2}. Green thick lines denote the mean KE and OE paths, and black contours indicate 10% significance.

that the broad positive anomaly over the western subarctic Pacific Ocean, north of the OE, is largely associated with the atmospheric response to the OE, which increases the westerlies and brings colder air from Asia, thus increasing the oceanic heat loss. Once this contribution is removed from the GEFA estimate, the heat flux anomaly is largely limited to the local OE SST footprint, clearly showing a heat flux feedback of about 14 Wm^{-2} K^{-1}consistent with the heat flux feedback found in this region by Frankignoul and Kestenare (2002) and Park et al. (2005). A negative anomaly remains downstream of the OE mean path, where the PDO SST anomaly is maximum, possibly reflecting in part the difficulty for GEFA to distinguish between the heat flux feedback associated with the OE with that of the PDO. Indeed, if PDO-KOE is used instead of the standard PDO, this signal is still present, but less significant (not shown).

Impact on synoptic activity

To investigate how the meridional shifts of the OE affect cyclogenesis, we estimate the Eady growth rate (EGR) response at 850 hPa, which is both driven by the OE SST footprint and associated with the large-scale atmospheric response, as for the heat flux. The former should be more local, reaching maximum amplitude in 2 or 3 weeks, at least for the OE (Smirnov et al. 2015), thus before the storm track and the large-scale response had time to fully develop by eddy-mean flow interactions (Ferreira and Frankignoul 2005 ; Deser et al. 2007). Hence, the EGR

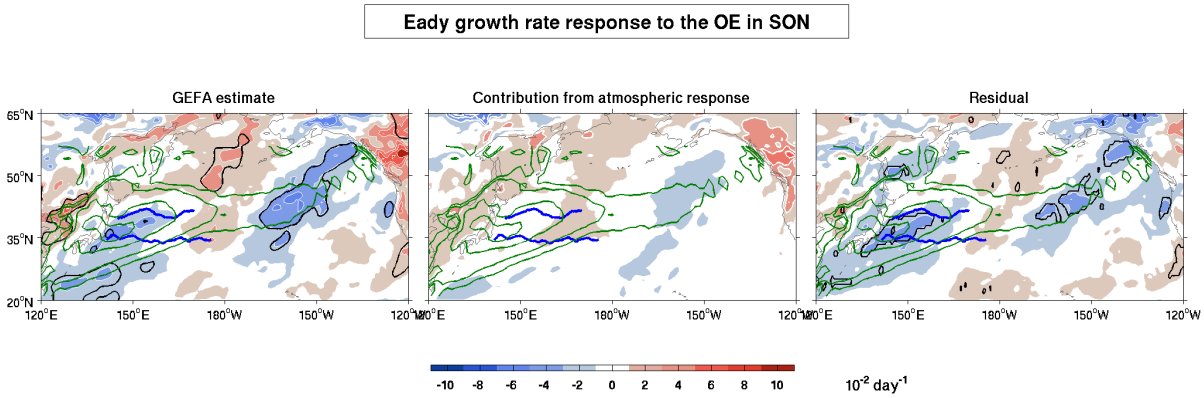

FIGURE 4.19 – SON response of the Eady growth rate at 850 hPa (CI = 2.10^{-2} day^{-1}) to the OE. Its shows the GEFA estimation is (left panel), the contribution from the atmospheric response (middle panel), and the residual (right panel). Red (blue) shading is for positive (negative) anomaly, dark blue lines denote the mean KE and OE paths, and black contours indicate 10% significance. Green contours denote the SON climatology, with contours at 50, 70 and 85.10^{-2} day^{-1}.

response is estimated as the heat flux feedback with monthly anomalies, using GEFA with a lag of 1 month (but separately for each season). Note that, like the surface heat flux, the synoptic variables are little sensitive to the addition of regressors into GEFA, probably because it is less effective at distinguishing between each forcing in more noisy variables.

Fig. 4.19 show the EGR response to the OE in SON (left panel), the contribution from the atmospheric response (middle panel) and the residual after the removal of this signal (right panel), together with the mean climatology of the EGR in SON (green curves). Although the EGR associated with the large-scale response to a northward shift of the OE front is small at lag 1 (Fig. 4.19, middle), it leads to a somewhat more localized EGR residual that better reflects the reduced baroclinicity caused by the weakening of the SST gradient south of the OE mean path (Fig. 4.20). Although the increased SST gradient north of the mean OE path and downstream of the KE has very little imprint, the local EGR response leads to a weakening and slight northward shift of the baroclinicity around its climatological maximum.

Unlike for the heat flux and the EGR, removing the eddy heat flux and storm track signal associated to the atmospheric response is irrelevant, as the eddy activity is intimately linked to the atmospheric response. Hence, the transient eddy activity is estimated by GEFA using seasonal means, as for SLP and Z250. Fig. 4.21 shows the result for v'T' and the storm track. The results are noisy and the statistical significance is limited. Nonetheless, the meridional eddy heat flux and the storm track activity seem slightly reduced in the KOE region where the EGR was reduced. There are also hints of a slight northward shift of the eddy activity, and a downstream increase of the storm track in the eastern part of the basin. Very similar results are found with PDO-KOE (not shown). Although these estimates are noisy, they are boradly consistent with the zonal wind response pattern of Fig. 4.17, which indicates a poleward shift of the jet. This is in broad agreement with Rivière (2009), who showed that positive eddy feedbacks

amplify latitudinal variations of baroclinicity downstream of the source region, and that a more poleward baroclinicity leads to a poleward shift of the eddy driven jet.

4.4.3 Response to the KE variability

The response to the variability of the KE shows a primarily equivalent barotropic tripolar structure, with positive anomalies over the sea of Okhotsk and western Canada, and a negative anomaly in the Pacific side of the polar vortex (Fig. 4.13 and 4.14). This pattern is very similar to the response found for ONDJ in the previous analysis by partial regression (chapter 3), suggesting that the results are robust, and do not reflect concomitant correlation with the other oceanic forcings considered in the present study. However, the positive anomaly over the Sea of Okhotsk is narrower and less extended eastward over the KOE region than in the previous analysis, which turns out to be due to the addition of the SIC regressor. A detailed discussion of the ONDJ response to the KE and its main dynamics has been given is the previous chapter, so it is not repeated here.

4.4.4 Response to the extratropical PDO

To assess the robustness of our estimateion of the influence of the extratropical part of the PDO in OND, the impact of adding an increasing number of oceanic regressors in GEFA is shown in Fig. 4.22. As discussed earlier, when the PDO in the only forcing, a clear signature of El Niño is associated with the PDO SST signature (Fig. 4.11), because the PDO is in part driven by ENSO (e.g., Schneider and Cornwell 2005 ; Newmann et al. 2016) and is thus well correlated with EN1 ($r = -0.55$ in ASO). The estimated atmospheric response thus mixes the response to the tropical and the extratropical forcing (not shown). The addition of the NPGO as forcing has no impact, since the PDO and NPGO are uncorrelated in ASO. However, as for the OE, adding the 3 R-EOFs of the tropical Indo-Pacific strongly impacts the estimation of the SST signature and the atmospheric response to the PDO, since the tropical and extratropical

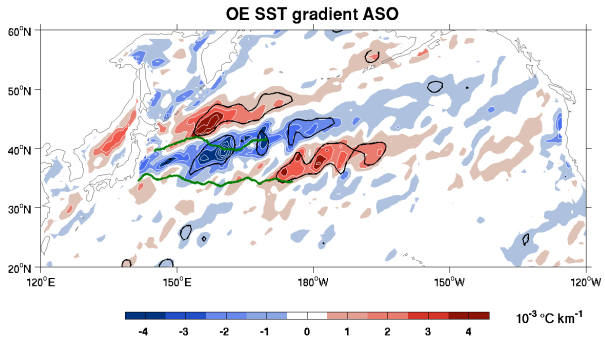

FIGURE 4.20 – OE SST gradient in ASO estimated by GEFA with the twelve regressors, corresponding to the SST pattern of the fourth panel in Fig. 4.16. Red (blue) shading is for positive (negative) anomaly, and black contours indicate 10% significance. Green lines denote the mean KE and OE paths.

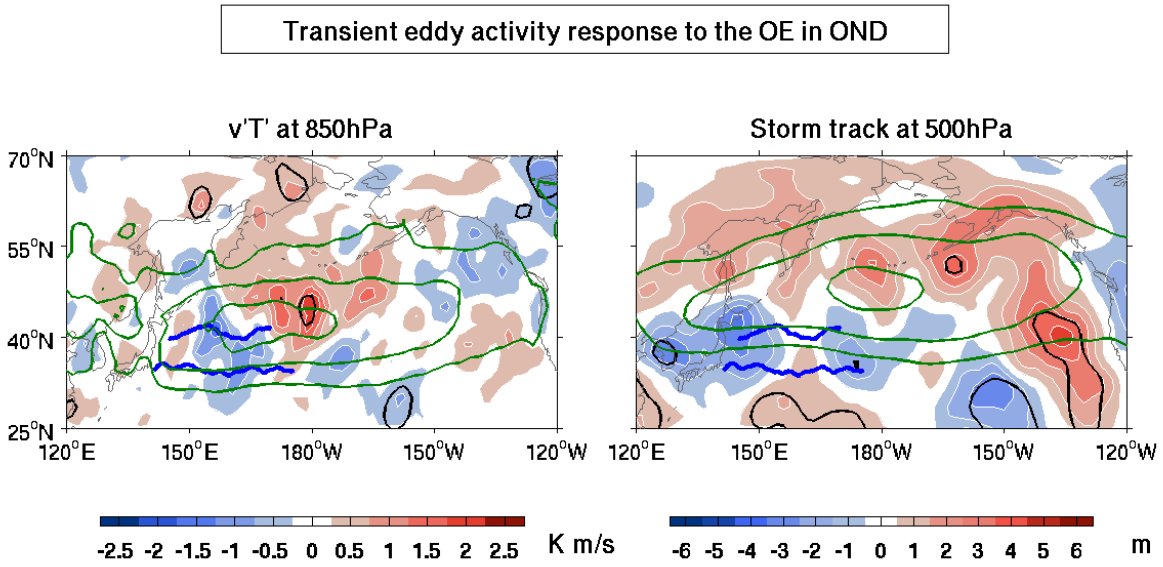

Figure 4.21 – OND response of (left) the meridional transient eddy heat flux at 850 hPa (CI = 0.5 Kms^{-1}) and (right) the storm track at 500 hPa (CI = 1 m) to the OE. Red (blue) shading is for positive (negative) anomaly, dark blue lines denote the mean KE and OE paths, and black contours indicate 10% significance. Green contours denote the OND mean climatology, with contours at (left) 6, 8, 10 and 12 Kms^{-1}, and (right) 40, 50 and 60 m.

SST signature of the PDO are now separated, with negligible SST anomalies south of 10°N (Fig. 4.22, upper panels). The SST signature shows the typical horseshoe pattern of the PDO, with a cooling in the KOE region and a warming eastward, southward and northward. This SST footprint generates a weakening of the SST gradient in the subpolar front, near 45°N, and a strengthening of the SST gradient to the south of it, resulting in a large-scale southward shift of the subpolar SST front, mostly in the central and eastern North Pacific (Fig. 4.23). In the North Pacific sector, the atmospheric response shows a broad low over the Bering Sea, albeit not significant at 250 hPa, and a weak high to the south of it, coarsely resembling the NPO. There are also wave-like barotropic signals over North America and Western Europe. Adding the Indian and Atlantic forcing and SIC has little impact, but adding the KE and OE reduces the SST cooling east of Japan while increasing the northeastern Pacific warming (Fig. 4.22, fourth row panels). The estimated atmospheric response varies little, however, except for a progressive strengthening of the low over the Bering Sea.

Although considering PDO-KOE instead of the standard PDO seems less appropriate for estimating the PDO impacts than for isolating the influence of the OE meridional shifts, it provides useful hints on the geographical origin of the PDO influence. Indeed, the cooling largely disappears over the KOE region and is only significant near the dateline, while the warming along the US west coast is stronger and more extended, as in Fig. 4.5. However, the tropical and extratropical SST footprints are not as well separated, since there is a small warming in the western equatorial Pacific. The SST gradient is still weakened along the subpolar SST front, but its strengthening at 35°N has disappeared (not shown). The estimated atmospheric response

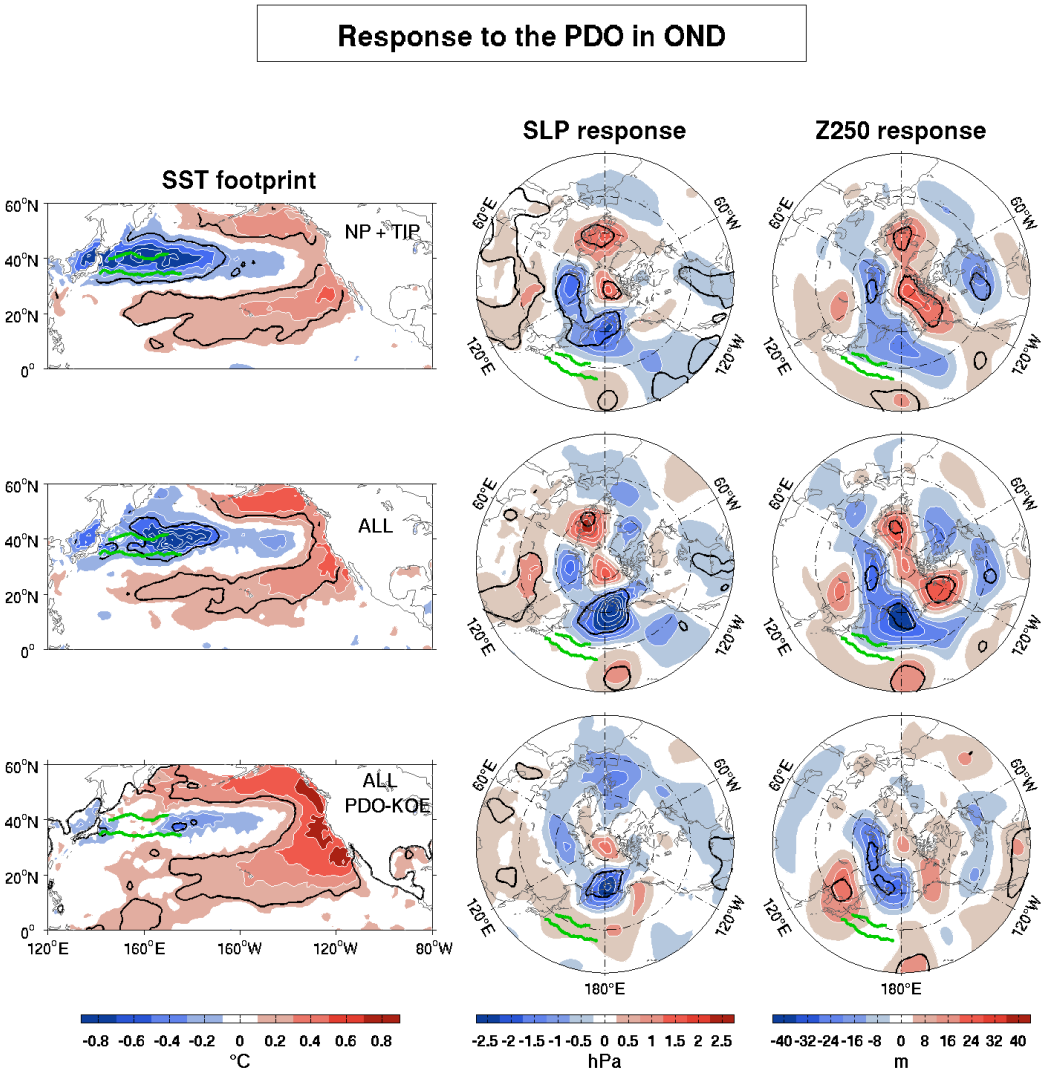

FIGURE 4.22 – (left column) SST signature of the PDO in ASO (CI = 0.2˚K) and the OND response of (middle column) SLP (CI = 0.5 hPa) and (right column) Z250 (CI = 10 m), north of 20˚N. The signature and response are assessed with (first row) the first two EOFs of NP and the first three R-EOFs of TIP, (second row) all the regressors except the KE and OE indices, (third row) all the regressors, and (fourth row) all the regressors but with the PDO-KOE. Red (blue) shading is for positive (negative) anomaly, and black contours indicate 10% significance. Latitude circles are shown every 20˚.

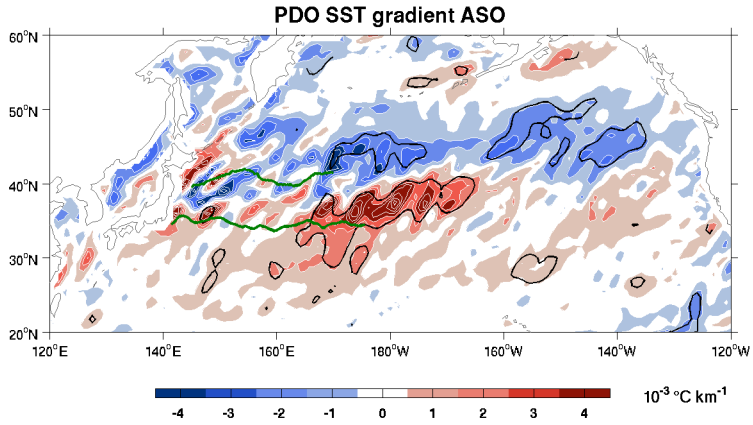

Figure 4.23 – PDO SST gradient in ASO estimated by GEFA with the twelve regressors, corresponding to the SST pattern of the third panel in Fig. 4.22. Red (blue) shading is for positive (negative) anomaly, and black contours indicate 10% significance. Green lines denote the mean KE and OE paths.

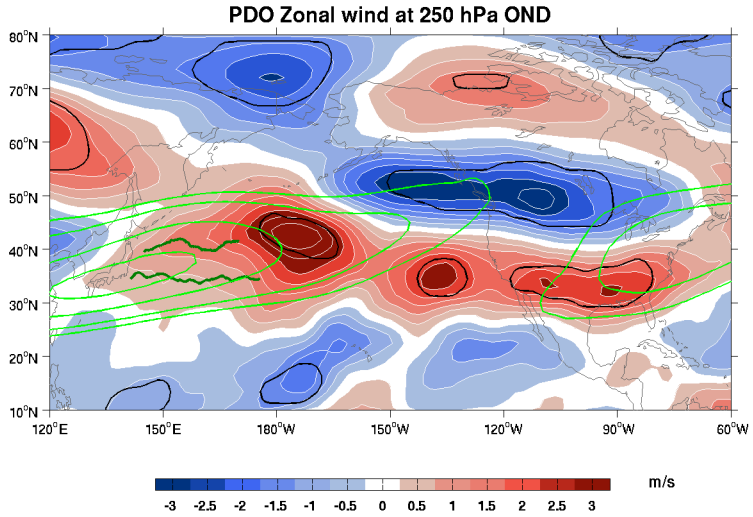

Figure 4.24 – Zonal wind response at 250 hPa to the PDO in OND, estimated by GEFA. Red (blue) shading is for positive (negative) anomaly, and contour intervals are 0.5 ms^{-1}. Green thick lines denote the mean KE and OE paths, and black contours indicate 10% significance. Green contours denote the OND zonal wind climatology, with contours at 25, 30, 40, 50 and 60 ms^{-1}

is a little weaker and more confined to the North Pacific sector, although the upper level high over the Sea of Japan is reinforced, so that the Z250 response is reduced to a north-south dipole over eastern Asia. Nonetheless, this pattern is overall not very different from the one with the standard PDO, suggesting that a significant part of the PDO influence arises from the warming in the northern and eastern Pacific and the resulting weaker subpolar SST front, and not from the KOE region, as was suggested by Gan and Wu (2013).

Overall, the atmospheric response to the PDO in OND (third row panels in Fig. 4.22) coar-

sely resembles the NPO in its positive phase, with a strong low over the Bering Sea reaching 4 hPa at sea level and 40 m at 250 hPa, and a smaller positive anomaly in the subtropical central North Pacific of 1 hPa at sea level and 8 m at 250 hPa. This indicates a strengthening and a northwestward shift of the Aleutian Low. Comparing the atmospheric responses to the PDO and the OE in Fig. 4.13 and 4.14 shows that they are not very different, but all the centers of action are slightly shifted. While the OE response resembles the WP teleconnection pattern, the PDO teleconnection slightly differs. Their zonal wind response at 250 hPa is a good illustration of the differences between their impacts, as they show a strong contrast. The PDO response leads to a strengthening of the upper-tropospheric jet in the North Pacific, and a southward shift of the jet over United States (Fig. 4.24), which is clearly different from the northward shift of the jet shown in Fig. 4.17 for the OE.

Heat flux feedback

Unlike in the OE case, the heat flux feedback to the PDO estimated by univariate and multivariate regression are quite different, as the inclusion of EN1 is necessary to separate the heat flux feedback driven by the extratropical part of the PDO from the persistent forcing of the PDO by ENSO. As it has been discussed by Lau and Nath (1996) and many others, it is not illustrated here. The heat flux associated with the extratropical PDO is shown in Fig. 4.18 (middle left panel). It shows a positive heat flux over the US west coast and the eastern subtropical Pacific, and a negative heat flux over the central basin, downstream of the KOE region, indicating a negative heat flux feedback, but little signal over the Gulf of Alaska. The upward heat flux in the subpolar region is linked to the atmospheric response and mostly disappears when looking at the residual (Fig. 4.18, middle right panel). The positive heat flux along the US west coast also appears to be largely linked to the atmospheric response and mostly disappears, while the negative heat flux feedback in the subtropical and central regions are unaffected. The amplitude is about 10 to 16 Wm^{-2} K^{-1}, which is of the same order of magnitude than the large-scale estimations of Frankignoul and Kestenare (2002) and Park et al. (2005).

Impact on synoptic activity

As for the OE, Fig. 4.25 shows the GEFA estimation of the PDO impact on the EGR (left panels), the contribution from the atmospheric forcing (middle panels), and the residual (right panels), together with the mean SON climatology of the EGR (green curves). As for the OE, the contribution from the atmospheric response is small during this season. The EGR response is basin-wide, with a negative anomaly over the KOE region and in the eastern part of the basin north of 35°N, and a positive anomaly in the subtropics. This pattern indicates a weakening of the maximum baroclinicity, and an enhancement of the subtropical baroclinicity. This is broadly in agreement with the SST gradient of Fig. 4.23, but the SST gradient anomaly is more concentrated over the central and eastern North Pacific, with no signal in the western KOE region. The same EGR pattern is found with the PDO-KOE, where the KOE cooling is substantially reduced, so how the weakening of the baroclinicity in the western KOE region arises remains unclear. On the other hand, the weakening of the baroclinicity, which also occurs

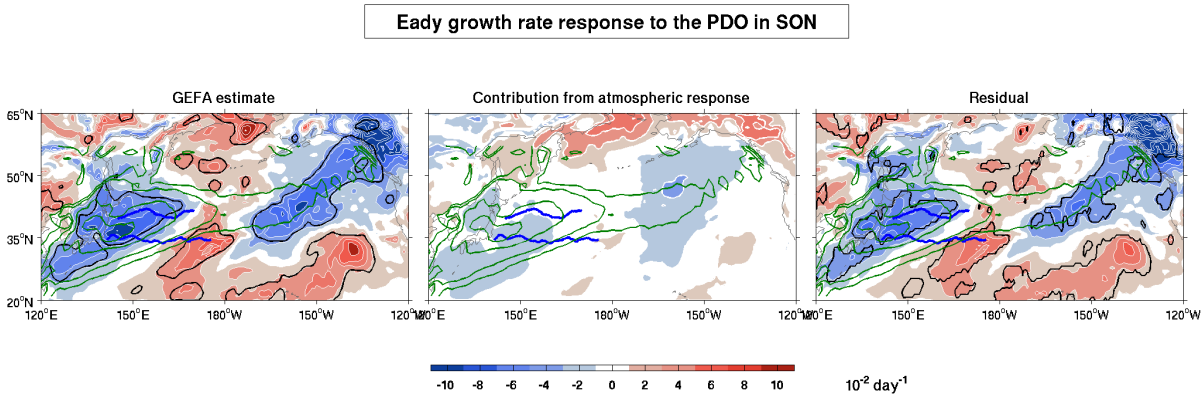

Figure 4.25 – SON response of the Eady growth rate at 850 hPa (CI = 2.10^{-2} day^{-1}) to the PDO. Red (blue) shading is for positive (negative) anomaly, dark blue lines denote the mean KE and OE paths, and black contours indicate 10% significance. Green contours denote the SON climatology, with contours at 50, 70 and 85.10^{-2} day^{-1}.

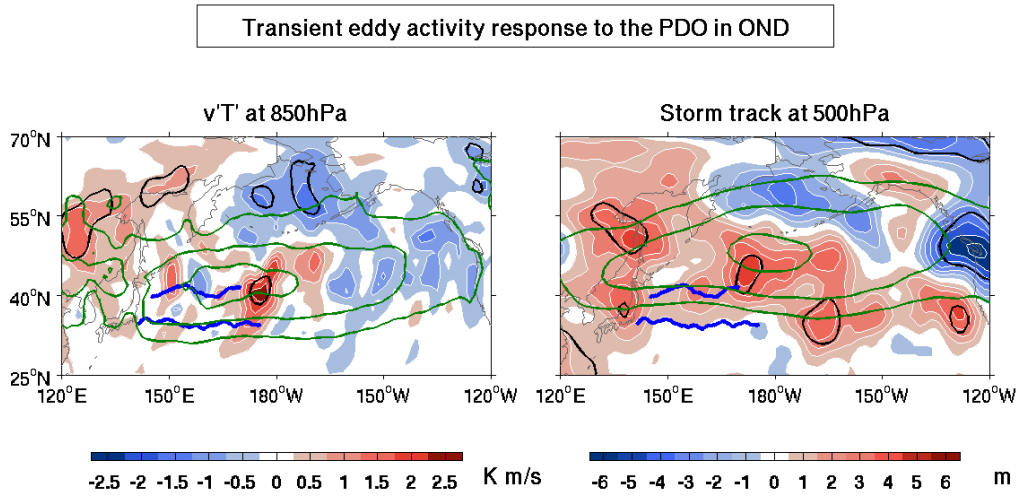

Figure 4.26 – OND response of (left) the meridional transient eddy heat flux at 850 hPa (CI = 0.5 Kms^{-1}) and (right) the storm track at 500 hPa (CI = 1 m) to the PDO. Red (blue) shading is for positive (negative) anomaly, dark blue lines denote the mean KE and OE paths, and black contours indicate 10% significance. Green contours denote the OND mean climatology, with contours at (left) 6, 8, 10 and 12 Kms^{-1}, and (right) 40, 50 and 60 m.

with PDO-KOE, is probably due to the weaker SST gradient in the subpolar front.

Fig. 4.26 shows the results for v'T' (left panel) and the storm track (right panel), together with the OND climatology of each variable (green curves). The meridional eddy heat flux pattern shows a strengthening downstream of the KOE region, and a weakening in the Bering Sea. The storm track signal indicates a strengthening of the storm activity downstream of the KOE region, and a reduced activity over the US west coast, indicating a strenghtening of the storm trak in the central North Pacific, and a southward shift of the storm track in the northeastern Pacific, in agreement with the zonal wind response (Fig. 4.24). According to Rivière (2009), a

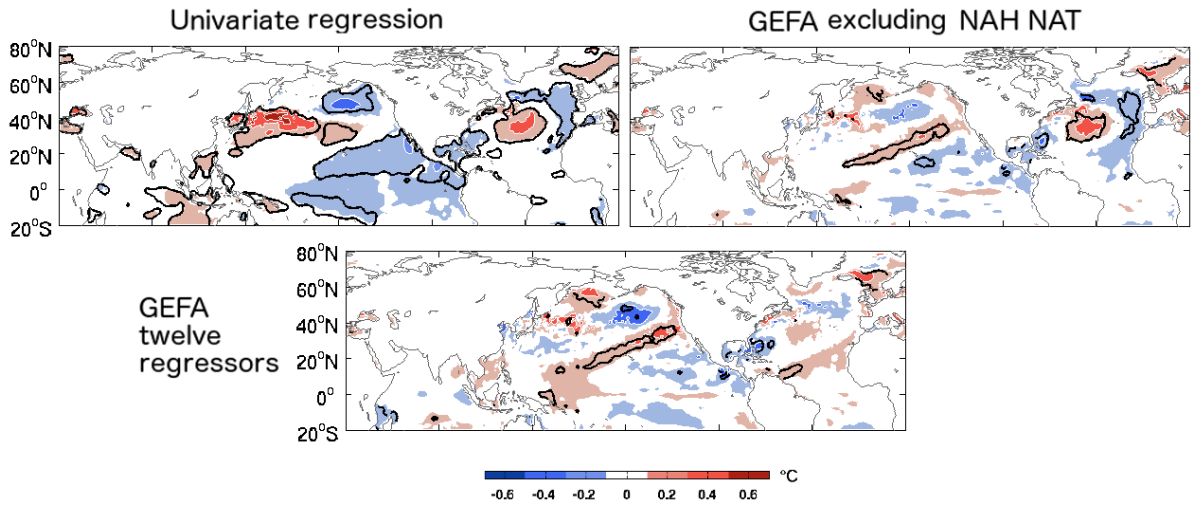

FIGURE 4.27 – SST signature of the OE in OND estimated by (upper left panel) univariate regression, (upper right panel) GEFA excluding NAH and NAT and (bottom panel) GEFA with all the regressors.

more equatorward baroclinicity favors cyclonic wave breaking event and pushes the eddy driven jet more equatorward, so the impact of the PDO could be understand as an equatorward shift of the eddy activity. However, the EGR, v'T' and storm track patterns do not match perfectly well, and if the baroclinicity is reduced in the western KOE region, it is not clear why the eddy activity is enhanced downstream. In summary, the mechanisms by which the PDO lead to an NPO-like signal over the North Pacific in OND remain to be clarified.

4.5 Atmospheric response in winter (DJF and FMA)

As recalled in the introduction, observational and modeling studies have shown that the North Pacific SST has a different impact on the atmospheric circulation in autumn-early winter and in late winter. We find indeed quite different atmospheric responses in DJF and FMA. As in the previous section, first the atmospheric response to all the forcings will be briefly described, and second the atmospheric response to the OE, the KE and the PDO will be discussed in more details.

4.5.1 The full GEFA results

As mentioned in section 4.3.2, there is too much collinearity in DJF, so it is necessary to reduce the number of regressors in this season. Since our focus is on the North Pacific forcings, we first considered the suppression of the North Atlantic forcing (NAH and NAT), since it substantially lowers the collinearity. However, GEFA was not effective at isolating the OE SST footprint. Figure 4.27 shows the OND SST anomalies associated to the OE in the case of (upper left panel) univariate regression, (upper right panel) GEFA excluding NAH and NAT and (bot-

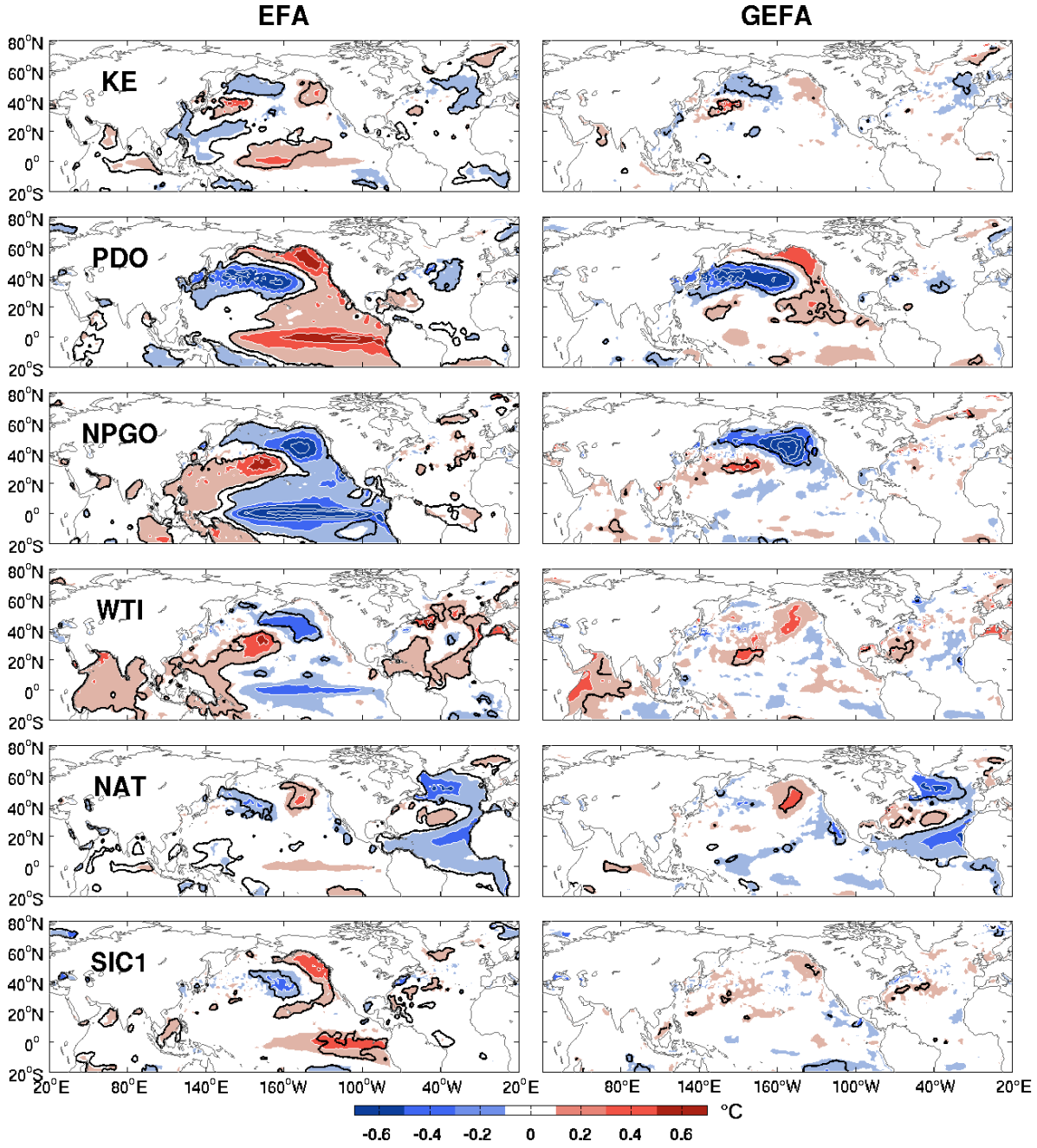

Figure 4.28 – SST signature in OND of each forcing as indicated in the upper left corner, in the case of univariate regression (left colmun) and multivariate regression (right column) with 11 regressors (excluding the OE). Red (blue) shading is for positive (negative) anomaly, and contour intervals are 0.2 ˚K.

tom panel) GEFA with all the regressors. Note that the calculation of the SST footprints does not suffer from multicollinearity, since it involves lag 0 ($d = 0$ and $\tau = 0$), so that the covariance matrix $C_{YY}(0)$ is symmetric and well conditioned (not shown). The large-scale SST anomalies associated with the OE in the univariate case reflect the high correlation between the OE and the PDO, the NPGO, IIM, NAH and NAT. When GEFA is applied with NAH and NAT excluded

(upper right panel), the OE shows negligible local SST footprint, while there are strong remote signals in the subtropical North Pacific and in the North Atlantic. This shows that the North Atlantic regressors should be retained to distinguish between the OE and the North Atlantic impact. However, adding the NAH and NAT into GEFA removes most of the North Atlantic SST anomalies, but the remote anomalies in the North Pacific are reinforced, and the local SST footprint of the OE is still negligible (bottom panel). Therefore, GEFA does not properly represent the OE forcing in this season. We thus renounce estimating the DJF response to the OE, and omit the OE regressor in GEFA, which substantially lowers the collinearity (section 4.3.2).

Fig. 4.28 shows the OND SST signature of the regressors indicated at the upper left corner. For brevity, the other regressors are not shown as they have a very similar SST signature as in ASO (Fig. 4.11 and 4.12). As before, GEFA is quite effective at isolating the different SST footprints, as they become properly confined to their region of definition. However, some remote anomalies remain : for instance, WTI and NAT are still associated with some SST signal in the Pacific. The KE also shows a non-local SST signature, as in ASO, and is associated with weak anomalies in the northern North Atlantic. Finally, the SIC is not associated with any strong SST signal.

The (extratropical) GEFA responses in DJF to all the forcings are shown in Fig. 4.29 for Z250 and Fig. 4.30 for SLP. The Z250 response to EN1 shows the typical ENSO teleconnection pattern, with a broad high in the tropical Pacific, a strengthening of the Aleutian Low and a wave-like pattern propagating towards the US, somewhat resembling the Pacific North American (PNA) pattern (e.g. Nigam 2003 ; Liu and Alexander, 2007). The SLP response shows the Southern Oscillation, which is associated with ENSO, whose northern edge only is visible in Fig. 4.30, and the strengthening of the Aleutian Low, with a maximum anomaly centered over the Gulf of Alaska. In late winter FMA, (Fig. 4.31, 4.32), the response to EN1 is similar over the North Pacific but more elongated, the wave-like pattern over the US has extended over the Arctic and the teleconnection now reaches southern Europe, in agreement with observational (e.g. Pozo-Vasquez et al. 2005) and numerical (e.g. Ineson and Scaife 2009) studies, which found that ENSO can extend its influence to the North Atlantic-European sector in late winter. The signal over the North Atlantic broadly resembles a positive NAO. Note that other studies (e.g. Moron and Gouirand 2003 ; Gouirand et al. 2007) found a negative NAO, because the ENSO influence on the North Atlantic shows a strong non-stationnarity over the last century, and distinct impacts are found before and after the 1970s, partially explained by multidecadal changes of the mean flow and alterations in ENSO amplitude and structure (Rodriguez-Fonseca et al. 2016).

In DJF, there is no significant response to EN2. In FMA, the response pattern shows a dipolar structure in the North Atlantic broadly resembling a negative NAO phase, in agreement with an ENSO impact on Europe in late winter. There is also a dipolar pattern in the northeastern Pacific. This response is similar to the pattern that Zhang et al. (2016) found by regression of the Z500 onto the Trans-Niño Index.

As in OND, the IIM shows a strong influence in DJF, especially over the North Atlantic, where it shows a strong barotropic negative AO/NAO pattern, reflecting a weakening of the

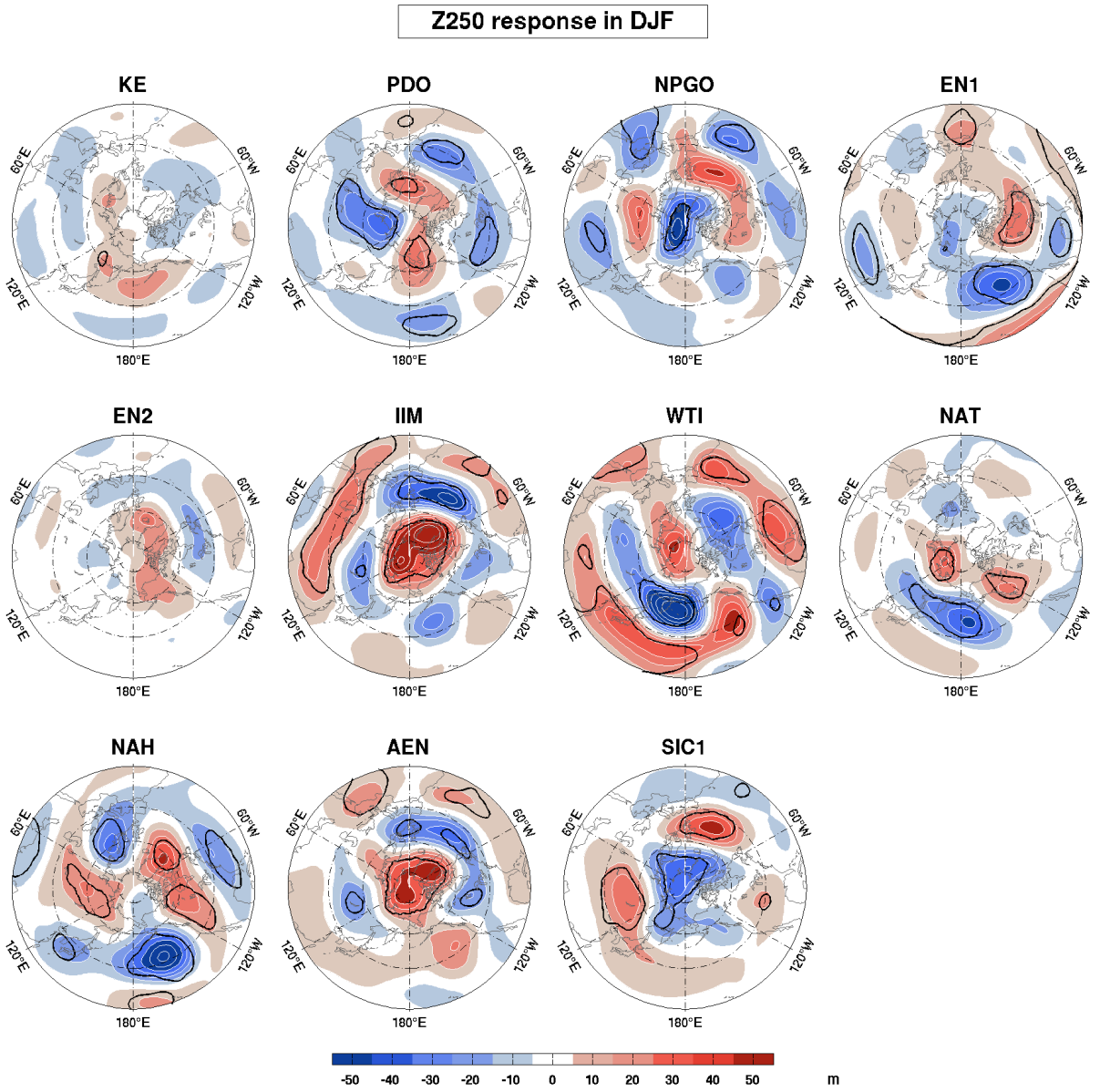

Figure 4.29 – Z250 response to the eleven predictors in DJF, north of 20˚N. Red (blue) shading is for positive (negative) anomaly, and contour intervals are 0.5 hPa. Thick black contours indicate 10% significance. Latitude circles are shown every 20˚.

polar vortex and a poleward shift of the eddy driven jet. In FMA, the same pattern is observed but with lower amplitude and slightly shifted west, and there are strong anomalies over the North Pacific, reflecting a southward shift of the jet in this region. The WTI also drives a strong extratropical barotropic response in DJF, especially over the North Pacific, where the pattern resembles the positive NPO, but with an elongated subtropical high anomaly. In FMA, the influence of WTI in the North Pacific is reduced to a subtropical high in the eastern Pacific, more significant in SLP, and there are hemispheric teleconnections in the upper troposphere.

The estimated response in DJF to the NPGO does not show any significant signal in the North Pacific, but exhibits a strong teleconnection over the North Atlantic and the North Pole.

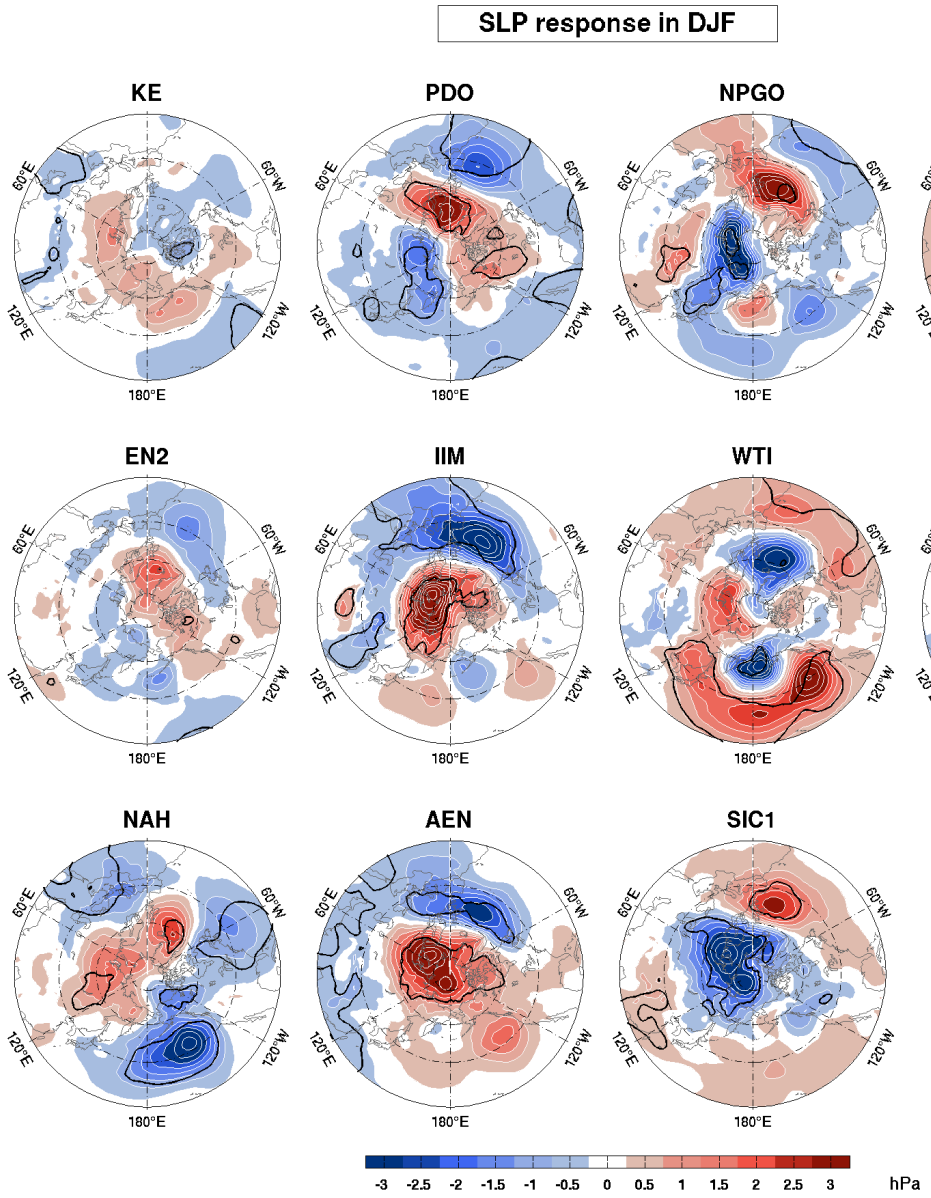

FIGURE 4.30 – As in Fig. 4.29, but for the SLP.

In FMA, there is a high over the Aleutian Islands and Alaska, mostly in SLP, and a broad SLP low over northern Eurasia, without corresponding signal in the upper troposphere. However, this signal only becomes statistically significant after the addition of SIC1 into GEFA, so the estimated response to the NPGO is not robust.

The influence of the Atlantic El Niño mode (AEN) in DJF is broadly similar to the response in OND, but stronger and more significant, and it strongly resembles the response to IIM, in both SLP and Z250. However, IIM and AEN are poorly correlated ($C_{12,4} = -0.1$, Fig. 4.9), so it does not reflect a flaw in the GEFA results. The main AEN impact is in the Atlantic sector, and it is related to a strengthening subtropical jet and a southward shift of the polar jet, in agreement with the simulations of Haarsma and Hazeleger (2007) discussed in the context of

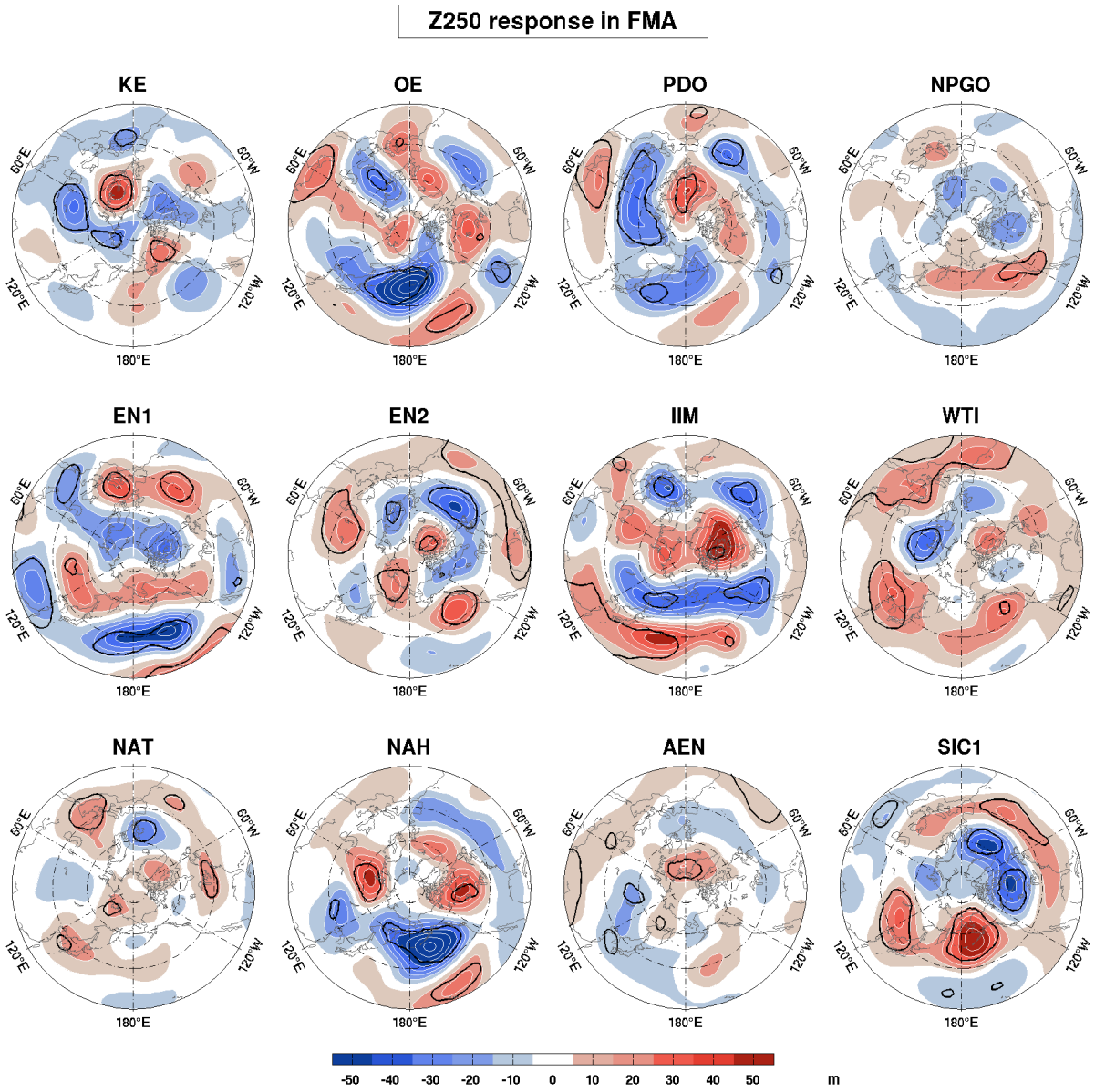

Figure 4.31 – As in Fig. 4.29, but for the FMA season.

the OND response. However, they found a maximum response in NDJ and FMA, while we find a maximum response in DJF.

As in OND, the response to NAT in DJF has a wave-like feature over the North Pacific. In FMA, the response is different and primarily consists of a weak barotropic low centered off the British Islands. On the other hand, the response to the NAH is similar in DJF and FMA. It shows a broad barotropic teleconnection over the North Pacific, indicating a strenghtened and shifted east Aleutian Low. Over the North Atlantic, the response is barely significant at sea level and not in the upper troposphere, but it is not very different from the negative NAO-like response found in OND, albeit shifted east. Czaja and Frankignoul (2002) similarly found no significant response to the NAH in the North Atlantic sector during late winter. Finally, in both

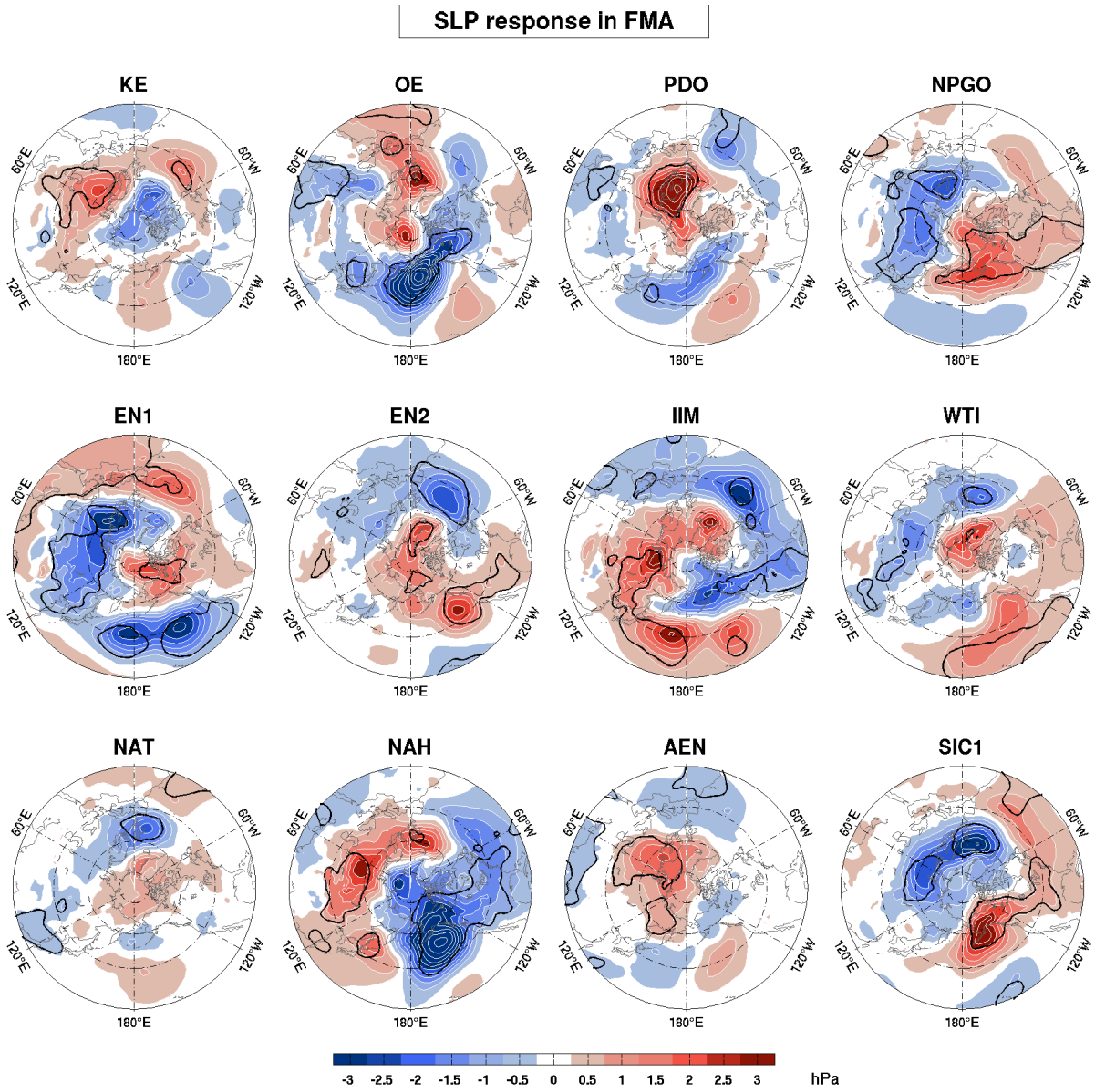

FIGURE 4.32 – As in Fig. 4.30, but for the FMA season.

DJF and FMA, the response to SIC1, whose pattern reflects increasing SIC in the Barents sea and decreasing SIC in the Chukchi sea, resembles the positive NAO, albeit shifted north, in agreement with Garcia-Serrano et al. (2015), plus a weakening of the Aleutian Low in FMA.

4.5.2 Late winter response to the OE variability

As in OND, the robustness of our estimates can be assessed by comparing the SST footprint of and the response to the OE meridional shifts as oceanic regressors are added (Fig. 4.33). As before, the SST signature of the OE is considered two months earlier, therefore in DJF. The local warming along the OE mean path is little affected by the presence of other regressors.

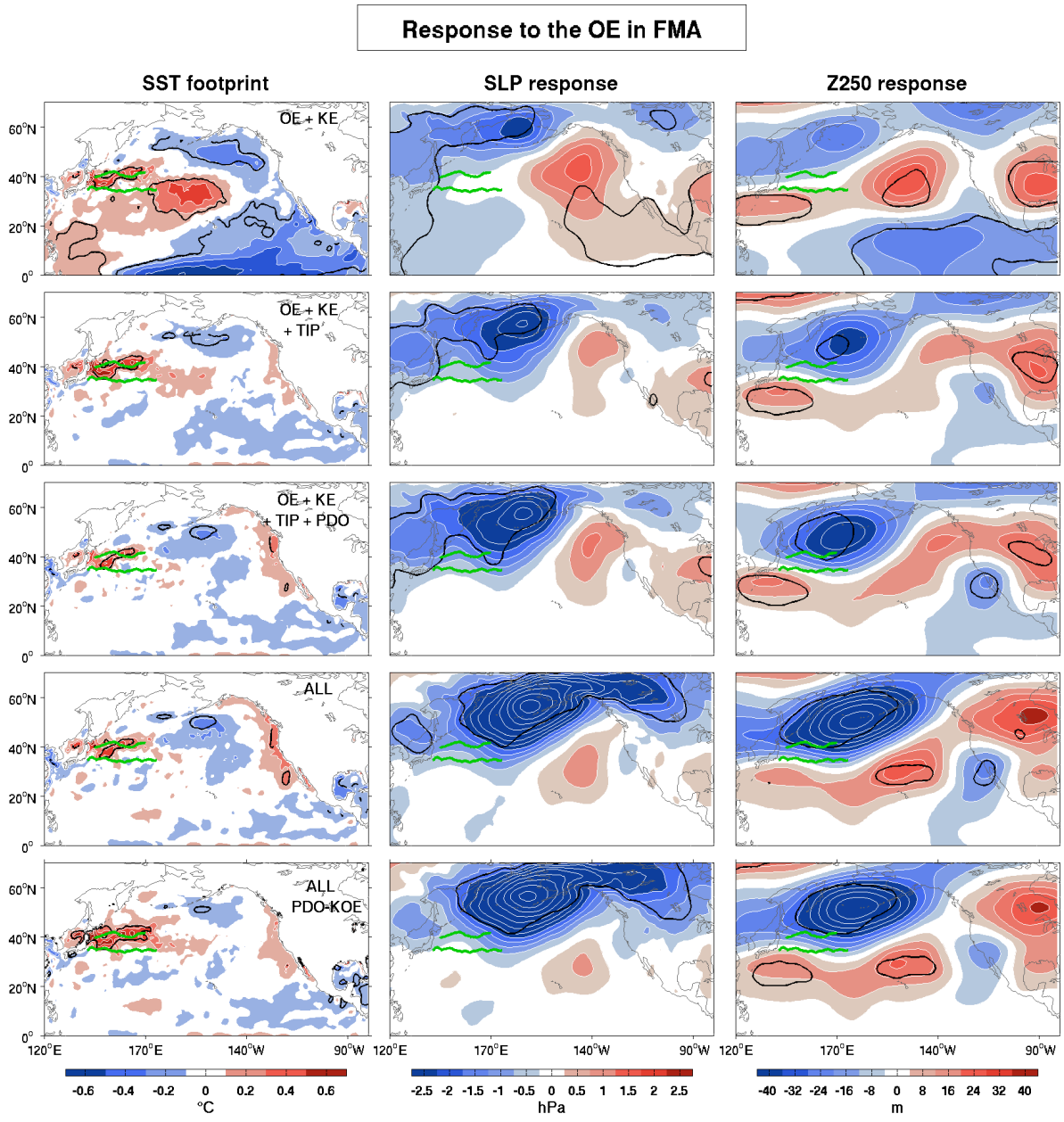

Figure 4.33 – (left column) SST signature of the OE in DJF (CI = 0.2°K) and the FMA response of (middle column) SLP (CI = 0.5 hPa) and (right column) Z250 (CI = 8 m) to the OE. The signature and response are assessed with (upper row) the OE index alone, (second row) the OE, KE and the first three R-EOFs of TIP, (third row) the OE, KE, the first three R-EOFs of TIP and the PDO, (fourth row) all the regressors, and (bottom row) all the regressors but with the PDO-KOE. Red (blue) shading is for positive (negative) anomaly, and black contours indicate 10% significance. Green lines denote the mean KE and OE paths.

However, there are large changes in the basin-wide SST pattern, which again strongly resembles a La Niña plus the PDO in its negative phase when only the OE and KE are considered in GEFA (upper panels). As the KE and OE are somewhat correlated ($r = 0.39$), adding the KE

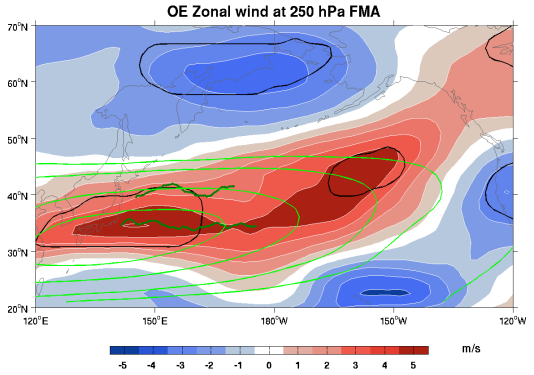

FIGURE 4.34 – Zonal wind response at 250 hPa to the OE in FMA, estimated by GEFA. Red (blue) shading is for positive (negative) anomaly, and contour intervals are 1 ms^{-1}. Dark green thick lines denote the mean KE and OE paths, and black contours indicate 10% significance. Light green contours denote the FMA zonal wind climatology, with contours at 25, 30, 40, 50 and 60 ms^{-1}

into the set of regressors has some impact, as it removes the SST warming south of the KE (not shown). Adding the tropical Indo-Pacific regressors has a strong effect, as most of the SST anomalies in the subtropics and in the northeastern Pacific disappear (Fig. 4.33, second row panels). Only the cooling south of Alaska remains. Adding the PDO and the other regressors primarily contributes to narrowing the SST anomaly along the OE, and enhancing the warming off the US west coast (third and fourth row panels). Interestingly, when the PDO-KOE is used instead of the standard PDO (bottom panels), these remote SST anomalies are much weaker and less significant, while the SST footprint of the OE shift becomes broader, as in OND.

The addition of regressors into GEFA progressively reinforces the atmospheric response found by GEFA once the KE and TIP are included, but does not strongly impact its pattern. Hence, this gives confidence in the estimation of the atmospheric response to the OE in FMA, which consists of a barotropic dipole, with a very strong and broad low over the Bering Sea, and a weaker elongated high in the subtropical North Pacific, albeit only significant in the upper troposphere. Note that using PDO-KOE does not alter the estimated response.

Overall, the atmospheric response to the OE in FMA is not very different from that in OND, somewhat resembling the NPO in positive phase, except for a much stronger low over the Bering Sea, reaching 6 hPa at sea level and 80 m at 250 hPa, and a much weaker and less significant subtropical high. Contrary to OND where the response indicated a clear poleward shift of the eddy driven jet, this structure is related to a slight poleward shift, but mostly a strengthening of the jet (Fig. 4.34).

Impact on synoptic activity

Fig. 4.35 shows the GEFA estimation of the OE impact on the Eady growth rate in JFM (left panel), the contribution from the atmospheric response (middle panel) and the residual (right panel), together with the JFM EGR climatology. Surprisingly, the GEFA estimates yields a strong positive anomaly over the central Pacific, in the subtropical gyre, downstream and

southward of the KE mean path, but no significant anomalies near the OE. The contribution from the atmospheric response is more substantial is this season, but with a small amplitude, so that once this signal is removed, the positive EGR anomaly in the subtropical gyre remains, albeit with weaker amplitude. There is thus no evidence of the northward shift in the meridional SST gradient driven by the OE, suggesting that the OE influence on the EGR was not well separated.

Fig. 4.36 shows the influence of the OE in FMA on v'T' (left panel) and the storm track (right panel). The transient eddy heat flux response shows a dipole pattern indicating a strengthened eddy heat flux downstream of the KOE region, and reduced eddy heat flux above Alaska. In broad accordance with the eddy heat flux, the storm track indicates a strengthening of the storm track activity in the eastern part of the basin and along the US west coast, albeit little significant, and a reduced storm activity over Alaska. While these response patterns are broadly consistent with a strengthened jet indicated in Fig. 4.34, they show no clear link with the changes in the SST or the SST gradient that are associated with the OE shift. Therefore, the impact of the OE in late winter remains unclear.

4.5.3 Response to the KE variability

The SST signature of the KE and its estimated influence on the atmosphere in DJF is not much affected by the addition of the other oceanic regressors, so we only show the case where the KE and the three TIP R-EOFs are included, and the case with all the regressors. (Fig. 4.37). The KE SST footprint in OND consists of a warming in the KOE confluence region, reaching 0.4˚K just south of the OE mean path near 160˚E, and a weak cooling in the western subarctic ocean that is not reduced when all the forcings are included. On the other hand, the warming along the US west coast looses significance when the NPGO and the SIC are included as regressors. This SST signature is very similar to the KE SST footprint in autumn/early winter (Fig. 4.11), except for a much smaller northeast Pacific warming. It is also similar to the SST signature

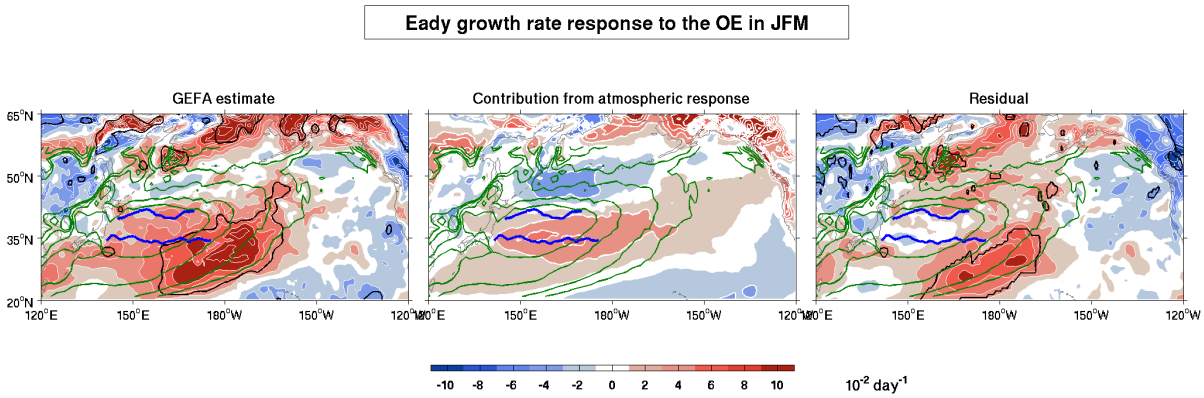

Figure 4.35 – JFM response of the Eady growth rate at 850 hPa (CI = 2.10^{-2} day^{-1}) to the OE. Red (blue) shading is for positive (negative) anomaly, dark blue lines denote the mean KE and OE paths, and black contours indicate 10% significance. Green contours denote the JFM climatology, with contours at 50, 70 and 85.10^{-2} day^{-1}.

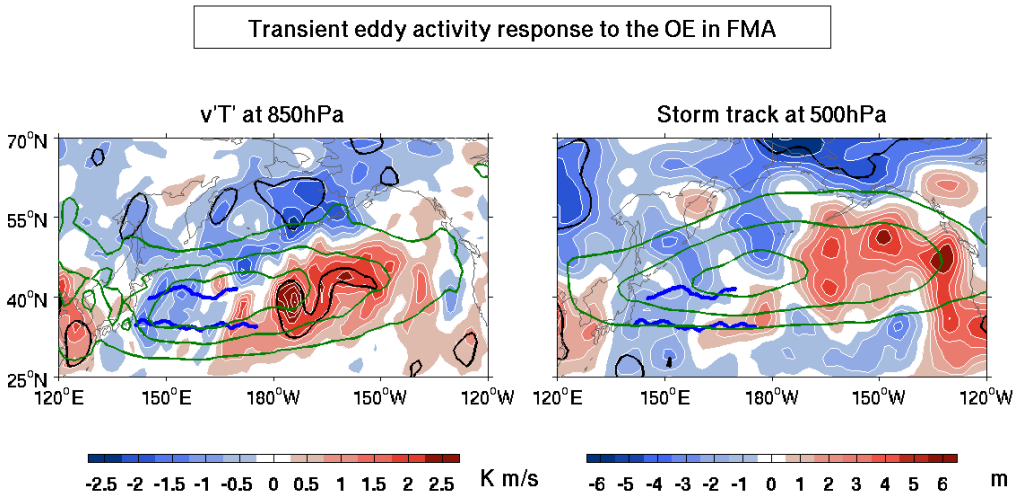

FIGURE 4.36 – FMA response of (left) the meridional transient eddy heat flux at 850 hPa (CI = 0.5 Kms^{-1}) and (right) the storm track at 500 hPa (CI = 1 m) to the OE. Red (blue) shading is for positive (negative) anomaly, dark blue lines denote the mean KE and OE paths, and black contours indicate 10% significance. Green contours denote the FMA mean climatology, with contours at (left) 6, 8, 10 and 12 Kms^{-1}, and (right) 40, 50 and 60 m.

found in SOND with the partial correlation method in Révelard et al. (2016) (chapter 3). As discussed in this chapter, the broad warming is in part driven by the intensified advection of warm water coming from the subtropics (Vivier et al. 2002 ; Kelly et al. 2010 ; Qiu et al. 2014), while the cooling in the subpolar gyre reflects the SST forced by the atmospheric fluctuations that affect the KE on short time scale and can be attributed to the intensification of the westerly winds coming from northeastern Siberia due to the high pressure anomaly that precede the KE (Révelard et al. 2016, Fig. 3).

Consistent with Révelard et al. (2016) and with the observational and modeling studies that have shown that the North Pacific Ocean feedback to the atmosphere is dominated by the early-winter response, and that the late winter one differs significantly (e.g. Peng and Whitaker 1999 ; Liu and Wu 2004 ; Liu et al. 2007 ; Frankignoul and Sennéchael 2007 ; Gan and Wu 2012 ; Taguchi et al. 2012), the estimated atmospheric response to the KE in DJF is weak and has little statistical significance, in fact none when only the KE and TIP are taken into account (Fig. 4.37, upper panels). However, the pattern is broady similar to the response found by partial regression in the previous chapter. When all the forcings are included, the signal is slightly reinforced and has an equivalent barotropic dipolar structure resembling the NPO in negative phase, but it is barely significant. Therefore, our analysis suggests that, in winter, the influence of the KE onto the atmospheric circulation is very small, or is masked by other much stronger teleconnections.

In FMA (Fig. 4.38), the warming of the KE associated with its stable path is clear seen when the KE, OE, and TIP regressors are considered, but it becomes weak and noisy once the PDO is included, while the cooling in the subarctic North Pacific disappears once the NPGO is taken into account. This may reflect that the KE strength is partly forced by the NPO (Ceballos et al. 2009), which also forces the NPGO, so that the KE variability is related to the strength of the

subtropical and subpolar gyres. Adding the other regressors, on the other hand, has negligible impact, although it leads to even noisier SST anomalies over the KE (lower panels).

Somewhat surprisingly, the estimated atmospheric response in the North Pacific sector is not sensitive to the progressive reduction of the KE SST footprint. The pattern primarily shows a dipolar structure in the northeastern Pacific, where only the upper tropospheric high is 10% significant. Hence, this analysis suggests that the KE variability has limited influence on the atmospheric circulation in late winter. When looking at the whole northern hemisphere (Fig. 4.32, 4.31), there are significant teleconnections over Eurasia, which are also insensitive to the number of regressors and show a barotropic high over Scandinavia, and a baroclinic structure over Russia. However, in view of the limited KE SST footprint and the weak North Pacific signal, it is difficult to attribute them to the KE variability.

4.5.4 Response to the PDO

Figure 4.39 shows the SST signature of the PDO in OND for an increasing number of oceanic regressors. Once the TIP is included in GEFA, the extratropical PDO SST signature depends very little on the number of regressors, largely resembling that in OND and leading to a weakening of the SST gradient near the subpolar front and a strengthening of the SST gradient in the KOE region and the subtropics, as illustrated in Fig. 4.40.

The estimated atmospheric response in DJF also varies little with the number of regressors once the TIP has been included, (Fig. 4.39). In the North Pacific sector, the latter tilts strongly

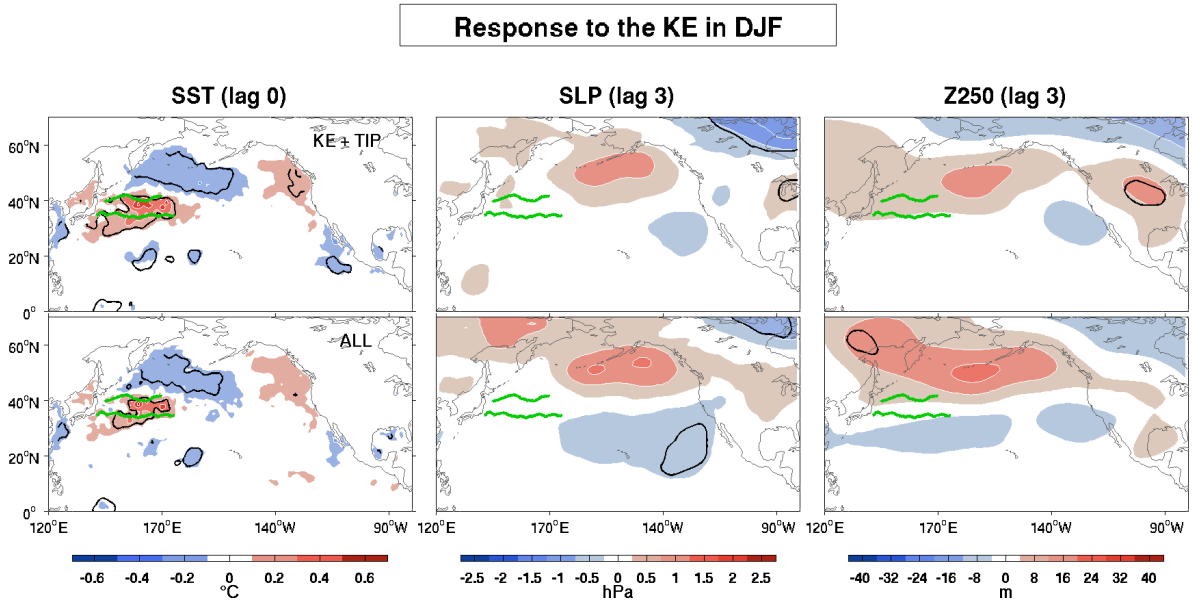

Figure 4.37 – (left column) SST signature of the KE in OND (CI = 0.2°K) and the DJF response of (middle column) SLP (CI = 0.5 hPa) and (right column) Z250 (CI = 8 m) to the OE. The signature and response are assessed with (upper row) the KE and the first three R-EOFs of TIP, (bottom row) all the regressors. Red (blue) shading is for positive (negative) anomaly, and black contours indicate 10% significance. Green lines denote the mean KE and OE paths.

westward with height, suggesting baroclinicity : the SLP high over western Canada is found at 250 hPa over the Bering Strait, the SLP low over the Sea of Okhotsk reinforces the Z250 low over Siberia, and the SLP low over the Hawaiian archipelago corresponds to the Z250 low in the subtropical North Pacific. This structure indicates a southward shift of the jet stream over the North Pacific (Fig. 4.41). There is also a barotropic low over northern Siberia and a strong barotropic teleconnection over the North Atlantic, resembling a negative phase of the NAO. Hence, the North Pacific signal differs from the deepening of the Aleutian Low found by Wen et al. (2010) and Liu et al. (2012), but the teleconnection to the NAO is similar.

The EGR anomaly indicates a southward shift of the zone of maximum baroclinicity in the northeastern Pacific (Fig. 4.42), in agreement with the SST gradient signature of the PDO that drives a southward shift of the subpolar front (Fig. 4.40). The meridional eddy heat flux (Fig. 4.43, left panel) shows a strengthening and a southward shift of the zone of maximum transient

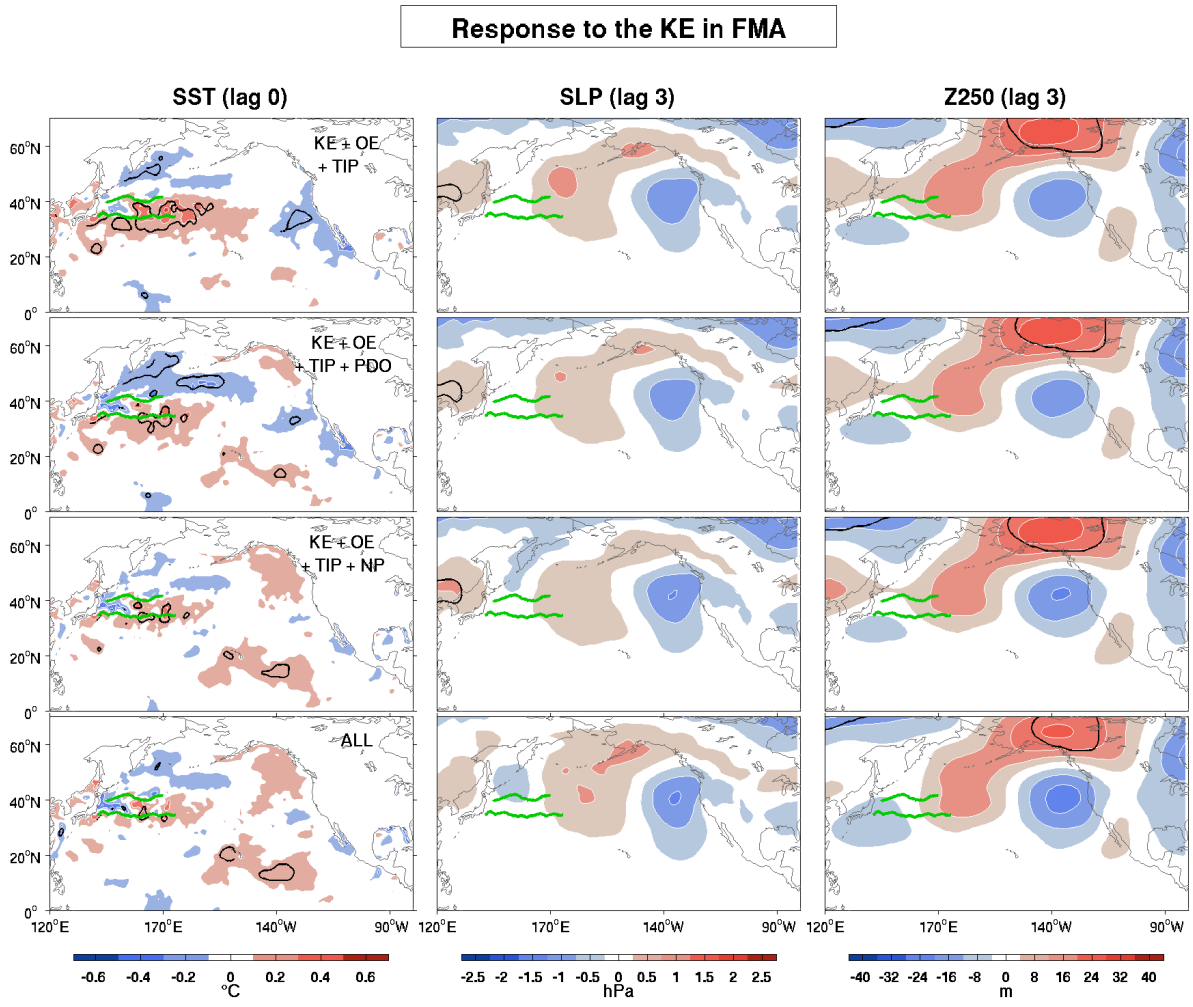

FIGURE 4.38 – As in Fig. 4.37, but for the KE SST signature DJF and the SLP and Z250 responses in FMA, estimated by GEFA with the regressors indicated at the upper right corner of the left panels.

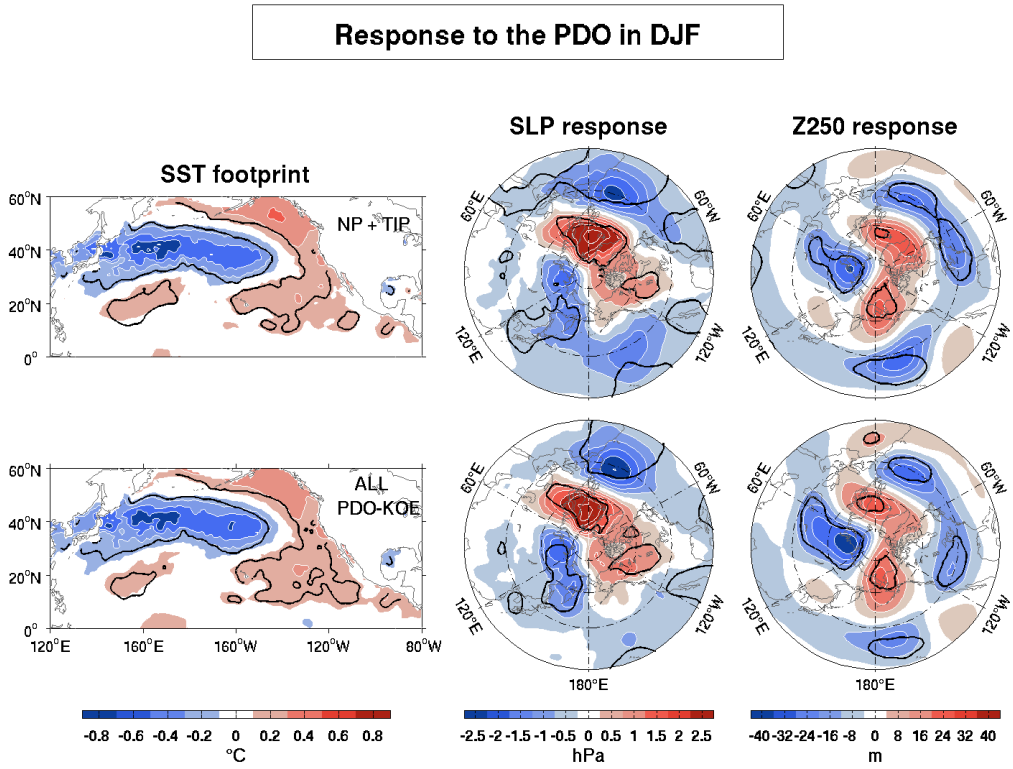

Figure 4.39 – (left column) SST signature of the PDO in OND (CI = 0.2˚K) and the DJF response of (middle column) SLP (CI = 0.5 hPa) and (right column) Z250 (CI = 10 m), north of 20˚N. The signature and response are assessed with (upper row) the first two EOFs of NP and the first three R-EOFs of TIP, and (bottom row) all the regressors. Red (blue) shading is for positive (negative) anomaly, and black contours indicate 10% significance. Latitude circles are shown every 20˚.

eddy heat flux, in agreement with the EGR anomaly. Correspondingly, the storm track anomaly (Fig. 4.43, right panel) also indicates a strengthening and a southward shift of the storm track in the western part of the Pacific. This is in broad agreement with the southward shift of the jet stream indicated by the 250 hPa zonal wind response of Fig. 4.41.

In FMA, the SST footprint of the extratropical PDO is very similar to the one in DJF (Fig. 4.44, first row panels), and similarly, the addition of the Indian and Atlantic oceans forcings and SIC has almost no impact (Fig. 4.44, second row panels). On the other hand, adding the KE and OE slightly modifies the SST pattern as the negative SST anomaly maximum in the KOE region weakens, the anomalies near Japan looses significance, and the warming off the west coast of North America strenghtens (Fig. 4.44, third row panels). As in OND, this pattern is linked to a large-scale southward shift of the SST gradient (not shown). Before the addition of the KE and OE into GEFA, no significant atmospheric signal is observed in the North Pacific (first and second row panels). Over the Atlantic, there is a dipole teleconnection pattern that is broadly similar to the NAO-like teleconnection found in DJF, but the high over Iceland is shifted east. The addition of the KE and the OE makes appear a dipolar structure, with a low over the KOE

region and the Aleutian Islands, and a high over the northeastern Pacific, albeit with limited statistical significance.

In order to separate better the OE and the PDO and to identify the location of the SST anomalies that mostly control the ocean-to-atmosphere impact, we also use PDO-KOE (Fig. 4.44, bottom panels). The warm SST anomaly in the eastern part is extended southward and eastward, and the cooling in the KOE region partly disappears, so that the negative anomaly is mostly located in the central basin, downstream of the KOE, and south of the KE. The teleconnection pattern is almost unchanged, but the NPO-like response over the Pacific is much stronger and more significant. As there is no increase in multicollinearity, this suggests that the central and eastern part of the extratropical PDO is what mostly controls the NPO-like atmospheric response, and that this response is masked by the response to the cooling in the KOE region, which is linked to a southward shift of the OE, acting in the opposite manner. This is supported by the fact that the NPO-like response is already observed as a response to PDO-KOE when the OE is not taken into account (not shown), albeit with lower amplitude and significance.

Therefore, the atmospheric response to the central and eastern part of the extratropical PDO is a NPO-like response, albeit shifted east, similar to the response in OND, but located further eastward. This pattern leads to a strenghtening and a slight poleward shift of the jet, and the eddy heat flux and storm track response estimates for the PDO-KOE also indicate a strenghtening and a slight poleward shift of the transient eddy activity (not shown).

Our estimated response to PDO-KOE in late winter thus resembles that found by Liu et al. (2012) in DJF and, less significatively, in MAM, except that their Z200 low was centered slightly southward. Since the OE was not included in their analysis, one may speculate that the PDO and OE forcing were less correlated in the twice longer period (1948-2010) that they considered, thus reducing their interferences.

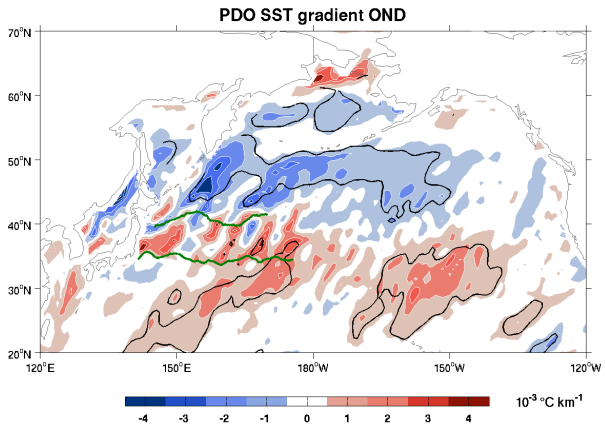

FIGURE 4.40 – PDO SST gradient in OND estimated by GEFA with the eleven regressors, corresponding to the SST pattern of the bottom left panel in Fig. 4.39. Red (blue) shading is for positive (negative) anomaly, and black contours indicate 10% significance. Green lines denote the mean KE and OE paths.

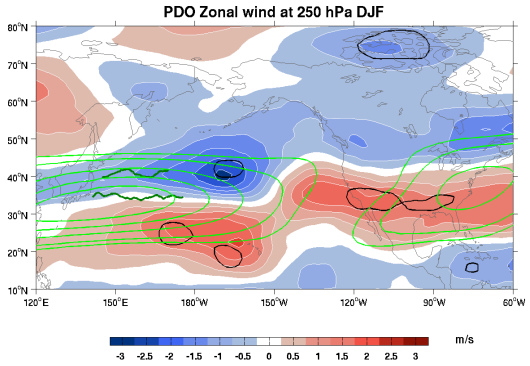

Figure 4.41 – Zonal wind response at 250 hPa to the PDO in DJF, estimated by GEFA. Red (blue) shading is for positive (negative) anomaly, and contour intervals are 0.5 ms^{-1}. Green thick lines denote the mean KE and OE paths, and black contours indicate 10% significance. Green contours denote the SON zonal wind climatology, with contours at 25, 30, 40, 50 and 60 ms^{-1}

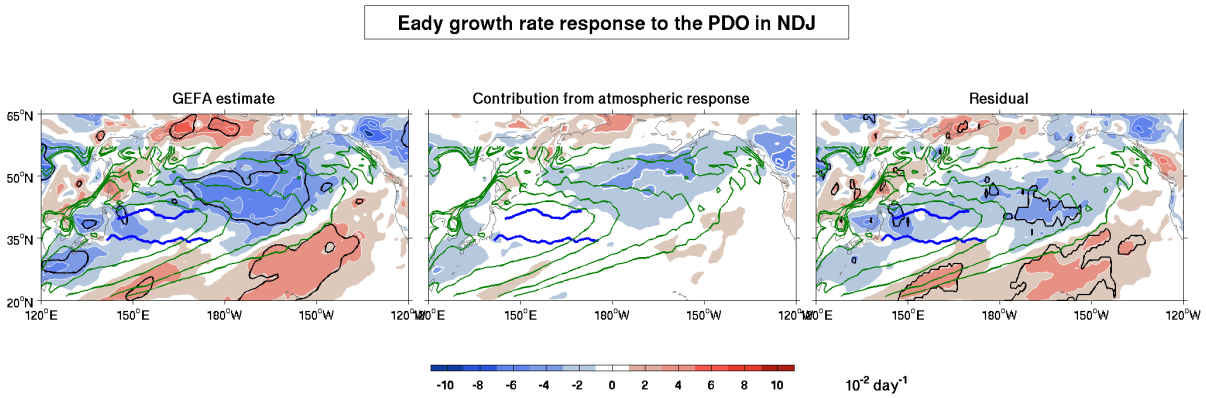

Figure 4.42 – NDJ response of the Eady growth rate at 850 hPa (CI = 2.10^{-2} day^{-1}) to the PDO. Red (blue) shading is for positive (negative) anomaly, dark blue lines denote the mean KE and OE paths, and black contours indicate 10% significance. Green contours denote the NDJ climatology, with contours at 50, 70 and 85.10^{-2} day^{-1}.

4.6 Discussion and conclusion

The atmospheric response to the variability of the OE, the KE, and the PDO was investigated in the cold season using ERA-Interim in 1979-2014. To differentiate their influence on the large-scale atmospheric circulation from the impact of other concomitant oceanic forcing, we used the multivariate GEFA method (Liu et al. 2008) and also represented the dominant modes of SST and SIC variability in the tropical and northern hemisphere. We assumed that the atmospheric response reaches its maximum amplitude after 2 months, consistent with multivariate regression and earlier modeling studies, and used seasonal means to increase the signal to noise ratio. The atmospheric response was investigated in three seasons, autumn (OND), winter (DJF) and late winter (FMA), and the robustness of our estimates assessed by investigating their sensitivity to an increasing number of regressors variables. Although the SST anomalies associated with

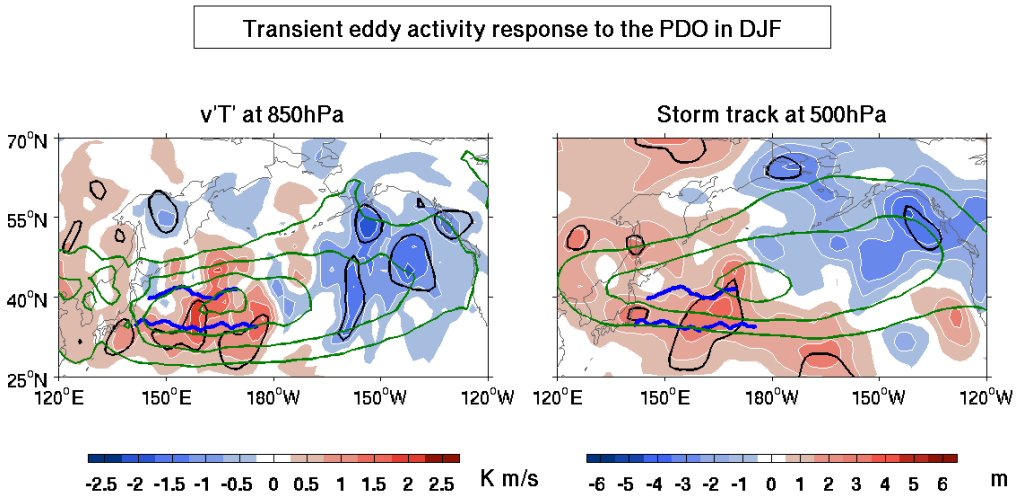

FIGURE 4.43 – DJF response of (left) the meridional transient eddy heat flux at 850 hPa (CI = 0.5 Kms^{-1}) and (right) the storm track at 500 hPa (CI = 1 m) to the PDO. Red (blue) shading is for positive (negative) anomaly, dark blue lines denote the mean KE and OE paths, and black contours indicate 10% significance. Green contours denote the DJF mean climatology, with contours at (left) 6, 8, 10 and 12 Kms^{-1}, and (right) 40, 50 and 60 m.

each single oceanic variable include remote anomalies and many cross-basin correspondences, reflecting the correlation between regressors, the multivariate approach was very efficient at confining the SST footprint of each regressor to its domain of definition. In particular, the SST footprint of the OE meridional shift was largely limited to the KOE region and separated from the basin-scale SST anomalies associated with the PDO, although their evolution is well correlated ; the ENSO signals were confined to the equatorial band, and the PDO and NPGO restricted to their extratropical signatures. This is opposite to the transformation used by Chen and Wallace (2016), where the ENSO signal was limited to a narrower equatorial band and the PDO had the equatorial component that characterize its decadal variations. Our estimation of the atmospheric response to the PDO should thus be understood as the response to the extratropical part of the PDO.

The influence of the meridional shifts of the OE, monitored by the changes in the maximum SST gradient, is robust in autumn ; a northward OE shift is followed by a positive NPO-like signal, typically reaching 2 hPa at sea level and 30 m at 250 hPa, and a WP-like teleconnection pattern at 250 hPa. Although the patterns are noisy, the estimated response of the Eady growth rate, the meridional eddy heat flux, and the storm track is broadly consistent with a northward shift of the maximum SST gradient, and in agreement with Rivière (2009), who showed that a more poleward baroclinicity favors anticyclonic wave breaking events, leading to a poleward shift of the eddy driven jet. We were not able to investigate the OE influence in winter, as there was too much multicollinearity in this season, and omitting regressors while keeping all the North Pacific ones never led to even satisfactorily isolating the OE SST footprint. On the other hand, a robust OE influence was found in late winter. The response pattern also shows a broadly NPO-like dipole, but the low over the Bering Sea is much stronger and slightly shifted

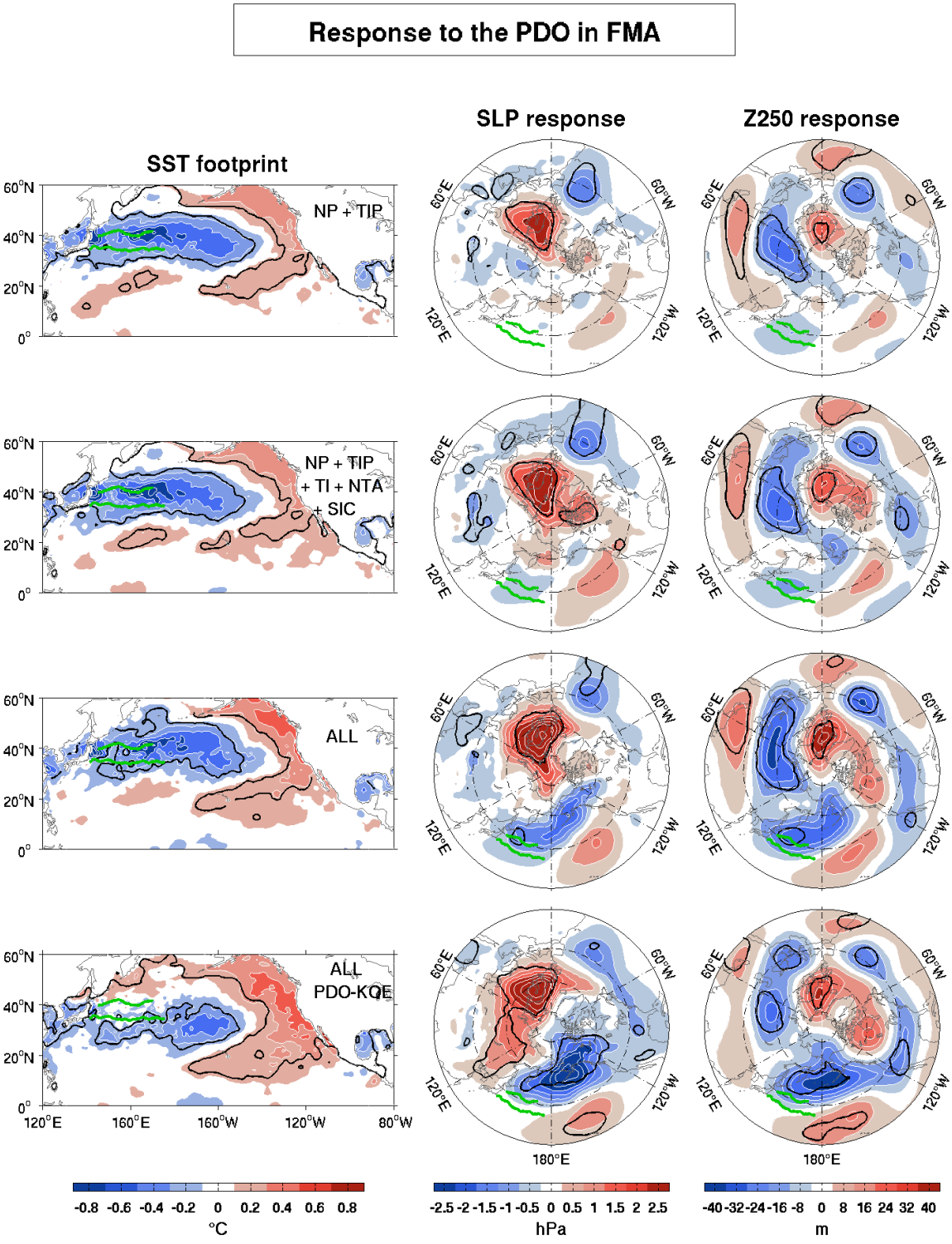

Figure 4.44 – As in Fig. 4.39, but for the SST signature in DJF and the SLP and Z250 responses in FMA, estimated by GEFA with the regressors indicated on the upper right corner of the left panels.

south, typically reaching 6 hPa at sea level and 80 m at 250 hPa, so that the westerly jet is strengthened and shifted poleward in the North Pacific. While the meridional eddy heat flux and storm track response estimates are consistent with a strengthened jet and eddy-mean flow interactions, the EGR response to the OE shifts shows no clear link with the associated SST and SST gradient changes. Although the anomalous heat release to the atmosphere could drive a baroclinic response that is rapidly changed into a larger equivalent barotropic response resembling a dominant mode of natural variability, as in Ferreira and Frankignoul (2005) and Deser et al. (2007), how the OE variability influences the atmospheric circulation in late winter remains unclear.

Since OE shifts and PDO are well correlated and both associated with large SST anomalies in the KOE region, we also used as PDO a PDO-KOE index defined by the first PC in the North Pacific with the KOE region excluded, which is less correlated with the OE and has a much smaller SST footprint in the KOE region. However, this did not affect the estimated response to the OE variability, confirming its robustness. In particular during autumn, the estimated response to the OE shifts is similar to the NPO/WP-like response found by FSKA, using partial regression onto a similar OE index based on a higher resolution SST product in 1982-2008 ; hence, partial regression could indeed be used to investigate the atmospheric response. On the other hand, our results differ from the high-resolution atmospheric response study of Smirnov et al. (2015), where a northward shift of the OE caused in DJFM a weakening of the Aleutian Low ; surprisingly, however, they also found that the OE shift was shifting the transient eddy heat flux poleward. To investigate the atmospheric response to the OE shift, Taguchi et al. (2012) used as OE index monthly SST anomaly averaged in a rectangular region of 5° latitude centered over the subarctic frontal zone. However, this does not clearly distinguish between the OE and other modes of SST variability, which in part motivated our study ; in 1979-2014 the index is as well correlated with our OE index ($r = 0.57$) and the PDO ($r = 0.6$), and weakly correlated with the KE Index ($r = 0.3$). Their estimated response during 1959-2006 is a PNA-like pattern with a strong weakening of the Aleutian Low in January (weaker in December), and a strengthening in February (weaker in March). The early winter response is very different from our estimated response to the OE in OND or to the PDO in OND or DJF, and perhaps more consistent with the OND response to the KE. However, this may also reflect difference in the analysis period, as suggested by Taguchi et al. (2012) and discussed below. In addition, numerical simulations have stressed the strong sensitivity of the atmospheric response to small changes in the background mean state, in particular between January and February (Peng et al. 1997 ; Peng and Whitaker, 1999 ; Brayshaw et al. 2008), which could affect results based on seasonal averages. Interestingly, however, the weakening of the Aleutian Low that they found in February is broadly consistent with our FMA response to the OE.

A robust response to the KE variability is found in autumn, with negligible sensitivity to the other regressors once the tropical Pacific impact is included ; it is barotropic pattern, with positive anomalies over the sea of Okhotsk and western Canada, and a negative anomaly in the Pacific side of the polar vortex, consistent with the partial regression analysis of Révelard et al. (2016). Despite the broad KE SST footprint in the KOE region, no significant atmospheric

response is found in winter. In late winter, the KE SST footprint becomes increasingly small and noisy along the KE path when the PDO and NPGO are added in GEFA. However, there is no change in the estimated response pattern, a barotropic high over Western Canada, and strong signals over Eurasia, which might thus reflect an concomitant external influence that was not taken into account, such as snow cover or the East Asian winter Monsoon, which strongly affect the climate in the Northwestern Pacific region and also varies on interannual and interdecadal timescales (Ha et al. 2012).

The PDO is followed in autumn by a NPO-like signal, with a strong low over the Bering Sea reaching 4 hPa at sea level and 40 m at 250 hPa, leading to a strengthening of the westerly jet in the central Pacific and its southward shift over North America, consistent with the eddy heat flux and storm track response estimates. The estimated response to PDO-KOE is weaker and more confined to the North Pacific sector, suggesting that only part of the PDO influence arises from SST in the northern and eastern Pacific. In winter, the PDO shifts the maximum baroclinicity and the storm track southward, consistent with the anomalous SST gradient and Gan and Wu (2013). The large-scale response strongly tilts westward with height in the North Pacific sector, suggesting baroclinicity, and there are large barotropic teleconnections, with a negative NAO-like signal in the North Atlantic sector. The North Pacific response differs from the deepening of the Aleutian Low found by Liu et al. (2012) in DJF, but the teleconnection to the NAO is similar. In late winter, the estimated response in the North Pacific, a barotropic dipolar signal, only becomes weakly significant when the OE regressor is included, but the upper level dipole over Asia and the negative NAO-like teleconnection are robust. Using PDO-KOE strongly strengthens the estimated North Pacific response, which becomes similar to a positive NPO pattern, albeit slightly shifted south. This suggests that in this season there is a negative interference between the response to the central and eastern part of the PDO and the strong response to the OE. Our estimated response to PDO-KOE in late winter broadly resembles that found by Liu et al. (2012) in DJF and, less significatively, in MAM, except that their SLP low was centered slightly southward. Since the OE was not included in their analysis, one may speculate that PDO and OE were less correlated in the longer 1948-2010 period, thus reducing their negative interferences.

Except perhaps in late winter, our estimated response to the PDO differs from the GEFA estimates of Wen et al. (2010), who considered all the months of the year in 1958-2007, and Liu et al. (2012) who estimated seasonal response in 1958-2007. They found that the PDO was associated with a strengthened Aleutian Low, whereas our results in OND and FMA indicate an NPO-like response, thus a poleward shift of the Aleutian Low. In DJF, the differences are even larger, as we find that the PDO leads to a weakening of the Aleutian Low at 250 hPa. The difference between our results and Liu et al. (2012)'s primarily comes from the different periods considered, and also from the different lag used in the analysis. Liu et al. (2012) used a lag of 1 month ($\tau = 1$ with $d = 0$) and the 1948-2010 period. If we apply our method to the 1958-2012 period, but with a lag of 1 month, we recover their result, i.e. a low over the North Pacific, albeit only significant over the Sea of Okhotsk (Fig. 4.45, a). However, if lag $\overline{3}$ is used instead of lag 1, the pattern is different (Fig. 4.45, b) as the high over Canada has shifted west, and the low over

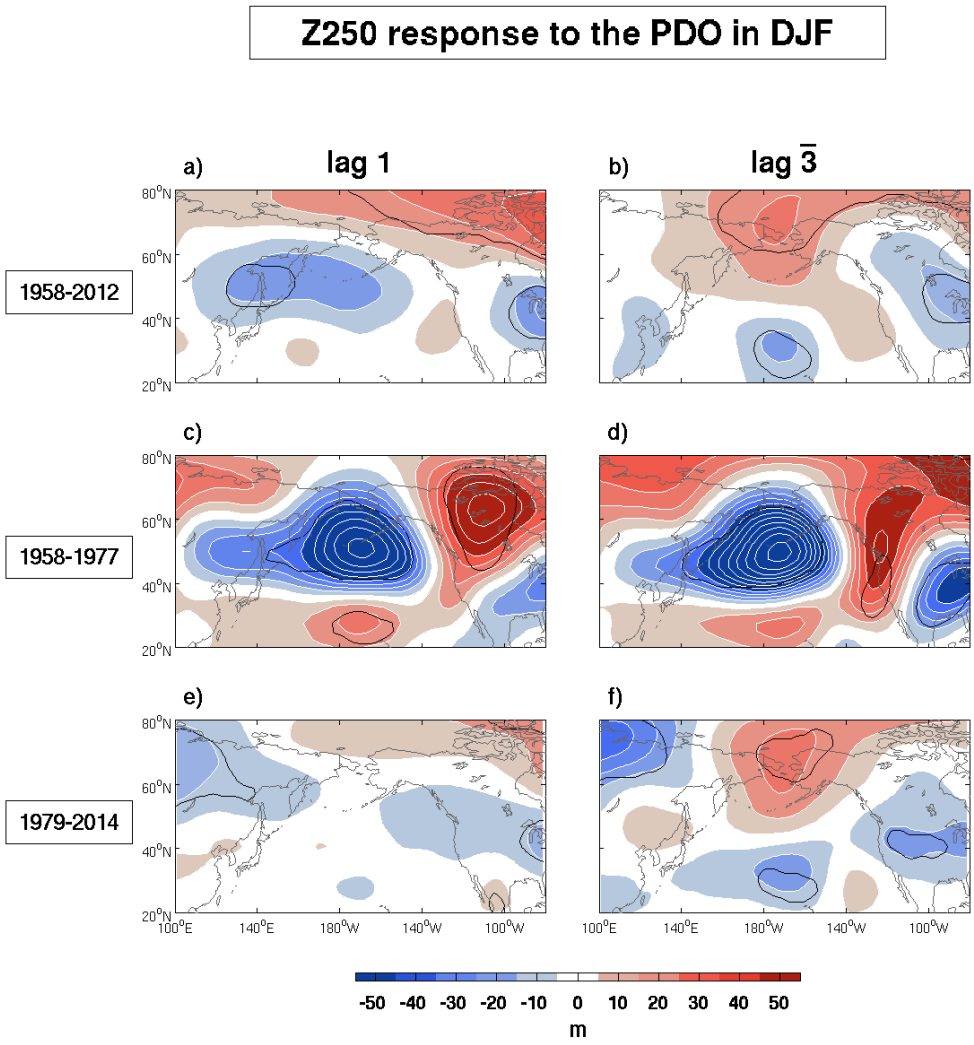

FIGURE 4.45 – DJF Z250 response to the PDO in (upper panels) 1958-2012, (middle panels) 1958-77 and (botto panels) 1979-2014 estimated with (left panels) a lag of 1 month as in Liu et al. (2012) and with (right panels) a lag of one season with 3-month seasonal means. Thick black contours indicate 10% significance.

the Aleutian Islands has shifted south, so the whole pattern resembles a negative NPO, similar to our estimates.

On the contrary, in 1958-1977, our estimated DJF response to the PDO is indeed a strong strengthening of the Aleutian Low (Fig. 4.45, d), and a similar pattern is obtained by using GEFA with a lag of 1 month and $d = 0$ as in Liu et al. (2012) (Fig. 4.45, c). This suggests that when the response is strong, it is not sensitive to the lag. However, it strongly differs from the negative NPO-like pattern that we found in 1979-2014 (Fig. 4.45, f), indicating a strong non-stationarity. At lag 1, there is no significant signal in the North Pacific at 250 hPa (Fig. 4.45, e), while at lag $\overline{3}$, the signal is very similar to the 1958-2012 pattern.

This strong non-stationarity in the atmospheric response is likely due to the changes in the mean state of the North Pacific circulation during the 1976-77 climate shift, which led to a deeper

and eastward shifted Aleutian Low (Trenberth and Hurrell 1994). Qiu et al (2014) have shown that the KE also exhibited a different behavior before and after 1977 (section 2.2). In fact, we had limited our analysis to 1979-2014 in order to avoid these large changes in the mean background circulation. However, Pak et al. (2014) detected another North Pacific climate shift in 1988, with strong changes in the relation between the NPO and the East Asian winter monsoon attributed to the strong weakening of the Siberian high after 1988. Hence, the atmospheric response to North Pacific forcing might also differ before and after 1988. This should be investigated, but with more limited samples the GEFA method may not be optimal. Other observational studies of the influence of the PDO (or of the Interdecadal Pacific Oscillation) have focused on its low-frequency behavior (e.g., Dai 2013 ; Dong and Dai 2015). However, such studies do not separate between tropical and extratropical influence, and they use simultaneous correlation or composites, which does not distinguish between forcing and response, even at low frequency (Frankignoul 1999).

In summary, the multivariate analysis is quite efficient in separating the SST footprints of the different regressors and in estimating the large-scale atmospheric response. However, GEFA does not seem to be as effective with noisier variables like the Eady growth rate or the transient eddy activity, as the GEFA estimates are noisy and sometimes difficult to relate to the SST or SST gradient anomalies linked to the oceanic forcing. We also considered the vertical wind and precipitation, which are even noisier fields, and we were not able to extract any significant signal. Another limitation of this method is that we were not able to include asymmetries in the analysis, i.e. separate the influence of the warm and cold phases of the oceanic forcing, even though the ENSO teleconnections are asymmetric (Hoerling et al. 1997 ; Straus and Shukla 2002), asymmetries in the response to the KE were found by composite analysis in Révelard et al. (2016), and numerical response studies increasingly show large response asymmetries (e.g., Seo et al. 2014). Attempts at separating the warm and cold phases of the different regressors led to less accurate separation of their SST footprint, in part because the correlation between the warm and cold phases of the different regressors were substantially lower. Since our result confirm earlier results based on partial correlation and composite analysis, the latter should therefore be the best way to investigate this question, provided that enough length of data are available.

Chapitre 5

Conclusion et perspectives

L'objectif de cette thèse était d'étudier l'influence de la variabilité océanique du Pacifique Nord sur la circulation atmosphérique à partir d'observations océaniques et de réanalyses atmosphériques. En particulier, nous nous sommes intéressés à l'influence de la variabilité des fronts associés aux courants de bord ouest, le Kuroshio et l'Oyashio, pour lesquels nous disposons d'indices pour décrire leur variabilité. Celle-ci étant corrélée avec d'autres modes de variabilités grande échelle de la SST telle que la PDO, nous avons tenté de différencier l'influence de ces courants à celui des autres modes de variabilité. Les interactions océan-atmosphère étant très dépendantes de l'état moyen de l'atmosphère et donc de la saison, nous nous sommes restreint à étudier la saison froide, pendant laquelle les échanges de chaleur sont les plus forts. Nous avons utilisé la réanalyse atmosphérique ERA-Interim, dont les données commencent en 1979.

Dans un premier temps, nous nous sommes focalisés sur l'influence de la variabilité de l'Extension du Kuroshio (KE), en utilisant le nouvel indice développé par Qiu et al. (2014) qui est défini par l'anomalie de hauteur de mer moyennée dans une région centrée sur le KE. Cet indice montre une forte variabilité basse fréquence, essentiellement à l'échelle décennale. Nous avons tout d'abord utilisé une analyse statistique de régression partielle avec décalage temporel, en filtrant en amont le signal lié aux téléconnexions ENSO, puis une analyse en composite, afin de différencier l'influence de la phase chaude de celle de la phase froide. Une analyse de la régression avec différents décalages temporels a montré que la réponse était bien estimée après un décalage de deux mois, en accord avec les simulations numériques qui suggèrent que la réponse aux anomalies de SST atteint son amplitude maximale après deux mois (e.g. Ferreira et Frankignoul 2005, Deser et al. 2007). L'index du KE étant très peu corrélé à celui de l'Oyashio, il n'a pas été nécessaire de prendre en compte l'Oyashio dans cette analyse, car des résultats similaires étaient obtenus avec une régression bivariable. Nous avons ainsi montré que la variabilité décennale du KE avait une influence significative sur la circulation atmosphérique de grande échelle entre les mois d'octobre et de janvier, mais que celle-ci devenait différente à partir de février. Ce résultat est en accord avec plusieurs autres études ayant montré des réponses atmosphériques drastiquement différentes entre les mois de janvier et février (Peng et Whitaker 1999 ; Liu et al. 2007 ; Gan et Wu 2012 ; Taguchi et al. 2012). Lorsque le KE est dans un état dynamique stable (l'index est positif), le courant est plus fort, sa trajectoire est plus au nord, et l'éner-

gie cinétique turbulente est réduite. Une plus forte advection des eaux chaudes provenant des subtropiques génère alors une anomalie grande-échelle de SST de 0.4˚-0.6˚K dans la région du KOE (Kuroshio Oyashio Extension), avec une anomalie maximale juste au sud de l'Oyashio. Le gradient de SST le long de l'Oyashio est alors plus fort et plus étendu vers l'est, bien que cela n'impacte pas la latitude de sa trajectoire. Ce réchauffement des eaux de surface génère un dégagement de chaleur de l'océan vers l'atmosphère (rétroaction négative), suivie par une ascension de l'air juste au dessus de l'anomalie maximum, ainsi qu'une augmentation de l'énergie potentielle de convection disponible et de la précipitation convective. Cependant, les signaux observés sont bruités, et nous n'avons trouvé aucun signal significatif dans la convergence des vents de surface ou les précipitations nettes. Concernant l'activité synoptique, l'état dynamique stable du KE génère une diminution de la baroclinicité le long du KE, et un déplacement vers le nord-est des flux méridiens de chaleur et de d'humidité par les tourbillons transitoires. Le rail des dépressions est renforcé en aval, dans le Gulf de l'Alaska et sur l'ouest du Canada. Le dégagement de chaleur et les anomalies dans les tourbillons transitoires sont probablement les mécanismes excitant des ondes de Rossby planétaires. Ces ondes prennent source dans la région du KOE et se propagent vers l'Arctique et l'Amérique du Nord, donnant lieu à des téléconnexions. La réponse atmosphérique à l'état stable du KE consiste en une anomalie positive de pression dans le centre du Pacifique Nord et sur la côte ouest des Etats-Unis, et une anomalie négative sur l'arctique, reflétant un renforcement du vortex polaire. Le signal se décale vers l'ouest avec l'altitude, ce qui est caractéristique de la baroclinicité. L'amplitude est de l'ordre de 0.6 hPa au niveau de la mer et de 20 m à 250 hPa, ce qui est faible comparé à la variabilité intrinsèque de l'atmosphère (rms de 4 à 8 hPa au niveau de la mer et de 60 à 120 m à 250 hPa). Cependant, cette amplitude est comparable aux estimations de la réponse aux fluctuations de l'Oyashio par FSKA ou Smirnov et al. (2015). Ces anomalies sont associées à une plus faible pénétration d'onde dans la stratosphère, d'où le renforcement du vortex polaire. Un mois plus tard, en NDJF, on observe une propagation du signal sur l'Europe. La propagation d'ondes explique la téléconnexion sur les Etats-Unis, mais le signal sur l'Europe est plus probablement dû à d'autres mécanismes tels que la propagation du signal depuis le vortex polaire vers la basse troposphère (Baldwin et Dunkerton 1999 ; Polvani et Waugh 2004), ou des changements dans le rail des dépressions et des interactions ondes-écoulement moyen (Chang 2004 ; Drouard et al. 2013). L'analyse en composite a montré que la phase froide avait peu d'impact, alors que les résultats pour la phase chaude étaient comparables à ceux obtenus par régression linéaire, mais de plus forte amplitude. Cette forte asymétrie peut s'expliquer par la différence entre l'impact d'une SST plus chaude comparée à celui d'une SST plus froide, une SST plus chaude générant plus d'instabilités convectives et impactant l'atmosphère sur une plus grande profondeur (Deser et al. 2004 ; Sheldon et Czaja 2014).

Tandis que nos résultats sont en accord avec l'analyse préliminaire de Qiu et al. (2014) qui ont utilisé le même indice et étudié l'impact sur les flux de chaleur mais sans différencier entre les saisons, ils sont assez différents des autres études basées sur des indices différents. En particulier, ils sont différents de ceux de FSKA qui ont utilisé comme indice le déplacement en latitude de l'isotherme de 14˚C à 200 m de profondeur. Cependant, leur indice a été développé

à partir d'observations très limitées, ce qui a nécessité un lissage temporel important. En outre, la variabilité du KE n'est pas bien déterminée par la température à 200 m de profondeur, et il aurait fallu disposer de mesures plus profondes. De plus, l'index de Qiu et al. (2014) ne reflète pas seulement un déplacement de la trajectoire du KE, mais des changements dynamiques plus globaux, y compris le caractère tourbillonnaire de la région, ce qui ne donne pas lieu à la même réponse atmosphérique. La non-stationnarité est également la raison de la disparité des résultats. En effet, des résultats différents des nôtres et similaires à ceux de O'Reilly et Czaja (2014) sont obtenus lorsque nous analysons la période 2002-10 sur laquelle leur index est défini, mais cette période est probablement trop courte pour étudier l'influence de la variabilité décennale du KE. Sur cette période, la signature en SST est d'ailleurs très différente de celle obtenue sur la période 1979-2012. Le réchauffement des eaux de surface associé à la phase stable du KE est moins grande échelle et limité à la zone le long du Kuroshio. Il serait donc intéressant de déterminer pourquoi les oscillations dynamiques du KE ne donnent pas lieu à la même signature en SST en fonction de la période considérée, et ainsi de comprendre si la disparité des résultats est due à la différence des échelles de temps entre les différents indices, à des non-stationnarités dans la dynamique océanique et atmosphérique, ou simplement à l'échantillonnage limité.

En revanche, nos résultats sont globalement comparables à ceux de Liu et al. (2007) et Gan et Wu (2012) qui ont étudié la réponse atmosphérique à une anomalie grande échelle de SST dans la région du KOE, semblable à l'anomalie de SST associée à l'index du KE sur la période 1979-2012. Ils ont trouvé que la réponse atmosphérique était maximale en début d'hiver (NDJ), et consistait en une anomalie positive équivalente barotrope de la pression dans le centre du Pacifique Nord, et une anomalie négative sur l'Alaska et l'ouest des Etats-Unis, avec également des téléconnexions sur l'Atlantique. De même, nos résultats ne diffèrent pas beaucoup si nous utilisons comme Taguchi et al. (2012) un index basé sur l'anomalie de SST dans la région centrée sur l'OE. Ceci suggère donc que l'impact de la SST liée au KE de celle liée à l'OE ou à la PDO n'est pas bien différencié lorsque l'on se base sur la SST moyennée sur un grand domaine.

Alors que la variabilité du KE est peu liée à celle des autres modes de variabilité de la SST extratropicale, celle de l'Extension de l'Oyashio (OE) est très corrélée à la PDO. Dans un deuxième temps, nous avons donc utilisé l'approche multivariable GEFA afin de différencier l'impact du KE et de l'OE de celui de la PDO et de la NPGO. Afin de représenter le forçage de l'océan de manière la plus exhaustive possible, nous avons inclus dans cette analyse les principaux modes de variabilité de la SST des océans Pacifique, Atlantique et Indien, ainsi que la couverture de glace de mer. Puisque de nombreux changements sont observés dans la réponse atmosphérique entre le début et la fin de l'hiver, nous avons étudié trois saisons séparément : le début d'hiver (OND), l'hiver (DJF), et la fin d'hiver (FMA). Afin de lisser la variabilité haute fréquence et d'augmenter le rapport signal/bruit, nous avons choisi de travailler avec des moyennes saisonnières, et estimons donc la réponse atmosphérique avec un décalage temporel de 3 mois (une saison) pour bien séparer cause et effet. Nous avons montré que l'analyse multivariable est très efficace pour distinguer les anomalies de SST associées aux différents modes de variabilité, bien que ceux-ci soient corrélés entre eux. L'analyse multivariable permet de séparer les parties tropicales et extratropicales des modes ENSO, PDO et NPGO, et de distinguer entre les anomalies

de SST associées aux fronts du KE et de l'OE de celles liées aux modes de variabilité grande échelle PDO et NPGO. Le fait que la méthode fonctionne remarquablement pour la SST nous permet d'être confiant sur l'estimation de la réponse atmosphérique à chacun des forçages.

Le déplacement vers le nord de l'OE génère en OND une réponse atmosphérique dipolaire ressemblant à l'Oscillation Nord Pacifique (NPO), reflétant un déplacement du jet stream vers le pôle dans le centre du Pacifique Nord. Bien que les signaux soient bruités, l'analyse de la baroclinicité et l'activité synoptique suggèrent que le déplacement vers le nord de l'OE génère un déplacement vers le nord de la baroclinicité, ce qui a pour effet de déplacer le jet stream plus au nord, en accord avec les simulations de Rivière (2009). En FMA, la réponse est assez similaire mais légèrement déplacée vers le nord, et l'anomalie négative est beaucoup plus forte. La réponse entraine donc plutôt un renforcement du jet stream. Cependant, l'impact sur l'activité synoptique ne nous permet pas de faire le lien avec le déplacement de l'OE. L'influence de l'OE en fin d'hiver reste donc à être clarifiée. Les résultats de l'OE en OND sont similaires à ceux trouvés par FSKA par régression partielle sur la période 1982-2008, ce qui suggère que la régression partielle est aussi une bonne méthode pour étudier l'influence de l'OE. Par contre, ces résultats sont différents de ceux de Taguchi et al. (2012), qui ont utilisé l'anomalie de SST moyennée sur un grand domaine et ont donc mélangé les forçages du KE de l'OE et de la PDO. Notre estimation de la réponse atmosphérique à l'OE est également différente de celle de l'expérience numérique de Smirnov et al. (2015). Cependant, leur réponse était sensible à la résolution du modèle.

Concernant le KE, nous retrouvons en OND les résultats obtenus dans la première partie par régression partielle, et nous n'observons aucune réponse significative en DJF et FMA. Notre analyse suggère donc que la variabilité du KE n'a pas d'influence à grande échelle en hiver et en fin d'hiver, ou bien que cette influence est faible et masquée par d'autres téléconnexions plus fortes.

La réponse à la PDO en OND est de type NPO, avec une forte anomalie négative de pression dans la mer de Bering, de l'ordre de 4 hPa au niveau de la mer et de 40 m à 250 hPa, reflétant un renforcement du jet sur le Pacifique central et un déplacement vers le sud au dessus de l'Amérique de Nord, en cohérence avec l'estimation de la réponse des tourbillons transitoires. En DJF, la PDO génère un déplacement vers le sud de la baroclinicité maximale et du rail des dépressions, en accord avec l'anomalie du gradient de SST qui montre un déplacement vers le sud du front de SST subpolaire. La réponse atmosphérique penche fortement vers l'ouest avec l'altitude, ce qui est caractéristique de la baroclinicité, et montre une forte téléconnexion sur l'Atlantique Nord ressemblant à l'Oscillation Nord-Atlantique (NAO). En FMA, la téléconnexion NAO est toujours robuste, mais la réponse atmosphérique sur le Pacifique Nord devient significative uniquement après l'ajout de l'OE comme régresseur, et montre un dipole nord sud de type NPO. Notre analyse suggère que pendant cette saison la réponse à la SST du Pacifique central et nord-est et la réponse à l'OE génèrent des interférences négatives, la réponse à l'OE masquant la réponse à la SST du Pacifique central et nord-est.

Nos résultats en DJF sont en accord avec ceux de Gan et Wu (2013) qui ont trouvé que la PDO en hiver était liée à un déplacement vers le sud du rail des dépressions les hivers d'après.

Par contre, nos résultats sont sensiblement différents de ceux de Wen et al. (2010) et Liu et al. (2012) qui ont utilisé la même méthode GEFA mais sur des périodes plus longues (1958-2007 et 1948-2010). La différence s'explique par la non-stationnarité de la réponse, mais également par la différence du décalage temporel choisi dans la méthode. Tandis que Wen et al. (2010) et Liu et al. (2012) ont estimé la réponse avec un décalage d'un mois (lag 1), nous avons choisi de travailler avec des moyennes saisonnières de trois mois et estimons donc la réponse atmosphérique avec un décalage d'une saison (lag $\overline{3}$). Or, en analysant la période 1958-2012, nous retrouvons leur résultat au lag 1, bien que moins significatif, et notre résultat au lag $\overline{3}$, mais ils sont assez différents. Par contre, sur la période 1979-2014, nous ne retrouvons pas leur résultat au lag 1, l'analyse ne montrant aucune réponse significative à 250 hPa sur la région du Pacifique Nord. Notre analyse suggère donc que la réponse de Wen et al. (2010) et Liu et al. (2012) n'est pas robuste. En revanche, la réponse atmosphérique à la PDO sur la période 1958-77 est différente et beaucoup plus forte, et montre un résultat semblable aux lag 1 et $\overline{3}$. La réponse à la PDO est donc fortement non stationnaire, et de plus amples analyses sont nécessaires pour déterminer la cause de cette non stationnarité.

Ainsi, nous avons montré que la variabilité du KE, de l'OE et de la PDO avait une influence significative sur l'atmosphère, bien que celle-ci soit de plus faible amplitude que la variabilité intrinsèque de l'atmosphère, ce qui rend le signal difficile à mettre en évidence par les observations. De ce fait, les mécanismes par lesquels cette réponse est établie n'ont pas pu être clairement mis en évidence par l'analyse multivariable. Nous avons estimé l'impact sur les tourbillons transitoires, mais les variables utilisées donnent lieu à des signaux très bruités ne nous permettant pas toujours de faire le lien avec l'anomalie de SST. D'autre part, la sensibilité à l'état moyen de l'atmosphère fait que la réponse atmosphérique est très dépendante de la saison, mais également de la période considérée. La non stationnarité est donc une question clé pour les recherches futures. Dans cette étude, nous avons utilisé la réanalyse ERA-Interim, qui commence en 1979. Ainsi, nous nous sommes affranchis du changement climatique de 1976-77, qui a profondément modifié l'état moyen de l'atmosphère dans le Pacifique Nord. Cependant, d'autres changements climatiques ont eu lieu, comme celui de 1988, mise en évidence par Pak et al. (2014). Il ne serait donc pas surprenant que la réponse atmosphérique soit différente avant et après 1988. Nous envisageons pour un travail futur d'étudier les périodes 1979-1988 et 1989-2014 séparément. Le problème est que les échantillons deviennent très limités, et la variabilité basse fréquence mal représentée.

Au final, étant donné que nous retrouvons avec l'analyse multivariable les résultats obtenus avec la régression partielle, notre travail avec la méthode multivariable suggère que la régression partielle est une méthode adéquate pour étudier l'influence de l'OE sur l'atmosphère, bien que l'OE soit très corrélé à la PDO. De plus, en utilisant la régression partielle, nous pouvons étudier l'asymétrie de la réponse atmosphérique, ce que nous n'avons pas pu faire avec la méthode multivariable, car en séparant les phases positives et négatives de chacun des forçages, la distinction entre leurs anomalies de SST associées en était affectée. Pourtant, des analyses préliminaires d'expériences numériques montrent que la réponse au front de l'OE est fortement asymétrique (Kwon, communication personnelle). L'idéal serait donc de disposer de longs échantillons de

données et de pouvoir faire une analyse en composite en tenant compte de l'état moyen de l'atmosphère et des régimes de temps dominants afin d'explorer la non-stationnarité. En outre, il serait intéressant de comprendre pourquoi nous observons des changements drastiques dans la réponse atmosphérique entre janvier et février, et pourquoi la réponse atmosphérique est la plus robuste en automne.

Annexe A

Univariate regression on SST footprints

To test the robustness of the GEFA results, we tried another approach. It consists of estimating by GEFA the SST footprint of the twelve regressors, and then using the time evolution of the SST footprints to do a lagged univariate regression. In other words, we use multivariate regression to estimate the SST footprints, then derive their time evolution by projecting them onto the SST variability, and use it as regressors for single lagged regression. It appeared that the results of this approach are very similar to the GEFA estimations, but they are more statistically significant. An example is given here for the OND response in eddy heat flux and storm track to the OE (Fig. A.1) and to the PDO (Fig. A.2).

The OND response in eddy heat flux to the OE shows an enhanced meridional eddy heat flux downstream of the OE at the dateline and further north, albeit with limited statistical significance (Fig. A.1, left upper panel). When using the univariate regression on the SST footprint (left bottom panel), this enhancement is broadly significant and more pronounced just north of the OE mean path. Similarly, the enhancement of the storm track activity observed over the Gulf of Alaska and along the US west coast in the GEFA estimation (upper right panel) is more significant and located further westward (north of the OE mean path) in the univariate approach (bottom right panel).

The same thing can be observed for the OND response to the OE. The GEFA estimation (Fig. A.2, upper panels) and the univariate regresson on the SST footprint (bottom panels) shows the same patterns, but the univariate approach leads to more statistical significance. The amplitude is slightly weaker, because the univariate regression is estimated at a lag of 2 months (to be coherent with our model that assumes $d = 2$), so $\tau = 0$ in Eq. (4.3.2), and $C_{YY}(0)$ is higher than $C_{YY}(1)$.

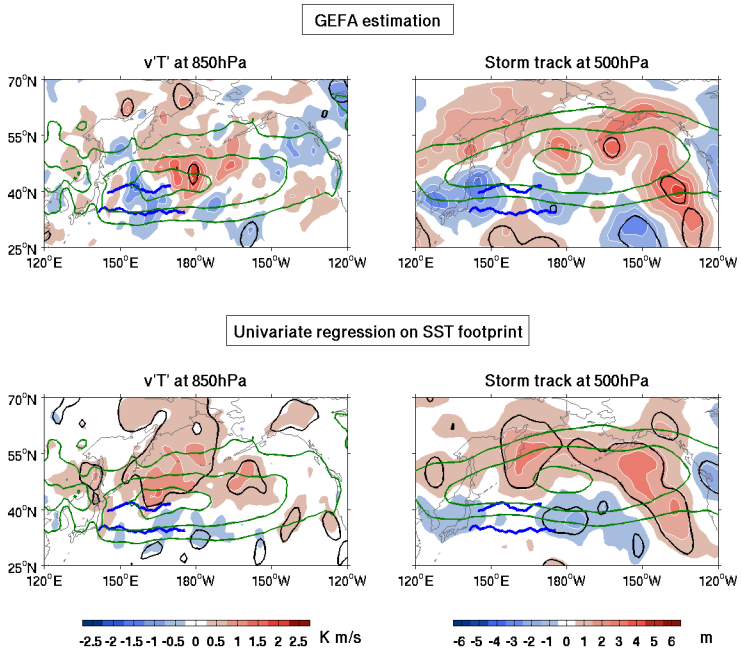

FIGURE A.1 – OND response of (left) the meridional transient eddy heat flux at 850 hPa (CI = 0.5 Kms^{-1}) and (right) the storm track at 500 hPa (CI = 1 m) to the OE. The GEFA estimation is given in the upper panels, and the univariate regression on the SST footprint is given in the bottom panels. Red (blue) shading is for positive (negative) anomaly, dark blue lines denote the mean KE and OE paths, and black contours indicate 10% significance. Green contours denote the OND mean climatology, with contours at (left) 6, 8, 10 and 12 Kms^{-1}, and (right) 40, 50 and 60 m.

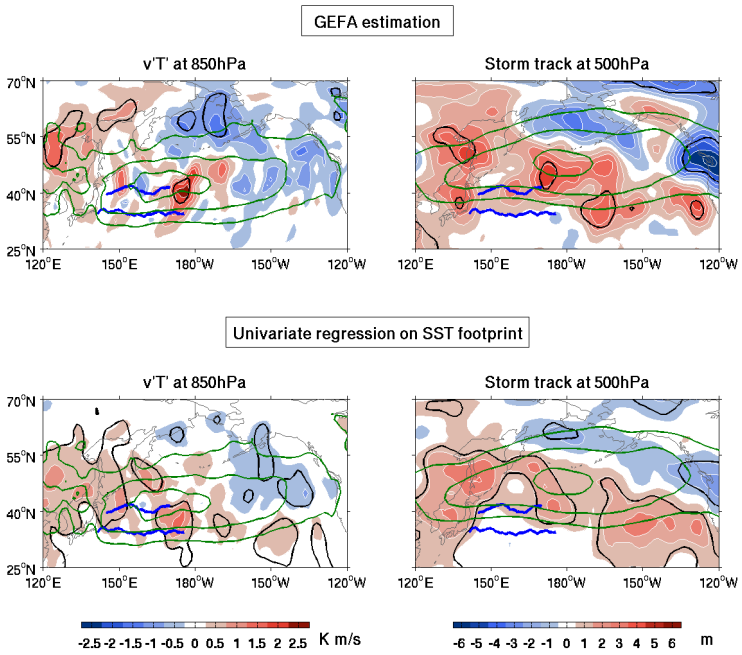

FIGURE A.2 – As in figure A.1, but for the PDO.

Table des figures

Bibliographie

[1] M. A. Alexander, I. Bladé, M. Newman, J. R. Lanzante, N. C. Lau, et J. D. Scott, "The atmospheric bridge : The influence of ENSO teleconnections on air-sea interaction over the global oceans," Journal of Climate **15**, 2205–2231 (2002).

[2] M. A. Alexander, L. Matrosova, C. Penland, J. D. Scott, et P. Chang, "Forecasting Pacific SSTs : Linear inverse model predictions of the PDO," Journal of Climate **21**, 385–402 (2008).

[3] D. G. Andrews, "On the interpretation of the eliassen-palm flux divergence," Quarterly Journal of the Royal Meteorological Society **113**, 323–338 (1987).

[4] K. Ashok, S. K. Behera, S. A. Rao, H. Weng, et T. Yamagata, "El Nino Modoki and its possible teleconnection," Journal of Geophysical Research : Oceans **112**, 1–27 (2007).

[5] M. P. Baldwin et T. J. Dunkerton, "Propagation of the Arctic Oscillation from the stratosphere to the troposphere," Journal of Geophysical Research **104**, 30937 (1999).

[6] T. P. Barnett et R. Somerville, "Advances in short term climate prediction," U.S. natioanl report to international union of geodesy and geophysics p. 1096–1102 (1983).

[7] L. Bengtsson, K. I. Hodges, et E. Roeckner, "Storm tracks and climate change," Journal of Climate **19**, 3518–3543 (2006).

[8] J. Bjerknes, "The recent warming of the North Atlantic," Rossby Memorial Volume p. 65–73 (1959).

[9] J. Bjerknes, "Atlantic Air-Sea Interaction," Advances in Geophysics **10**, 1–82 (1964).

[10] J. Bjerknes, "Global ocean-atmosphere interaction," Rapports et Procés-Verbaux **162**, 108–199 (1972).

[11] M. L. Blackmon et N.-C. Lau, "Regional characteristics of the Northern Hemisphere wintertime circulation : A comparison of the simulation of a GFDL general circulation model with observations," Journal of the Atmospheric Sciences **37**, 497–514 (1980).

[12] M. L. Blackmon, "A Climatological Spectral Study of the 500 mb Geopotential Height of the Northern Hemisphere," Journal of the Atmospheric Sciences **33**, 1607–1623 (1976).

[13] S. Borlace, W. Cai, et A. Santoso, "Multidecadal ENSO amplitude variability in a 1000-yr simulation of a coupled global climate model : Implications for observed ENSO variability," Journal of Climate **26**, 9399–9407 (2013).

[14] G. Branstator, "Circumglobal teleconnections, the jet stream waveguide, and the North Atlantic Oscillation," Journal of Climate **15**, 1893–1910 (2002).

[15] D. J. Brayshaw, B. J. Hoskins, et M. Blackburn, "The Basic Ingredients of the North Atlantic Storm Track. Part I : Land–Sea Contrast and Orography," Journal of Atmospheric Sciences **66**, 2539–2558 (2009).

[16] D. J. Brayshaw, B. Hoskins, et M. Blackburn, "The Storm-Track Response to Idealized SST Perturbations in an Aquaplanet GCM," Journal of the Atmospheric Sciences **65**, 2842–2860 (2008).

[17] C. S. Bretherton, M. Widmann, V. P. Dymnikov, J. M. Wallace, et I. Bladé, "The effective number of spatial degrees of freedom of a time-varying field," Journal of Climate **12**, 1990–2009 (1999).

[18] C. Cassou, C. Deser, L. Terray, J. Hurrell, et M. Drevillon, "surface temperature conditions in the North Atlantic and their impact upon the atmospheric circulation in early winter," Journal of Climate **17**, 3349–3363 (2004).

[19] L. I. Ceballos, E. Di Lorenzo, C. D. Hoyos, N. Schneider, et B. Taguchi, "North Pacific gyre oscillation synchronizes climate fluctuations in the eastern and western boundary systems," Journal of Climate **22**, 5163–5174 (2009).

[20] E. K. M. Chang, "Are the Northern Hemisphere winter storm tracks significantly correlated ?" Journal of Climate **17**, 4230–4244 (2004).

[21] E. K. M. Chang, S. Lee, et K. L. Swanson, "Storm track dynamics," Journal of Climate **15**, 2163–2183 (2002).

[22] E. K. M. Chang, "Downstream Development of Baroclinic Waves As Inferred from Regression Analysis," Journal of the Atmospheric Sciences **50**, 2038–2053 (1993).

[23] X. Chen et J. M. Wallace, "Orthogonal PDO and ENSO indexes," Journal of Climate **29**, 3883–3892 (2016).

[24] X. Chen et J. M. Wallace, "ENSO-like variability : 1900-2013," Journal of Climate **28**, 9623–9641 (2015).

[25] K. C. Chhak, E. Di Lorenzo, N. Schneider, et P. F. Cummins, "Forcing of low-frequency ocean variability in the Northeast Pacific," Journal of Climate **22**, 1255–1276 (2009).

[26] A. Czaja et C. Frankignoul, "Decadal buoyancy forcing in a simple model of the subtropical gyre," Journal of Physical Oceanography **29**, 3145–3159 (1999).

[27] A. Czaja et C. Frankignoul, "Observed impact of Atlantic SST anomalies on the North Atlantic oscillation," Journal of Climate **15**, 606–623 (2002).

[28] A. Dai, "The influence of the inter-decadal Pacific oscillation on US precipitation during 1923–2010," Climate Dynamics **41**, 633–646 (2013).

[29] R. E. Davis, "Predictability of Sea Surface Temperature and Sea Level Pressure Anomalies over the North Pacific Ocean," Journal of Physical Oceanography **6**, 249–266 (1976).

[30] D. Decremer, C. E. Chung, A. M. L. Ekman, et J. Brandefelt, "Which significance test performs the best in climate simulations ?" Tellus, Series A : Dynamic Meteorology and Oceanography **66**, 23139 (2014).

[31] D. P. Dee, S. M. Uppala, A. J. Simmons, P. Berrisford, P. Poli, S. Kobayashi, U. Andrae, M. A. Balmaseda, G. Balsamo, P. Bauer, P. Bechtold, A. C. M. Beljaars, L. van de Berg, J. Bidlot, N. Bormann, C. Delsol, R. Dragani, M. Fuentes, A. J. Geer, L. Haimberger, S. B. Healy, H. Hersbach, E. V. Hólm, L. Isaksen, P. Kållberg, M. Köhler, M. Matricardi, A. P. Mcnally, B. M. Monge-Sanz, J. J. Morcrette, B. K. Park, C. Peubey, P. de Rosnay, C. Tavolato, J. N. Thépaut, et F. Vitart, "The ERA-Interim reanalysis : Configuration and performance of the data assimilation system," Quarterly Journal of the Royal Meteorological Society **137**, 553–597 (2011).

[32] T. L. Delworth et M. E. Mann, "Observed and simulated multidecadal variability in the Northern Hemisphere," Climate Dynamics **16**, 661–676 (2000).

[33] C. Deser, G. Magnusdottir, R. Saravanan, et A. S. Phillips, "The Effects of North Atlantic SST and Sea Ice Anomalies on the Winter Circulation in\nCCM3. Part II : Direct and Indirect Components of the Response," Journal of Climate p. 857–876 (2004).

[34] C. Deser, R. A. Tomas, et S. Peng, "The transient atmospheric circulation response to North Atlantic SST and sea ice anomalies," Journal of Climate **20**, 4751–4767 (2007).

[35] E. Di Lorenzo, N. Schneider, K. M. Cobb, P. J. S. Franks, K. Chhak, A. J. Miller, J. C. McWilliams, S. J. Bograd, H. Arango, E. Curchitser, T. M. Powell, et P. Rivière, "North Pacific Gyre Oscillation links ocean climate and ecosystem change," Geophysical Research Letters **35**, 2–7 (2008).

[36] E. Di Lorenzo, V. Combes, J. E. Keister, P. T. Strub, A. C. Thomas, P. J. S. Franks, M. D. Ohman, J. C. Furtado, A. Bracco, S. J. Bograd, W. T. Peterson, F. B. Schwing, S. Chiba, B. Taguchi, S. Hormazabal, et C. Parada, "Synthesis of Pacific Ocean Climate and Ecosystem Dynamics," Oceanography **26**, 68–81 (2013).

[37] B. Dong et A. Dai, "The influence of the Interdecadal Pacific Oscillation on Temperature and Precipitation over the Globe," Climate Dynamics **45**, 2667–2681 (2015).

[38] M. Drouard, G. Rivière, et P. Arbogast, "The North Atlantic Oscillation Response to Large-Scale Atmospheric Anomalies in the Northeastern Pacific," Journal of the Atmospheric Sciences **70**, 2854–2874 (2013).

[39] D. Ferreira et C. Frankignoul, "The transient atmospheric response to midlatitude SST anomalies," Journal of Climate **18**, 1049–1067 (2005).

[40] C. Frankignoul, "A cautionary note on the use of statistical atmospheric models in the middle latitudes : Comments on 'decadal variability in the North Pacific as simulated by a hybrid coupled model'," Journal of Climate **12**, 1871–1872 (1999).

[41] C. Frankignoul et E. Kestenare, "The surface heat flux feedback. Part I : Estimates from observations in the Atlantic and the North Pacific," Climate Dynamics **19**, 633–648 (2002).

[42] C. Frankignoul, N. S. Chael, Y. O. Kwon, et M. A. Alexander, "Influence of the meridional shifts of the Kuroshio and the Oyashio Extensions on the atmospheric circulation," Journal of Climate **24**, 762–777 (2011).

[43] C. Frankignoul, N. Chouaib, et Z. Liu, "Estimating the observed atmospheric response to SST anomalies : Maximum covariance analysis, generalized equilibrium feedback assessment, and maximum response estimation," Journal of Climate **24**, 2523–2539 (2011).

[44] C. Frankignoul, A. Czaja, et B. L'Heveder, "Air – Sea Feedback in the North Atlantic and Surface Boundary Conditions for Ocean Models," Journal of Climate **11**, 2310–2324 (1998).

[45] C. Frankignoul et K. Hasselmann, "Stochastic climate models, Part II Application to sea-surface temperature anomalies and thermocline variability," Tellus **29**, 289–305 (1977).

[46] C. Frankignoul et E. Kestenare, "Observed Atlantic SST anomaly impact on the NAO : An update," Journal of Climate **18**, 4089–4094 (2005).

[47] C. Frankignoul et E. Kestenare, "Air-sea interactions in the tropical Atlantic : A view based on lagged rotated maximum covariance analysis," Journal of Climate **18**, 3874–3890 (2005).

[48] C. Frankignoul et N. Sennéchael, "Observed influence of North Pacific SST anomalies on the atmospheric circulation," Journal of Climate **20**, 592–606 (2007).

[49] C. Frankignoul, N. Sennéchael, et P. Cauchy, "Observed atmospheric response to cold season sea ice variability in the arctic," Journal of Climate **27**, 1243–1254 (2014).

[50] B. Gan et L. Wu, "Modulation of atmospheric response to north pacific sst anomalies under global warming : A statistical assessment," Journal of Climate **25**, 6554–6566 (2012).

[51] B. Gan et lixin Wu, "Seasonal and Long-Term Coupling between Wintertime Storm Tracks and Sea Surface Temperature in the North Pacific," Journal of Climate **26**, 6123–6136 (2013).

[52] J. Garcia-Serrano, C. Frankignoul, G. Gastineau, et A. de la Camara, "On the predictability of the winter Euro-Atlantic climate : Lagged influence of autumn Arctic sea ice," Journal of Climate **28**, 5195–5216 (2015).

[53] G. Gastineau, F. D'Andrea, et C. Frankignoul, "Atmospheric response to the North Atlantic Ocean variability on seasonal to decadal time scales," Climate Dynamics **40**, 2311–2330 (2013).

[54] I. Gouirand, V. Moron, et E. Zorita, "Teleconnections between ENSO and North Atlantic in an ECHO-G simulation of the 1000-1990 period," Geophysical Research Letters **34**, 1–5 (2007).

[55] E. Guilyardi, P. Delecluse, S. Gualdi, et A. Navarra, "Mechanisms for ENSO phase change in a coupled GCM," Journal of Climate **16**, 1141–1158 (2003).

[56] K. J. Ha, K. Y. Heo, S. S. Lee, K. S. Yun, et J. G. Jhun, "Variability in the East Asian Monsoon : A review," Meteorological Applications **19**, 200–215 (2012).

[57] R. J. Haarsma et W. Hazeleger, "Extratropical atmospheric response to equatorial Atlantic cold tongue anomalies," Journal of Climate **20**, 2076–2091 (2007).

[58] K. Hasselmann, "Stochastic climate models : Part I. Theory," Tellus A **28**, 473–485 (1976).

[59] C. Haworth, "Some relationships between sea surface temperature anomalies and surface pressure anomalies," Quarterly Journal of the Royal Meteorological Society **104**, 131–146 (1978).

[60] M. P. Hoerling, a. Kumar, et M. Zhong, "El Nino, La Nina, and the nonlinearity of their teleconnections," Journal of Climate **10**, 1769–1786 (1997).

[61] M. Honda, S. Yamane, et H. Nakamura, "Impacts of the Aleutian-Icelandic low seasaw on surface climate during the twentieth century," Journal of Climate **18**, 2793–2802 (2005).

[62] B. J. Hoskins et K. I. Hodges, "New Perspectives on the Northern Hemisphere Winter Storm Tracks," Journal of the Atmospheric Sciences **59**, 1041–1061 (2002).

[63] B. J. Hoskins, I. N. James, et G. H. White, "The Shape, Propagation and Mean-Flow Interaction of Large-Scale Weather Systems," Journal of the Atmospheric Sciences **40**, 1595–1612 (1983).

[64] B. J. Hoskins et D. J. Karoly, "The Steady Linear Response of a Spherical Atmosphere to Thermal and Orographic Forcing," Journal of the Atmospheric Sciences **38**, 1179–1196 (1981).

[65] B. J. Hoskins et P. J. Valdes, "On the Existence of Storm-Tracks," Journal of Atmospheric Sciences **47**, 1854–1864 (1990).

[66] J. W. Hurrell et C. Deser, "North Atlantic climate variability : The role of the North Atlantic Oscillation," Journal of Marine Systems **78**, 28–41 (2009).

[67] M. M. Hurwitz, P. A. Newman, et C. I. Garfinkel, "On the influence of North Pacific sea surface temperature on the Arctic winter climate," Journal of Geophysical Research Atmospheres **117**, 1–13 (2012).

[68] O. Isoguchi et H. Kawamura, "Seasonal to interannual variations of the western boundary current of the subarctic North Pacific by a combination of the altimeter and tide gauge sea levels," Journal of Geophysical Research : Oceans **111**, 1–17 (2006).

[69] T. M. Joyce, Y. O. Kwon, et L. Yu, "On the relationship between synoptic wintertime atmospheric variability and path shifts in the Gulf Stream and the Kuroshio Extension," Journal of Climate **22**, 3177–3192 (2009).

[70] G. Judge, R. Hill, W. Griffiths, H. Lutkepohl, et T. Lee, *Introduction to the Theory and Practice of Econometrics* (Second Edition New York : John Wiley and Sons, 1988).

[71] E. Kalnay, M. Kanamitsu, R. Kistler, W. Collins, D. Deaven, L. Gandin, M. Iredell, S. Saha, G. White, J. Woollen, Y. Zhu, M. Chelliah, W. Ebisuzaki, W. Higgins, J. Janowiak, K. C. Mo, C. Ropelewski, J. Wang, A. Leetmaa, R. Reynolds, R. Jenne, et D. Joseph, "The NCEP/NCAR 40-year reanalysis project," Bulletin of the American Meteorological Society **77**, 437–471 (1996).

[72] K. A. Kelly, R. J. Small, R. M. Samelson, B. Qiu, T. M. Joyce, Y. O. Kwon, et M. F. Cronin, "Western boundary currents and frontal air-sea interaction : Gulf stream and Kuroshio Extension," Journal of Climate **23**, 5644–5667 (2010).

[73] M. Kendall, A. Stuart, et J. Ord, *Kendall's advanced theory of statistics* (Fifth Edition New York : Oxford University Press, 1991).

[74] R. A. Kerr, "A North Atlantic Climate Pacemaker for the Centuries," Science **288**, 1984 LP – 1985 (2000).

[75] F. Kobashi, S. P. Xie, N. Iwasaka, et T. T. Sakamoto, "Deep atmospheric response to the North Pacific oceanic subtropical front in spring," Journal of Climate **21**, 5960–5975 (2008).

[76] Y.-H. Kuo, S. Low-Nam, et R. J. Reed, "Effects of Surface Energy Fluxes during the Early Development and Rapid Intensification Stages of Seven Explosive Cyclones in the Western Atlantic," Monthly Weather Review **119**, 457–476 (1991).

[77] Y. Kushnir, W. A. Robinson, I. Bladé, N. M. J. Hall, S. Peng, et R. Sutton, "Atmospheric GCM response to extratropical SST anomalies : Synthesis and evaluation," Journal of Climate **15**, 2233–2256 (2002).

[78] Y. O. Kwon, M. A. Alexander, N. A. Bond, C. Frankignoul, H. Nakamura, B. Qiu, et L. Thompson, "Role of the gulf Stream and Kuroshio-Oyashio systems in large-scale atmosphere-ocean interaction : A review," Journal of Climate **23**, 3249–3281 (2010).

[79] Y. O. Kwon et T. M. Joyce, "Northern hemisphere winter atmospheric transient eddy heat fluxes and the gulf stream and Kuroshio-Oyashio extension variability," Journal of Climate **26**, 9839–9859 (2013).

[80] Y.-O. Kwon et C. Deser, "North Pacific Decadal Variability in the Community Climate System Model Version 2," Journal of Climate **20**, 2416–2433 (2007).

[81] M. Latif et T. Barnett, "Causes of decadal climate variability over the North Pacific and North America," Science **266**, 634–637 (1994).

[82] M. Latif et T. P. Barnett, "Decadal climate variability over the North Pacific and North America : Dynamics and predictability," Journal of Climate **9**, 2407–2423 (1996).

[83] N.-C. Lau, A. Leetmaa, M. J. Nath, et H.-L. Wang, "Influences of ENSO-Induced Indo – Western Pacific SST Anomalies on Extratropical Atmospheric Variability during the Boreal Summer," Journal of Climate **18**, 2922–2942 (2005).

[84] N.-C. Lau et M. J. Nath, "The role of the "atmospheric bridge in linking tropical Pacific ENSO events to extratropical SST anomalies," Journal of Climate **9**, 2036–2057 (1996).

[85] M. E. Linkin et S. Nigam, "The North Pacific Oscillation-West Pacific teleconnection pattern : Mature-phase structure and winter impacts," Journal of Climate **21**, 1979–1997 (2008).

[86] Q. Liu, N. Wen, et Z. Liu, "An observational study of the impact of the North Pacific SST on the atmosphere," Geophysical Research Letters **33** (2006).

[87] Z. Liu, "Dynamics of interdecadal climate variability : A historical perspective," Journal of Climate **25**, 1963–1995 (2012).

[88] Z. Liu et M. Alexander, "Atmospheric bride, oceanic tunnel, and global climate teleconnections," Reviews of Geophysics **45**, 1–34 (2007).

[89] Z. Liu, L. Fan, S. I. Shin, et Q. Liu, "Assessing atmospheric response to surface forcing in the observations. Part II : Cross validation of seasonal response using GEFA and LIM," Journal of Climate **25**, 6817–6834 (2012).

[90] Z. Liu, Y. Liu, L. Wu, et R. Jacob, "Seasonal and long-term atmospheric responses to reemerging North Pacific Ocean variability : A combined dynamical and statistical assessment," Journal of Climate **20**, 955–980 (2007).

[91] Z. Liu et N. Wen, "On the assessment of nonlocal climate feedback. Part II : EFA-SVD and optimal feedback modes," Journal of Climate **21**, 5402–5416 (2008).

[92] Z. Liu, N. Wen, et L. Fan, "Assessing atmospheric response to surface forcing in the observations. Part I : Cross validation of annual response using GEFA, LIM, and FDT," Journal of Climate **25**, 6796–6816 (2012).

[93] Z. Liu et L. Wu, "Atmospheric response to North Pacific SST : The role of ocean-atmosphere coupling," Journal of Climate **17**, 1859–1882 (2004).

[94] E. D. Lorenzo, K. M. Cobb, J. C. Furtado, N. Schneider, B. T. Anderson, A. Bracco, M. A. Alexander, et D. J. Vimont, "Central Pacific El Niño and decadal climate change in the North Pacific Ocean," Nature Geoscience **3**, 762–765 (2011).

[95] Z. Lui, N. Wen, et Y. Liu, "On the assessment of nonlocal climate feedback. Part I : The generalized equilibrium feedback assessment," Journal of Climate **21**, 134–148 (2008).

[96] N. J. Mantua, S. R. Hare, Y. Zhang, J. M. Wallace, et R. C. Francis, "A Pacific Interdecadal Climate Oscillation with Impacts on Salmon Production," Bulletin of the American Meteorological Society **78**, 1069–1079 (1997).

[97] R. Masunaga, H. Nakamura, T. Miyasaka, K. Nishii, et Y. Tanimoto, "Separation of climatological imprints of the Kuroshio Extension and Oyashio fronts on the wintertime atmospheric boundary layer : Their sensitivity to SST resolution prescribed for atmospheric reanalysis," Journal of Climate **28**, 1764–1787 (2015).

[98] S. Minobe, A. Kuwano-Yoshida, N. Komori, S.-P. Xie, et R. J. Small, "Influence of the Gulf Stream on the troposphere." Nature **452**, 206–9 (2008).

[99] S. Minobe, M. Miyashita, A. Kuwano-Yoshida, H. Tokinaga, et S. P. Xie, "Atmospheric response to the Gulf Stream : Seasonal variations," Journal of Climate **23**, 3699–3719 (2010).

[100] T. Miyasaka, H. Nakamura, B. Taguchi, et M. Nonaka, "Multidecadal modulations of the low-frequency climate variability in the wintertime North Pacific since 1950," Geophysical Research Letters **41**, 2948–2955 (2005).

[101] V. Moron et I. Gouirand, "Seasonal modulation of the El Niño-southern oscillation relationship with sea level pressure anomalies over the North Atlantic in October-March 1873-1996," International Journal of Climatology **23**, 143–155 (2003).

[102] H. Nakamura, "Decadal changes in the North Pacific oceanic frontal zones as revealed in ship and satellite observations," Journal of Geophysical Research **108**, 3078 (2003).

[103] H. Nakamura, "Midwinter Suppression of Baroclinic Wave Activity in the Pacific," Journal of the Atmospheric Sciences **49**, 1629–1642 (1992).

[104] H. Nakamura, T. Sampe, A. Goto, W. Ohfuchi, et S. P. Xie, "On the importance of midlatitude oceanic frontal zones for the mean state and dominant variability in the tropospheric circulation," Geophysical Research Letters **35**, 1–5 (2008).

[105] H. Nakamura, T. Sampe, Y. Tanimoto, et A. Shimpo, "Observed associations among storm tracks, jet streams and midlatitude oceanic fronts," Geophysical Monograph **147**, 329–345 (2004).

[106] H. Nakamura et A. Shimpo, "Seasonal variations in the Southern Hemisphere storm tracks and jet streams as revealed in a reanalysis dataset," Journal of Climate **17**, 1828–1844 (2004).

[107] H. Nakamura et T. Yamagata, *Recent Decadal SST Variability in the Northwestern Pacific and Associated Atmospheric Anomalies* (Springer Berlin Heidelberg, Berlin, Heidelberg, 1999), p. 49–72.

[108] J. Namias, "A 5-year experiment in the preparation of seasonal outlooks," Monthly Weather Review **92**, 449–464 (1964).

[109] J. Namias, "Stability of an expanded circumpolar vortex," Journal of Atmospheric Sciences **22**, 728–729 (1965).

[110] J. Namias, "Interactions of circulation and weather between hemispheres," Monthly Weather Review **October-De**, 482–486 (1963).

[111] J. Namias et D. R. Cayan, "Large-scale air-sea interactions and short-period climatic fluctuatioins," Science **214**, 869–876 (1981).

[112] P. J. Neiman et M. a. Shapiro, "The life cycle of an extratropical marine cyclone. Part I : frontal-cyclone evolution and thermodynamic air-sea interaction," Mon. Wea. Rev. **121**, 2153–2176 (1993).

[113] M. Newman, M. A. Alexander, T. R. Ault, K. M. Cobb, C. Deser, E. Di Lorenzo, N. J. Mantua, A. J. Miller, S. Minobe, H. Nakamura, N. Schneider, D. J. Vimont, A. S. Phillips, J. D. Scott, et C. A. Smith, "The Pacific decadal oscillation, revisited," Journal of Climate **29**, 4399–4427 (2016).

[114] M. Newman, G. P. Compo, et M. A. Alexander, "ENSO-forced variability of the Pacific decadal oscillation," Journal of Climate **16**, 3853–3857 (2003).

[115] S. Nigam, "Teleconnections," Encyclopedia of Atmospheric Sciences p. 2243–2269 (2003).

[116] K. Nishii, H. Nakamura, et Y. J. Orsolini, "Cooling of the wintertime Arctic stratosphere induced by the western Pacific teleconnection pattern," Geophysical Research Letters **37**, 1–6 (2010).

[117] M. Nonaka, H. Nakamura, Y. Tanimoto, T. Kagimoto, et H. Sasaki, "Decadal Variability in the Kuroshio – Oyashio Extension Simulated in an," Journal of Climate **19**, 1970–1989 (2005).

[118] M. Nonaka, H. Nakamura, B. Taguchi, N. Komori, A. Kuwano-Yoshida, et K. Takaya, "Air-sea heat exchanges characteristic of a prominent midlatitude oceanic front in the South Indian Ocean as simulated in a high-resolution coupled GCM," Journal of Climate **22**, 6515–6535 (2009).

[119] M. Nonaka, H. Nakamura, Y. Tanimoto, et H. Sasaki, "Interannual-to-decadal variability in the Oyashio and its influence on temperature in the subarctic frontal zone : An eddy-resolving OGCM simulation," Journal of Climate **21**, 6283–6303 (2008).

[120] W. A. Nuss et S. I. Kamikawa, "Dynamics and boundary later processes in two asian cyclones," Monthly Weather Review **118**, 755–771 (1990).

[121] C. H. O'Reilly et A. Czaja, "The response of the pacific storm track and atmospheric circulation to kuroshio extension variability," Quarterly Journal of the Royal Meteorological Society **141**, 52–66 (2015).

[122] M. Ogi, B. Taguchi, M. Honda, D. G. Barber, et S. Rysgaard, "Summer-to-winter sea-ice linkage between the Arctic ocean and the Okhotsk sea through atmospheric circulation," Journal of Climate **28**, 4971–4979 (2015).

[123] S. Okajima, H. Nakamura, K. Nishii, T. Miyasaka, et A. Kuwano-Yoshida, "Assessing the importance of prominent warm SST anomalies over the midlatitude north pacific in forcing large-scale atmospheric anomalies during 2011 summer and autumn," Journal of Climate **27**, 3889–3903 (2014).

[124] Y. M. Okumura, "Origins of tropical pacific decadal variability : Role of stochastic atmospheric forcing from the South Pacific," Journal of Climate **26**, 9791–9796 (2013).

[125] O. H. Ottera, M. Bentsen, H. Drange, et L. Suo, "External forcing as a metronome for Atlantic multidecadal variability," Nature Geoscience **3**, 688–694 (2010).

[126] J. E. Overland, J. M. Adams, et N. A. Bond, "Decadal variability of the Aleutian low and its relation to high-latitude circulation," Journal of Climate **12**, 1542–1548 (1999).

[127] S. Park, C. Deser, et M. Alexander, "Estimation of the surface heat flux response to sea surface temperature anomalies over the global oceans," Journal of climate **18**, 4582–4599 (2005).

[128] S. Peng et W. A. Robinson, "Relationships between atmospheric internal variability and the responses to an extratropical SST anomaly," Journal of Climate **14**, 2943–2959 (2001).

[129] S. Peng, W. A. Robinson, et M. P. Hoerling, "The modeled atmospheric response to midlatitude SST anomalies and its dependence on background circulation states," Journal of Climate **10**, 971–987 (1997).

[130] S. Peng et J. S. Whitaker, "Mechanisms determining the atmospheric response to midlatitude SST anomalies," Journal of Climate **12**, 1393–1408 (1999).

[131] D. W. Pierce, T. P. Barnett, N. Schneider, R. Saravanan, D. Dommenget, et M. Latif, "The role of ocean dynamics in producing decadal climate variability in the North Pacific," Climate Dynamics **18**, 51–70 (2001).

[132] S. Pierini, "Kuroshio extension bimodality and the North Pacific oscillation : A case of intrinsic variability paced by external forcing," Journal of Climate **27**, 448–454 (2014).

[133] S. Pierini, "A Kuroshio Extension System Model Study : Decadal Chaotic Self-Sustained Oscillations," Journal of Physical Oceanography **36**, 1605–1625 (2006).

[134] R. A. Plumb, "Three-Dimensional Propagation of Transient Quasi-Geostrophic Eddies and Its Relationship with the Eddy Forcing of the Time—Mean Flow," Journal of the Atmospheric Sciences **43**, 1657–1678 (1986).

[135] R. A. Plumb, "On the Three-Dimensional Propagation of Stationary Waves," Journal of the Atmospheric Sciences **42**, 217–229 (1985).

[136] L. M. Polvani et D. W. Waugh, "Upward wave activity flux as a precursor to extreme stratospheric events and subsequent anomalous surface weather regimes," Journal of Climate **17**, 3548–3554 (2004).

[137] A. D. Pozo-Vazquez, S. R. Gamiz-Fortis, J. Tovar-Pescador, M. J. Esteban-Parra, et Y. Castro-Diez, "North Atlantic winter SLP anomalies based on the autumn ENSO state," Journal of Climate **18**, 97–103 (2005).

[138] B. Qiu, "Kuroshio and Oyashio Currents," Encyclopedia of Ocean Sciences : Second Edition p. 1414–1425 (2008).

[139] B. Qiu, "The Kuroshio Extension System : its large-scale variability and role in the midlatitude ocean-atmosphere interaction," Journal of Oceanography **58**, 57–75 (2002).

[140] B. Qiu, "Kuroshio Extension Variability and Forcing of the Pacific Decadal Oscillations : Responses and Potential Feedback," Journal of Physical Oceanography **33**, 2465–2482 (2003).

[141] B. Qiu, "Interannual Variability of the Kuroshio Extension System and Its Impact on the Wintertime SST Field," Journal of Physical Oceanography **30**, 1486–1502 (2000).

[142] B. Qiu et S. Chen, "Decadal Variability in the Large-Scale Sea Surface Height Field of the South Pacific Ocean : Observations and Causes," Journal of Physical Oceanography **36**, 1751–1762 (2006).

[143] B. Qiu et S. Chen, "Eddy-mean flow interaction in the decadally modulating Kuroshio Extension system," Deep-Sea Research Part II : Topical Studies in Oceanography **57**, 1098–1110 (2010).

[144] B. Qiu et S. Chen, "Eddy-Induced Heat Transport in the Subtropical North Pacific from Argo, TMI, and Altimetry Measurements," Journal of Physical Oceanography **35**, 458–473 (2005).

[145] B. Qiu, S. Chen, N. Schneider, et B. Taguchi, "A coupled decadal prediction of the dynamic state of the kuroshio extension system," Journal of Climate **27**, 1751–1764 (2014).

[146] A. Révelard, C. Frankignoul, N. Sennéchael, Y. O. Kwon, et B. Qiu, "Influence of the decadal variability of the Kuroshio Extension on the atmospheric circulation in the cold season," Journal of Climate **29**, 2123–2144 (2016).

[147] G. Rivière, "Effect of Latitudinal Variations in Low-Level Baroclinicity on Eddy Life Cycles and Upper-Tropospheric Wave-Breaking Processes," Journal of the Atmospheric Sciences **66**, 1569–1592 (2009).

[148] B. Rodriguez-Fonseca, R. Suarez-Moreno, B. Ayarzaguena, J. Lopez-Parages, I. Gomara, J. Villamayor, E. Mohino, T. Losada, et A. Castano-Tierno, "A review of ENSO influence on the North Atlantic. A non-stationary signal," Atmosphere **7**, 1–19 (2016).

[149] M. J. Rodwell et C. K. Folland, "Atlantic air–sea interaction and seasonal predictability," Quarterly Journal of the Royal Meteorological Society **128**, 1413–1443 (2002).

[150] N. H. Saji, B. N. Goswami, P. N. Vinayachandran, et T. Yamagata, "A dipole mode in the tropical Indian Ocean," Nature **401**, 360–363 (1999).

[151] R. Salmon et M. C. Hendershott, "Large-Scale Air-Sea Interactions With a Simple General Circulation Model," Tellus **28**, 228–242 (1976).

[152] T. Sampe, H. Nakamura, A. Goto, et W. Ohfuchi, "Significance of a midlatitude SST frontal zone in the formation of a storm track and an eddy-driven westerly jet," Journal of Climate **23**, 1793–1814 (2010).

[153] F. Sanders et J. R. Gyakum, "Synoptic-dynamic climatology of the "bomb"," Monthly Weather Review **108**, 1589–1606 (1980).

[154] R. Saravanan, G. Danabasoglu, S. C. Doney, et J. C. McWilliams, "Decadal Variability and Predictability in the Midlatitude Ocean – Atmosphere System," Journal of Climate **13**, 1073–1097 (2000).

[155] Y. N. Sasaki, S. Minobe, et N. Schneider, "Decadal Response of the Kuroshio Extension Jet to Rossby Waves : Observation and Thin-Jet Theory*," Journal of Physical Oceanography **43**, 442–456 (2013).

[156] N. Schneider et A. J. Miller, "Predicting Western North Pacific Ocean climate," Journal of Climate **14**, 3997–4002 (2001).

[157] N. Schneider et B. D. Cornuelle, "The forcing of the Pacific Decadal Oscillation," Journal of Climate **18**, 4355–4373 (2005).

[158] N. Schneider, A. J. Miller, et D. W. Pierce, "Anatomy of North Pacific decadal variability," Journal of Climate **15**, 586–605 (2002).

[159] R. B. Scott et B. Qiu, "Predictability of SST in a stochastic climate model and its application to the Kuroshio extension region," Journal of Climate **16**, 312–322 (2003).

[160] R. Seager, Y. Kushnir, N. H. Naik, M. A. Cane, et J. Miller, "Wind-driven shifts in the latitude of the Kuroshio-Oyashio extension and generation of SST anomalies on decadal timescales," Journal of Climate **14**, 4249–4265 (2001).

[161] R. Seager, A. R. Karspeck, M. A. Cane, Y. Kushnir, A. Giannini, A. Kaplan, B. Kerman, et J. Velez, "Predicting Pacific decadal variability," (2004).

[162] Y. Sekine, "Anomalous southward intrusion of the Oyashio east of Japan : 1. Influence of the seasonal and interannual variations in the wind stress over the North Pacific," Journal of Geophysical Research **93**, 2247–2255 (1988).

[163] Y. Sekine, "Anomalous southward intrusions of the Oyashio east of Japan 2. Two-layer numerical model," Journal of Geophysical Research **104**, 3049–3058 (1999).

[164] T. Semmler, T. Jung, et S. Serrar, "Fast atmospheric response to a sudden thinning of Arctic sea ice," Climate Dynamics **46**, 1015–1025 (2016).

[165] Y. Seo, S. Sugimoto, et K. Hanawa, "Long-term variations of the Kuroshio Extension path in winter : Meridional movement and path state change," Journal of Climate **27**, 5929–5940 (2014).

[166] L. Sheldon et A. Czaja, "Seasonal and interannual variability of an index of deep atmospheric convection over western boundary currents," Quarterly Journal of the Royal Meteorological Society **140**, 22–30 (2014).

[167] R. J. Small, S. P. DeSzoeke, S. P. Xie, L. O'Neill, H. Seo, Q. Song, P. Cornillon, M. Spall, et S. Minobe, "Air-sea interaction over ocean fronts and eddies," Dynamics of Atmospheres and Oceans **45**, 274–319 (2008).

[168] D. Smirnov, M. Newman, et M. A. Alexander, "Investigating the role of ocean-atmosphere coupling in the North Pacific ocean," Journal of Climate **27**, 592–606 (2014).

[169] D. Smirnov, M. Newman, M. A. Alexander, Y. O. Kwon, et C. Frankignoul, "Investigating the local atmospheric response to a realistic shift in the Oyashio sea surface temperature front," Journal of Climate **28**, 1126–1147 (2015).

[170] G. W. Stewart, "Collinearity and least squares regression," Statistical Science **2**, 68–100 (1987).

[171] S. Sugimoto, "Influence of SST anomalies on winter turbulent heat fluxes in the eastern Kuroshio-Oyashio confluence region," Journal of Climate **27**, 9349–9358 (2014).

[172] S. Sugimoto et K. Hanawa, "Roles of SST anomalies on the wintertime turbulent heat fluxes in the kuroshio-oyashio confluence region : Influences of warm eddies detached from the kuroshio extension," Journal of Climate **24**, 6551–6561 (2011).

[173] B. Taguchi, H. Nakamura, M. Nonaka, N. Komori, A. Kuwano-Yoshida, K. Takaya, et A. Goto, "Seasonal evolutions of atmospheric response to decadal SST anomalies in the North Pacific subarctic frontal zone, observations and a coupled model simulation," Journal of Climate **25**, 111–139 (2012).

[174] B. Taguchi, H. Nakamura, M. Nonaka, et S. P. Xie, "Influences of the Kuroshio/Oyashio extensions on air-sea heat exchanges and storm-track activity as revealed in regional atmospheric model simulations for the 2003/04 cold season," Journal of Climate **22**, 6536–6560 (2009).

[175] B. Taguchi, S. P. Xie, N. Schneider, M. Nonaka, H. Sasaki, et Y. Sasai, "Decadal variability of the Kuroshio Extension : Observations and an eddy-resolving model hindcast," Journal of Climate **20**, 2357–2377 (2007).

[176] K. Takaya et H. Nakamura, "A Formulation of a Phase-Independent Wave-Activity Flux for Stationary and Migratory Quasigeostrophic Eddies on a Zonally Varying Basic Flow," Journal of the Atmospheric Sciences **58**, 608–627 (2001).

[177] H. Tokinaga, Y. Tanimoto, S. P. Xie, T. Sampe, H. Tomita, et H. Ichikawa, "Ocean frontal effects on the vertical development of clouds over the western North Pacific : In situ and satellite observations," Journal of Climate **22**, 4241–4260 (2009).

[178] K. E. Trenberth, G. W. Branstator, D. Karoly, a. Kumar, N. C. Lau, et C. Ropelewski, "Progress during TOGA in understanding and modeling global teleconnections associated with tropical sea surface temperatures," Journal of Geophysical Research-Oceans **103**, 14291–14324 (1998).

[179] K. E. Trenberth et D. P. Stepaniak, "Indices of El Nino evolution," Journal of Climate **14**, 1697–1701 (2001).

[180] K. E. Trenberth, "A quasi-biennial standing wave in the Southern Hemisphere and interrelations with sea surface temperature," Quarterly Journal of the Royal Meteorological Society **101**, 55–74 (1975).

[181] K. E. Trenberth et J. M. Caron, "Estimates of Meridional Atmosphere and Ocean Heat Transports," Journal of Climate **14**, 3433–3443 (2001).

[182] K. E. Trenberth et J. W. Hurrell, "Decadal atmosphere-ocean variations in the Pacific," Climate Dynamics **9**, 303–319 (1994).

[183] D. J. Vimont, "The contribution of the interannual ENSO cycle to the spatial pattern of decadal ENSO-like variability," Journal of Climate **18**, 2080–2092 (2005).

[184] F. Vivier, K. a. Kelly, et L. A. Thompson, "Heat Budget in the Kuroshio Extension Region : 1993–99," Journal of Physical Oceanography **32**, 3436–3454 (2002).

[185] T. Wagawa, S.-I. Ito, Y. Shimizu, S. Kakehi, et D. Ambe, "Currents Associated with the Quasi-Stationary Jet Separated from the Kuroshio Extension," Journal of Physical Oceanography **44**, 1636–1653 (2014).

[186] B. Wang, J. Liu, H. J. Kim, P. J. Webster, et S. Y. Yim, "Recent change of the global monsoon precipitation (1979-2008)," Climate Dynamics **39**, 1123–1135 (2012).

[187] C. Z. Wang, "Atlantic climate variability and its associated atmospheric circulation cells," Journal of Climate **15**, 1516–1536 (2002).

[188] N. Wen, Z. Liu, Q. Liu, et C. Frankignoul, "Observed atmospheric responses to global SST variability modes : A unified assessment using GEFA," Journal of Climate **23**, 1739–1759 (2010).

[189] L. Wu et Z. Liu, "North Atlantic decadal variability : Air-sea coupling, oceanic memory, and potential Northern Hemisphere resonance," Journal of Climate **18**, 331–350 (2005).

[190] S. P. Xie, "Satellite observations of cool ocean-atmosphere interaction," Bulletin of the American Meteorological Society **85**, 195–208 (2004).

[191] S.-P. Xie, T. Kunitani, A. Kubokawa, M. Nonaka, et S. Hosoda, "Interdecadal Thermocline Variability in the North Pacific for 1958–97 : A GCM Simulation," Journal of Physical Oceanography **30**, 2798–2813 (2000).

[192] S. Yang, S. H. Yoo, R. Yang, K. E. Mitchell, H. van den Dool, et R. W. Higgins, "Response of seasonal simulations of a regional climate model to high-frequency variability of soil moisture during the summers of 1988 and 1993," Journal of Hydrometeorology **8**, 738–757 (2007).

[193] S. Yoshiike et R. Kawamura, "Influence of wintertime large-scale circulation on the explosively developing cyclones over the western North Pacific and their downstream effects," Journal of Geophysical Research Atmospheres **114**, 1–15 (2009).

[194] L. Yu et R. A. Weller, "Objectively analyzed air-sea heat fluxes for the global ice- free oceans (1981-2005)," Bulletin of the American Meteorological Society **88**, 527–539 (2007).

[195] T. Zhang, M. P. Hoerling, J. Perlwitz, et T. Xu, "Forced atmospheric teleconnections during 1979-2014," Journal of Climate **29**, 2333–2357 (2016).